NONLINEAR OPTICAL WAVES IN CATIONIC POLYMERIZATION SYSTEMS: FACILE ROUTES TO 3-D POLYMER AND METALLODIELECTRIC FUNCTIONAL MICROSTRUCTURES

NONLINEAR OPTICAL WAVES IN CATIONIC POLYMERIZATION SYSTEMS: FACILE ROUTES TO 3-D POLYMER AND METALLODIELECTRIC FUNCTIONAL MICROSTRUCTURES

By

Dinesh Kumar Basker B.Tech

A Thesis
Submitted to the School of Graduate Studies in Partial Fulfillment of the
Requirements for the Degree
Doctor of Philosophy in Chemistry

McMaster University

DOCTORATE OF PHILOSOPHY (2016) McMASTER UNIVERSITY

(Chemistry) Hamilton, Ontario

TITLE:	Nonlinear optical waves in cationic polymerization systems: facile routes to 3-D polymer and metallodielectric functional microstructures
AUTHOR:	Dinesh Basker B.Tech
SUPERVISOR:	Dr.Kalaichelvi Saravanamuttu
NUMBER OF PAGES:	262

Abstract

Optical nonlinear phenomena occur in a material when the response of a material's property to the applied optical field depends nonlinearly on the strength of the applied field. Cationic polymerization induced refractive index change (Δn) (nonlinear response of material's property) in epoxide systems was exploited to elicit modulation instability (MI) and self-trapping (optical nonlinear phenomena) of incoherent light. Demonstration of nonlinear waveforms in cationic polymerization systems revealed that (i) the dynamics of MI can be controlled by polymerization kinetics. This adds a new dimension to the studies of MI in nonlinear systems, as the dynamics of the process so far has been predominantly described by optical parameters such as intensity, wavelength and coherence. Our study shows for the first time that MI occurs only when a balance is struck between photoresponsive time (determined by polymerization rate) and magnitude of Δn (determined by the extent of cross-linking). Thus, it showed that the dynamics of the process can be tuned by polymerization kinetics. Also nonlinear phenomena in cationic systems provide facile routes to robust three dimensional polymer and metallodielectric functional microstructures. (ii) Utilizing the correlation between polymerization kinetics and MI dynamics, thermomechanically stable epoxide-siloxane blend systems were developed for the fabrication of MI induced 3D polymer waveguide microstructures. These blend systems are mechanically robust, thermally stable as well as they satisfy the prerequisites for the occurrence of MI. (iii) Metallodieletric (polymer microstructures embedded with gold and silver nanoparticles) 3D microstructures were fabricated in epoxide-siloxane blend systems by combining *in-situ* synthesis with MI. (iv) Also *in-situ* synthesis of gold nanoparticles in epoxide-siloxane matrix was combined with photopolymerization to generate gold nanoparticles fractal aggregates embedded thin films. And these metallodielectric flexible thin films were shown as effective SERS substrates. (v) Optical nonlinearity offered by the photocationic polymerization of epoxide was exploited to show self-trapping of incoherent beam, another nonlinear phenomenon which occurs under similar conditions to MI. Based on self-trapping of incoherent beam in photopolymerizable epoxide system, a new 3D printing technique was developed.

Acknowledgement

I would like to thank my supervisor Dr. Kalaichelvi Saravanamuttu for providing me the opportunity to be a part of an excellent research group. Her open-mindedness towards new research ideas and her genuine enthusiasm about new results greatly motivated my doctoral studies.

I would like to thank my committee members Dr. Harald Stover and Dr. Ayse Turak for their continuous support and positive feedbacks throughout my research. Special thanks to Dr. Mike Brook for his valuable photochemistry inputs.

I had the luxury of working with some wonderful support staffs, facility managers and PIs. I would like to thank Dr. Nick Burke from Dr. Harald Stover's lab for training me on their group's optical microscope, Dr. Mike Brook for letting me use his lab facilities, Dr. Alex Adronov for letting me use his NIR/UV/Vis spectrometer and Raman Spectrometer, Dr. Steve Kornic and Megan Fair for training and helping me with Raman spectrometer and FTIR spectrometer, Frank Gibbs from BIMR for his help with DSC and TGA, Antoni Dabkowski and Hanna Dabkowski for letting me use their lab facilities, Dr. Glynis de Silveira, Dr. Carmen Andrei and Chris Butcher from Canadian Centre for Electron Microscopy (CCEM) and Marcia from McMaster Hospital for their assistances with SEM, TEM and optical microscopy, Dr. Danielle Covelli from Biointerfaces institute for her help with surface characterization, Elizabeth Takacs from McMaster manufacturing research institute (MMRI) for training and helping

me with tensile testing, Terry Wagg from MMRI for his assistance with mold manufacturing.

Working in lab was so much fun because of the amazing people in my research group. Many thanks to Matthew R. Ponte, Liqun Qiu, Alexander Hudson, Hao lin, Ian Dean hosein and Derek Morim for their interesting research inputs and valuable discussions I had with them. Special thanks to Oscar for helping me in the final stage of my research work.

Special thanks to my high school headmaster Mr. Lekshmiganthan Lekkureddy, who motivated me to take post-graduation studies, words cannot describe his selfless service not only to me but also for the entire student community. I would like to thank my undergraduate supervisor Dr. B. Kothandaraman, who introduced the epoxide chemistry to me and Dr. V.Subrahmanian, who taught me critical thinking.

Finally, I would like to thank my parents, Gajalakshmi and Basker and my brother Murali Dharan, I could not have done my research without their support. Especially my mom, she is the invisible force behind my success. I dedicate this work to my lovely mom.

Table of contents

Chapter 5 Spontaneous formation of Au nanoparticle fractals in epoxy films and their application as free-standing substrates for NIR Surface Enhanced Raman Spectroscopy…………………………………………………………..189

List of figures

List of tables

List of schemes

Chapter 1 Introduction

Nonlinear wave is one of the fundamental entities of nature. These waves are observed in solid state and plasma physics, chemical reaction kinetics, fluid dynamics, gravity and optics. Nonlinearity in optical waves originates from the interaction of light with matter and results in a wide range of nonlinear optical phenomena such as frequency mixing processes, self and cross-phase modulation, stimulated Brillouin scattering, multi photon absorption, optical solitons, self-trapping and modulation instability, etc. Whenever a new nonlinear medium is introduced in the field of nonlinear optics, it leads to a series of new discoveries. Motivated by this, modulation instability and self-trapping of optical beams are studied in this research work in cationic polymerization systems for the first time.

The introduction chapter is presented in four parts, starting with the review of nonlinear optical effects relevant to the studies presented in this thesis: self-trapping and modulation instability, followed by the review of nonlinear optical materials with an emphasis on polymeric materials in second part, and in third part application of linear and nonlinear optical techniques for the fabrication of polymer and metallodielectric micro and macro structures is presented, followed by a brief overview about cationic polymerization. Finally, the objective of this research work and the arrangement of this thesis are presented.

1.1. Self-trapping of optical beams

Self-trapping of waves has been observed in various systems like sound waves,[1] matter waves[2] and electromagnetic waves.[3–6] In optics, self-trapping of electromagnetic waves in nonlinear media results in spatial solitons, which can be understood as follows:[7,8] One of the characteristics of wave propagation in linear dispersive media is its tendency to broaden due to diffractive and dispersive effects. Such broadening occurs both in space and time. In temporal domain, different frequency components propagate with different velocities in media that possess chromatic dispersion, leading to broadening of temporal pulse width. In spatial domain, phase fronts propagating in linear media undergo slight angular deviation with respect to the propagation axis and therefore propagate at different phase velocity resulting in spatial broadening. Such spatio-temporal broadening can be curbed in a nonlinear media, when the beam increases the refractive index of the media forming a waveguide structure and guides itself in the induced waveguide. As a result, a self-trapped beam or a spatial soliton forms. As shown in figure 1.1 solitons are the exact balance between linear diffraction and nonlinearly induced self-lensing or self-focusing. Thus, under certain conditions, the beam creates a potential *via* nonlinearity and bounds itself in the induced potential.

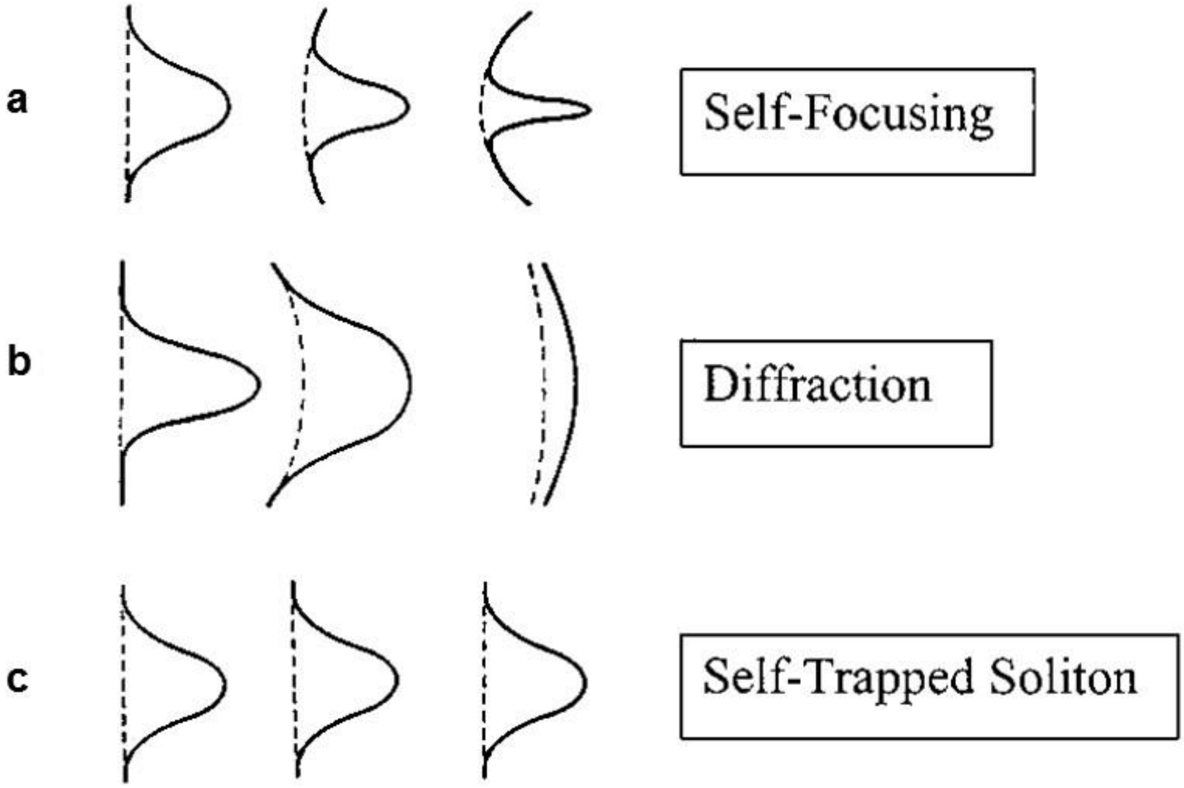

Figure 1.1 Schematic showing phase fronts (dashed line) and spatial beam profile (solid line) a) self-focusing beam b) diffracting beam c) self-trapped beam. Reprinted with permission from IEE.[8]

1.1.1. Soliton solution for nonlinear Schrödinger equation

Self-trapped optical beam or soliton formation can be explained by solving nonlinear Schrödinger (NLS) like equation, which governors the propagation of light in nonlinear media. NLS for optical waves is derived from Maxwell's equations for the electric field associated with the propagating optical wave in nonlinear media. Although the origin of nonlinearity in these media can be from different mechanisms like Kerr effect or photorefractive effect or Pockels effect, all these nonlinear effects make the refractive index of the media dependent on the intensity of the propagating optical wave. This intensity dependent refractive index balances the natural divergence of the beam resulting in self-trapped beam or soliton. The process can be mathematically explained in a Kerr type nonlinear media using NLS as follows (the approach can be extended to other types of nonlinearity as well): The equation for the electric field E associated with optical field propagating in nonlinear Kerr media is given by,[9]

$$\nabla^2 E - \frac{1}{c^2}\frac{\partial^2 E}{\partial t^2} - \frac{1}{\epsilon_0 c^2}\frac{\partial^2 P}{\partial t^2} = 0 \qquad (3)$$

where ϵ_0 is the vacuum permittivity, c is the speed of light and P is the induced polarization in the medium. P consists of two parts

$$P(r, t) = P_L(r, t) + P_{NL}(r, t)$$

where P_{NL} and P_L are nonlinear and linear part of induced polarization in the medium respectively. In case of a continuous wave (cw) wave self-trapping a general solution for equation (3) can be obtained of the form:[10]

$$E(r, t) = A(r)\exp^{i\beta 0z} \qquad (4)$$

$\beta = 2\pi n_0/\lambda$, is the propagation constant. Function A describes the evolution of the propagating beam envelope. The beam propagates along the z direction and diffracts or self-traps in the two transverse directions x and y. x, y and z are the cartesian coordinates corresponding to the polar coordinate r and θ. Applying the slowly varying approximation (paraxial approximation) and including the nonlinear and diffractive effects to the envelope A (where $\partial^2 A/\partial z^2$ is negligible), solution (4) satisfies the nonlinear parabolic equation (5) (where the first term represents the propagation of envelope A in z direction and second term in the parenthesis shows the diffraction of beam in the transverse directions and third term accounts for the nonlinearity of the medium, $n_{nl}(I)$ is the intensity dependent refractive index) used to model the spatial self-trapping of optical beam in different nonlinear systems and the term n_{nl} can be modified based on the type of nonlinearity used.

$$2i\beta_0 \frac{\partial A}{\partial z} + \left(\frac{\partial^2 A}{\partial x^2} + \frac{\partial^2 A}{\partial y^2}\right) + 2\beta_0\, k_0 n_{nl}(I) A = 0 \qquad (5)$$

By using appropriate substitutions, it is possible to show that equation (5) represent the (2+1) dimensional nonlinear Schrödinger equation[10] (similar to equation (4)). In 1964, Chiao, Garmire, and Townes[11] and Talanov[12] independently studied equation, similar to (5) to understand the spatial self-trapping of optical beam in Kerr media. A year later, Kelly showed[13] that the solution to NLS (equation (4)) is unstable in Kerr medium due to transverse instability and the only way to stabilize the solution is to make one of the transverse dimensions redundant (for example, making a slab waveguide). Few years later, Dawes and Marburger numerically found[14] that the solution to equation (4) can be stabilized in a saturable nonlinear media. Thus the presence of a stable solution to equation (4), (under nonlinear conditions) proves the existence of soliton. These ideas laid the foundation for the later experimental works and saturable nonlinear media i.e., a material in which the increase in refractive index has upper limit, (cease to increase with intensity) turned out to be an important material for all the later soliton works.

1.1.2. Self-trapping of coherent beam

At the beginning, optical spatial solitons were studied only with coherent sources both theoretically and experimentally. The first experimental evidence of spatial soliton was demonstrated by Ashkin and Bjorkholm in 1974 using circularly symmetric laser beam.[15] Sodium vapour was used as saturable nonlinear source. This was the first demonstration of self-trapping in self-focusing nonlinear medium *i.e.,* in a medium where refractive index increases with intensity. In this case, the refractive index is maximum at the center of the beam and gradually decreases towards the periphery. Therefore, the phase velocity is minimum at the center and maximum at the tail of the beam resulting in bending of phase front (figure 5a) and consequent self-focusing. Diffraction opposes this self-focusing and the interplay results in robust spatial soliton. It took another 10 years for the next experimental demonstration of soliton. This time, the reorientational nonlinearity of liquid CS_2 was used to make 1-D spatial soliton with coherent irradiation source.[16] These experiments provided the guidelines for subsequent demonstration of 1-D bright solitons in solids and polymers with coherent input beam. Although Kerr media provided an ideal platform for doing theoretically works on solitons, instability of (2+1) D soliton in Kerr media restricted the experimental works to planar waveguide geometry (which eliminates one of the transverse dimensions).

1.1.3. Self-trapping of incoherent beam

Until 1996, solitons were believed to be purely coherent entities because of the highly uncorrelated nature of incoherent sources. An incoherent beam consists of a randomly varying bright-dark speckle patterns fluctuating at femtosecond scale. Instantaneous media (which were used for studying coherent solitons) would capture these randomly varying speckles result in several tiny transient waveguides, which would intersect and cross with one another randomly. Net result of this process would prevent the self-trapping of an incoherent beam envelope. Also there are major differences in diffraction of a spatially incoherent beam compare to a coherent beam. In coherent beam the complex amplitudes of the field are phase correlated all the time, where as in an incoherent beam the amplitudes of the field vary in time in a completely uncorrelated manner. Therefore the diffraction of a coherent beam is given by the Fresnel integral over the complex amplitude of the beam, while the integral over the time average of the modulus of complex amplitude gives the diffraction of an incoherent beam. And also the diffraction of an incoherent beam is always larger than a coherent beam of same width. Because of these reasons, the following critical conditions are to be satisfied for the occurrence of incoherent solitons:[17–19]1) the nonlinear medium should exhibit noninstantaneous response with response time longer than the average phase fluctuation time of the incoherent source. Such medium would respond to the time averaged envelope of the source rather than the instantaneous speckles of the incoherent field. 2) The multimodal beam should induce a multimodal waveguide in the nonlinear medium, otherwise it can guide only a small fraction of modes coinciding with it, losing the rest of the optical field. 3) Like any other solitons, optical self-trapping requires self-consistency: the beam should be able to guide itself in the induced waveguide. After understanding all these stringent requirements, Mitchell *et al*. demonstrated the first experimental evidence of self-trapping of a partially spatially incoherent beam in 1996. They used the biased photorefractive crystal with noninstantaenous nonlinearity (which satisfied the above mentioned requirements) to show partially spatially incoherent soliton formation.

1.1.4. Self-trapping of white light

The first incoherent self-trapping work used a quasi-monochromatic laser beam scattered off a rotating diffuser, which is partially spatially incoherent. Later work from the same group illustrated self-trapping in temporally and spatially incoherent white light from an incandescent source. Self-trapping of white light beam is challenging than the partially spatially incoherent laser beam as the former is made of rapid phase fluctuating, multi-modal broad band optical field. White light contains many randomly varying speckles (dark and bright patches) caused by random variation of phase in space at femtosecond time scale. So it is necessary to curb the diffraction of these randomly varying speckled optical beam for white light self-trapping. This can be achieved only in a nonlinear media with response time much longer than the rate of change of the beam's speckle pattern. Thus, only a non-instantaneous media, which respond to the time-averaged intensity (temporally and spatially smooth, when averaged over time) can facilitate white light self-trapping. Segev *et al* showed the first experimental demonstration of white light self-trapping by using photorefractive crystal. They utilized the non-instantaneous photorefractive screening nonlinearity from photorefractive crystal to achieve white light self-trapping. This was a significant work that provided the conditions for white light self-trapping in nonlinear media. These novel works about incoherent solitons opened way for many more important results such as the discovery of gray fundamental dark incoherent solitons,[20,21] elliptic incoherent solitons,[22,23] anti-dark incoherent states[24] and suppression of transverse modulation instability.[25,26] These works stimulated new theoretical works about the behaviour of incoherent beams in nonlinear media but experimental works have made limited progress due to the lack of suitable nonlinear media.

1.1.5. Self-trapping of optical field in photopolymers

Photopolymeriable medium, a photochemical system with inherent non-instantaneous nonlinearity, resolved the limitations of convectional nonlinear media. Self-trapping of optical field had been demonstrated in photopolymerizable media by 1996. Nonlinearity supporting soliton propagating in these media originates from the dependence of change in refractive index on optical intensity. Kewitsch *et al*. showed[27] that the refractive index change or the nonlinear response in photopolymers arises from an irreversible chemical reaction i.e., polymerization, which is fundamentally different from other types of nonlinear effects like Kerr effect or photorefractive effect. Because of this radically new nonlinear mechanism, the nonlinear equation describing the propagation of optical field in photopolymers shows unique behaviour such as transient yet pronounced self-trapping solution and non-locality in time. And also the very nature of the origin of nonlinearity (polymerization reaction) makes the system noninstantaneous. They empirically co-related the refractive index change ($\Delta n'(x, y, z, t)$) associated with free radical polymerization in space and time to optical field intensity through the following expression,

$$\Delta n'(x, y, z, t) = \Delta n_0 \{1\text{-exp}\,[-\frac{1}{U_0}\int_0^{t-\tau} |E(t')|^2 dt']\} \qquad (6)$$

where Δn_0 is the maximum refractive index change induced in the polymer medium, τ is the monomer radical lifetime, U_0 is the critical energy required to induce polymerization and E (t) is the amplitude of the electric field. From the empirical relation and experimental results (plot of

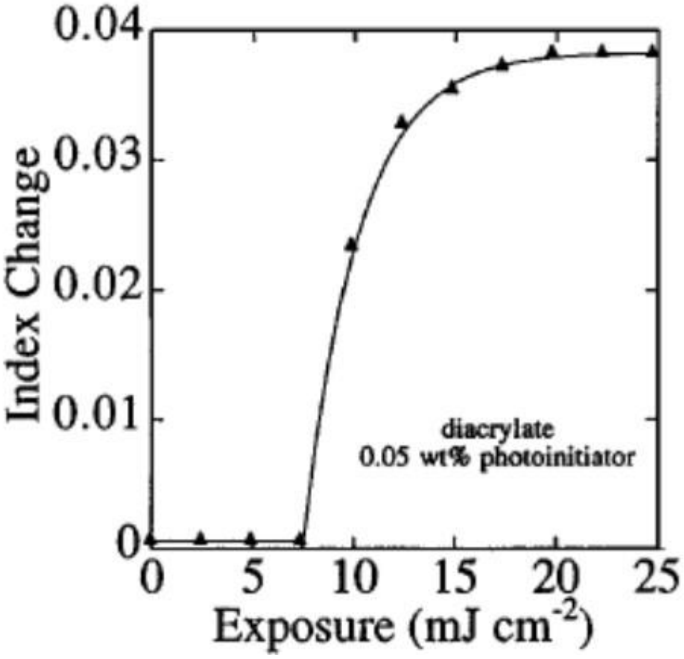

Figure 1.2 Refractive index change as a function of optical exposure. Reprinted with permission from optical society of America.[27]

Δn' as a function of optical energy, figure 1.2), they derived the following conclusions:[27,28] 1) the index response to optical field in photopolymers shows three distinct stages, at the first stage formation of short chains and radical scavenging result in flat or no effective change in index, at the second stage the increase in molecular weight and corresponding increase in density results in larger change in refractive index and at the final stage because of the termination of polymerization reaction the refractive index saturates. This saturable nonlinearity is another distinct feature of photopolymers compare to Kerr type nonlinearity. 2) From equation (6), it can be seen that the index response lags by a time period of τ from the time of application of optical field. This is because the index response results from the propagation stage of polymerization rather than the initiation stage (which happens immediately after photo irradiation) 3) the average intensity required for self-trapping in photopolymers should be below an approximate threshold value, which is given by $I_{avg} < U_0/\tau$, above this threshold value the system would have been polymerized even before the optical field experienced the index change. These findings laid the foundation for future self-trapping and other nonlinear phenomena studies in photopolymers.

In our group,[29–33] we have studied self-trapping of both coherent and incoherent light by exploiting the noninstataneous satruable index change provided by the photopolymerizable organosiloxane system. Our studies of coherent beam self-trapping in free radical polymerizable system gave new insights about coherent beam self-trapping mechanism and new form of nonlinear light propagation in photopolymerizable system. One of the works focused on examining the self-trapping of continuous wave laser beam at intensities ranging 10 orders of magnitude (3.2×10^{-5} to 12 732 $W\cdot cm^{-2}$).[33] This study showed the rich diversity of self-trapping dynamics at different intensity regime. Figure 1.3 shows the occurrence of different events at different intensity regime during the self-trapping process. At low intensities (3.2 $x10^{-5}$ to 1.6 $x10^{-2}$ W· cm^{-2}), higher order optical modes were excited and the process generated a multimodal waveguide. The multimodal nature of the waveguide originates from the nonuniformity in refractive index change along the waveguide. As the rate of change of refractive index is directly proportional to the intensity, the rate of change is slow at low intensities. This slow rate leads to the emergence of nonuniform refractive index change along the waveguide, resulting in a multimodal waveguide capable of supporting higher order modes. At medium intensities (19 $x10^{-2}$ to 16 W· cm^{-2}), spatial diffraction rings, a new form of nonlinear light propagation was observed. The rings occur due to self-phase modulation, an optical nonlinear phenomenon, which occurs under conditions similar to self-trapping. At high intensities (159 to 1.2732 $x10^{4}$ W· cm^{-2}), the beam got disintegrated to individual filaments through modulation instability (explained in detail in the following section), a noise induced instability phenomenon, which gets amplified under nonlinear conditions. This study showed that the self-trapping dynamics can be controlled by polymerization kinetics.

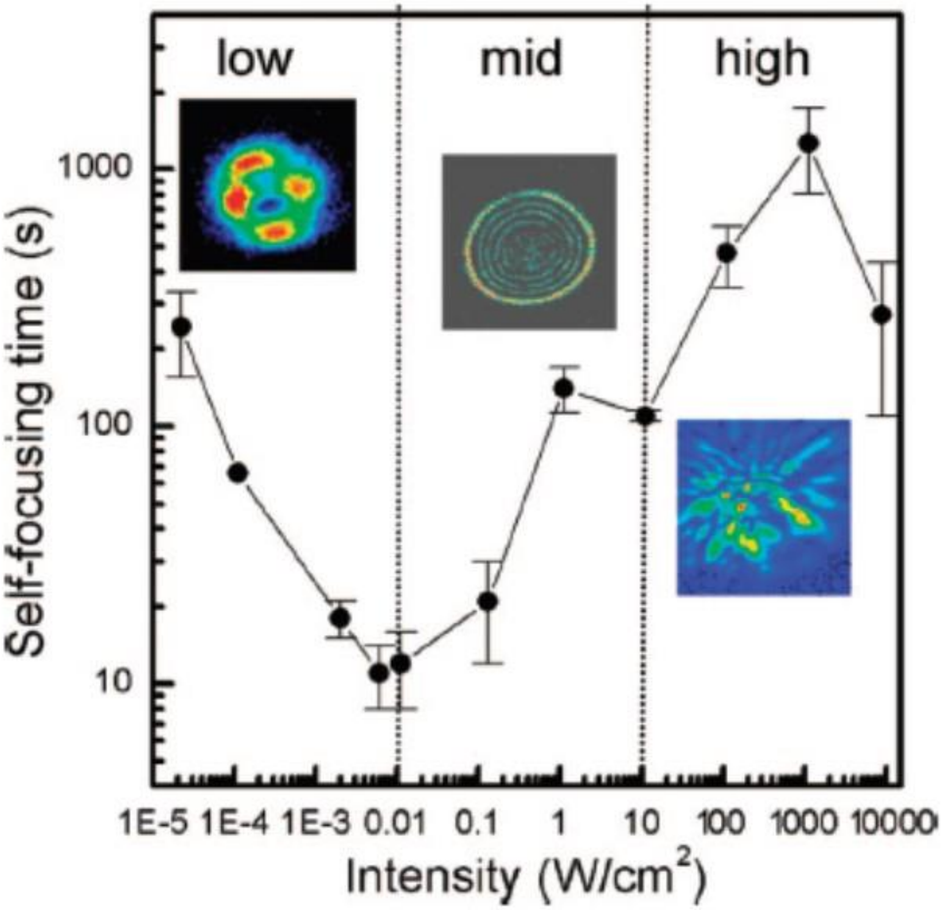

Figure 1.3. Different events at different intensity regime during the self-trapping of coherent beam in photopolymer. Reprinted with permission from American chemical society.[33]

1.1.6. Self-trapping of white light in photopolymer

In addition to the works of coherent light self-trapping, works from our group showed the first experimental evidence of incoherent white light self-trapping in photopolymeriable system by exploiting the non-instantaneous nonlinearity.[30] One of the most important prerequisites for white light self-trapping is non-instantaneous photoresponse. The photochemical reaction (photopolymerization) that provides the optical intensity dependent refractive index change or nonlinear response is inherently slow compare to the femtosecond scale random phase and amplitude fluctuations of white light. Self-trapping of white light in photopolymers can be understood as follows: The process begins by initiating free radical polymerization. As the rate of polymerization is directly proportional to the intensity, it varies according to the (time-averaged) intensity profile of the beam. Because intensity of the beam is maximum at the axial region and decays radially from this point, polymerization induced refractive index change follows the same behaviour resulting in a gradient refractive index or a lens. Thus the propagating beam instead of undergoing diffraction, self-focuses as it encountered a lens. From the focal point of the first lens, the beam induces a second lens to focus even further. This reciprocal lensing and focusing leads to the self-trapping of the white light beam in photopolymer. As the photopolymerization index refractive index change is irreversible, the process results in a permanent multi modal waveguide structure. We also studied the dynamics of white light self-trapping in photopolymer and showed that the process can be controlled through polymerization kinetics. One of our other studies probed the interaction of two parallel propagating and mutually incoherent white light beam in photopolymerizable system and showed that the beams undergo repulsion or attraction or filamentation depending upon the separation distance between the beams. The beams attracted one another, when the separation distance corresponded to the width of individual beam and repelled at distances much larger than their width. Filamentation occurred at distances shorter than the individual beam width. These interactions originated from the concentration gradient driven diffusion in the polymerization system. These studies provided the fundamental understanding about nonlinear light propagation in photopolymerizable medium, which is widely utilized in the research presented here.

1.2. Modulation instability

Another closely related nonlinear phenomenon to self-trapping is modulation instability. The phenomenon of modulation instability (MI) is prevalent in several nonlinear dispersive systems.[34–43]Instability is a general characteristic of propagating waves in nonlinear media and observed in diverse systems such as plasma waves,[44] water waves,[45,46] sand dunes,[47] matter-waves[48,49] and electromagnetic waves.[50–52] It occurs when a continuous wave solution is weakly perturbed and the perturbation grows exponentially due to the interplay between the nonlinearity and the group-velocity dispersion. The phenomenon of long wavelength instability was first predicted in nonlinear optics by Bespalov and Talanov in 1966. Initially, MI process was exploited in temporal domain for generating short trains of optical pulses.

1.2.1 Modulation instability in temporal domain

Hasegawa theoretically showed generation of short trains of soliton pulses using induced MI.[53] At that time, glass fibers were used as nonlinear dispersive

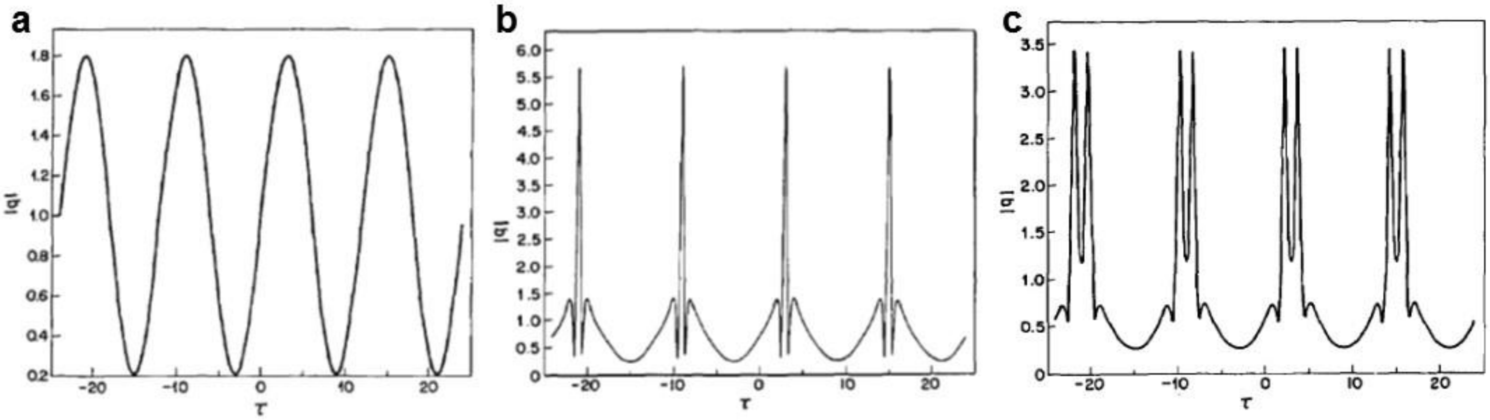

Figure 1.4 Profiles of modulation envelope with changing propagation distance parameter a) $\xi = 0$ b) $\xi = 1.24$ c) $\xi = 1.79$. Reprinted with permission from the optical society.[53]

medium to generate short pulses with controlled pulse width and repetitive rate. MI of the optical field caused the former (reduced pulse width) and externally applied amplitude modulation controlled the later (pulse repetitive rate). The approach started with considering the propagation of optical-field envelop in glass fiber, which obeys the nonlinear Schrödinger equation. (Notations used by the original papers are preserved in this research presented here)

$$i\frac{\partial q}{\partial \xi} + \frac{1}{2}\frac{\partial^2 q}{\partial \tau^2} + |q|^2 q = -i\,\Gamma q \qquad (1)$$

where $\xi = 10^{-9}\, x/\lambda$, $\tau = (10^{-4.5}/(-\lambda k'')^{1/2})\,(t-(x/u_g))$, $q=10^{4.5}(\pi n_2)^{1/2}\phi$, $\Gamma=10^{9}\lambda\gamma$ x is the propagation distance, λ is the wavelength used for calculation, u_g is the group speed, t is the time and n_2 is the Kerr coefficient, γ the loss rate and ϕ is the electric field amplitude of the pulse envelope. The continuous wave (cw) described in Eq. 1 is instable for a wavelength > π/q_0 with a weak perturbation.

Thus, MI of this cw wave was induced by applying an external modulation field with a wavelength of λ_m and modulation depth of A_m. Under these conditions, Eq. 1 was numerically solved and the results are shown in figure 1.4. Initially uniform envelopes splits into individual pulse with increasing propagation distance. Also in the same work generation of pulses with desired widths and repetition rates by changing the fiber parameters and external modulation field parameters was shown. Following the theoretical work, MI in temporal domain was experimentally demonstrated in single mode fiber using mode-locked neodymium doped yttrium aluminium garnet laser as cw source.[54] Unlike the theoretical work (where MI was induced externally), MI was elicited by the amplification of embedded noise in the system. Results from these experiments revealed one of the fundamental characteristics of noise induced MI: presence of a threshold intensity for the occurrence of MI, which is evident from figure 1.5 showing the broadening and splitting of the center peak with laser powers above a specific threshold value. At lower powers, the output spectrum is similar to the source spectrum and with increasing power the appearance of sidebands becomes apparent. Formation of such pulse train in optical fibers through MI can be understood in both temporal and frequency domains as follows:[53–58] In time domain, MI converts the input light wave into a sinusoidal wave by deepening the modulation depth.

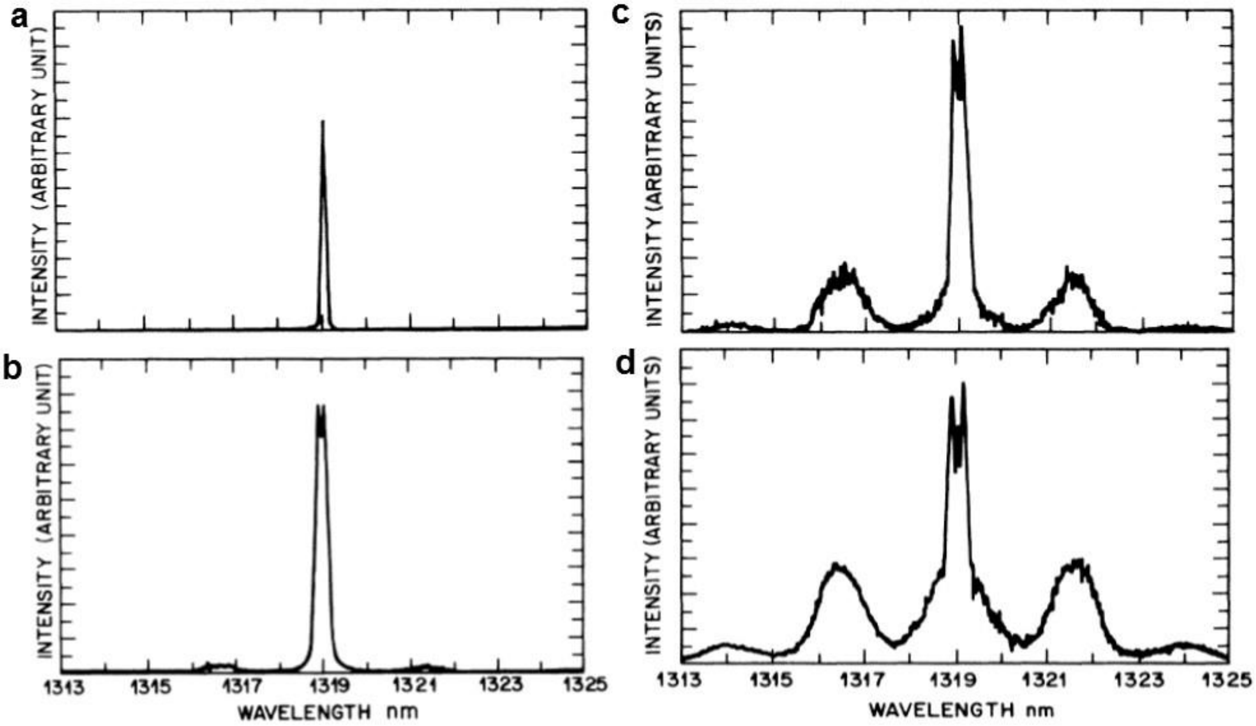

Figure 1.5 Output power spectra of the laser as a function of peak power in the fiber a) low power b) 5.5 W c) 6.1 W d) 7.1 W. Appearance of MI induced sidebands are seen in b, c and d. Reprinted with permission from American physical society.[54]

These sinusoidal waves undergo higher order soliton compression, forming well separated train of pulses. The instantaneous wavelength and the group velocity dispersion of the output signal give a clear picture of sinusoidal wave compression and deepening of modulation depth explaining the MI in temporal domain. In the frequency domain, the output spectrum consists of a pump (source frequency) with stokes and anti-stokes sidebands. These side bands are excited by four-photon mixing and amplified exponentially with distance due to MI. As the process repeats, many stokes and anti-stokes sidebands are generated and the interference of these sidebands result in pulse train. Thus, it was a significant work that showed the first experimental evidence of MI induced optical pulse train generation and also demonstrated the fundamental principles of MI. These findings played a major role in studying MI in temporal domain and its application in generating short width optical pules with high repetition rate.

1.2.2. Modulation instability in spatial domain

Similar to the fascinating effects of MI in temporal domain, MI in spatial domain leads to spontaneous pattern formation, which was extensively studied in chemistry,[59] biology[60]and optics. Although the underlying mechanisms supporting the instability process might significantly differ from one system to another, the universal nature of the process is evident from the similarity in features observed in all the spontaneous pattern formation systems. In optics, instability leads to disintegration of a plane wave or broad optical beam propagating in a nonlinear medium and generates individual 1D filaments and 2D spots in spatial domain, analogous to splitting of a cw wave into short train pulses in temporal domain.

Modulation instability of spatially incoherent source

Initially MI was considered purely as a coherent process and believed to occur only in nonlinear systems with perfect spatial and temporal coherence.[61–63] Later it was shown theoretically[64] and experimentally,[17,65] that MI can also occur in partially spatially incoherent optical systems. These results proved the possibility of MI in many weakly correlated nonlinear systems. The significance of incoherent MI is the existence of a well-defined threshold nonlinearity: MI occurs only when the nonlinearity exceeds this threshold value. Presence of this threshold is unique to incoherent MI, as coherent systems show no such threshold. This behaviour can be understood as the balance between two counteracting processes happening in incoherent systems: the growth of perturbations on top of a uniform wave front under nonlinear condition and the linear diffusive washout of the perturbations resulting from the incoherence of the system. When the nonlinearity is below the threshold value, the perturbations get washout by the strong linear diffusive processes (diffraction and dispersion), whereas above threshold, the modulation depth increases and the perturbations get amplified, thereby showing MI.

Demonstration of MI in incoherent systems showed the possibility of one-dimension (1D) and two-dimension (2D) spontaneous pattern formation through amplification of small perturbations or noise in weakly correlated nonlinear systems, when the nonlinearity exceeds a threshold value. Examples of such systems are high temperature superconductors,[66] atomic gases at slightly higher temperature than the Bose-Einstein condensation temperature,[67] gravitational systems[68] and electrons in semiconductors in the proximity of quantum Hall regime.[69] All these nonlinear systems with slight wave disorder function show pattern formation, suggesting that the underlying physics of incoherent MI is universal. In optics, investigation of incoherent MI was motivated by the demonstration of incoherent solitons[70] (explained in details in the next sections). These soliton are observed in noninstantaneous media, when the response time of the media is few orders of magnitude longer than the average phase fluctuation time of the incoherent wave front. Here the nonlinear refractive index change inducing the soliton formation relies on the time averaged intensity of the optical field. The existence of incoherent solitons proved the possibility for incoherent MI, since both processes occur under similar conditions. First evidence of incoherent MI in optical waves was shown by Soljacic *et al*. They analytically and numerically solved nonlinear paraxial wave equation to demonstrated MI in self-focusing noninstantaneous medium (Kerr type, saturable medium) for the incoherent input beam with Lorentzian angular power spectrum. Their findings showed a threshold nonlinearity for the occurrence of MI and dependence of the threshold on the spatial degree of coherence.

Shortly after the theoretical demonstration, MI was experimentally shown by the same group. They validated the following theoretical predictions made about MI in incoherent systems:

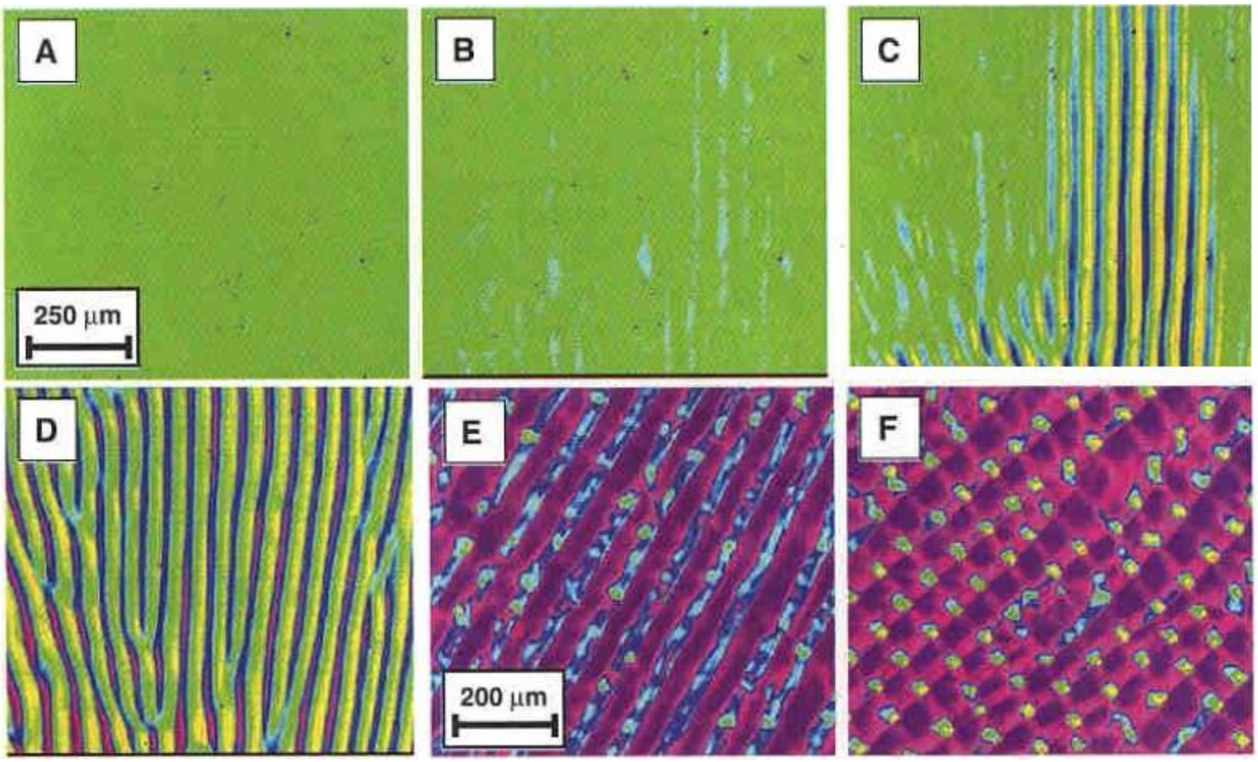

Figure 1.6 Intensity profile at the output face of the crystal, A-F: increasing input bias field. Reprinted with permission from American Association for advancement of science.[17]

1) the phenomenon occurs only in noninstantaneous media with response time much lower than the phase fluctuation time (femtoseconds) of the optical wave front, 2) presence of a sharp threshold nonlinearity below which the perturbations decay and above which the perturbations form quasi-periodic patterns, 3) the correlation distance of the input source defines the threshold, 4) and saturation of nonlinearity alone arrests the growth rate of MI. A noninstantaneous nonlinear medium (strontium-barium niobate crystal with photorefractive screening nonlinearity) satisfying these prerequisites was used to validity the theoretical

predictions of incoherent MI Nonlinear refractive index change in the medium is given by the relationship,

$$\delta n = \Delta n_o \,[\,1 + (I_o/I_{sat})]\,[I(r)/\,(I(r) + I_{sat})] \qquad (2)$$

where I_o is the intensity of the signal beam, I_{sat} is the background beam intensity and I(r) is the local intensity as a function of coordinate r, Δn_o is the electro-optic refractive index change. Upon increasing the external voltage, δn increases and when the δn value reached the threshold, the uniform optical field disintegrated into 1D filaments (figure 1.6C & 1.6D). With further increase of external voltage the filaments split into 2D array of ordered spots (figure 1.6E &1.6F). Thus with the experimental verification, the theoretical predications made by Soljacic *et al* become the guidelines for all the future incoherent MI works.

1.2.3. Modulation instability of incoherent white light

As discussed in the previous sections, demonstration of incoherent MI showed the possibility of observing this phenomenon in weakly correlated systems and proved the underlying physics of this phenomenon is universal. But the sources used in all these works are only partially spatially incoherent and temporally coherent (laser beam passed through a rotating diffuser to introduce spatial incoherence (quasimonochromatic)). Extension of MI to white light, which is spatially and temporally incoherent, similar to sun light is intriguing and also nonlinear interaction of such broad continuum of temporal frequencies provides new fundamental understanding about MI dynamics. Buljan *et al*[71] proposed the theory to describe white light MI in noninstantaneous medium. Apart from confirming the guidelines provided by Soljacic *et al* for incoherent MI, white light MI showed another two characteristic features: 1) entire temporal frequency spectrum becomes collectively unstable above the threshold nonlinearity and all temporal frequencies get an intensity structure with the same spatial periodicity, both these features imply that white light MI is a collective effect. 2) Temporal spectrum of perturbations growing on top of the underlying uniform wave front self-adjusts itself above threshold nonlinearity to enable the collective instability process and different wavelengths act with different strength in the MI process.

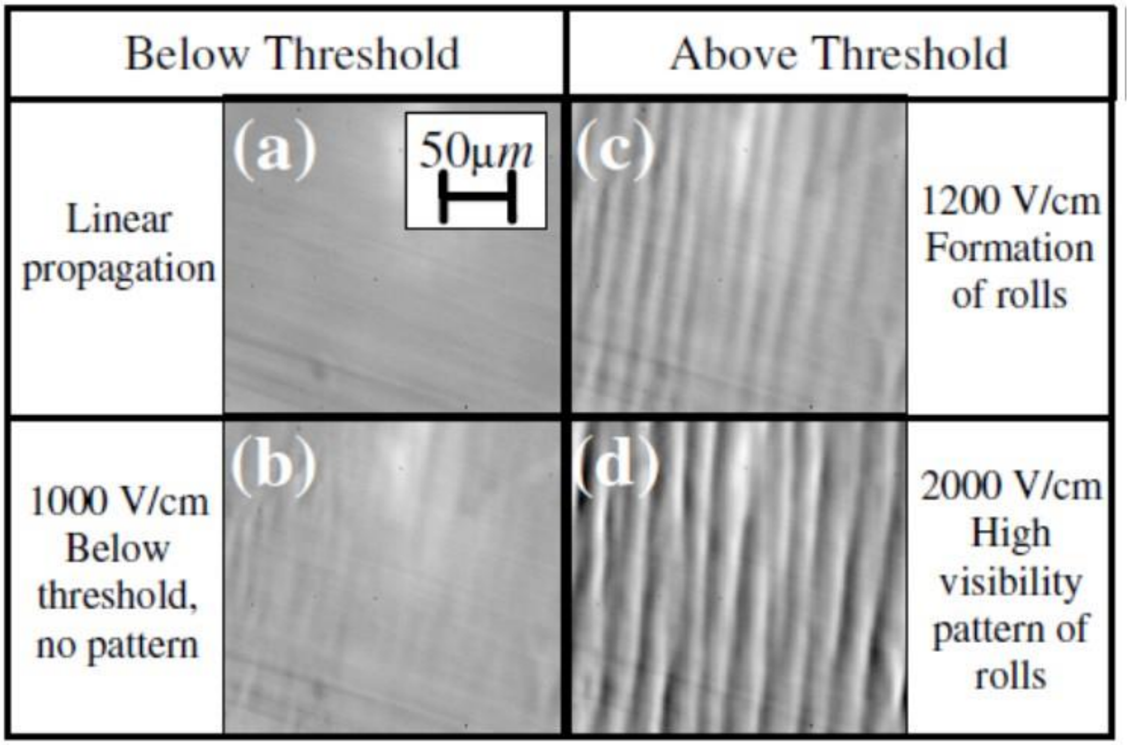

Figure 1.7 Intensity distribution at the output face of the crystal at different bias voltage. Reprinted with permission from the American physical society.[72]

These theoretical predictions were experimentally confirmed by Schwartz *et al*. using incandescent light bulb as illuminating sources and SBN: 60 crystal as nonlinear system.[72] The results are shown in figure 1.7, indicating occurrence of MI above threshold value of nonlinearity and as predicted by the theoretical work, all the temporal frequencies collectively showed single threshold and pattern periodicity, indicating that the white light MI is a collective effect. The results also showed the influence of individual temporal frequencies, where the higher frequencies contributed more to the intensity pattern modulation depth compare to lower frequencies. But the entire temporal spectrum self-adjusts and provides a collective pattern with same periodicity. These experimental results showed the spontaneous pattern formation in a spatially and temporally incoherent system and paved the fundamental guidelines for studying MI in similar systems.

1.2.4. Modulation instability in soft matter

In the previous sections, the possibility of MI in various nonlinear systems was shown both theoretically and experimentally. One of the interesting nonlinear systems is soft matter (SM),[73] which includes polymers, liquid crystals, colloids, foams, gels and biomatters. Light-induced refractive index change originating from various mechanisms like molecular orientation,[74] chemical bond formation,[75] concentration gradient[76] and charge separation[77] provide the optical nonlinear response in these systems. Studies of MI in SM confirmed the universal nature of the phenomenon and also showed fascinating new features.[78–81]

In our group, we have extensively studied incoherent white light MI in polymer medium[75,82–86] and demonstrated spontaneous pattern formation by exploiting the photo-induced refractive index change provided by the polymerization reaction. We used the free radical polymerization reaction in organosiloxane system, which satisfies all the prerequisites for incoherent MI and also the refractive index change induced by this irreversible polymerization reaction generates permanent structures corresponding to the MI induced patterns. These works demonstrated the rich nonlinear dynamics offered by the photopolymerization system and the possibility of developing this phenomenon into a polymer and metellodielectric microstructure fabrication process.

1.3. Nonlinear optical media

Optical nonlinear phenomena (including the ones mentioned above) are not observed when light travels in free space. Nonlinearity originates from the interaction of optical field with the medium through which it travels, rather than the optical field itself. Existence of optical field modifies the properties of the medium and the medium in turn influences the behaviour of the optical field. Behaviour of optical field in a dielectric medium depends on the relationship between the polarization density vector P(r, t) of the medium and the electric field vector E(r, t) associated with optical field present in the medium.[87] In a linear medium, polarization has a linear relationship with electric field

$$P = \epsilon_0 \chi E, \qquad (7)$$

where ϵ_0 is the permittivity of free space and χ is the electric susceptibility of the dielectric medium, whereas in a nonlinear medium, P and E has a nonlinear relationship.[87] Origin of nonlinearity may be microscopic or macroscopic. The polarization describing the behaviour of optical field in a medium is the product of individual dipole moment p induced by the electric field E in the medium and the number density of dipole moments N. Nonlinear behaviour may originate from either N or p.

Induced dipole moment p is linearly related to electric field E for relatively small optical intensities. But at high intensities i.e. values closer to interatomic intensities, which are typically 10^5~10^9 V/m, the relationship between p and E becomes nonlinear.[88] This can be explained using simple Lozentz model[87] for electric field induced dipole moment p = -ex, where x is the displacement of mass m with charge –e, under the influence of electric force –eE. In case, the restraining force is proportional to the displacement x, then the induced dipole moment p and the corresponding polarization P are linearly related to E and the medium is linear, but if the restraining force is a nonlinear function of displacement then the induced dipole moment p and polarization P becomes a nonlinear function of E and the medium is nonlinear. Under such circumstance, the function describing the relationship between P and E is given by the Taylor series expansion as follows,[87]

$$P = \epsilon_0 (\chi^{(1)} E + \chi^{(2)} EE + \chi^{(3)} |E|^2 E + \ldots) \qquad (8)$$

The first term is related to the linear response of the material and it dominates at small values of E, the second term represents the quadratic or second order nonlinearity and the third term corresponds to third order and so on. Equation (8) sets the basis for the classification of nonlinear media, which are broadly classified into Kerr media, photorefractive media and photopolymers. First two nonlinear media rely on the response of higher order susceptibilities (third and second respectively) to optical field for nonlinear effects whereas photopolymers rely on photoinduced chemical reaction.

1.3.1. Kerr media

Nonlinearity in Kerr media is due to the electro-optic effect. It is caused by the drifting of bound electrons (polarization) under the influence of an externally applied electric field (associated with optical field). The nonlinear polarization (responsible for the nonlinear effects in Kerr media) induced in Kerr media is given by, $P_{NL} = \epsilon_0 \chi^{(3)} |E|^2 E$, the third term in equation (8). Refractive index change associated with this nonlinear polarization is given by[7]

$$n = n_0 + 2n_2 |E|^2 \quad \text{or} \quad n = n_0 + \Delta n \qquad (9)$$

where n_0, is the linear refractive index and n_2, nonlinear refractive index induced in the Kerr media. Second term in equation (9) is the intensity dependent refractive index change. Higher order susceptibility, stimulated in Kerr media to elicit nonlinear effects and the nonlinear refractive index change in equation (9) can be related as follows,

$$\chi_{eff} = \chi^{(1)} + 3\chi^{(3)} |E|^2 \qquad (10)$$

where χ_{eff} is the effective susceptibility in Kerr media, the nonlinear refractive index n_2 and χ_{eff} can be related by utilizing the generally accepted relationship,[87]

$$n^2 = 1 + \chi_{eff} \qquad (11)$$

by substituting equation (9) on the left hand side and equation (10) on right hand side of equation (11),

$$(n_0 + 2n_2 |E|^2)^2 = 1 + \chi^{(1)} + 3\chi^{(3)} |E|^2 \quad (12)$$

Correct to terms of order $|E|^2$, equation (12) can be expanded as,

$$n_0^2 + 4 n_0 n_2 |E|^2 = 1 + \chi^{(1)} + 3\chi^{(3)} |E|^2 \quad (13)$$

equation (13) shows that the linear and nonlinear refractive indices are related to susceptibility as follows

$$n_0 = 1 + \chi^{(1)} \quad (14)$$

$$n_2 = \frac{3\,\chi\,(3)}{4\,n0} \quad (15)$$

this nonlinear refractive index (equation (15) associated with $\chi^{(3)}$ is responsible for the Kerr effect and it played a major role in nonlinear optics by paving way for analytical solutions of numerous problems. For example, the stable solution of 1D-spatial soliton in Kerr media as discuss in previous section. All most all materials show a non-zero $\chi^{(3)}$ and consequent Kerr effect but the value of $\chi^{(3)}$ is very small and therefore only few selected materials have measurable Kerr response which can be used for studying nonlinear optical effects. Because of the small $\chi^{(3)}$ values, huge intensities of the order of (GW/cm^2) are required to induce refractive index change.[11] Other problem associated with Kerr media is that the instantaneous unsaturable nonlinear response, which limits certain nonlinear phenomena like incoherent soliton and incoherent modulation instability. Thus the Kerr media acted as ideal substrate for initial nonlinear optics studies but due to the above mentioned restrictions, its applications were limited.

1.3.2. Photorefractive media

Photorefractive materials have been known for more than 40 years. These are non-centrosymmetric dielectric single crystalline materials showing $\chi^{(2)}$ nonlinearity. The nonlinear polarization induced in photorefractive media is given by $P_{NL} = \epsilon_0 \chi^{(2)} E_1 E_2$, corresponding to the second term in equation (8). In presence of an external electric field when $E_2 = E_0$ at the optical frequency, the electro-optic effect modifies the refractive index of the medium as follows,[87]

$$\Delta n_0 = -\frac{1}{2} n_0^3 r_{eff} E_0 \quad (16)$$

where r_{eff} is the electro-optic tensor and n_0 is the unperturbed refractive index of the medium. Photorefractive effect induced in the doped crystalline media (applies to most photorefractive media) can be understood from the following three steps:[89] 1) Generation of mobile charge carriers through photoexcitation, 2) transportation of the charge carriers through electric force, 3) non-local re-trapping of the charge carriers. These steps can be briefly explained as follows: Photorefractive materials, which are typically dielectrics or semiconductors are doped with donors or acceptors dopants with energy gap deep inside the forbidden energy level. They act as charge carriers, which can be photo-excited into quasi full valence band for holes and quasi empty conduction band for electrons. Typically electrons are responsible for the observed electro-optic effect in photorefractive materials. Upon excitation to conduction band, the electrons are free to move. When the exciting optical field is non-uniform in space, these electrons undergo redistribution or transportation through diffusion or by electric force. They move from regions of high concentration to regions of low concentration and the redistribution can be influenced by applying external bias field. After the characteristic dielectric relaxation time, these electrons are re-trapped in locations different from their original location by either ionized donors or by acceptors. This charge separation gives rise to an electric field within the medium, which varies in space i.e. the electric field is different in an illuminated region compare to a dark region. This spatial difference in the electric field distribution results in spatially varying refractive index change due to electro-optic effect (Pockels effect). Screening nonlinearity resulting from the above mentioned process provides an intensity dependent refractive index of the form[87]

$$\Delta n\left(I(r)\right) = \frac{\Delta n_0}{1+(I(r)/I_b)} \qquad (17)$$

where I (r) is the optical intensity and I_b is the background intensity resulting from the dark beam or the field proportional to the conductivity of the material in dark. Δn_0 is the induced refractive index change in the medium, which can be expressed as,[87]

$$\Delta n_0 = -\frac{1}{2} n_0^3 r_{eff} \frac{V}{L} \quad (18)$$

where V is the applied bias voltage and L is the distance between the electrodes. The significance of Δn_0 in equation (18) is that, it is inherently saturable when the electrons transportation and the resulting space charge field reaches equilibrium. At this stage, the refractive index ceases to increase. And also the response time of the medium, which depends on the dielectric relaxation time is inversely proportional to the intensity of the applied optical field.[90] The response time can be varied from few nanoseconds to minutes by varying the intensity.[91] Thus the photorefractive materials with saturable and noninstantaneous nonlinearity paved the way for observation of new family of solitons and variety of other interesting nonlinear phenomena.[92–96]

1.3.3. Quadratic nonlinear media

Quadratic nonlinear media are different from both Kerr and photorefractive media as the nonlinearity doesn’t originate from the optical field induced change in refractive index or any other physical properties of the media. Here the nonlinearity purely relies on strong interaction and energy exchange between two or more beams at different frequencies mediated by $\chi^{(2)}$ or second order nonlinearity.[87] Because of these features, quadratic nonlinearity can be realized only in limited class of materials such as non-centrosymmetric materials (for example, KTP, $LiNbO_3$, $LiIO_3$, $LiTaO_3$) in which the phase matching conditions are satisfied. Nonlinear polarization induced in these types of media is given by $P_{NL} = \epsilon_0\chi^{(2)} E_1E_2$ and nonlinear phenomena like self-trapping occurs when E_1 and E_2 interact under specific conditions to yield a third field through parametric wave mixing process. The possibility of nonlinear effects in quadratic media was theoretically demonstrated by Karamzin and Sukhorukov, they investigated the mutual focusing of beam through parametric process and identified the implication of that process on soliton formation.[97] Recently Torruellas *et al*., experimentally showed the spatial soliton formation in potassium titanyl phosphate (KTP) in second harmonic generation settings[98] and Schiek *et al*., demonstrated soliton propagation in planar waveguide made of lithium niobate ($LiNbO_3$).[99] Not only soliton formation but also MI of optical field was demonstrated in quadratic media by Fuerst *et al*., by exploiting the dynamic interaction of two strongly coupled fundamental and harmonic fields.[100] Thus the saturable nonlinearity provided by quadratic media (saturation originates from the conversation of total electromagnetic energy) supports and provides another platform for exploring various nonlinear optical phenomena.

1.3.4. Polymer nonlinear media

Polymers or organic media are emerging as one of the promising systems for studying nonlinear optical phenomena because of the larger second order susceptibility value, their ease of processing and high damage threshold.[101–109] Nonlinearity in polymers originates from various mechanisms like reorientation of molecules,[110,111] (in liquid crystalline chromopore attached polymers) photorefractive effect[112,113] (polymers with photorefractive chromophore) and photopolymerization induced refractive index change.[27,29,30] Here, these mechanisms are briefly discussed. Liquid crystals, which show reorientation nonlinearity are materials with a phase in between solid crystal and liquid. Of the various liquid crystalline phases, second order nonlinear effects are observed in the nematic phase where the molecules are aligned in elongated rod-like configuration and chiral smectic phase where the molecules are aligned at an angle. Under the influence of external forces, these liquid crystalline molecules orient themselves in the direction of the field and transform to birefringent materials with ordinary and extraordinary refractive indices.[114–116] Also in presence of such an external field, a torque is induced in these anisotropic materials that rotates the molecules along the major axis and aligns them in the direction of applied field vector. The interaction energy density (f_{el}) associated with electric field induced orientation is given by

$$f_{el} = -\frac{\epsilon_0 \Delta\epsilon}{2}\left[(n.E)^2\right] \quad (19)$$

where $\Delta\epsilon = \epsilon_{\parallel} - \epsilon_{\perp}$ is the anisotropic permittivity, $\epsilon_{\parallel}$ and $\epsilon_{\perp}$ are the parallel and perpendicular components of permittivity respectively, which are related to the ordinary and extraordinary refractive indices of the media, n is the unit vector and E is the applied electric filed vector. When the molecules reorient or arrange themselves coplanar to the applied electric field against the induced torque for minimizing the energy density, the electric permittivity becomes positive $\Delta\epsilon > 0$. This increase in permittivity results in corresponding increase in the refractive index of the media, thus paving the way for the occurrence of nonlinear phenomenon like self-focusing. The change in refractive index is intensity dependent and it saturates at a threshold value Known as Freederickz transition when the unit vector (corresponding to the direction of the molecules) is perpendicular to the applied field. Also the induced refractive index change is noninstataneous, of the order of milliseconds as it originates from molecular reorientation through elastic force restoration. Incorporation of this saturable, noninstataneous liquid crystal nonlinear molecules in polymers results in thermally and mechanically stable nonlinear media.

Photorefractive polymers are another important class of optical nonlinear polymers. Nonlinearity in this class of materials not only originates from optical field induced charge separation (as in inorganic photorefractive materials, which is explained in previous section) but also from orientational effect. [112,113] The orientational enhancement effect, which is specific to organic or polymer based nonlinear media results from the ability of the molecules to orient under the influence of external forces. Orientation of molecules is achieved by electric field poling, non-centrosymmetric crystallization and Langmuir-Blodgett film formation.[117] Electric field poling is the most widely used method to induce orientational nonlinearity in photorefractive polymers. It is done by heating the polymer above its glass transition temperature (T_g) where it gets rubbery and by applying an electric field to get the required orientation. Then the polymer is cooled below its T_g in presence of the electric field to freeze the induced orientation permanently. Nonlinearity induced by the electric field poling process in polymer with photorefractive chromophore is described by two nonlinear susceptibility tensors $\chi^{(2)}_{333}$ and $\chi^{(2)}_{311}$, which are given by,[117]

$$\chi^{(2)}_{333}(-\omega;\omega_1;\omega_2) = NFE\mu\beta_z(-\omega;\omega_1;\omega_2)/5\mathrm{KT} \qquad (20)$$

$$\chi^{(2)}_{311}(-\omega;\omega_1;\omega_2) = NFE\mu\beta_z(-\omega;\omega_1;\omega_2)/15\mathrm{KT} \qquad (21)$$

where N is the number density of the chromophore in the polymer matrix, F is the factor containing local field correction, μ is the dipole matrix element, β is the vectorial component of the hyperpolarizability (nonlinear response of the molecule), K is the Boltzmann constant and T is the temperature. The product $\mu\beta_z$, is called the molecular figure of merit for the chromophore incorporated in the polymer. Figure of merit is an important parameter, which is used as a guide for designing photorefractive polymers with high second order susceptibility value. Thus the photorefractive polymers with high second order susceptibility value provide the combined advantage of organic matrix with inorganic like nonlinear properties for studying nonlinear optical phenomena.

Apart from photorefraction (photorefractive polymer) and molecular reorientation (liquid crystal molecules functionalized polymers), there are few other mechanisms that lead to photoinduced refractive index change in polymer systems and thereby support nonlinear light propagation. Recently, a study from our group showed nonlinear light propagation in hydrogel doped with NaI and Ru (bpy)$_3$Cl$_2$ by utilizing the optical intensity dependent refractive index change provided by photo induced oxidation of I^- (iodide) by Ru(bpy)$_3^{2+}$ (Tris(bipyridine)ruthenium(II)). Upon photo irradiation of the hydrogel with NaI and Ru (bpy)$_3$Cl$_2$ the following sequence of reactions occur (scheme1):[118]

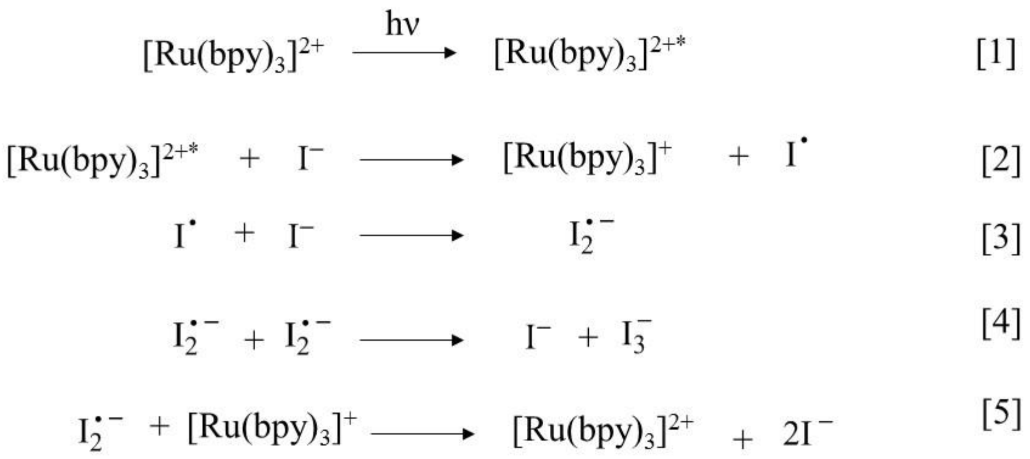

Scheme 1.1. Photoinduced oxidation of iodide by tris(bipyridine)ruthenium(II)). Adapted with permission from American chemical society.[118]

Ru (bpy)$_3$Cl$_2$ which absorbs in blue green region (λ_{max} of 460 nm), upon excited by a green laser (532 nm) results in a triplet state (eq. 1). This excited state species oxidizes iodide (I^-) to iodide radical (eq. 2), which reacts with excess iodide to generate other species such as diiodide radical and triiodide (eq. 3 & 4) or recombine with $[Ru(bpy)_3]^+$ to form Ru (bpy)$_3$Cl$_{2.}$ The triiodide species generated in the reaction is expected to have higher polarizability based on Lorentz-Lorenz relationship and therefore has larger refractive index compare to its precursor. Thus regions enriched with triiodide has significant refractive index difference compare to the surrounding region. This photoinduced refractive index difference originating from triiodide was exploited to self-trap a coherent beam. The significance of this work is that system is reversible. When the light source (laser beam) is turned off, the triiodide species diffuses into the hydrogel and the refractive index gradient gets erased. This is one of the detailed studies of reversible nonlinear polymer system and it shows potential practical applications.

1.3.5. Photochemical nonlinear media

By 1990s, an important mechanism supporting the nonlinear propagation of optical field in photosensitive materials was proposed.[27,119] In contrast to other mechanisms, here the refractive index change in response to illumination field originates from an irreversible photochemical reaction called photopolymerization. In a typical photopolymerization process,[120] large amount of reactive species (free radical) are generated by irradiating photopolymerizable monomer containing photoinitiator (which absorbs light at a particular wavelength) with actinic radiation (radiation encompassing UV to visible end of the spectrum). These free radicals initiate a chain reaction by attacking the monomers, resulting in large number of monomers with reactive end groups. These monomers with reactive end groups propagate by consuming more monomers through chain reaction to form higher molecular weight polymer chains. This chemical reaction (polymerization) leads to cumulative increase in local density and corresponding increase in refractive index. The reaction providing the refractive index change is intensity dependent. The correlation between the polymerization reaction and the intensity of irradiation source can be understood by considering the individual steps involved in the reaction, namely initiation, propagation and termination. Of these steps, initiation and propagation contribute to the change in refractive index and both these steps are directly related to the intensity of incident light source, which can be explained as follows: The rate of initiation (r_i) of a free radical polymerization reaction is given by,[120]

$$r_i = \Phi_i I_0 [1\text{-}exp (-\epsilon l [PI])] \qquad (22)$$

where I_0 is the intensity of incident light, l is the sample thickness, ϵ is the molar absorptivity, [PI] is the photoinitiator concentration and Φ_i is the quantum yield of the initiation (number of initiation species per photon absorbed). Thus the rate of initiation is directly proportional to the intensity of the incident light and the rate of propagation (r_p) is given by,

$$R_p = (k_p/k_t^{0.5}) \{\Phi_i I_0 [1\text{-}exp (-\epsilon l [PI])]\}^{0.5}[M] \qquad (23)$$

where K_p and K_t are the rate constants of propagation and termination respectively and [M] is the monomer concentration. It can be seen from equation (23), the propagation step is also intensity dependent. In addition to the correlation shown in equation (23), the intensity dependence of propagation step is also due to the following two factors: 1) higher intensity leads to higher sample temperature, which facilitates molecular mobility and corresponding increase in monomer to polymer conversion 2) and increasing intensity results in increased time lag between polymerization and volume shrinkage, which provides an excess free volume and thus increases molecular mobility. Thus the polymerization reaction provides an intensity dependent nonlinear response (refractive index change). Also this reaction is inherently noninstataneous and saturable. The noninstataneous nature comes from the fact that the reaction time can be controlled from few seconds to hours by varying the intensity of the irradiation source and the presence of the termination step makes the system saturable. With all these characteristics, photopolymerizable media act as an ideal system for studying nonlinear optical phenomena.

Several groups exploited the nonlinearity provided by photopolymeriable systems to study nonlinear phenomena both theoretically and experimentally.[27,119,121–127] One of the significant theoretical models describing the intensity dependent refractive index change in photopolymerization system proposed by Kewitsch was discussed in previous section. Later, Shoji *et al.* showed the following improvised model to describe the temporal evolution of photopolymerization induced refractive index change Δn (r, z, τ) , which included the threshold behaviour of polymerization[123] (occurrence of polymerization after a specific intensity threshold (Kewitsch observed the threshold behaviour experimentally but didn't include in the model))

$$\frac{\partial \Delta n}{\partial \tau} = A\left(1 - \frac{\Delta n}{\Delta n_s}\right)\begin{cases} |E|^2 - I_{th}\ , & |E|^2 \geq I_{th} \\ 0, & |E|^2 < I_{th} \end{cases} \quad (24)$$

where Δn_s is the maximum refractive index change, I_{th} is the threshold intensity and A is the coefficient describing the polymerization rate. The solution provided by nonlinear paraxial wave equation (5) (describing the self-trapping of optical beam in nonlinear media) incorporated with the improvised model for refractive index change (equation 24) matches exactly the experimental result, proving the validity of the new model. In addition to the conclusions drawn by Kewitsch, Shoji *et al*. showed that when I_{th} is small, a multimodal waveguide is induced in the medium, whereas at larger I_{th} the process generated a single mode waveguide. Following these theoretical works various nonlinear phenomena like dark beam self-trapping,[32] soliton interactions,[128]vortex beam generation[129] and modulation instability[75] were studied in photopolymerizable systems.

1.4. Nonlinear optical fabrication processes

One of the major outcomes from the studies of optical nonlinear phenomena such as self-trapping and MI in photopolymerizable media is the development of simple yet elegant optical micro-components and microstructures fabrication techniques based on these phenomena. Various polymer microstructures fabricated using these two nonlinear phenomena would be briefly reviewed in this section.

1.4.1 Light-induced self-written optical waveguides (LISW)

After the initial theoretical and experimental demonstration of self-trapping in photosensitive materials, self-written optical waveguides were fabricated in photopolymers by using the principle of self-trapping. Unlike other nonlinear media (Kerr, photorefractive (where the self-trapping is transient in nature)), self-trapping in photopolymers results from the permanent refractive index change and the process generates a long-lasting optical waveguide microstructure corresponding to the profile of the self-trapped beam. Initially, such waveguide structures were fabricated using optical

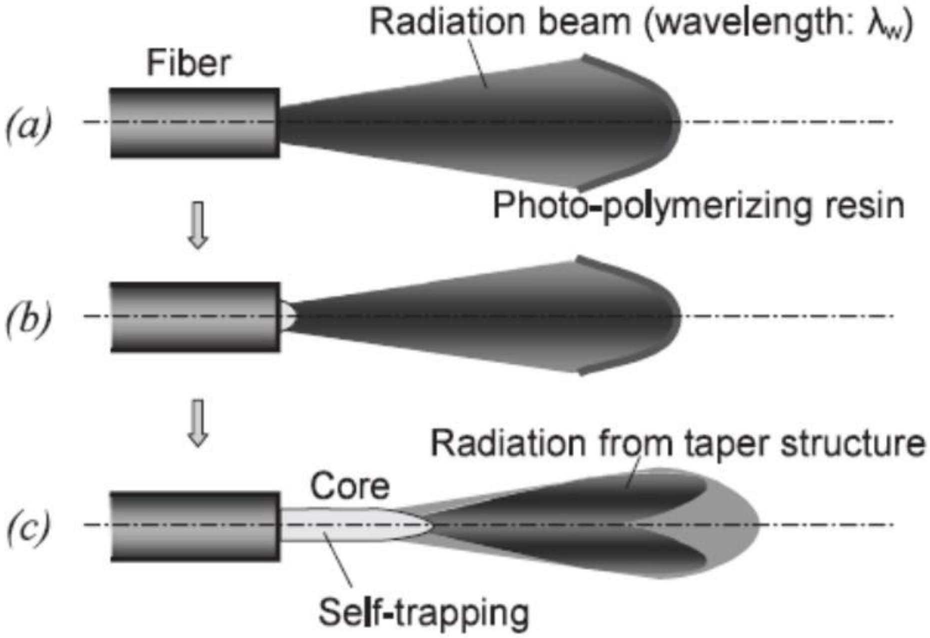

Figure 1.8 Growth mechanism of self-written optical waveguide. Reprinted with permission from IEICE.[130]

fiber and the process[119,130] is schematically shown in figure 1.8. In the first step, the tip of the fiber is inserted into photopolymerizable resin and Gaussian shaped beam from the fiber irradiates the resin (figure 1.8a). Curing or polymerization begins from the core tip, where the intensity is maximum (figure 1.8b) and the core grows longitudinally because of the self-trapping of the irradiating beam in the higher refractive index core (figure 1.8c). Rapid growth takes place until the attenuation of irradiation intensity below the threshold intensity for self-trapping. At the same time, the region surrounding the core which receives lesser intensity (compare to the core) undergoes corresponding degree of curing or polymerization, resulting in lesser change in refractive index compare to the core. This lower refractive index region acts as cladding and thus an optical waveguide with higher refractive index core surrounded by lower refractive index cladding is formed by the self-trapping process. This technique was widely used for making optically integrated circuits.[88,130,131]

Apart from waveguide structures, it was shown that complex three-dimensional structures such as open-cellular structures and artificial compound eye can be fabricated using the self-trapping phenomena. Jacobsen *et al*. fabricated polymer microstructures with truss features (shown in figure 1.9a) using the principles of self-trapping.[132–134] In their works, they used a two dimensional mask instead of an optical fiber (which was used in previous works) to create the required pattern. In particular, for making the truss features, they used intersecting waveguides. It was shown previously, that waveguides

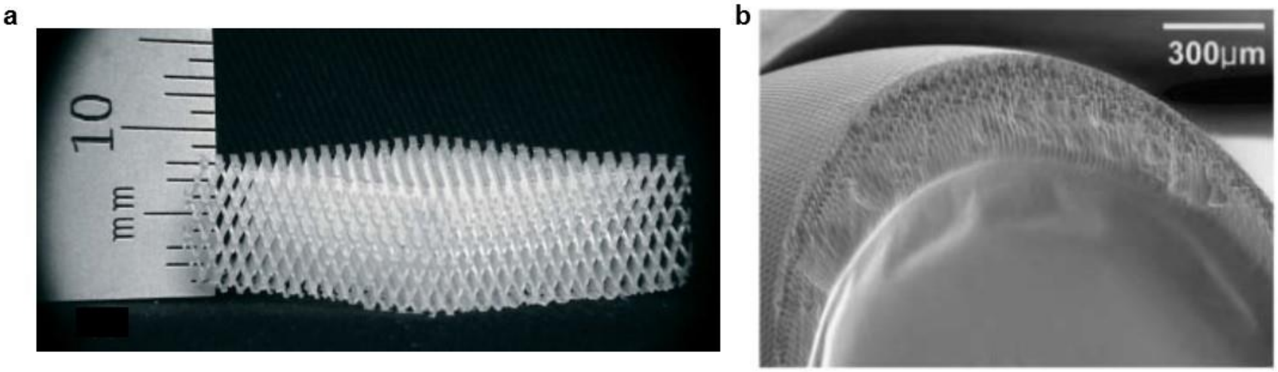

Figure 1.9 a) Polymer micro-truss structure by self-trapping b) artificial compound eye by microlens assisted self-trapping. Reprinted with permission from John Wiley and Sons[132] and American association for advancement of science.[135]

intersecting at an angle greater than 9^0 would propagate through one another without merging. This idea was used to make the truss features by intersecting multiple self-propagating waveguides at appropriate orientation. Jeong *et al*. showed that not only passive structures but also complex active structures can be made using self-trapping.[135] They made the artificial compound eye shown in figure 1.9b by using micro-lens assisted self-trapping in photopolymerizable resin. In this case, waveguide structures were formed by passing UV light through a low Fresnel number microlens and the beam was self-trapped after crossing the focal plane by the polymerization induced refractive index change. These examples show the degree of complexity achieved by microstructure fabrication techniques based of optical self-trapping in polymers.

1.4.2. Metallodielectric and metallic microstructures by self-trapping

In addition to the fabrication of complex structures, self-trapping based microstructure fabrication technique can be used to make metallodielectric microstructures. This was demonstrated by the works from our research group.[86,136] In this work, metallodielectric structure was formed by self-trapping a cw laser in a photopolymerizable organosiloxane medium doped with silver (Ag) nanoparticles. Free radical polymerization induced by the laser beam in the organosiloxane medium provided the required refractive index change for the self-trapping process and the Ag nanoparticles present in the medium got embedded in the self-trapped beam. As the refractive index change induced by the beam is irreversible, permanent waveguide microstructure embedded with Ag nanoparticles were formed. It was shown that the Ag nanoparticles, much smaller than the wavelength of the laser beam, neither hindered the propagating beam nor impaired the self-trapping process. Thus, this work showed optical self-trapping as a viable single step, room temperature route for fabricating three-dimensional metallodielectric structures. Not only metallodielectric but also metallic microstructures were fabricated using the self-trapping approach. T.A. Schaedler *et al*. made metallic microstructures by combining optical self-trapping with electroless metal plating.[137] In their work, solid microlattice structures were formed by intersecting self-trapped waveguides in photopolymerizable resin and these microlattices were used as templates for electroless metal plating. Final metallic microstructures were formed by etching the polymer templates. These are some of the examples showing the versatility of optical self-trapping based microstructure fabrication techniques.

1.4.3. MI induced microstructure fabrication

Similar to self-trapping, MI of optical field in nonlinear polymer media has also been utilized for fabricating polymer and metallodielectric microstructures. Pioneering results in MI induced microstructure fabrication have been demonstrated by our research group. These works exploited the spontaneous pattern formation of incoherent white light in nonlinear media under certain specific conditions (these conditions were explained in detail in previous section). As free radical polymerizable organosiloxane medium (shown in scheme 2)[138] satisfies all the necessary prerequisites for white light MI, all these works were carried out using this material. In the very first work,[75] MI induced polymer microstructures were fabricated as follows: Collimated broad beam of white light from quartz-tungsten halogen lamp was shone on the entrance face of a polymethylmethacrylate cuvette. Striations on the wall of the cuvette imposed a weak perturbation or noise on the optical field, which would have been negligible under linear conditions, got amplified by the photopolymerization induced nonlinear refractive index change. Because of this nonlinear temporal evolution of refractive index change, the initially uniform beam was subjected to MI. Figure 1.10 shows the MI induced disintegration of uniform optical field into individual spots over time at the exit face of the cuvette and these individual spots are

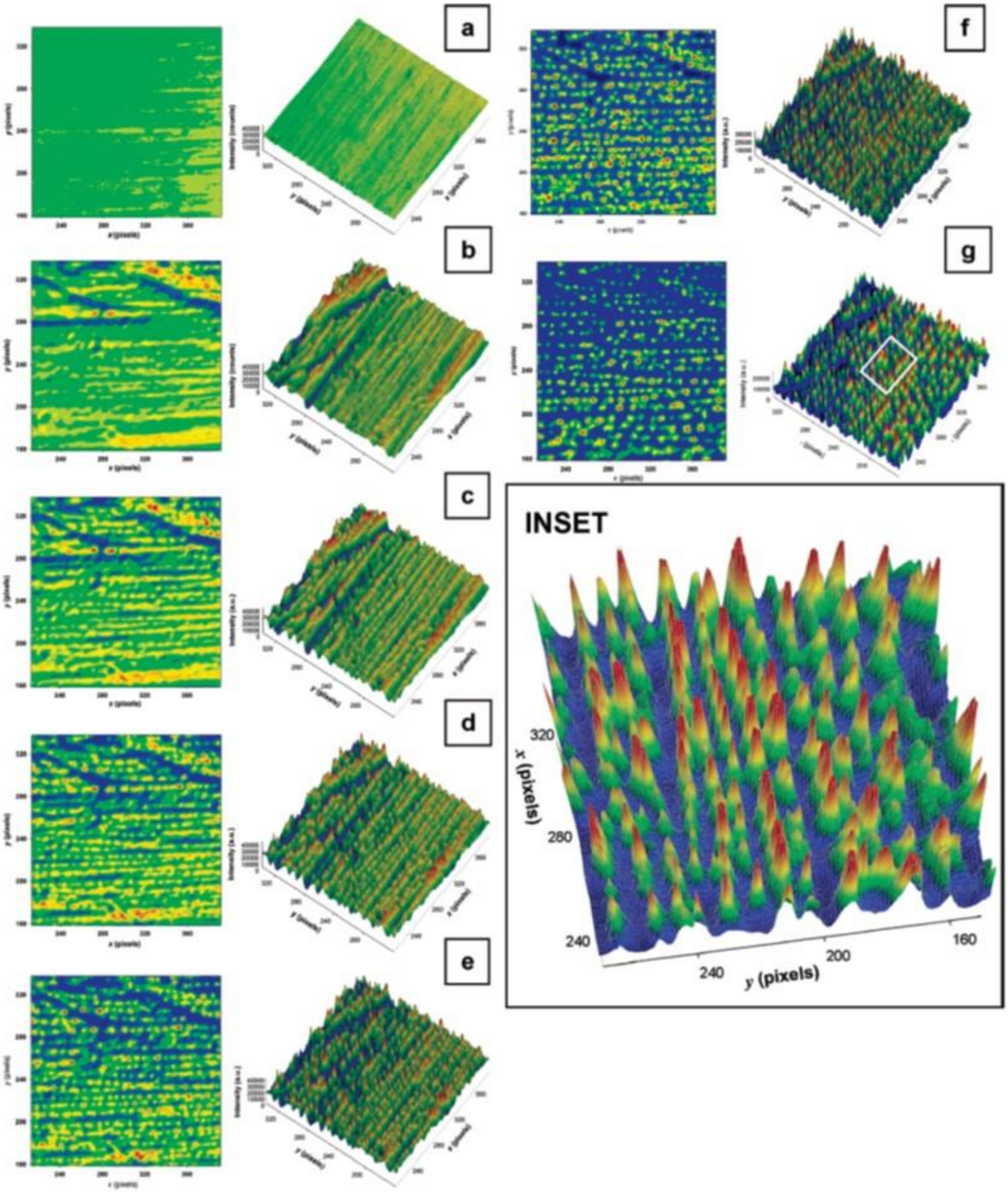

Figure 1.10 MI induced disintegration of optical field over time. Reprinted with permission from American chemical society.[75]

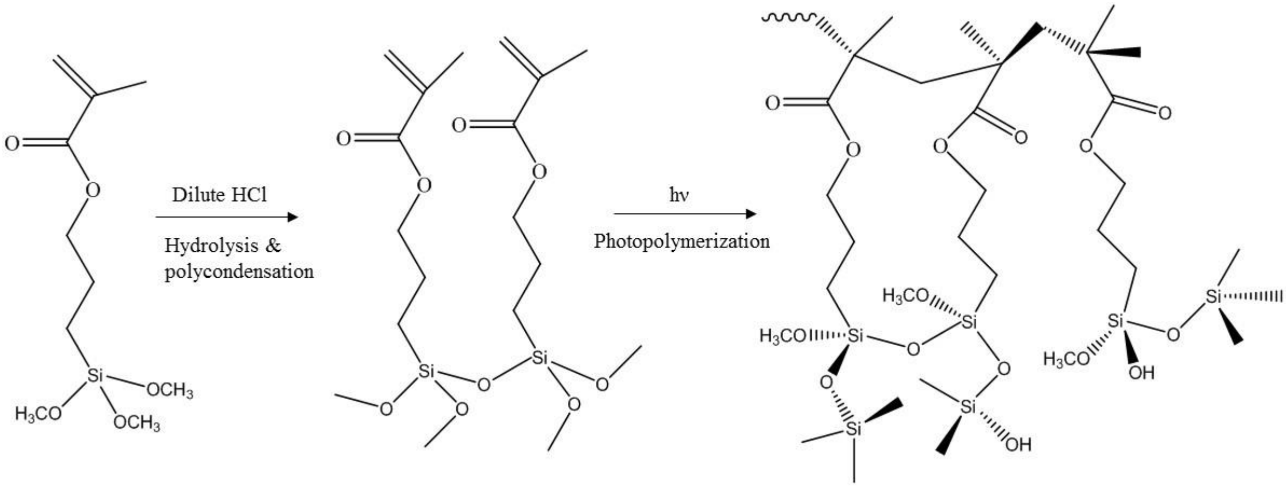

Scheme 1.2. Hydrolysis and polycondensation of the organo siloxane units to oligomers and subsequent photopolymerization through the methylmethacrylate units. Adapted from (138)

transverse cross-section of self-trapped light filaments propagating in their own self-induced waveguide channels. As the MI induced waveguide channels had originated from an irreversible polymerization reaction, they imprinted corresponding polymer microstructures permanently. In this way, tens of thousands of polymer waveguide structures were fabricated using the principles of MI.

1.4.4. MI induced complex structures

The polymer waveguide structures mentioned in the previous section were randomly positioned in space, as they originated from inherent random noise in the system. Latter works from our group, had shown the possibility of fabricating complex microstructured lattices like square,[75] near cubic,[82] simple cubic,[85] BBC[83] and hexagonal[84] geometries. Such optical microstructured lattices are typically generated through complex holographic lithographic techniques involving the interference of mutually coherent laser sources. 1D and 2D periodic lattices are generated through the interference of 2 and 3 mutually coherent laser beams respectively, whereas a 3D periodic lattice is generated by from the interference of 4 in-phase lasers. We used incoherent white light from incandescent bulb for generating complex periodic mircostructured lattices using the principles of MI. In one of works we have shown the spontaneous generation of 3D lattices using an orthogonal pair of white light beams propagating simultaneously in a free radical polymerizable medium. Formation of random 3D waveguide microstructure in polymerizable medium through MI was explained in the previous section. Similar sequence of events occur for the beams undergoing MI but instead of using 1 beam, 2 mutually orthogonal beam are used in this work and the dynamic interaction between the beams simultaneously undergoing polymerization induced MI resulted in 3D lattices with near cubic symmetry. Self-alignment of MI induced filaments was driven by intersection and mutual refractive index change of these filaments. Intersection of filaments occur because each individual filament acts as spatial soliton. During collision, solitons can pass through each other without losing their identity i.e., spatial intensity distribution. Thus the intersection between mutually orthogonal filaments formed due to simultaneous MI of the beams generated 3D near cubic microstructured lattices. In another work, we have shown a single-step route for fabricating black and bright hexagonal and square polymer lattices by using MI (figure 1.11). These complex structures were formed by introducing hexagonal or square array of amplitude depression (dips) on the beam. When the patterned beam initiated free radical polymerization induced refractive index change, under these nonlinear conditions, the dips developed into hexagonal or square array of polymer lattices, while the bright interstitial regions subjected to MI induced filamentation. These filaments with a characteristic diameter (d_f), organised themselves into a variety of geometries depending upon the shape and dimension of the interstitial bright region. When the width of the interstitial regions was > 2 d_f, the filaments were randomly arranged, whereas for the width of < 2d_f, the filaments got orderly self-organised around the dips. For the width of ~ 2d_f the filaments got organised into long range hexagonal or square symmetry. This work demonstrated the sophistication of this technique for fabricating complex geometries, which would be difficult to achieve through conventional lithography.

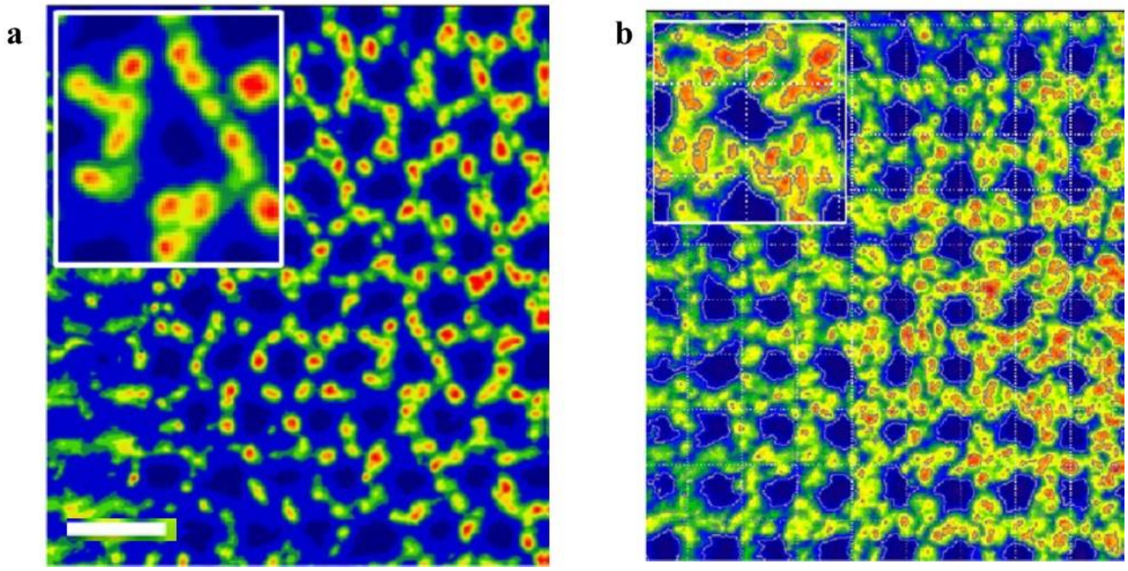

Figure 1.11 Optochemical self-organised structures a) hexagonal lattice b) square lattice, scale bar =400 μm. Reprinted with permission from American chemical society.[84]

Also we made metallodielectric microstructures by eliciting MI of incoherent white light in silver nanoparticles doped organosiloxane medium.[86] MI occurs due to the free radical polymerization induced refractive index change. As the polymerization is irreversible, MI induced filaments transformed into permanent cylindrical microstructures doped with silver nanoparticles. This is entirely different from the metallic structures mentioned in the previous section, as these structures were made with using the self-trapping of a template structure, whereas our metallodielectric structures were spontaneous generated in single step. Thus our group has developed MI and self-trapping based microfabrication technique as a powerful single-step, room temperature route for making complex three dimensional microstructures. However, all these structures were made with a single material (methacrylate functionalized organosiloxane) using free radical polymerization.

1.4.5. Stereolithographic 3D printing

Photopolymerization reaction that supports the nonlinear phenomena such as MI and self-trapping has also been widely used in 3D printing, an emerging microstructure fabrication technique. Working principle of stereolithograpy based 3D printing, which relies on photoplymerization can be briefly explained as follows:[139,140] first, a 3D digital version of the objected to be printed is made using computer aided design and the file is converted to a printer readable system called Standard Tessellation Language (STL). The STL system slices the 3D digital object into number of 2D layers. Then every slice is sequentially projected one after another onto the photopolymerizable liquid monomer bath using an appropriate light source (UV laser).

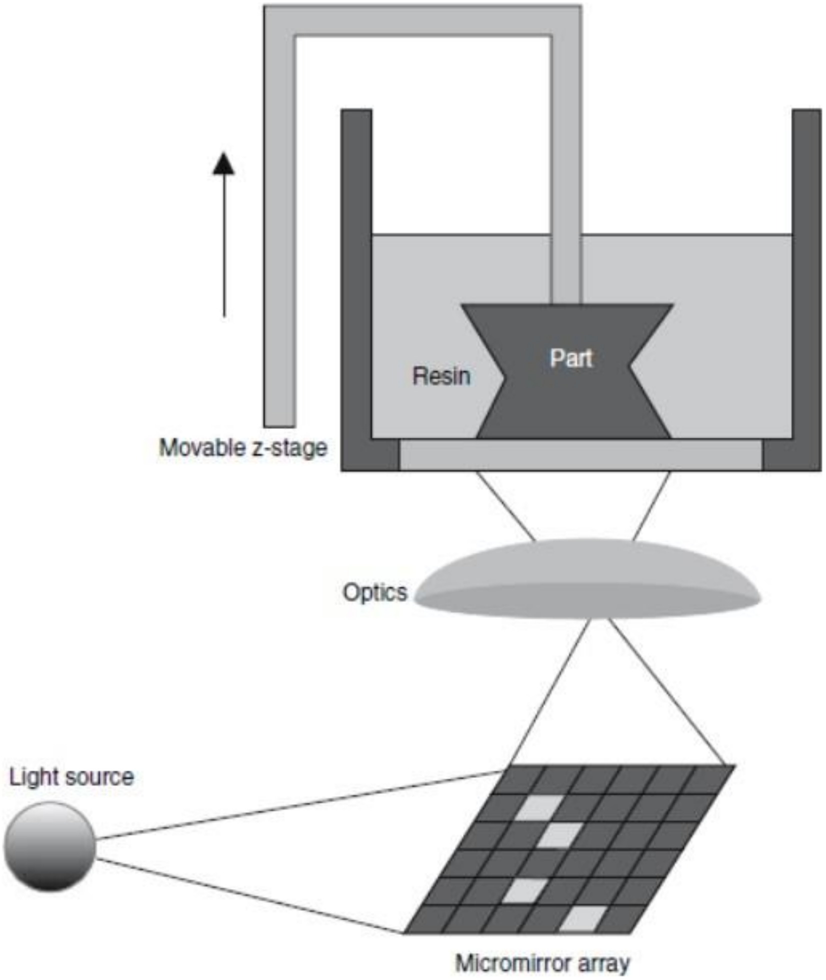

Figure 1.12 Principle of photopolymerization based 3D printing. Reprinted with permission from springer.[140]

As the first layer polymerizes, it adheres to the bottom of the z stage and the stage is moved upwards (as shown in figure 1.12). Then the next slice is projected and the same process is repeated until the entire structure is made. This process was developed by Charles Hull in 1984 and till date the same principle is used in all the commercial stereolithography based 3D printers.[141–145]

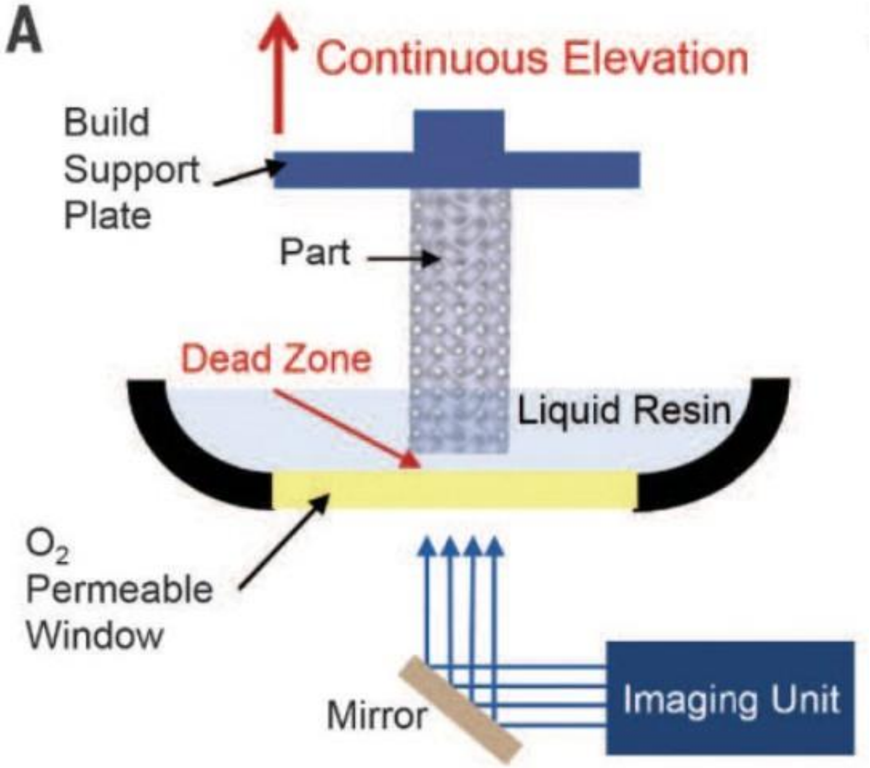

Figure 1.13 Woking principle of CLIP. Reprinted with permission from American association for advancement of science.[146]

One of the major hindrances in developing this technique for mass production is the slow print speed. Currently, it takes few hours to print a centimeter long structure. Recent work from Desimone's group provided a solution for this problem, which increased the print speed by an order of magnitude.[146]

Their method exploited the ability of oxygen to inhibit the free radical polymerization reaction (oxygen either quenches the photoexcited initiators or generates unreactive peroxide by combining with the free radical formed by photocleaved initiators) and showed controlled oxygen exposure can be used to increase the efficiency of stereolithography based 3D printing. Figure 1.13 shows the working principle of their technique. Here, stereolithography is conducted above a thin oxygen permeable layer, which enables a continuous liquid interface production (CLIP) by creating a “dead zone” (thin uncured liquid layer between the advancing cured part and the window). Similar to the conventional stereolithographic 3D printing, the image of the objected to be printed is projected onto the resin but the presence of this liquid interface provides a continuous renewal of uncured resin and thus makes the process nonstop. This is fundamentally different from the present stereolithographic 3D printing approach, where the UV exposure, resin renewal and movement of the cured part are done in separate steps. Thus, the continuous process increases the print speed by an order of magnitude while maintaining the part accuracy or resolution offered by stereolithographic 3D printing. This work shows the significance of improvisation or value addition to this 30 years old technology and provides the motivation to work on developing new 3D printing techniques based on photopolymerization.

1.4.6. Nonlinear 3D printing

Stereolithographic 3D printing technique mentioned in the previous section has a resolution of 10 microns, which is not sufficient to satisfy the growing demands for device miniaturization and multifunctionalization requiring sub-micron resolution. One of the ways to circumvent this problem is to use two photon polymerization, a nonlinear optical effect induced photopolymerization process capable of providing sub-micron or nanometer resolution.[147,148] Unlike single photon polymerization, here the polymerization is initiated by simultaneously absorbing two photons at longer wavelength, usually in the infrared (IR) region. As the polymerization reaction is initiated only by longer wavelength sources, the photons penetrate deep inside the monomer volume (monomers have negligible absorption at this spectral region) and initiate polymerization only in the vicinity of the focal volume. Because the focal spot is a three dimensional volume element, this process inherently polymerizes the entire volume element resulting in 3D structure.

The nonlinearity of two photon absorption process and the corresponding improvement in spatial resolution in 3D structure fabrication process can be understood as follows:[149] to initiate photopolymerization, the photon must be first absorbed by the initiator or monomer. During this process there is a transfer of energy and momentum from the optical field to the medium, which is represented by the imaginary part of the nonlinear susceptibility tensor. Change in energy (dW) per unit time and unit volume from the optical field to the material is given by,

$$\frac{dW}{dt} = \left\langle \underset{E}{\rightarrow}\underset{P}{\rightarrow} \right\rangle \tag{25}$$

where E is the electric filed vector and P is the polarization induced in the medium and the bracket denotes time averaging. P is expressed in terms of nonlinear susceptibility tensors (equation 8) and χ^3, the third order nonlinear susceptibility tensor contributes to the two photon absorption process. Equation 26 shows the correlation between the nonlinear susceptibility tensor and the two photon energy absorption rate,

$$\frac{dW}{dt} = \frac{8\pi^2 \omega}{c^2 n^2} I^2 \, Im[\chi^3] \qquad (26)$$

where ω is the frequency of the optical field and n is refractive index of the medium. It is clear from the equation 26 that the two photon absorption process originates from nonlinear optical effect and the absorption rate is quadratically dependent on the intensity of the irradiation source. Nonlinear absorption combined with quadratic dependence of irradiation intensity are important mechanisms for improving the resolution of two photon fabrication process. Because of these mechanisms, the two photon absorption is limited to an extremely small cross-section and the polymerization reaction is confined to the 3D volume element or voxel in the vicinity of the laser focus.

First evidence of two photon polymerization induced 3D microstructure fabrication was demonstrated by Satoshi Kawata *et al.* They made a 7μm diameter

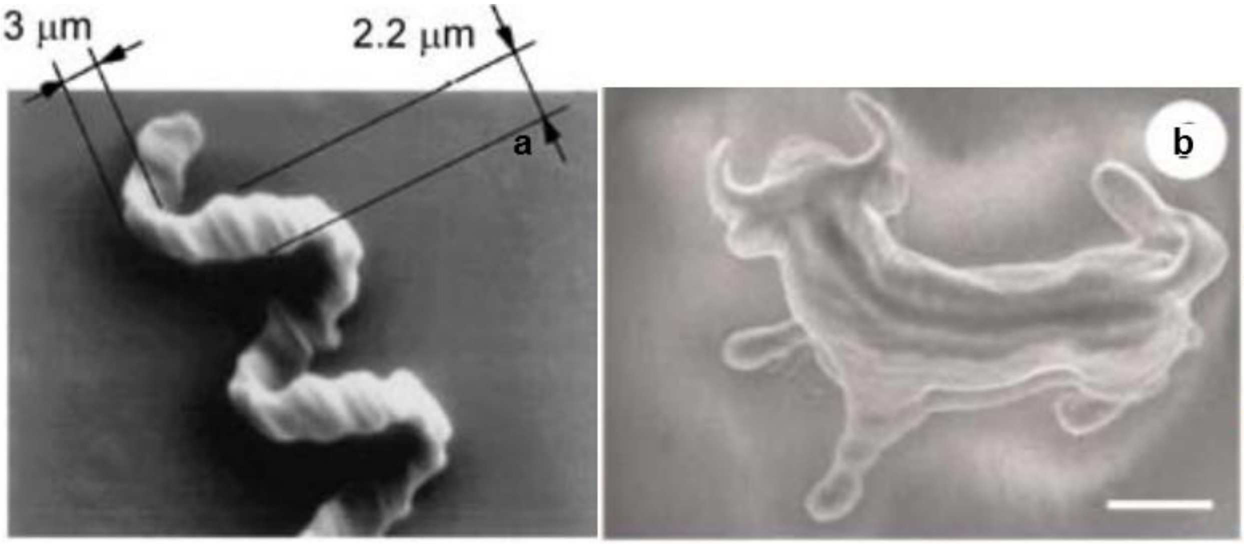

Figure 1.14 a) First experimental demonstration of two photon polymerization based 3D microfabrication b) subdiffraction limit structure by two photon polymerization (scale bar 2 μm). Reprinted with permission from optical society of America[148] and Nature publishing group.[150]

and 50 μm long spiral coil with 1.3 μm X 2.2 μm line cross section[148] (figure 1.14a). Because of the use of low numerical aperture lens, the feature size was larger than the potential resolution offered by the technology. However, this work showed the feasibility of fabricating sub-micron 3D polymer structure using two photon polymerization. Later work from the same group showed the fabrication of 120 nm 3D polymer structure (figure 1.14b) defying the diffraction limit.[150] This was achieved by combining the quadratic dependence of two photon absorption probability (nonlinear effect) with the requirement of critical exposure energy (due to the scavenging of photoinduced radicals by oxygen) for initiating the polymerization. These two factors defied the diffraction limit and generated nanometer size voxel. Following these initial works, two photon polymerization based micro fabrication technique has been used in various fields like optoelectronics,[151] photonic,[152] micromachines and MEMS,[153] microfluids,[154] biomedical devices[155] and so forth. Recent works combined the principles of two photon polymerization microfabrication technique with computer aided 3D printing and showed the possibility of printing nanometer features, exceeding the resolution (~ 10 micron) offered by the current 3D printing techniques.[156157] These works show the potential offered by nonlinear optical effect based microfabrication techniques.

1.5. Cationic polymerization

Almost all the photopolymerization induced nonlinear optical effects and the microstructure fabrication techniques based on the principles of these optical effects mentioned in the previous sections are carried out using free radical polymerization. Another less explored polymerization mechanism both in nonlinear optical studies and microstructure fabrication works is cationic polymerization. It offers the following merits over free radical polymerization:[158–162] 1) the reaction is not air or oxygen sensitive and thus eliminates the requirement of inert atmosphere during polymerization. 2) Once initiated, cationic polymerization is non-terminating and proceeds in the absence of light. This process is called dark reaction and results in further polymerization either on thermal post treatment or on standing and this clearly distinguishes cationic polymerization from free radicals, which extinguish by various bimolecular termination and arrest polymerization in the absence of light. 3) Cationically polymerizable monomers and oligomers are inherently less toxic compare to acrylate and methacrylate monomers used in free radical polymerization. 4) Cationic ring opening polymerization of epoxides provide less volume shrinkage and thus afford better surface adhesion compare to free radical based polymerization systems. 5) Cationic polymerizable systems possess better thermal and mechanical properties compare to free radical polymerizable systems.

Considering the potential offered by cationic polymerization, all the research works presented in this thesis used cationic polymerization. Here, a brief overview of cationic polymerization is presented. Cationic polymerization initiated by photogenerated acid generated from onium salts was first proposed by Crivello in 1978.[163] Onium salts with their thermal stability and latency in presence of highly reactive monomer at ambient temperature played a major role in the development of photocationic polymerization.[164] Onium salt photoinitiators are ionic compounds made of a cationic and an anionic compound. The cationic portion determines the photochemistry of the compound such as the photosensitivity, absorption characteristics and quantum yield. It also controls the thermal stability of the salt. The anionic portion, counterpart of the cationic compound, determines the strength of the acid generated during the photolysis and its initiating efficiency. Also it controls the reactivity of the propagating ion

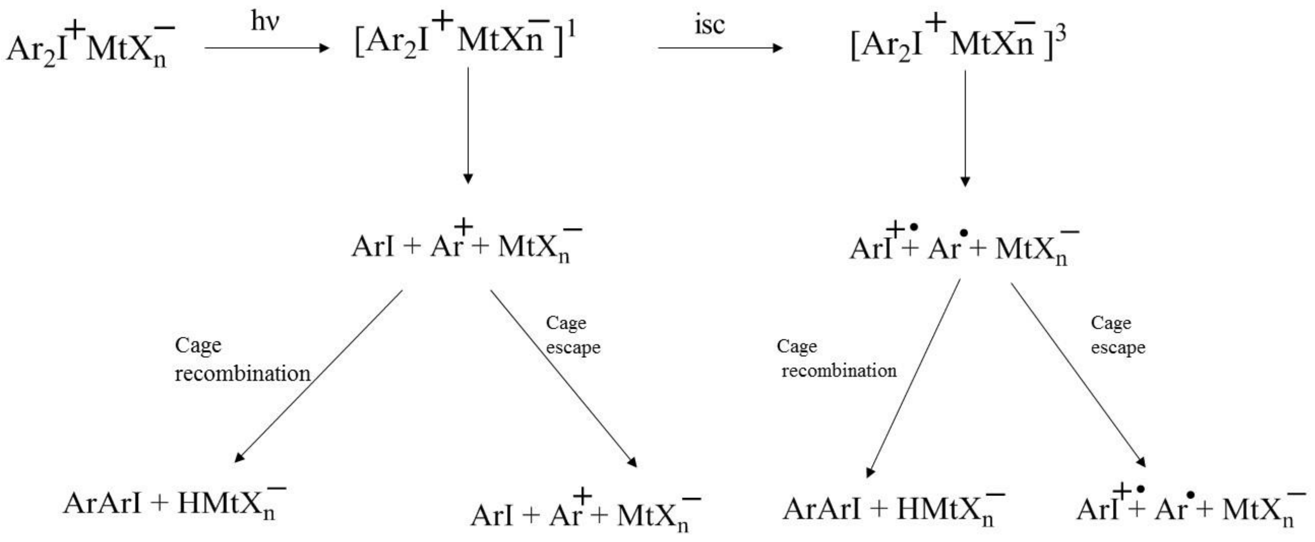

Scheme 1.3 Photodecomposition mechanism of diarlyiodonium salt. Reprinted with permission from John Wiley and Sons.[156]

pair during polymerization and thus affects the kinetic of the polymerization reaction. The mechanism of photoacid generation is shown in scheme 1.3, using iodonium salt.[159] Photolysis of onium salt induces both homolytic and heterolytic cleavage results in highly reactive cation, radical-cation and radical species. But these are not primary initiators of the polymerization reaction. Cations and radical cations formed by photolysis, react with suitable proton donor such as water or alcohol present in the monomer to form Bronsted acid and the polymerization is initiated by this Bronsted acid. Similar scheme can be shown for the photolysis of sulphonium salt based initiators. The diaryliodonium and triarylsulphonium salts are considered "universal photoinitiators" for cationic polymerization, as they can initiate polymerization of every known cationically polymerizable monomers. It was also shown that both diarlyiodonium and triarylsulphonium salts can be photosensitized through photoinduced electron transfer from an excited photosensitizer.[165–169] Thus by using appropriate dyes, the photosensitivity of these salts can be extended to the visible spectral region.

1.5.1. Cationically polymerizable monomers

Photocationic polymerization has been used to carry out ring opening polymerization[159,169] of epoxy monomers, cyclic acetals, cyclic ethers and lactones as well as carbocationic addition polymerization of unsaturated monomers[170,171] such as vinyl ethers, N-vinylcarbazole and styrene. The range of cationically polymerizable monomers is shown in scheme 1.4. As mentioned before, cationic polymerization provides a number of merits over free radical polymerization and the availability of broad range of cationically polymerizable monomers, with a feasibility of incorporating heteroatoms in main chain adds to the advantages of cationic polymerization. Off these monomers, epoxides form an important class of cationically polymerizable monomers for both nonlinear optical studies and microstructure fabrication due to their high reactivity, mechanical and thermal properties, chemical resistance and excellent adhesion to various substrates. One of the extensively used epoxy resins for photolithographic based microstructure fabrication is Su8.[172] The resin formulation consists of a multifunctional (8 functional groups) epoxy, Bisphenol A Novolak epoxide oligomer and a photoinitiator. Upon UV irradiation, the photoinitiator generators protonic acid, which initiates the cationic polymerization of the epoxy. Because of the presence of 8 reactive sites in each monomer unit of Su8, high degree of cross-linking can be achieved. This leads to high mechanical and thermal stability of the photolithographic structures made from Su8. Thus Su8 proves the significance of epoxy in microstructure fabrication. However, being a proprietary formulation,[172] it offers very little room for photochemical modifications. For this research we used cycloaliphatic epoxy, one of the less explored epoxides in the area of photolithographic microstructure fabrication. Photochemistry of cycloaliphatic epoxide is well understood and most importantly the kinetic of cycloaliphatic epoxy polymerization can be controlled by modifying the polymerization system. These keys aspects motivated us to work with cycloaliphatic epoxy for this research work.

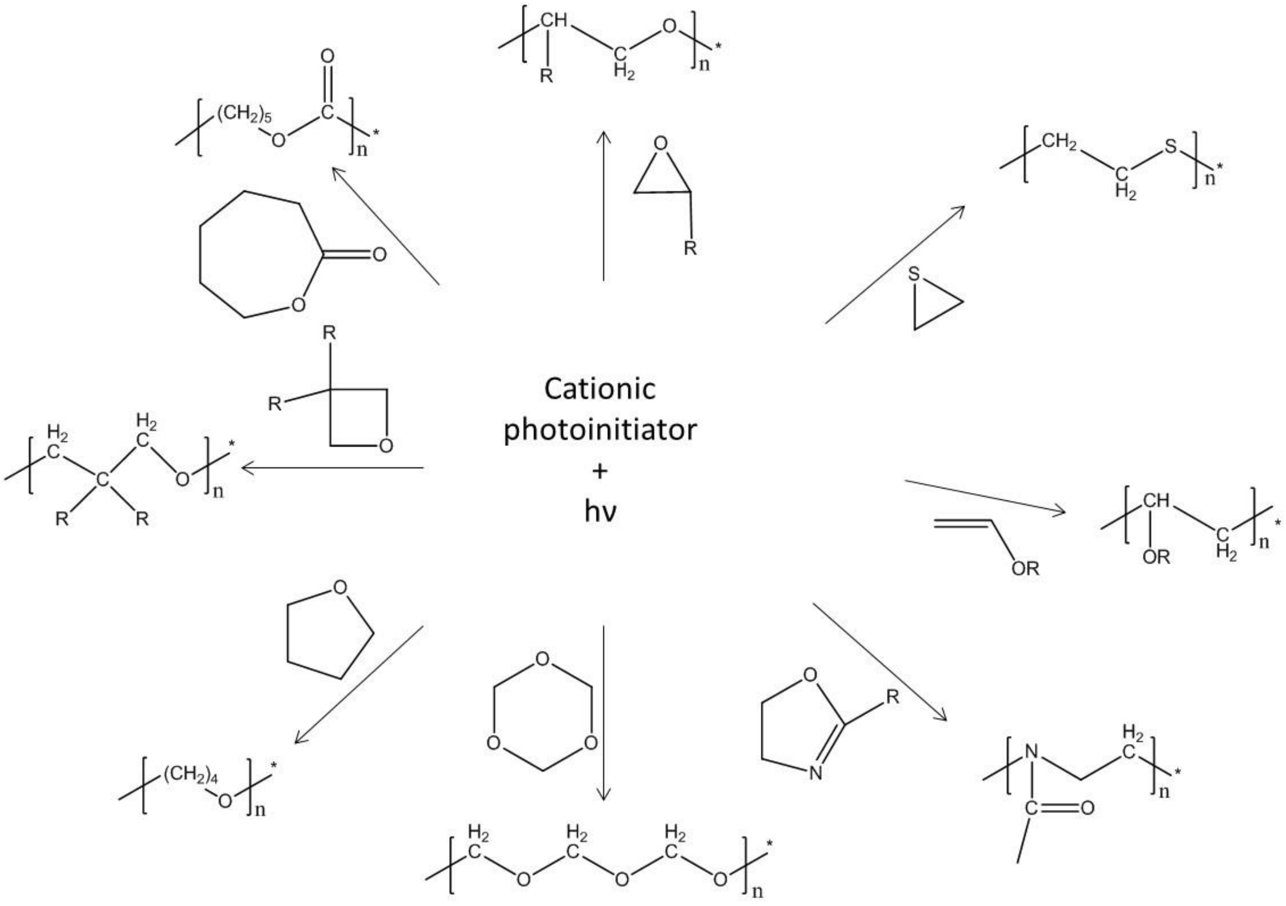

Scheme 1.4 Cationically polymerizable monomers. Reprinted with permission from John Wiley and Sons.[156]

1.6. Research objectives: Nonlinear waves in cationic polymerization systems

As mentioned in the previous sections, nonlinear propagation of optical field originates from the interaction of light with the media and not from the optical field itself. Thus, the nonlinear optical phenomena such as MI and self-trapping is strongly influence by the type of nonlinear media employed for the studies. Our group has carried out detailed studies of MI and self-trapping of spatially and temporally incoherent white light in free radical polymerizable organosiloxane medium. Earlier, these nonlinear phenomena were studies only with Kerr media and photorefractive media. And investigation of these effects in photopolymerizable media by our group provided interesting results and showed the feasibility of exploiting these nonlinear optical effects for 3D polymer microstructure fabrication. These works motivated to study MI and self-trapping for the first time in cationic polymerizable epoxide systems.

The aim of this thesis is to perform a systematic study of MI and self-trapping in cationically polymerizable epoxide systems. And use these effects to develop a facile route to fabricate 3D polymer and metallodielectric microstructures. In chapter 2, we presented the MI induced spontaneous pattern formation in visible light cationically polymerizable epoxide systems and showed the way to control the dynamics of MI using polymerization kinetics for the first time. This was followed by mechanical and thermal properties studies of epoxide-siloxane blend systems showing MI induced waveguide microstructures formation in chapter 3. In chapter 4, fabrication of gold and silver nanoparticles embedded epoxide-siloxane waveguide microstructures was demonstrated by combining MI with *in-situ* synthesis. The gold/epoxide-siloxane polymer nanocomposite studied in chapter 4 was used to make free standing thin film near infrared (NIR) surface enhanced Raman scattering (SERS) substrate and its SERS activity was demonstrated using Eosin Y in chapter 5. In chapter 6, a new 3D printing technique based on optical self-trapping for making continuous structures was demonstrated. Finally, a summary of contributions from all these works and potential ideas for future work were presented in chapter 7. Chapter 2 and 6 were initially prepared as manuscripts for publication and contains significant written input from my supervisor Dr. Kalaichelvi Saravanamuttu. Entire thesis was subjected to turnitin similarity checking.

References

(1) Zeise, E. K. *Phys. Rev. Lett.* **1981**, *46* (24), 1588–1591.

(2) Anker, T.; Albiez, M.; Gati, R.; Hunsmann, S.; Eiermann, B.; Trombettoni, A.; Oberthaler, M. K. *Phys. Rev. Lett.* **2005**, *94*, 020403 1–4.

(3) Hasegawa, A.; Tappert, F. *Appl. Phys. Lett.* **1973**, *142* (23), 142–144.

(4) Soljac, M. and M. S. *Phys. Rev. A* **2000**, *62*, 043817–1 043817–6.

(5) Crosignani, B.; Fisica, D.; Aquila, L.; Bordoni, F. U.; Porto, P. Di; Fisica, D.; Aquila, U.; Bordoni, F. U. *J. Opt. Soc. Am. B* **1993**, *10* (3), 446–453.

(6) Tzoar, N.; Gersten, J. I. *Physcial Rev. B* **1971**, *4* (10), 3540–3547.

(7) Segev, M. *Opt. Quantum Electron.* **1998**, *30*, 503–533.

(8) Stegeman, G. I. A.; Christodoulides, D. N.; Segev, M. *IEEE J. Quantum Electron.* **2000**, *6* (6), 1419–1427.

(9) F.L. Pedrotti and L.S. Pedrotti. *Introduction to optics*, Second.; New Jersey, **1993.**

(10) Agrawal, Y. S. K. and G. P. *Optical solitons*; Academic Press, USA, **2003**.

(11) Chiao, R. Y.; Garmire, E.; Townes, C. H. *Phys. Rev. Lett.* **1964**, *13* (15), 479–483.

(12) V.I.Talanov. *Radio Phys.* **1964**, *7*, 254.

(13) Kelley, P. L. *Physcial Rev. Lett.* **1965**, *15* (26), 1005–1008.

(14) Marburger, E. L. D. and J. H. *Phys. Rev.* **1969**, *179* (3), 862–868.

(15) Bjorkholm, J. E.; Ashkin, A. A. *Phys. Rev. Lett.* **1974**, *32* (4), 129–135.

(16) A. Barthelemy, S. M. and C. F. *Opt. Commun.* **1985**, *55* (3), 201–206.

(17) Detlef Kip, Marin Soljacic, Mordechai Segev, Eugenia Eugenieva, D. N. C. *Science.* **2000**, *290*, 495–498.

(18) Mitchell, M.; Chen, Z.; Shih, M.; Segev, M. *Phys. Rev. Lett.* **1996**, *77* (3), 490–493.

(19) Conti, C.; Peccianti, M.; Assanto, G. *Phys. Rev. Lett.* **2004**, *92* (11), 113902–1 4.

(20) Christodoulides, D. N.; Coskun, T. H.; Mitchell, M.; Chen, Z.; Segev, M. *Phys. Rev. Lett.* **1998**, *80* (23), 5113–5116.

(21) Chen, Z.; Mitchell, M.; Segev, M.; Coskun, T. H.; Christodoulides, D. N. *Science (80-.).* **1998**, *280* (May), 889–892.

(22) Eugenieva, E. D.; Christodoulides, D. N. *Opt. Lett.* **2000**, *25* (13), 972–974.

(23) Katz, O.; Carmon, T.; Schwartz, T.; Segev, M. *Opt. Lett.* **2004**, *29* (11), 1248–1250.

(24) Coskun, T. H.; Christodoulides, D. N.; Kim, Y.; Chen, Z.; Soljacic, M. *Phys. Rev. Lett.* **2000**, *84* (11), 2374–2377.

(25) Lin, Y.; Lee, R.; Kivshar, Y. S. *J. Opt. Soc. Am. B* **2008**, *25* (4), 576–581.

(26) Armaroli, A.; Trillo, S.; Ingegneria, D.; Saragat, V.; Fratalocchi, A.; Fisica, D.; Sapienza, R.; Moro, P. A. *Phys. Rev. A* **2009**, *80*, 053803 1–9.

(27) Kewitsch, A. S.; Yariv, A. *Opt. Lett.* **1996**, *21* (1), 24–26.

(28) Manabu Kagami, T. Y. and H. I. *Appl. Phys. Lett.* **2001**, *79* (8), 10791081.

(29) Zhang, J.; Kasala, K.; Rewari, A.; Saravanamuttu, K. *J. Am. Chem. Soc.* **2006**, *128*, 406–407.

(30) Zhang, J.; Saravanamuttu, K.; Ls, O. *J. Am. Chem. Soc.* **2006**, *280* (23), 14913–14923.

(31) Ana B. Villafranca, and K. S. *J. Phys. Chem. C* **2015**, *112* (44), 17388–17396.

(32) Kasala, K.; Saravanamuttu, K. *J. Am. Chem. Soc.* **2012**, *134*, 14195–14200.

(33) Villafranca, A. B.; Saravanamuttu, K. *J. Phys. Chem. C* **2008**, *112* (44), 17388–17396.

(34) V.I.Talanov and V.Bespalov, *JETP Lett.* **1966**, *3*, 307.

(35) Benjamin, T. B.; Feir, J. E. *J. Fluid Mech.* **1967**, *27*, 417–430.

(36) Zakharov, V. E.; Ostrovsky, L. a. *Phys. D Nonlinear Phenom.* **2009**, *238* (5), 540–548.

(37) Brinkman, A. H. and W. F. *IEEE J. Quantum Electron.* **1980**, *16* (7), 694–697.

(38) Anderson, D.; Lisak, M. *Opt. Lett.* **1984**, *9* (10), 468–470.

(39) V.I.Korneev, N. N. A. and. *Theor. Math. Phys* **1986**, *69* (2), 189–194.

(40) Zakharov, V. E.; Gelash, a. a. *Phys. Rev. Lett.* **2013**, *111* (5), 054101.

(41) Erkintalo, M.; Hammani, K.; Kibler, B.; Finot, C.; Akhmediev, N.; Dudley, J. M.; Genty, G. *Phys. Rev. Lett.* **2011**, *107* (25), 253901.

(42) Sørensen, S. T.; Larsen, C.; Møller, U.; Moselund, P. M.; Thomsen, C. L.; Bang, O. *J. Opt. Soc. Am. B* **2012**, *29* (10), 2875.

(43) Godin, T.; Combes, Y.; Ahmad, R.; Rochette, M.; Sylvestre, T.; Dudley, J. M. *Opt. Lett.* **2014**, *39* (7), 1885–1888.

(44) Yoshi H. Ichikawa, T. S. and T. T. *J. Phys. Soc. Japan* **1973**, *34* (4), 1089–1092.

(45) Onorato, M.; Osborne, A. R.; Serio, M.; Bertone, S. *Phys. Rev. Lett.* **2001**, *86* (25), 5831–5834.

(46) Kharif, C.; Pelinovsky, E. *Eur. J. Mech. - B/Fluids* **2003**, *22* (6), 603–634.

(47) Melo, H. P. M.; Parteli, E. J. R.; Andrade, J. S.; Herrmann, H. J. *Phys. A Stat. Mech. its Appl.* **2012**, *391* (20), 4606–4614.

(48) Konotop, V. V.; Salerno, M. **2001**, No. 1, 1–4.

(49) Strecker, K. E.; Partridge, G. B.; Truscott, A. G.; Hulet, R. G. *Nature* **2002**, *417* (6885), 150–153.

(50) G.P.Agarwal. *Nonlinear Fiber Optics 4th edn*; 2007.

(51) Abdullaev, F. K.; Darmanyan, S. a; Bischoff, S.; Sørensen, M. P. *J. Opt. Soc. Am. B* **1997**, *14* (1), 27.

(52) Stenflo, P. K. S. and L. *IEEE Trans. Plasma Sci.* **2001**, *29* (2), 267–270.

(53) Hasegawa, A. *Opt. Lett.* **1984**, *9* (7), 288–290.

(54) Tai, K.; Hasegawa, a.; Tomita, a. *Phys. Rev. Lett.* **1986**, *56* (2), 135–138.

(55) Tai, K.; Tomita, a.; Jewell, J. L.; Hasegawa, a. *Appl. Phys. Lett.* **1986**, *49* (5), 236.

(56) Dianov, E. M.; Mamyshev, P. V; Prokhorov, A M.; Chernikov, S. V. *Opt. Lett.* **1989**, *14* (18), 1008–1010.

(57) Agarwal, G. P. *Phys. Rev. A* **1989**, *39* (7), 3406–3413.

(58) Solli, D. R.; Herink, G.; Jalali, B.; Ropers, C. *Nat. Photonics* **2012**, *6* (7), 463–468.

(59) Lee, K. J.; McCormick, W. D.; Ouyang, Q.; Swinney, H. L. *Science* **1993**, *261* (5118), 192–194.

(60) Maini, P. K.; Painter, K. J.; Chau, H. N. P. *J. Chem. Soc., Faraday Trans.* **1997**, *93* (20), 3601–3610.

(61) Mamyshev, P. V; Bosshard, C.; Stegeman, G. I. *J. Opt. Soc. Am. B* **1994**, *11* (7), 1254–1260.

(62) Iturbe-Castillo, M. D.; Torres-Cisneros, M.; Sánchez-Mondragón, J. J.; Chávez-Cerda, S.; Stepanov, S. I.; Vysloukh, V. a.; Torres-Cisneros, G. E. *Opt. Lett.* **1995**, *20* (18), 1853.

(63) Leblond, H.; Cambournac, C. *J. Opt. A Pure Appl. Opt.* **2004**, *6* (4), 461–468.

(64) Soljacic, M.; Segev, M.; Coskun, T.; Christodoulides, D.; Vishwanath, A. *Phys. Rev. Lett.* **2000**, *84* (3), 467–470.

(65) Kip, D.; Sears, S. M. *J.Opt.Soc.Am. B* **2002**, *19* (3), 502–512.

(66) Wang, L. M.; Wang, C.-Y.; Chen, G.-M.; Kuo, C. N.; Lue, C. S. *New J. Phys.* **2015**, *17* (3), 033005.

(67) Bloch, I. *Nat. Phys.* **2005**, *1* (1), 23–30.

(68) Gammie, C. F. *Astrophys. J.* **2001**, *553*, 174.

(69) Chemla, D. S.; Shah, J. *Nature* **2001**, *411* (6837), 549.

(70) Mitchell, M.; Segev, M. *Nature* **1997**, *387* (6636), 880–883.

(71) Buljan, H.; Šiber, A.; Soljačić, M.; Segev, M. *Phys. Rev. E* **2002**, *66* (3), 035601.

(72) Schwartz, T.; Carmon, T.; Buljan, H.; Segev, M. *Phys. Rev. Lett.* **2004**, *93* (22), 223901.

(73) Conti, C.; Ruocco, G.; Trillo, S. *Phys. Rev. Lett.* **2005**, *95* (18), 183902.

(74) Peccianti, M.; Conti, C.; Assanto, G.; Luca, A. De; Umeton, C. *Earth. Moon. Planets* **2004**, *432*, 733–738.

(75) Burgess, I. B.; Shimmell, W. E.; Saravanamuttu, K. *J. Am. Chem. Soc.* **2007**, *129* (15), 4738–4746.

(76) Reece, P. J.; Wright, E. M.; Dholakia, K. *Phys. Rev. Lett.* **2007**, *98* (20), 203902.

(77) Jisha, C. P.; Kuriakose, V. C.; Porsezian, K. *J. Opt. Soc. Am. B* **2008**, *25* (4), 674.

(78) Conti, C.; Ghofraniha, N.; Ruocco, G.; Trillo, S. *Phys. Rev. Lett.* **2006**, *97* (12), 123903.

(79) El-Ganainy, R.; Christodoulides, D. N.; Musslimani, Z. H.; Rotschild, C.; Segev, M. *Opt. Lett.* **2007**, *32* (21), 3185.

(80) Anyfantakis, M.; Loppinet, B.; Fytas, G.; Pispas, S. *Opt. Lett.* **2008**, *33* (23), 2839.

(81) Matuszewski, M.; Krolikowski, W.; Kivshar, Y. S. *Opt. Express* **2008**, *16* (2), 1371–1376.

(82) Burgess, I. B.; Ponte, M. R.; Saravanamuttu, K. *J. Mater. Chem.* **2008**, *18* (35), 4133.

(83) Kasala, K.; Saravanamuttu, K. *J. Mater. Chem.* **2012**, *22*, 12281.

(84) Kasala, K.; Saravanamuttu, K. *Langmuir* **2013**, *29*, 1221–1227.

(85) Ponte, M. R.; Welch, R.; Saravanamuttu, K. *Opt. Express* **2013**, *21* (4), 4205–4214.

(86) Qiu, L.; Saravanamuttu, K. *J. Opt.* **2012**, *14* (12), 125202.

(87) W.Boyd, R. *Nonlinear Optics*, Third.; Academic Press, USA: New York, 2007.

(88) Nie, B. W. *Adv. Mater.* **1993**, *5* (7), 520–545.

(89) Hall, T. J.; Jaura, R.; Connors, L. M. *Prog.Quant.Electr.* **1985**, *10*, 77–146.

(90) M.-F.Shih, M.Segev, G.C.Valley, G.Salamo, B. C. and P. D. P. *Electron. Lett.* **1995**, *31* (10), 826–827.

(91) Segev, M.; Shih, M.; Valley, G. C. *J.Opt.Soc.Am. B* **1996**, *13* (4), 706–718.

(92) Fleischer, J. W.; Segev, M.; Efremidis, N. K.; Christodoulides, D. N. *Nature* **2003**, *422* (March), 147–150.

(93) Jeng, C.; Su, Y.; Hong, R.; Lee, R. *Opt. Express* **2015**, *23* (8), 10266–10271.

(94) Konar, S.; Biswas, A. *Opt. Mater. (Amst).* **2013**, *35* (12), 2581–2603.

(95) Barsi, C.; Fleischer, J. W. *Opt. Express* **2015**, *23* (19), 46–51.

(96) Hao, L.; Hou, C.; Wang, Q. *Opt. Laser Technol.* **2014**, *56*, 326–333.

(97) Sukhorukov.A.P and Karamzin. Y *JETP Lett.* **1974**, *20* (11), 339–341.

(98) William E.Torruellas, Zuo Wang, David J.Hagan, Eric W. Vanstrylan, and G. I. S. *Physcial Rev. Lett.* **1995**, *74* (25), 5036–5039.

(99) Siviloglou, G. A.; Makris, K. G.; Iwanow, R.; Schiek, R.; Christodoulides, D. N.; Stegeman, G. I.; Min, Y.; Sohler, W. *Opt. Express* **2006**, *14* (12), 5508–5516.

(100) Fuerst, R. A.; Baboiu, D.; Lawrence, B.; Torruellas, W. E.; Stegeman, G. I.; Trillo, S.; Wabnitz, S.; Bordoni, F. U.; Castiglione, V. B. *Physcial Rev. Lett.* **1997**, *78* (14), 2756–2759.

(101) Verbiest, T.; Persoons, A.; Dynamics, B. *Macromol.Symp.* **1996**, *102*, 347–354.

(102) Yesodha, S. K.; Sadashiva, C. K.; Tsutsumi, N. *Prog.polym.Sci* **2004**, *29*, 45–74.

(103) Prasad, P. N.; Williams, D. J. *INTRODUCTION TO NONLINEAR OPTICAL EFFECTS IN MOLECULES AND POLYMERS*; John Wiley & Sons, Inc.: New York, 1991.

(104) Williams, B. D. J. *Angew. Chemie - Int. Ed.* **1984**, *23*, 690–703.

(105) Burland, D. M.; Miller, R. D.; Walsh, C. A.; Field, E. E.; Dynamics, P. *Chem. Rev.* **1994**, *94*, 31–75.

(106) Wang, W.; Chen, D.; Fetterman, H. R.; Shi, Y.; Steier, W. H.; Dalton, L. R.; Chow, M. D.; Wang, W.; Chen, D.; Fetterman, H. R.; Steier, W. H.; Dalton, L. R. *Appl. Phys. Lett.* **1995**, *67* (13), 1806–1808.

(107) Shi, Y.; Steier, W. H.; Yu, L.; Chen, M.; Dalton, L. R.; Yu, L.; Chen, M.; Dalton, L. R. *Appl. Phys. Lett.* **1997**, *1131* (1991), 111–114.

(108) Priimagi, A.; Ogawa, K.; Virkki, M.; Mamiya, J.; Kauranen, M. *Adv. Mater.* **2012**, *24*, 6410–6415.

(109) Wu, W.; Qin, J.; Li, Z. *Polymer (Guildf).* **2013**, *54* (17), 4351–4382.

(110) Trollsas, M.; Orrenius, C.; Sahle, F.; Gedde, U. W.; Hult, A.; Hermann, D.; Rudquist, P.; Komitov, L.; Lagerwall, S. T.; Lindstro, J. *J. Am. Chem. Soc.* **1996**, *118*, 8542–8548.

(111) Nataj, N. H.; Mohajerani, E.; Nemati, H.; Moheghi, A.; Yazdanbakhsh, M. R.; Goli, M.; Mohammadi, A. *Jounral Appl. Polym. Sci.* **2013**, *127*, 456–462.

(112) Moerner, W. E.; Silence, S. M.; Hache, F.; Bjorklund, G. C. *J.Opt.Soc.Am. B* **1994**, *11* (2), 320–330.

(113) Marder, S. R.; Kippelen, B.; Jen, A. K.; Peyghambarian, N. *Nature* **1997**, *388*, 845–851.

(114) Assanto, G.; Karpierz, M. A. *Liq. Cryst.* **2009**, *36* (10-11), 1161–1172.

(115) Assanto, G.; Peccianti, M. *IEEE J. Quantum Electron.* **2003**, *39* (1), 13–21.

(116) Liu, J. Y.; Robinson, M. G.; Johnson, K. M.; Walba, D. M.; Ros, M. B.; Clark, N. A.; Shao, R.; Doroski, D.; Liu, J.; Johnson, K. M.; Walba, D. M. *Appl. Phys. Lett.* **1991**, *70*, 3426–3430.

(117) Samyn, C.; Verbiest, T. *Macromol.Rapid.Commun* **2000**, *21*, 1–15.

(118) Morim, D. R.; Vargas-Baca, I.; Saravanamuttu, K. *J. Phys. Chem. Lett.* **2016**, *7*, 1585–1589.

(119) Frisken, S. J.; Section, O. C. *Opt. Lett.* **1993**, *18* (13), 1035–1037.

(120) Decker, C. *Polym. Int.* **1998**, *45*, 133–141.

(121) Kewitsch, A. S.; Yariv, A.; Kewitsch, A. S.; Yariv, A. *Appl. Phys. Lett.* **1996**, *68* (4), 455–457.

(122) Kagami, M.; Yamashita, T.; Ito, H.; Kagami, M.; Yamashita, T.; Ito, H. *Appl. Phys. Lett.* **2001**, *79* (8), 1079–1081.

(123) Shoji, S.; Kawata, S.; Sukhorukov, A. A.; Kivshar, Y. S. *Opt. Lett.* **2002**, *27* (3), 185–187.

(124) Maruo, S.; Ikuta, K. *Appl. Phys. Lett.* **2000**, *76* (19), 2656–2658.

(125) Monro, T. M.; Miller, P. D. *Opt. Express* **1998**, *23* (4), 268–270.

(126) Tanya M. Monro, L. Poladian, and C. M. de S. *Phys. Rev. E* **1998**, *57*, 1104.

(127) Monro, T. M.; Sterke, C. M. De. *J.Opt.Soc.Am. B* **1999**, *16* (10), 1680–1685.

(128) Kasala, K.; Saravanamuttu, K. *Appl. Phys. Lett.* **2008**, *93*, 051111–1 051111–051113.

(129) Ambrosio, A.; Marrucci, L.; Borbone, F.; Roviello, A.; Maddalena, P. *Nat. Commun.* **2012**, *3*, 989.

(130) Kagami, M.; Yamashita, T.; Yonemura, M. *IEICE TRANS. ELECTRON* **2007**, *E90-C* (5), 1061–1070.

(131) Eldada, L.; Member, S.; Shacklette, L. W. *IEEE J. Sel. Top. quantum Electron.* **2000**, *6* (1), 54–68.

(132) Jacobsen, B. A. J.; Barvosa-carter, W.; Nutt, S. *Adv. Mater.* **2007**, *19*, 3892–3896.

(133) Jacobsen, A. J.; Barvosa-carter, W.; Nutt, S. *Acta Mater.* **2008**, *56*, 1209–1218.

(134) Jacobsen, A. J.; Barvosa-carter, W.; Nutt, S. *Acta Mater.* **2008**, *56*, 2540–2548.

(135) Jeong, K.; Jeong, K.; Kim, J.; Lee, L. P. *Science.* **2006**, *312*, 557–561.

(136) Qiu, L.; Saravanamuttu, K. *J.Opt.Soc.Am. B* **2012**, *29* (5), 1085–1093.

(137) Schaedler, T. A. *Science.* **2011**, *334*, 962–965.

(138) Zhang, J. Self-trapping of incoherent white light, 2005.

(139) Hull, C. W. United States Patent [19] US 4,575,330, 1986.

(140) Liska, R.; Schuster, M.; Infu, R.; Turecek, C.; Fritscher, C.; Seidl, B.; Schmidt, V.; Kuna, L.; Haase, A.; Varga, F.; Lichtenegger, H.; Stampfl, J. *J.Coat.Techno.Res* **2007**, *4* (4), 505–510.

(141) Modrek, B. US 4,996,010, 1991.

(142) Gothait, H.(Object Geometries Ltd), US 6,259,962 B1, **2001**.

(143) Cooke, M. N.; Fisher, J. P.; Dean, D.; Rimnac, C.; Mikos, A. G. *J Biomed Mater Res Part B Appl Biomater* **2002**, *64B*, 65–69.

(144) Gross, B. C.; Erkal, J. L.; Lockwood, S. Y.; Chen, C.; Spence, D. M. *Anal. Chem.* **2014**, *86*, 3240–3253.

(145) Chang, P. S.; Parker, T. H.; Patrick, C. W.; Miller, M. J. *Jounral Craniofacial Surg.* **2003**, *14* (2), 164–170.

(146) Tumbleston, J. R.; Shirvanyants, D.; Ermoshkin, N.; Johnson, A. R.; Kelly, D.; Chen, K.; Pinschmidt, R.; Rolland, J. P.; Ermoshkin, A.; Samulski, E. T.; Joseph, M. *Scienceexpress* **2015**, No. March, 1–7.

(147) Denk, W.; Strickler, J. H.; Webb, W. W.; Series, N.; Apr, N. *Science,* **1990**, *248* (4951), 73–76.

(148) Maruo, S.; Nakamura, O.; Kawata, S. *Opt. Lett.* **1997**, *22* (2), 132–134.

(149) Sun, H.; Kawata, S. *Two-Photon Photopolymerization and 3D Lithographic Microfabrication*; Springer_verlag, 2004.

(150) Satoshi Kawata, H.-B. S. *Nature* **2001**, *412*, 697–698.

(151) Kawata, S.; Sun, H. *Appl. Surf. Sci.* **2003**, *209*, 153–158.

(152) Deubel, M.; Freymann, G. V. O. N.; Wegener, M.; Pereira, S.; Busch, K.; Soukoulis, C. M. *Nature* **2004**, *3* (July), 2–5.

(153) Xia, B. H.; Wang, J.; Tian, Y.; Chen, Q.; Du, X.; Zhang, Y. *Adv. Mater.* **2010**, *22*, 3204–3207.

(154) Therriault, D.; White, S. R.; Lewis, J. A. *Nature* **2003**, *2*, 265–272.

(155) Doraiswamy, A.; Jin, C.; Narayan, R. J.; Mageswaran, P.; Mente, P.; Modi, R. *Acta Biomater.* **2006**, *2*, 267–275.

(156) Kelloma, M. *Ann. Med.* **2008**, *40*, 268–280.

(157) Bertsch, A.; Vogt, C. *Rapid Prototyp. J.* **2000**, *6* (4), 259–266.

(158) J.V.Crivello. *Ann.Rev.Mater.Sci* **1983**, *13*, 173–190.

(159) Crivello, J. V.; Sangermano, M. *Macromol. Mater. Eng.* **2014**, *299*, 775–793.

(160) Sangermano, M.; Applicata, S.; Torino, P.; Duca, C. *Pure Appl.Chem* **2012**, *84* (10), 2089–2101.

(161) Vitale, A.; Sangermano, M.; Bongiovanni, R.; Burtscher, P.; Moszner, N. *Materials (Basel).* **2014**, *7*, 554–562.

(162) Kaur, M.; Srivastava, A. K. *Jounral Macromol. Sci. Part C Polym. Rev.* **2002**, *C42* (4), 481–512.

(163) Crivello, J. V. *UV Curing Sci. Technol. ed* **1978**.

(164) Crivello, J. V. *Jounral Macromol. Sci. Part A Polym. Chem.* **1999**, *37*, 4241–4254.

(165) Dektar, J. L.; Hacker, N. P. *J.Org.Chem* **1990**, *55* (8), 639–647.

(166) Fouassier, G. M. and J. P. *J. Polym. Sci. Part A Polym. Chem.* **1991**, *29* (431), 1113–1124.

(167) Gomurashvili, Z.; Crivello, J. V. *J. Polym. Sci. Part A-Polymer Chem.* **2001**, *39* (1), 1187–1197.

(168) Crivello, J. V. *J. Polym. Sci. Part A Polym. Chem.* **2009**, *47*, 866–875.

(169) Crivello, J. V. *J. Macromol. Sci. Part A Pure Appl. Chem.* **2009**, *46*, 474–

483.

(170) Sangermano, M.; Spera, S.; Bongiovanni, R.; Priola, A.; Busetto, C. *Macromol.chem.Phys.* **2000**, *201*, 2441–2446.

(171) Sangermano, M.; Malucelli, G.; Morel, F.; Decker, C.; Priola, A. *Eur. Polym. J.* **1999**, *35*, 639–645.

(172) Campo, A. del; Greiner, C. *J. Micromechanics Microengineering* **2007**, *17* (6), R81–R95.

Chapter 2

Spontaneous Emergence of Nonlinear Light Waves and Self-Inscribed Waveguide Microstructure during the Cationic Polymerization of Epoxides

Dinesh K. Basker,

Reprinted with permission from (Basker, D. K.; Brook, M. A.; Saravanamuttu, K. Spontaneous Emergence of Nonlinear Light Waves and Self-Inscribed Waveguide Microstructure during the Cationic Polymerization of Epoxides. *J. Phys. Chem. C* **2015**, *119*, 20606−20617.) Copyright (2015) American Chemical Society

Abstract

We report spontaneous pattern formation due to modulation instability (MI) of a broad, uniform, incandescent beam as it propagates through a fluid medium undergoing cationic ring-opening polymerization of epoxide moieties and show that the dynamics of the process can be controlled through polymerization kinetics. By strong contrast, MI in the half century-old field of nonlinear light propagation has until now been described predominantly in terms of optical parameters such as coherence, intensity and wavelength. The increase in refractive index (Δn) originating from the crosslinking polymerization of biscycloaliphatic epoxy monomers pushes the system into a nonlinear regime, where normally negligible spatial noise becomes greatly amplified. The perturbed optical field stabilizes by spontaneously dividing into thousands of self-trapped filaments of light. Because each filament inscribes a permanent microscopic channel along its propagation path, the initially isotropic fluid medium solidifies into a densely packed array of self-induced waveguides. These experiments demonstrated the strong correlation between the kinetics of cationic polymerization and dynamics of MI; the beam becomes unstable only within a narrow parameter range where a critical balance is struck between the photoresponse speed (determined by polymerization rate) and the magnitude of Δn (determined by extent of crosslinking). The former needs to be sufficiently fast to respond to noise while the latter must be large enough to generate high-refractive index seeds that trigger MI. Outside of this range, MI is entirely

suppressed. This study reveals that nonlinear waveforms emerge in a familiar, widely employed epoxide photopolymer system, which for the first time highlights the possibility of tuning MI through the kinetics of a photochemical reaction.

2.1. Introduction

2.1.1. Modulation Instability: a Nonlinear Mechanism of Pattern Formation in Polymers

The coupling of nonlinear spatial and temporal pattern formation processes to polymeric systems has given rise to a rich diversity of research areas ranging from frontal polymerization, spontaneous pattern formation, dewetting, oscillatory gels to controlled phase separation. Research in these fields provides insight into the fascinating complexity of nonlinear dynamics and opens unprecedented routes to active, intelligent materials.[1] We introduced a fundamentally new nonlinear mechanism of polymer pattern formation that connects nascent free-radical photopolymerization with the modulation instability (MI) of optical fields.[2,3] For example, we showed that a broad, uniform beam of light launched into a methacrylate-derivatised siloxane sol spontaneously divides into a densely packed population (> 10,000 cm^{-2}) of identical filaments, which each inscribe and become self-trapped within a polymer microchannel – *an optical waveguide* – along its propagation path. Each filament is a nonlinear waveform, and similar to a self-trapped beam[4–6] is characterised by divergence-free, waveguided propagation through the medium. MI in photopolymers exhibits the off-equilibrium conditions, positive feedback mechanism and amplification of concentration gradients that are characteristic of self-organization and pattern formation processes.[2] However, a critical difference in our approach compared to these other processes is that MI is elicited by applying an externally applied optical field, which can be precisely tailored to control pattern formation in photopolymers. We have exploited this property to generate an entirely new family of functional 3-D polymer waveguide architectures (*vide infra*).

The origins and mechanisms underlying MI during free-radical photopolymerization have been detailed elsewhere.[2] Briefly, the MI of a uniform beam propagating through a photopolymerizable medium arises from adventitious noise that is inherent to the system. Noise leads to weak spatial inhomogeneities in optical intensity and corresponding variations in polymerization rate. Regions undergoing even slightly greater rates of polymerization develop increased changes in refractive index (Δn) relative to their surroundings. According to waveguide theory, light becomes preferentially entrapped within regions of (even slightly) enhanced Δn[7] These higher index regions therefore essentially serve as seeds, which trigger the continual and reciprocal amplification of both polymerization rate and intensity. The optical field grows increasingly unstable as it develops large intensity modulations in this way, and spontaneously divides into filaments – microscopic threads of light – that propagate without diverging through self-induced waveguides in the medium. Temporal variations in the spatial intensity profiles of waveguides provide detailed, *in situ* insight into the spatial and temporal dynamics of this nonlinear process of pattern formation.[2]

While filaments seeded by noise are randomly positioned in space, we have shown that by deliberately patterning beams with periodic amplitude modulations (controlled spatial noise), it is possible to corral filaments (and their self-induced waveguides) into optical (and microstructural) lattices with square,[2] near-cubic,[8] simple cubic,[9] BCC,[10] woodpile[10] and hexagonal[11] geometries. This process of *optochemical organization* has proven to be a powerful single-step, room temperature route to complex 3-D waveguide architectures. Such microstructures would be impossible to generate through conventional techniques. Because each element of an optochemically organized lattice is a multimode, multi-wavelength waveguide, these microstructures possess highly efficient light collecting, imaging and beam-shaping properties.

2.1.2. Modulation Instability of Incoherent White Light

An important feature of MI in free-radical polymerizable systems is that pattern formation can be elicited with *incandescent* white light. Due to extremely weak correlations of phase and amplitude, a beam of incandescent light can be described as a chaotic[12] distribution of intensity speckles, which fluctuate randomly in space on the femtosecond timescale.[13] Considered impossible for over three decades in the field, the nonlinear propagation of this spatially and temporally incoherent wavepacket as a self-trapped beam[13] and as MI-induced filaments was first demonstrated in a photorefractive crystal.[14] Very low intensity light was employed in these experiments to deliberately delay the photoresponse of the crystal; such a *non-instantaneous*[13] response (>> femtosecond timescale) is sensitive only to the time-averaged intensity profile of the beam and not to its individual intensity speckles which, due to their rapid femtosecond fluctuations, would otherwise disrupt the formation of nonlinear incoherent waves. We showed that the *inherently* non-instantaneous kinetics of free-radical polymerization, which typically spans milliseconds to seconds, facilitates nonlinear propagation of incoherent waves over a wide range of intensities.[2,4] Moreover, Δn originating from free-radical polymerization saturates over time (as polymerizable units are depleted) and is sufficiently large to self-consistently support all the modes and wavelengths of incandescent light.[4,13,14] The free-radical polymerizable system has therefore emerged as a versatile medium to elicit MI, study the dynamics[15] and interactions[16] of nonlinear incoherent waves and the optochemical organization of a variety of 3-D waveguide architectures.[8–11]

Nonlinear light waves are at once universal and diverse,[17] emerging in a wide variety of photoresponsive materials such as Kerr media and photorefractive crystals yet sharing the same basic prerequisite of an intensity-dependent Δn. Our studies of MI in free-radical photopolymerizable systems exploited this dichotomy: photoinitiated free-radical polymerization satisfies the *general* prerequisite of an intensity-dependent Δn required for MI; here, densification associated with the formation of covalent bonds during chain formation typically leads to a spatially localized increase in refractive index. At the same time, the non-instantaneous, saturable and relatively large values of Δn unique to polymerization systems satisfies the *specific* requirements for MI of incandescent waves;[2] in fact, the spatial and temporal evolution of Δn that is characteristic of free-radical polymerization has also revealed a suite of new nonlinear forms of coherent laser light.[18–21]

2.1.3. Modulation Instability in Epoxide Systems

Based on the striking diversity of nonlinear optical waves in free-radical polymerization systems alone, we anticipate that photopolymerization systems in general will provide rich opportunities to elicit and study the dynamics of nonlinear waveforms and spontaneous pattern forming processes, and open routes for the optochemical organization of functional microstructures. This forms the motivation of the study presented here, which examines MI and spontaneous pattern formation in a system that is entirely different to free-radical polymerization: the visible-light initiated cationic crosslinking polymerization of aliphatic epoxide monomers.[22,23] *Significantly, this system allows systematic control of the kinetics of polymerization and as a result, provides for the first time a facile mechanism to correlate molecular-level kinetics with the nonlinear dynamics of the optical field.* This contrasts with existing theoretical frameworks of MI, which describe the nonlinear process exclusively in terms of optical parameters such as intensity, wavelength and coherence.[24] Since epoxide photopolymerization is extensively employed in the fabrication of microeletromechanical systems (MEMS),[25] an understanding of MI and pattern formation during photopolymerization is therefore critical to these technologies.

2.2. Experimental

2.2.1. Materials

3, 4-Epoxycyclohexylmethyl-3',4'-epoxycyclohexane carboxylate (**1**), benzyl alcohol (**2**) and camphorquinone (97 % purity) (**3**) were purchased from Sigma Aldrich (Oakville, ON, Canada) and used without further purification. Following the method described by Crivello *et al.*,[Error! Bookmark not defined.] camphorquinone (2,3-bornanedione; λ_{max} = 468 nm) and bis(4-t-butyl)iodonium hexafluroantimonate (Hampford Research Inc., Stratford, CT, United States) (**4**) were employed as the photosensitizer (PS) and initiator (I), respectively.

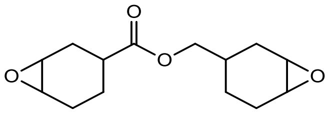

1

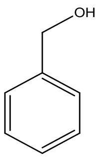

2

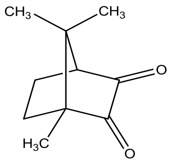

3

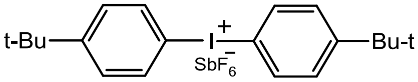

4

2.2.2. Preparation of Photosensitive Epoxide Sols

Photopolymerizable solutions for experiments of modulation instability (MI) were prepared by combining benzyl alcohol, I and PS with the biscycloaliphatic epoxy monomer and stirring for 48 hrs. Compositions listed in

Table 2.1 are labeled according to the amount (weight percent) of benzyl alcohol present; all compositions contained 2.5 wt.% and 1.5 wt.% of PI and PS, respectively. Prior to use, the homogenized sols were filtered through a polytetrafluoroethylene (PTFE) membrane (0.2 µm pore size, Pall Corporation USA) and placed in a homemade, cylindrical PTFE cell with optically transparent, glass windows and a physical pathlength of 4.0 mm.

Table 2.1 Composition of photosensitive epoxide sols, which are labeled according to their benzyl alcohol concentrations; all compositions contained 2.5 wt.% and 1.5 wt.% of PI and PS, respectively

Sol	**Epoxide monomer (wt.%)**	**Benzyl alcohol (wt.%)**
EB10	86	10
EB15	81	15
EB20	76	20
EB25	71	25
EB30	66	30
EB35	61	35
EB40	56	40
EB45	51	45
EB50	46	50

2.2.3. Optical Assembly

Figure 2.1 shows the optical set-up employed for experiments of MI**Error! Bookmark not defined.**[2] In a typical experiment, white light emitted by a quartz tungsten halogen (QTH) lamp (Cole-Parmer 9741-50, Illinois, USA) was collimated by a planoconvex lens (F.L = 250 mm, d = 25.4 mm) and launched onto the entrance face of the sample cell (diameter = 15 mm, pathlength = 4 mm; transparency = 320 nm - 800 nm) containing the photosensitive sol. At the entrance face, the optical power was ~1 mW (at 468 nm). The spatial intensity profile of the beam at the exit face of the cell was focused through a pair of plano-convex lenses (F.L. = 250 mm, d = 25.4 mm) onto a high-resolution, progressive scan, charged-coupled device (CCD) (1360 (H) x 1024 (V) of 4.65 μm square pixels; sensitivity range = 350 nm to 1150 nm; WinCamD^{TM} digital camera, Data Ray Inc., USA). All optical components were mounted onto a rail and could be translated along the optic axis with a resolution of ± 0.25 mm. The entire assembly was mounted on a vibration-isolated optical table (flatness of ±0.13 mm). All optical components were purchased from Newport Corporation, CA, USA.

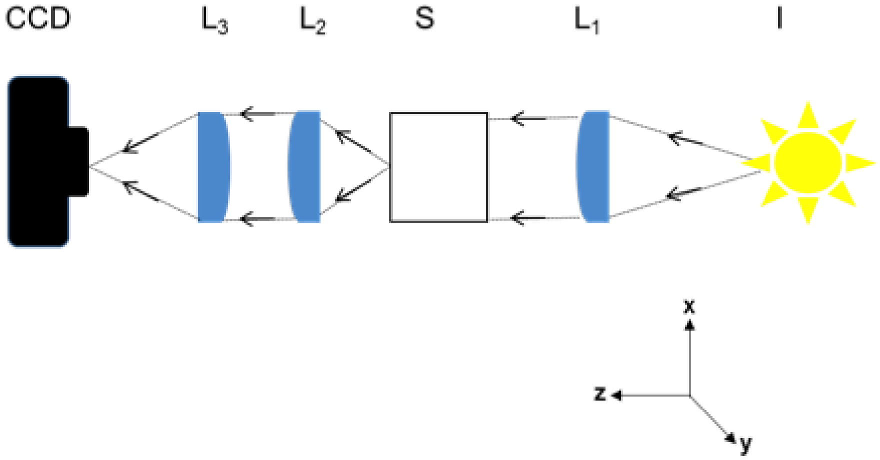

Figure 2.1. Optical asembly for experiments of modulation instability. Incandescent light from a QTH lamp (L) was collimated by a plano-convex lens (L_1) and launched into the cell containing the photopolymerizable epoxide sol (S). The spatial intensity profile of the beam at the sample exit face was imaged by a pair of planoconvex lenses (L_2 and L_3) onto a CCD camera.

2.2.4. Characterization of Photopolymerized Epoxy Samples

Differential scanning calorimetry (DSC) of photopolymerized samples was carried out with a TA instruments DSC 2910; samples were placed in standard Al pans under N_2 purge and heated between -50 °C to 70 °C at 10 °C min^{-1}; T_g was calculated from the inflection point of the DSC curve. The solubility of polymerized epoxy samples was determined by calculating their gel content after extraction in chloroform, acetone or benzyl alcohol, respectively, using:

$$W_f = (W_1/W_0) \text{ x } 100 \% \qquad [1]$$

where W_f is the % gel content after extraction, W_0, the initial weight of the sample (in grams) and W_1, its weight upon extraction in the solvent for 1 hour and drying in air. Samples were weighed on an analytical balance with an accuracy of 0.1 mg and tolerance of ± 10 mg.

IR spectra were recorded on a Bruker Vertex 70 FTIR (resolution = 4 cm^{-1} room temperature DTG detector) using the platinum ATR (equipped with a diamond crystal). To acquire spectra, homogenized epoxide sols were spread thinly on the ATR sample holder and then uniformly photopolymerized with white light delivered by an optical fiber illuminator (λ = 400 nm to 700 nm; power = 25 mW). The conversion of epoxides during polymerization was followed by monitoring temporal changes of the integrated area under the absorbance peak at 789 cm^{-1}, which is attributed to the ring stretching vibration.[26]

2.2.5. Characterization of Optical Waveguide Microstructures

Optical micrographs of photopolymerized samples containing waveguides were acquired with an Olympus BX51 microscope equipped with a Q-Imaging Retiga EXi digital camera and driven by ImagePro® software. Raman spectroscopic mapping of waveguide structures was carried out at an excitation wavelength of 785 nm with a Reinshaw Invia Laser Raman spectrometer fitted with motorized stages that enabled a mapping spatial resolution of 0.1 μm. Maps were acquired at (a) 799 cm^{-1} (corresponding to the ring stretching vibration of epoxide groups) and (b) 1003 cm^{-1} band (corresponding to the in-plane C-H deformation vibration of the benzyl alcohol solvent).

2.3. Results and Discussion

2.3.1. Photopolymerizable Epoxide System

The epoxide system for MI experiments employed the dye-sensitized initiator system developed by Crivello *et al*. for visible-light initiated, cationic polymerization of a wide range of epoxide substrates.[22] The initiation mechanism elucidated in detail by Crivello *et al.* is briefly summarized in Scheme 2.1: irradiation of the dye camphorquinone (λ_{max} = 468 nm) with incandescent white light in the presence of the non-basic hydrogen donor, benzyl alcohol, generates α-hydroxybenzyl and camphorquinone-derived radicals (Eqn. [1]). The latter can undergo dimerization, hydrogen abstraction reactions or oxidation by the diaryliodonium salt, bis(4-butylphenyl) iodonium hexafluoroantimonate. The α-hydroxybenzyl radical is oxidized by the diaryliodonium salt to a α-hydroxybenzyl cation and diaryliodine radical (Eqn. [2]); the cation undergoes spontaneous deprotonation to form benzylaldehyde and the Brønsted acid, $HSbF_6$ (Eqn. [3]). The acid is the primary initiator of the ring-opening cationic polymerization of biscycloaliphatic epoxy monomers employed in MI experiments. The diaryliodine radical generated in Eqn. [2] forms aryl iodine and an aryl radical (Eqn. [4]), which can in turn abstract hydrogen from benzyl alcohol to generate the α-hydroxybenzyl radical that participates in the decomposition of the diaryliodonium salt (Eqn. [2]). This mechanism couples the blue-light sensitivity of camphorquinone with a chain reaction where α-hydroxybenzyl radicals, generated photochemically and non-photochemically, induce decomposition of the diaryliodonium salt to the Brønsted acid. Significantly, the rate of polymerization as well as the overall conversion of epoxide moieties increases with the concentration of benzyl alcohol[23] as it yields α-hydroxybenzyl radicals, which in turn determine the concentration of the Brønsted acid. We exploit this dependence in MI experiments to systematically vary polymerization kinetics through the concentration of benzyl alcohol (*vide infra*).

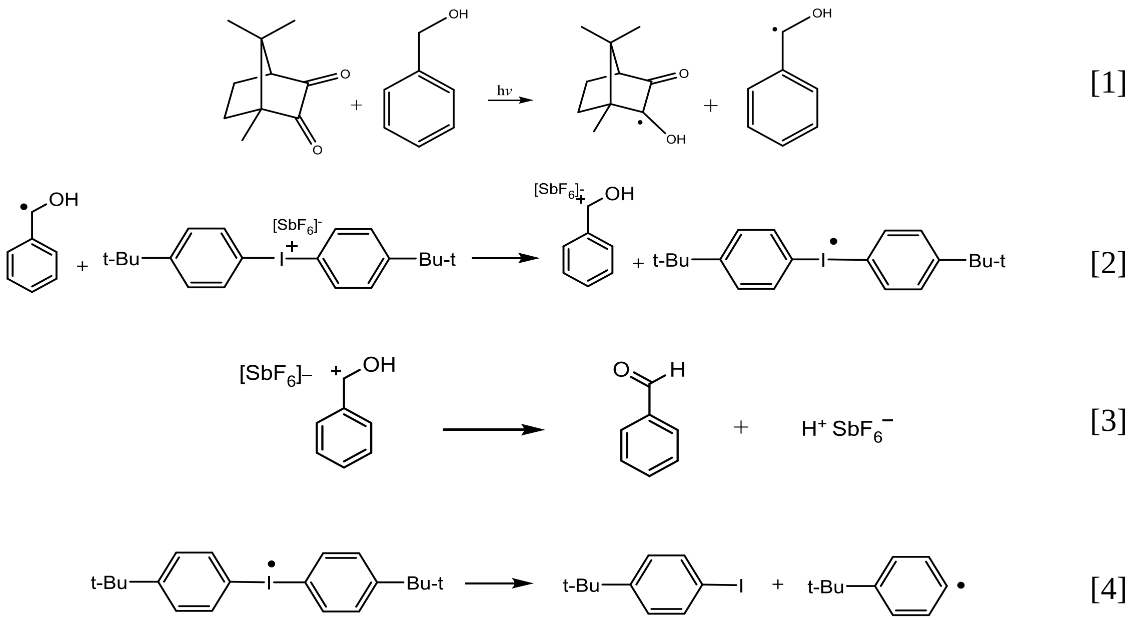

Scheme 2.1. Initiation mechanism of visible-light induced cationic polymerization of epoxides.[22]

2.3.2. Modulation Instability and Spontaneous Pattern Formation through Photoinitiated Cationic Polymerization

In a typical experiment of MI, a collimated beam of incandescent light was launched into a cell containing the photopolymerizable epoxide sol with a benzyl alcohol content of 25 wt.%; the beam was broad enough to uniformly illuminate the entire entrance face of the sample diameter = 15 mm). The spatial intensity profile of the beam was then monitored at the exit face of the sample (z = 4.0 mm); intensity profiles collected in Figure 2.2 show that the initially uniform beam developed weak modulations in intensity (2.2b-c), which increased in amplitude over time (2.2d-e) and ultimately divided into a stable population of filaments (2.2f). Although at long times, the filaments decreased slightly in

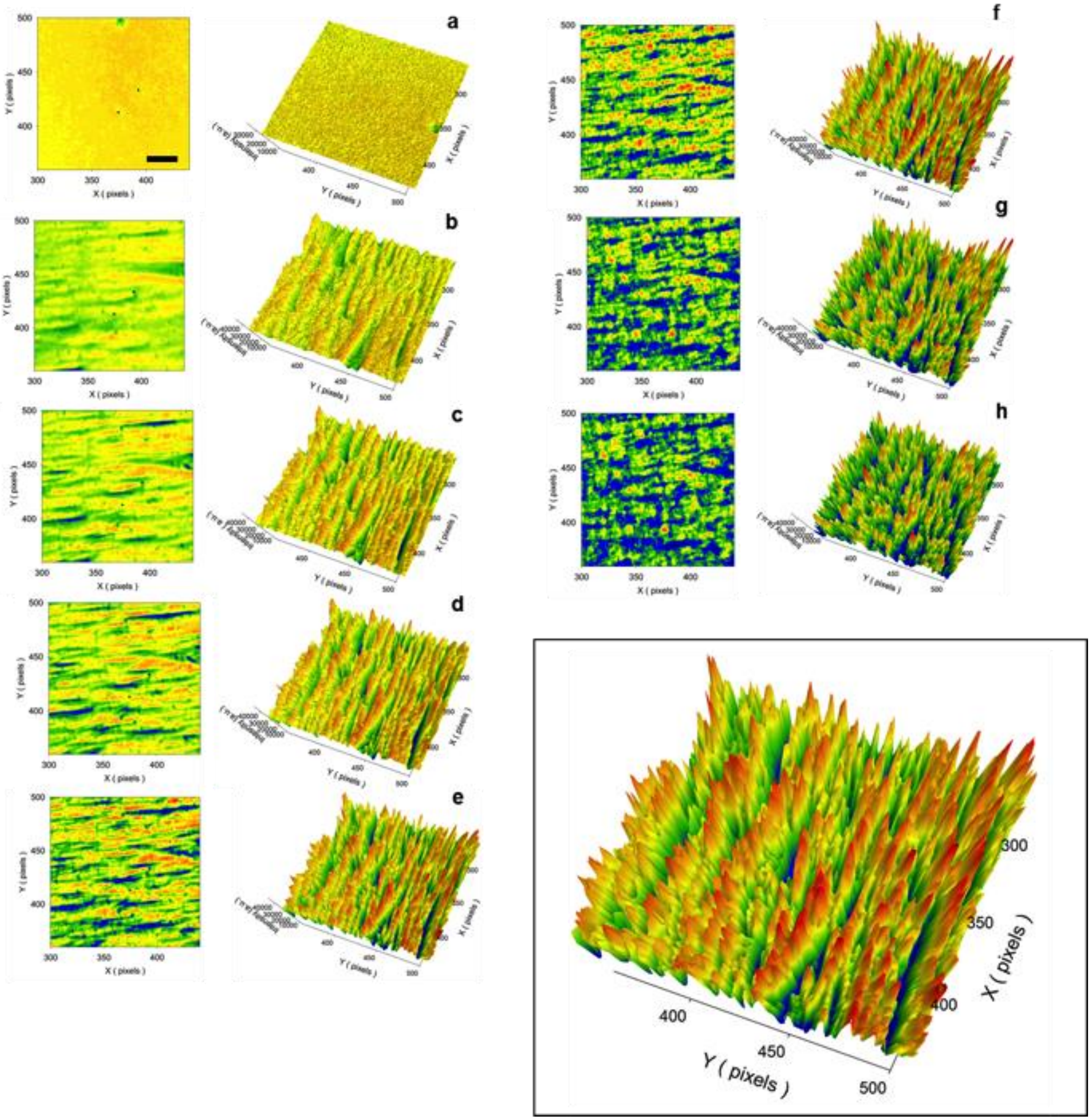

Figure 2.2. Temporal evolution of the spatial intensity profile of a white light beam at the exit face (*z* = 4 mm) of a photopolymerizable epoxide sample at t = (a) 0 s, (b) 90 min (c) 102 min (d) 114 min (e) 128 min (f) 142 min (g) 180 min and (h) 220 min. 2-D and 3-D profiles are shown. Scale bar in (a) = 250 μm and applies to all images. The inset is a magnified version of (f).

intensity (2.2g), no further changes were detected in their dimension or position for as long as they were monitored (up to 360 min).

Figure 2.2 reveals that refractive index changes (Δn, *(0.001)*)[27] associated with crosslinking polymerization of epoxide monomers elicits MI of the optical field. This process is schematically depicted in Figure 2.3 and can be understood as follows: the system comprising the uniform incandescent beam and epoxide sol is necessarily embedded with *noise* –inhomogeneities in the optical field and fluid medium that fluctuate randomly in time and space. Noise leads to corresponding minor temporal and spatial variations in intensity, which under linear conditions - in the absence of polymerization - are negligible. This is because they blur rapidly and become “washed out” due to the natural divergence and broadening of the optical field; this effect is particularly enhanced in the case of incandescent light, which due to its spatial and temporal incoherence, suffers significantly greater divergence compared to coherent laser sources.[28] Therefore at t = 0 s, the beam appears effectively uniform at the exit face of the sample (Figure 2.2a).

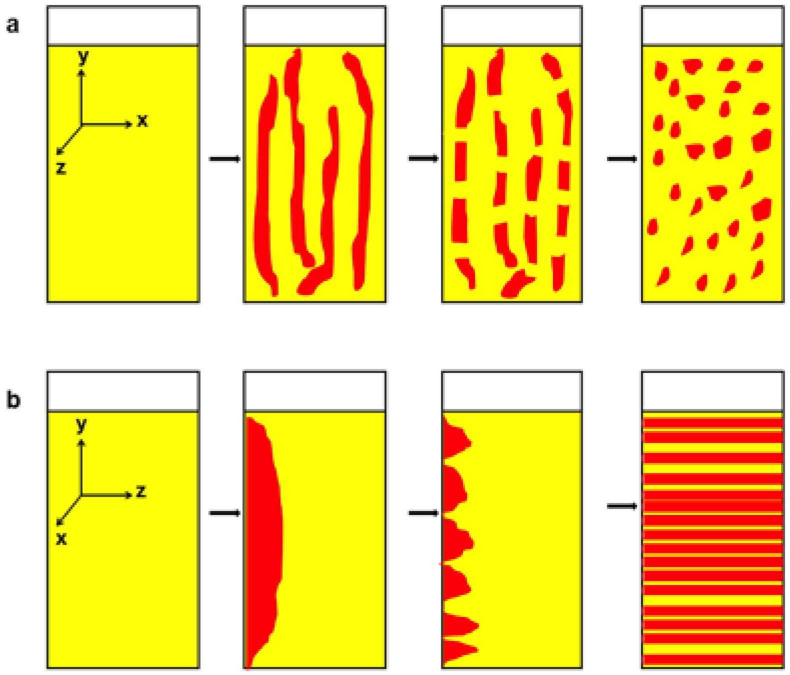

Figure 2.3. Scheme showing temporal evolution of modulation instability in a photopolymerizable system from (a) transverse and (b) longitudinal directions with respect to the beam propagation axis (*z*). Red = polymerized regions; Yellow = monomer fluid

Noise has a striking impact on the nascent photopolymerizing medium. Because the rate of cationic photopolymerization is intensity-dependent, weak spatial variations in intensity due to noise induce slightly different rates of polymerization. Regions with greater degrees of crosslinking (and densification as free monomers become covalently linked) generate a larger Δn. In this way, initially small inhomogeneities in polymerization rates lead to variations in Δn across the entrance face of the sample – we henceforth refer to these spatially localized regions of enhanced refractive index as *MI seeds*. Seeds that attain a critical value in refractive index change $(\Delta n_1)^2$ push the system into a nonlinear regime: here, optical intensity preferentially accumulates within the higher-index seeds[7] and in turn induces even greater contrasts in polymerization rates (and Δn) relative to the surroundings. In this way, MI seeds grow rapidly and anisotropically, along the propagation path of the beam (Figure 2.3b). As light preferentially gravitates towards and becomes entrapped within the high-index MI seeds, the initially uniform beam begins to divide spontaneously and develops the intensity modulations observed in Figure 2.2b-e. As light concentrates within MI seeds, these local regions undergo greater rates of polymerization and grow preferentially along the propagation path of the beam. A positive feedback loop is established in which modulations in intensity and refractive index continually amplify within the medium until a second critical threshold of Δn_2 is reached;[2] at this point, the optical field stabilizes by collapsing into a population of stable self-trapped filaments of incandescent white light. Each filament is entrapped within a narrow channel – waveguide – with a greater refractive index relative to its surroundings. At the sample exit face, MI is observed as the spontaneous transformation of the uniform beam into a large population of tightly confined spots of white light (Figure 2.2f-g).

Because index changes due to polymerization are irreversible, waveguides induced by self-trapped filaments are permanently inscribed in the medium; the epoxide sol transforms from an isotropic, homogeneous fluid into a tightly packed population of waveguide channels. Optical micrographs of the transverse (Figure

2.4a) and longitudinal (Figure 2.4b) cross-sections of a polymerized sample show that the waveguides propagate along the entire length of through the medium. A control experiment showed that waveguides were not generated when the sample was rotated (at an approximate speed of 30 rpm) so that it was uniformly irradiated from all directions (Figure 2.4c). This indicates that the interplay between the medium and the optical field, which amplifies noise and seeds MI, builds up cumulatively over time along the propagation direction of the beam. Rapidly changing the beam propagation direction disrupts this process and inhibits MI.

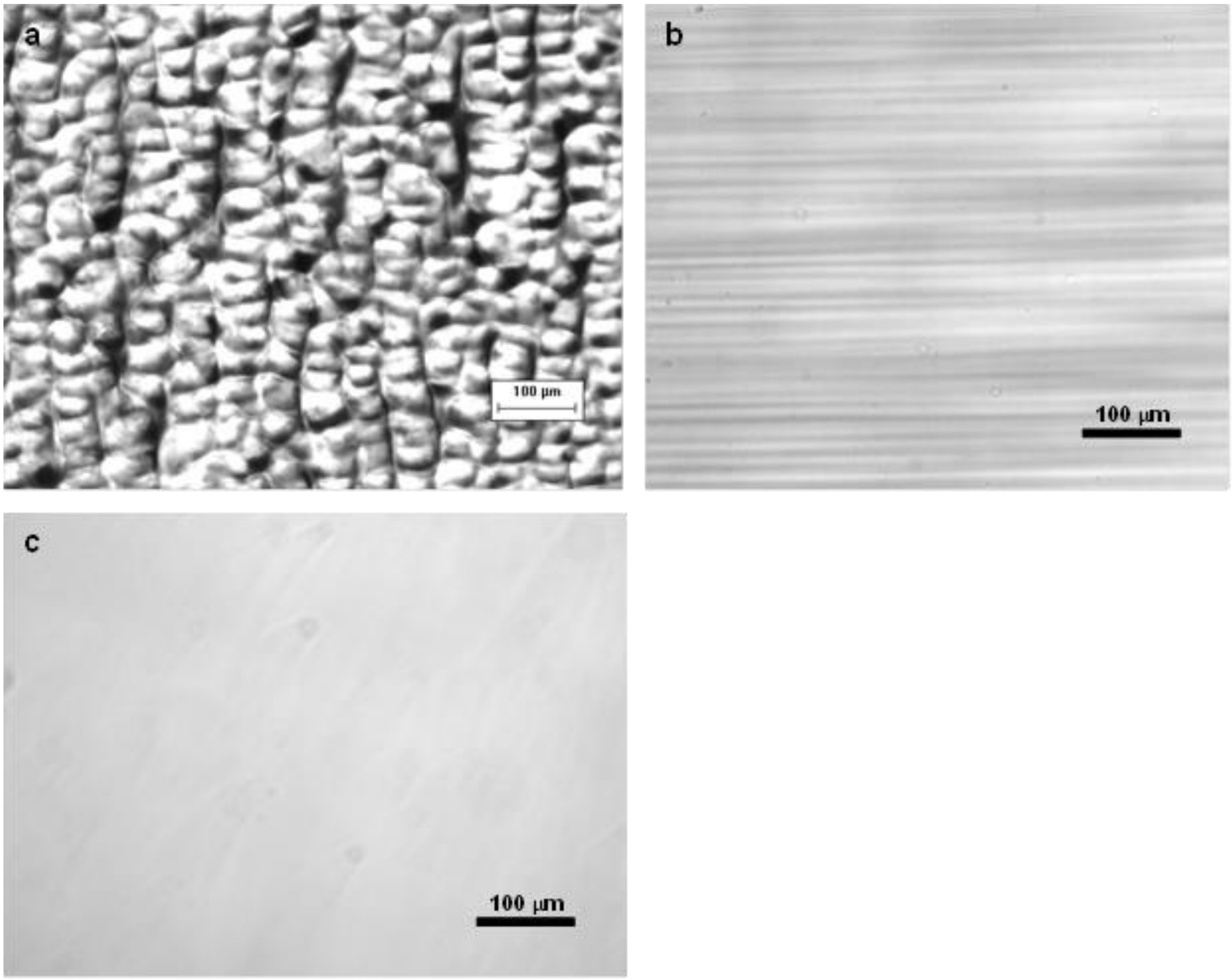

Figure 2.4. Transmission optical micrographs acquired in the (a) transverse and (b) longitudinal directions of waveguides induced through modulation instability in epoxide system EB25. (c) Micrograph of an identical sample that was uniformly irradiated from all directions.

2.3.3. Effects of Benzyl Alcohol on Polymerization Kinetics

Results in Figure 2.2 show that Δn originating from cationic polymerization satisfies the strict prerequisites for the nonlinear propagation of a spatially and temporally incoherent white light beam (*vide supra*).[14] We found that by varying the kinetics of the cationic polymerization process and the conversion of epoxide moieties, it is possible not only to tune the dynamics of MI but also to entirely suppress it.

We prepared epoxide systems with monotonically increasing amounts of benzyl alcohol from 10 wt.% to 50 wt.% to systematically examine the effects of polymerization kinetics on the dynamics of MI. Crivello and Ortiz showed that benzyl alcohols cause significant acceleration of polymerization kinetics and increased conversion of epoxide moieties.[23] The increase in concentration of initiating species with amount of benzyl alcohol (Scheme 2.1) can contribute to an acceleration of polymerization. Additionally, in the presence of benzyl alcohol, polymerization can proceed through an activated monomer (AM) mechanism,[23] which as shown below can lead to an increase in polymerization rate.

The typical ring opening mechanism of epoxide polymerization (active chain end (ACE)) is shown in Scheme 2.2.[22]

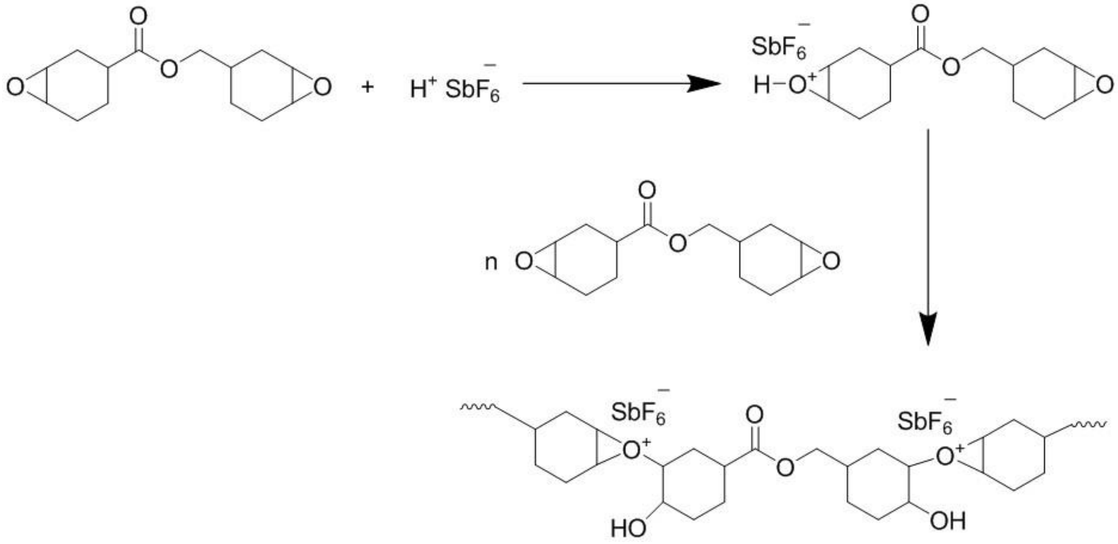

[5]

[6]

Scheme 2.2. Active chain end mechanism of epoxide polymerization[22]

Scheme 2.3 shows that polymerization can proceed through an activated monomer mechanism in the presence of benzyl alcohol.[23] Here, the hydroxyl group of the benzyl alcohol attacks the growing oxonium chain, (Eq. 8) resulting in rapid proton transfer from the propagating chain- end to the monomer (Eq. 9). In this way, the chain-transfer nature of the activated monomer mechanism leads to an increase in polymerization rate. The formation of benzyl ether groups at the polymer chain end also contribute to increased polymerization rates. Benzyl ether groups can act as sites for free radical hydrogen abstraction by photogenerated aryl radicals (Eq. 11; also refer to the appropriate equation in Scheme 1) and then be oxidized by diaryl iodonium to the corresponding benzylic cation (Eq. 12). The latter provide additional initiating species (Eq. 13).

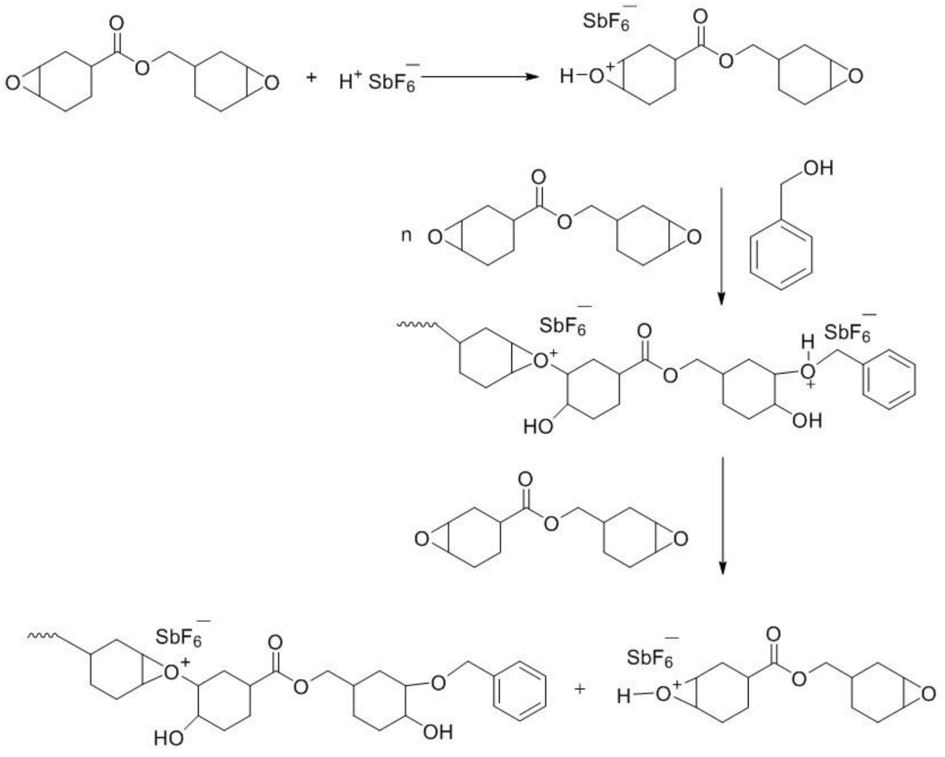

[7]

[8]

[9]

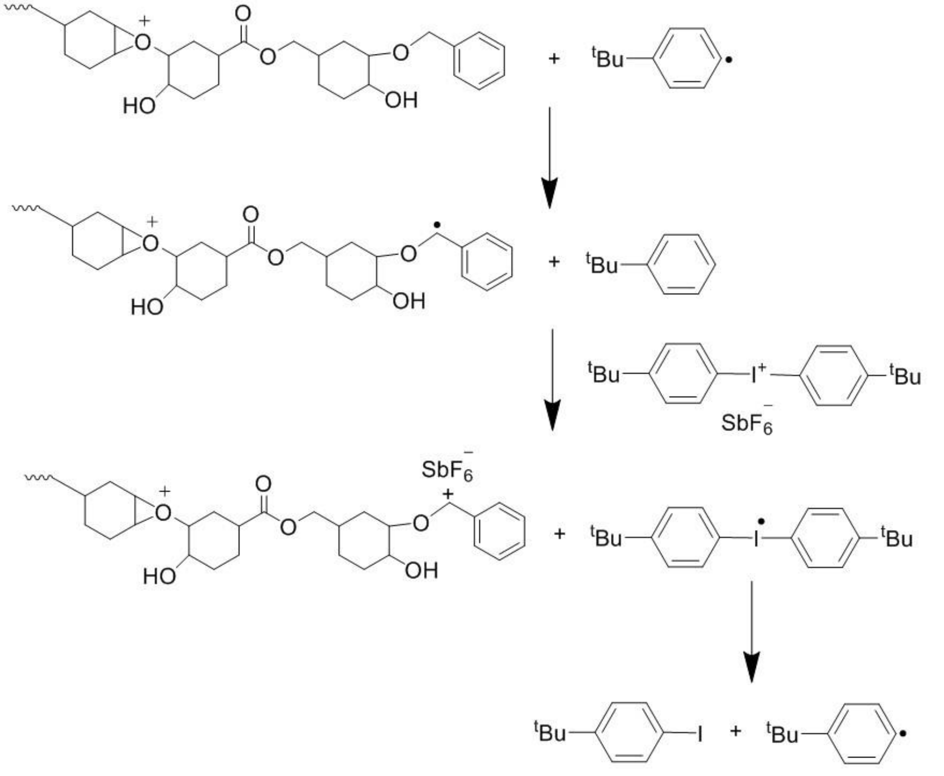

[10]

[11]

[12]

[13]

Scheme 2.3. Activated monomer mechanism of polymerization of epoxide monomers in the presence of benzyl alcohol.[23]

Cumulatively, the above-mentioned processes lead to an overall increase in polymerization rate with the amount of benzyl alcohol. Based on this, we reason that the two critical parameters governing MI, (i) magnitude of Δn, and the (ii) photoresponse speed of the medium, could be controlled through the amount of benzyl alcohol. The magnitude of Δn is determined by the extent of densification caused by the conversion of epoxide moieties through crosslinking polymerization. The photoresponse speed – how quickly the system responds to the optical field and undergoes a change in refractive index – is determined by the rate of polymerization. Therefore, the acceleration of polymerization in the presence of increasing amounts of benzyl alcohol should both increase densification as well as the photoresponse speed.

Differences in the extent of conversion of epoxide moieties and crosslinking were immediately evident in the physical consistencies of epoxy polymers. Samples containing different amounts of benzyl alcohol but photopolymerized under otherwise identical conditions ranged from viscous fluids (10 wt.%, 15 wt.% benzyl alcohol), non-flowing gels (20 wt.%), hard solid (25 wt.% – 35 wt.%), viscous fluid (40 wt.%) to fluids (45 wt.%, 50 wt.%) (Figure 2.5). All samples were uniformly irradiated at ~1 mW for 150 minutes.

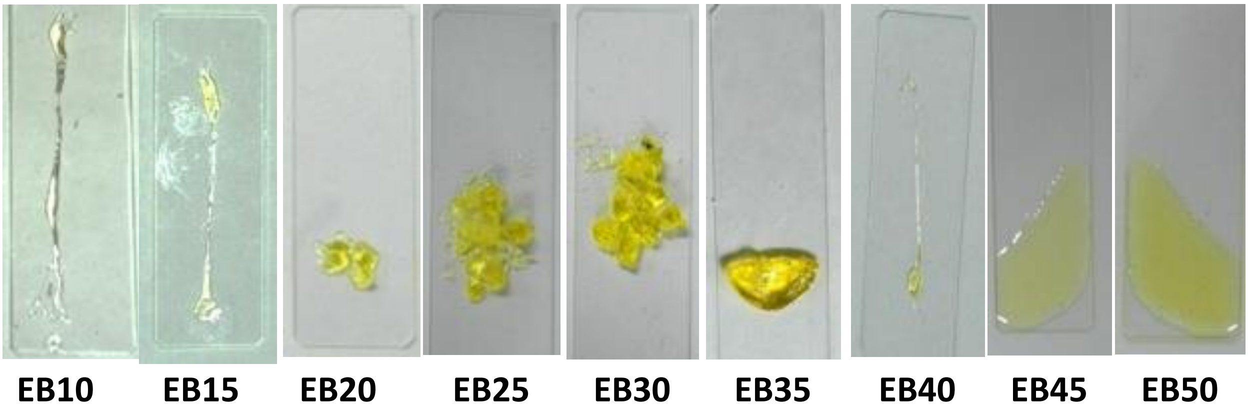

Figure 2.5. Photographs of epoxy samples placed on microscope slides. Samples were prepared with varying amounts of benzyl alcohol (10 wt.% to 50 wt.%) and photopolymerized under identical conditions (~1 mW mW, 150 min.).

Measurements of the glass transition temperature (T_g) of the bulk samples allowed a more explicit differentiation of the samples (Table 2.2). Solid samples generated from systems with 25 wt.% - 30 wt.% of benzyl alcohol possessed the highest T_gs. For example, the T_g increased by ≈ 36º C when the original benzyl alcohol content of the samples increased from 10 wt.% to 25 wt.%, but declined significantly once the benzyl alcohol amount was increased to 40 wt.%. This trend suggests that maximum conversion of epoxide units and therefore, extent of cross-linking are achieved in samples containing between 25 wt.% to 40 wt.% of benzyl alcohol.

Table 2.2. Glass transition temperatures of epoxy samples polymerized in the presence of increasing concentrations of benzyl alcohol

Material Code	**GlassTransition temperature (Tg) [°C]**
EB10	14.6
EB15	16.6
EB25	50.7
EB30	30.1
EB40	-6.7
EB50	-31.8

Increased epoxide conversion within a narrow composition range is further supported by FT-IR spectral measurements, which monitored the conversion of epoxide moieties in a selected range of samples initially containing 10 wt.%, 35 wt.% and 50 wt.% of benzyl alcohol, respectively; photopolymerized under identical conditions, the sample with 35 wt.% benzyl alcohol showed at least a two-fold increase in percentage conversion (68 %) of epoxide moieties after 1500 s of irradiation relative to samples with 10 wt.% and 50 wt.% of alcohol, which showed conversions of 35 % and 20 %, respectively. (Figure 2.6).

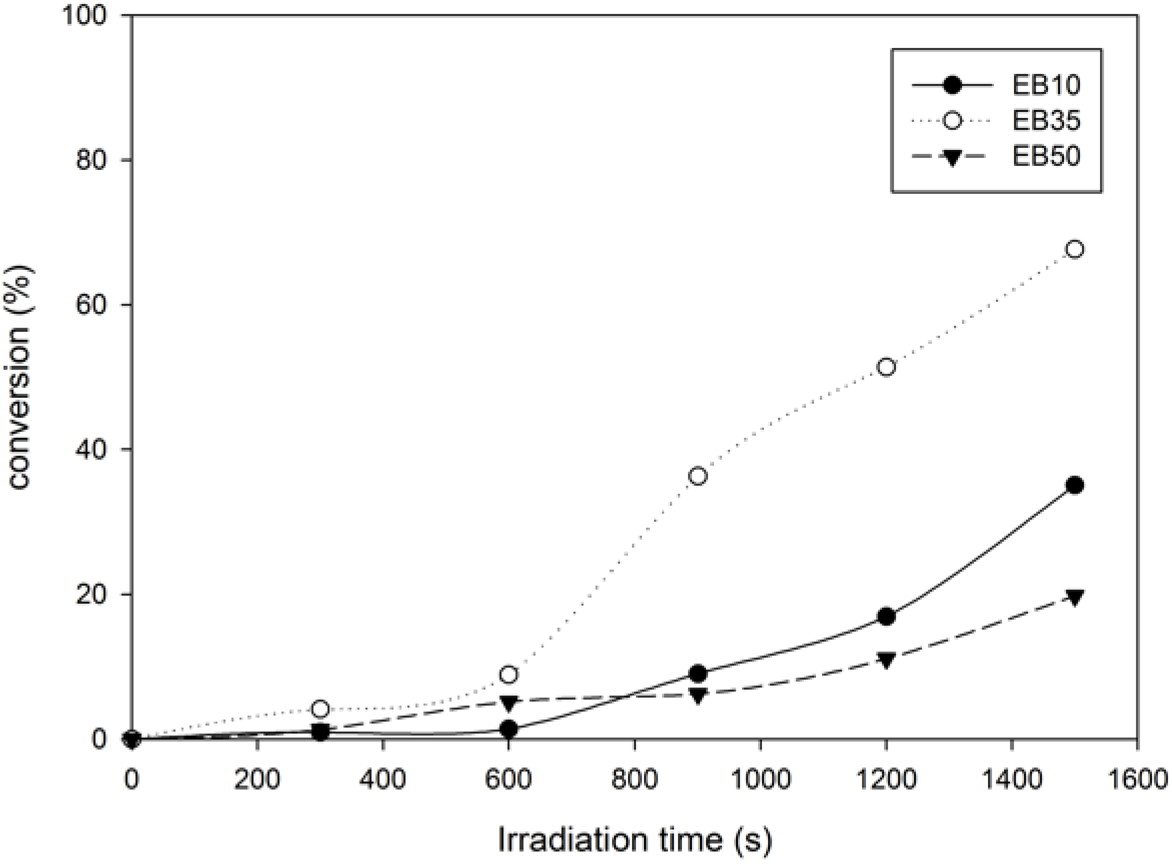

Figure 2.6. Temporal plot of the % conversion of epoxide moieties in systems containing 10 wt.% (EB10), 35 wt.% (EB35) and 50 wt.% (EB50) of benzyl alcohol. Conversion (%) was calculated by monitoring the IR absorbance band at 789 cm^{-1} attributed to epoxide ring stretching vibration.

2.3.4. Effects of Polymerization Kinetics on MI: the Fine Balance between Polymerization Rate (Speed of Photoresponse) and Extent of Crosslinking (Magnitude of Δn)

We carried out MI experiments in systems with varying amounts of benzyl alcohol, keeping all optical parameters that affect MI (intensity, coherence and wavelength range)[24] constant. Spatial intensity profiles of the incandescent beam were acquired at *z* = 4.0 mm at t = 150 minutes (Figure 2.7). There are striking differences in the behaviour of the systems, with MI observed only in a narrow range of samples containing between 25 wt.% to 40 wt.% of benzyl alcohol (Figures 2.2, 2.7e-h). In systems with the smallest (10 wt.%, 15 wt.%) amounts of benzyl alcohol, the white light beam retained its uniform profile and did not become unstable after irradiation for 150 minutes (Figure 2.7b-c). In these cases, the beam remained uniform while propagating through the medium even after prolonged (~8 hour) exposure times. Although there was evidence of instability and the emergence of localized high-intensity regions in the system containing 20 wt.% of benzyl alcohol, the beam did not undergo complete filamentation (Figure 2.7d). However, no changes were observed in beams propagating in samples containing 45 wt.% and 50 wt. % of benzyl alcohol (Figure 2.7i-j). Optical micrographs of the transverse cross-sections of samples that underwent MI are collected in Figure 2.8. Micrographs reveal the tightly packed array of waveguides induced by the self-trapped filaments; because MI originates from random noise, the waveguides are randomly positioned in space.[2]

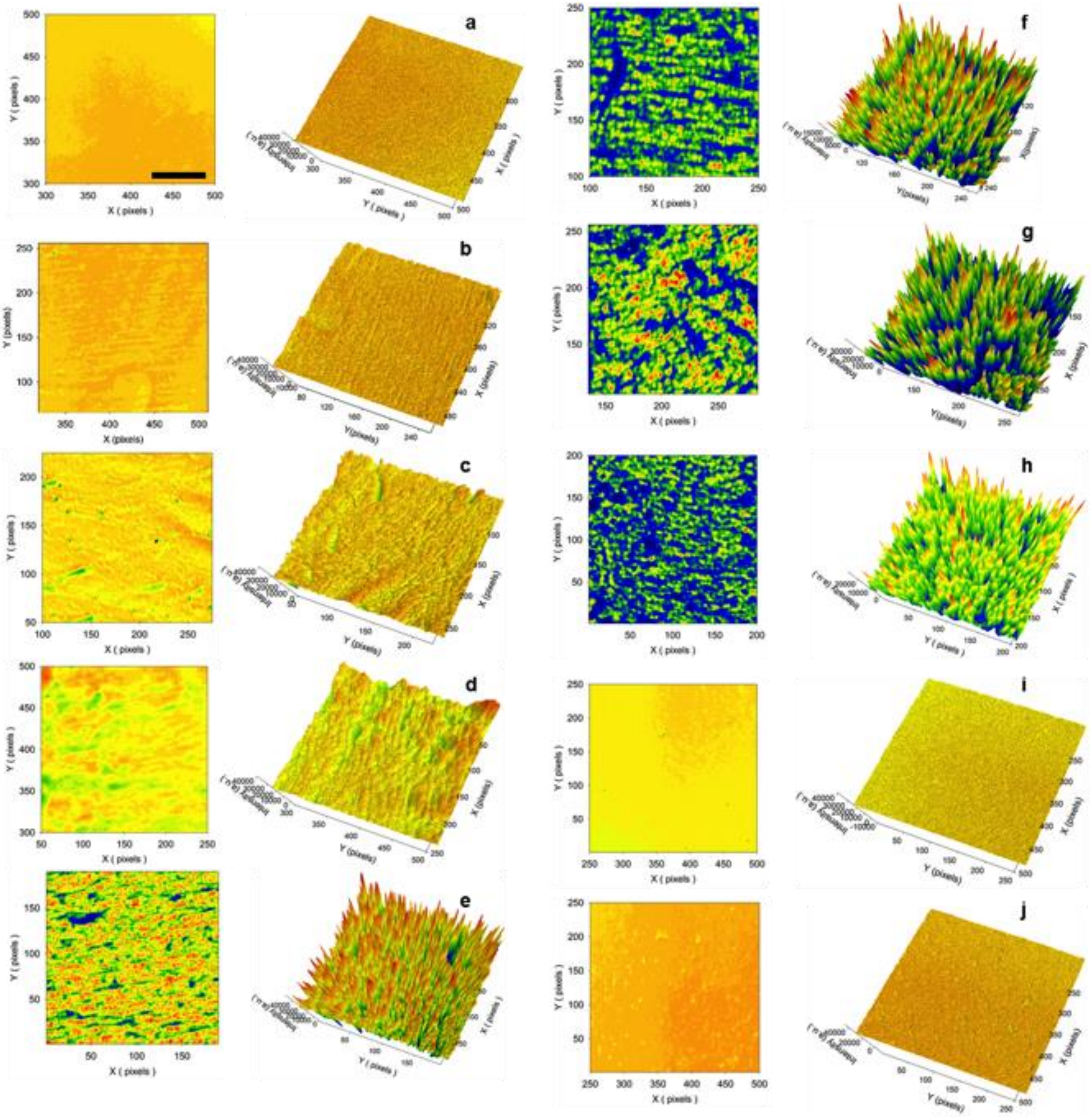

Figure 2.7. 2-D and 3-D spatial intensity profiles of white light after propagation through epoxide samples over a pathlength (*z*) of 4 mm.Profiles acquired in a sample with 10 wt.% of benzyl alcohol after irradiation for (a) 0 s and (b) 150 min. Profiles were also acquired at 150 min. for samples with benzyl alcohol concentrations of (c) 15 wt.%, (d) 20 wt.% (e) 25 wt.%(f) 30 wt.% (g) 35 wt.% (h) 40 wt.% (i) 45 wt.% and (j) 50 wt.%. Scale bar in (a) = 500 μm and applies to all images.

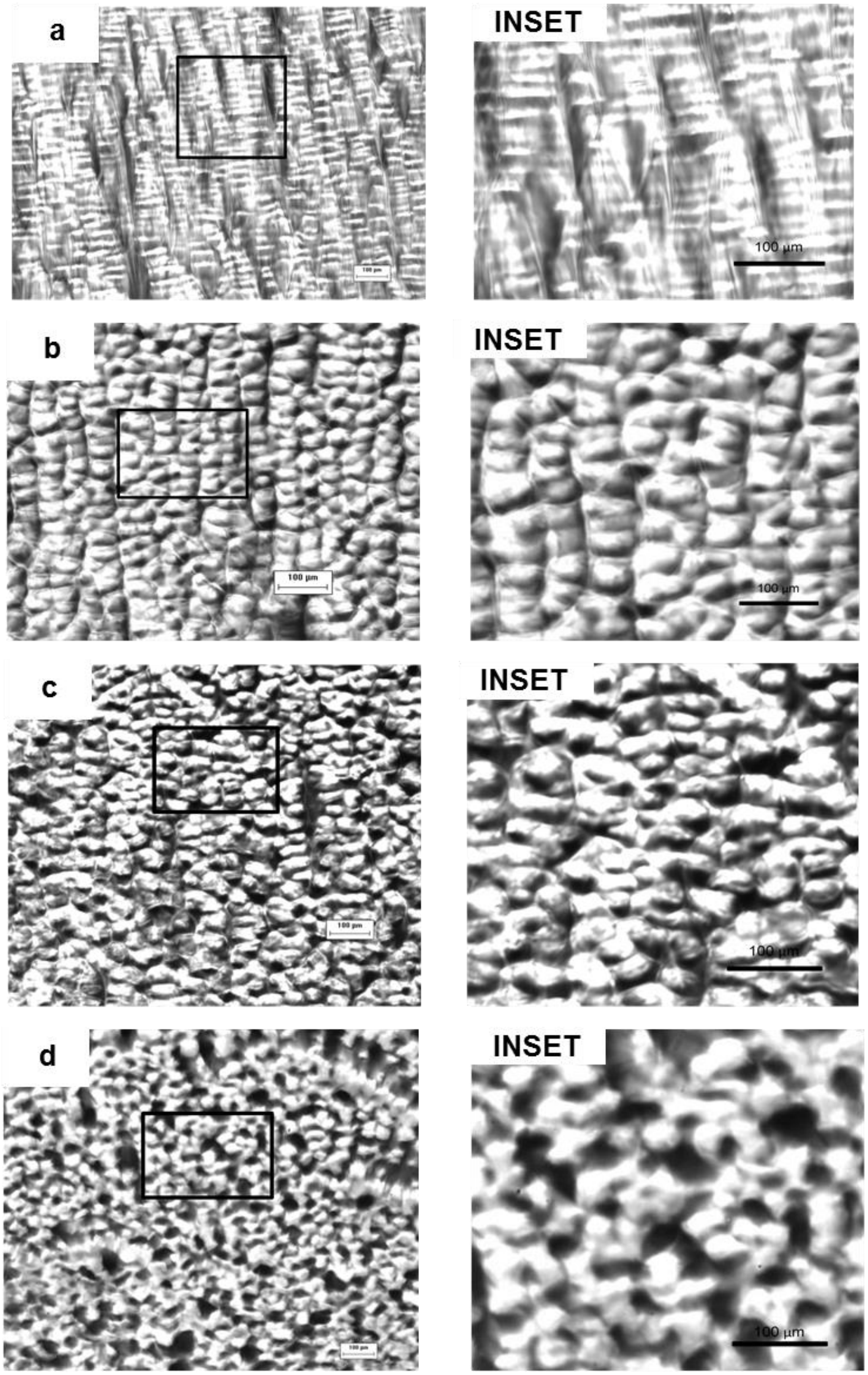
a
100 µm
INSET
100 µm
b
100 µm
INSET
100 µm
c
100 µm
INSET
100 µm
d
100 µm
INSET
100 µm

Figure 2.8. Cross-sectional transmission optical micrographs of waveguides induced through modulation instability in epoxide systems with benzyl alcohol concentrations of(a) 25 wt.% (b) 30 wt.% (c) 35 wt.% and (d) 40 wt.%. Magnified images of regions framed in black are provided as insets for each sample.

The results in Figure 2.7 reveal the strong correlation between polymerization rate, extent of crosslinking, and emergence of MI. For samples with < 20 wt.% of benzyl alcohol, the relatively low concentration of initiating species leads to correspondingly small polymerization rates (Section 4.3). In MI experiments, these systems remain in the linear regime throughout the experiment (t = 150 min.) during which the beam continues to propagate without suffering any perturbations (Figure 2.7b-c). Importantly, the same systems transform from fluids to brittle solids after very long times (8 hr.) of irradiation, indicating that polymerization continues to occur at long times albeit at slower rates; however, MI was not observed even at these times. We reason that the smaller polymerization rates in these samples greatly *reduce* the photoresponse speed. The importance of the inherently non-instantaneous (>>fs) response of the polymerizable medium to elicit MI of incoherent light was discussed in Section 1. However, the photoresponse speed of systems with < 20 wt.% benzyl alcohol appears to be so greatly reduced that they are unable to “record” the spatial noise in the medium and generate MI seeds rapidly enough to trigger instability. In this case, their extremely slow photoresponse renders the systems insensitive to the spatial inhomogeneities – noise - that fluctuate over time; the medium responds instead to a spatially smoothed version of the optical field. Polymerization is effectively uniform throughout the medium and the propagating beam remains unmodulated (Figure 2.7b-c). The faster photoresponse due to increased polymerization rate in the system containing 20 wt.% of benzyl alcohol elicited weak intensity modulations but did not lead to filamentation (Figure 2.7d). This suggests that although MI seeds had been rapidly attained, leading to modulations in the uniform beam, the extent of crosslinking was insufficient to generate a large enough Δn required for filamentation. Consistent with this reasoning, a further increase in the amount of benzyl alcohol to 25 wt.% resulted in significantly stronger intensity modulations and ultimately, filamentation (Figure 2.7e). In this composition, both the polymerization rate and the extent of crosslinking were sufficient to generate the fast photoresponse and Δn, respectively to elicit MI.

MI was observed in samples containing up to 40 wt.% benzyl alcohol (Figure 2.7e-h); however, at 45 wt.% and 50 wt.% amounts of the alcohol, the system reverted to linear behaviour and the beam remained uniform (Figure 2.7i-j). The gradual decrease in T_g when the amount of benzyl alcohol was increased above 25 wt.% (Table 2.2) and change in consistency from hard solid to free-flowing fluid indicate a decrease in polymerization and extent of cross-linking; this was further supported by the significant decrease in percentage conversion of epoxide moieties in samples containing 50 wt.% of benzyl alcohol (Figure 2.6). As a result, these systems have fast photoresponses but their smaller molecular weight polymer chains cannot form seeds with sufficiently large values of Δ*n* to elicit MI.

The interplay between the photoresponse speed (rate of initiation) and magnitude of Δ*n* (degree of crosslinking) is particularly apparent when comparing the behaviour of samples containing 40 wt.% and between 10 wt.% and 15 wt.% of benzyl alcohol; the former displayed MI (Figure 7h) but yielded final products with significantly smaller values of T_g compared to samples with 10 wt.% - 15 wt.% of alcohol (Table 2.2). The latter did not undergo MI even after prolonged (8 hr.) irradiation (Figure 2.7b-c). The system containing 40 wt.% alcohol has a sufficiently fast photoresponse, which can respond to rapidly fluctuating spatial noise and in this way, generate MI seeds. The smaller initiation rates in samples with only 10 % - 15 % alcohol generate greater molecular-weight chains (with greater T_g values) but polymerization occurs over a timescale that greatly exceeds the timescale of noise fluctuations; the system therefore responds to a time-averaged version of the optical field and effectively remains in the linear regime. Systems containing between 25 wt.% to 40 wt.% of benzyl alcohol fall within a narrow region where perfect balance is struck between the generation of sufficiently large degrees of crosslinking (and high-index MI seeds) and sufficiently fast photoresponse times.

2.3.5. Role of Micro-Phase Separation during MI

At increased polymerization rates, high-index seeds are achieved not only due to the increased crosslinking but also due to the partial phase separation of these high-density, cross-linked polymer chains from the solvent/monomer mixture. Network heterogeneity due to spontaneous phase separation of cross-linked epoxy polymers has been previously reported.[29] The polymerizing epoxy chains, initially swollen with monomer-solvent mixtures, deswell and expel fluid mixture once they attain a critical cross-link density. During MI, this micro-scale phase separation of high-density, cross-linked polymer chains further enhances the contrast in refractive index between the MI seeds and their surroundings. Large values of Δn ensure better light-confinement, more intense self-trapped filaments and stronger self-induced waveguides. In our system, phase separation is enhanced by the particularly poor solubility of epoxy polymers in the benzyl alcohol solvent; solubility parameters listed in Table 2.3 highlight the poor compatibility between benzyl alcohol and epoxy polymer relative to acetone and chloroform. This was demonstrated in measurements of the gel content of the photopolymerized epoxy material (25 wt.% benzyl alcohol); while the epoxy dissolved completely in acetone and chloroform, the gel retained 67 % of weight after attempted solubilization in benzyl alcohol.

Table 2.3. Residual gel content (%) of photopolymerized epoxide sample EB25 after extraction in different solvents. Hildrebrand solubility parameters are provided for the solvents and a similar epoxide

Solvent	**Solubility parameter ($MPa^{1/2}$)**[30]	**Gel content (wt %)**
Acetone	19.7	0
Chloroform	18.7	0
Benzyl alcohol	24.6	67

Solubility parameter of 3,4-Epoxycyclohexylmethyl-3',4'-epoxycyclohexane carboxylate = 18.3[31]

Phase separation of waveguides comprising high-density, cross-linked epoxy polymer from the benzyl alcohol solvent was apparent through Raman spectral mapping of the sample resulting from MI in 25 wt.% benzyl alcohol. Maps of the benzyl alcohol acquired at 1003 cm^{-1} (aromatic in-plane C-H deformation vibration) and epoxide monomer at 799 cm^{-1} (epoxide ring stretching vibration) show that residual monomer and alcohol are primarily localized outside of the waveguides (Figure 2.9).

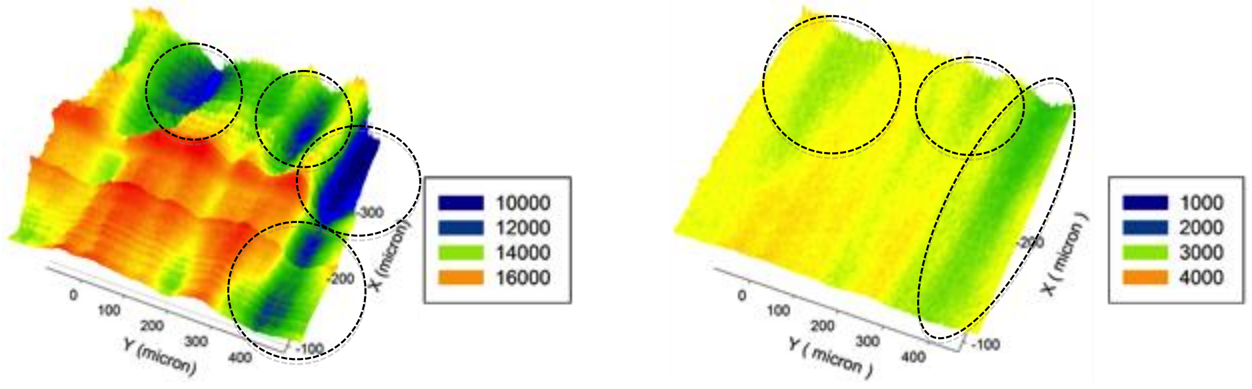

Figure 2.9. Raman spectral maps of (a) 1003 cm^{-1} band (in-plane CH deformation of benzyl alcohol aromatic ring) and (b) 799 cm^{-1} band (epoxide ring stretching) of an epoxy (EB25) sample containing MI-induced waveguides; dips encircled in dotted black correspond to the transverse cross-sections of waveguides. The maps show depletion of both epoxide monomers and benzyl alcohol solvent from the polymerized waveguide regions. Intensity (a.u.) colour maps are included.

2.4. Summary and Outlook

Nonlinear conditions are generated during the photoinitiated cationic polymerization of bifunctional epoxide monomers by a broad incandescent beam. Δn associated with the cross-linking of epoxides satisfies the strict prerequisites for MI of the spatially and temporally incoherent optical field. Systematic variation of polymerization kinetics revealed that MI occurred only within a narrow range of parameters when the photoresponse of the system (determined by polymerization rate) is fast enough to "record" noise in the system and the magnitude of Δn (determined by the extent of crosslinking) is large enough to seed MI. Outside of this narrow range, MI is entirely suppressed.

Because Δn due to epoxide polymerization is irreversible, waveguides inscribed by self-trapped filaments remain permanently inscribed in the medium. These microstructures serve as frozen replicas that provide insight into the spatial distribution of nonlinear waveforms generated by MI. They also represent a powerful room temperature route relying only on visible, low-energy incandescent light to generate functional 3-D waveguide architectures, which would be extremely difficult, expensive and time-consuming to fabricate through conventional techniques.

References

(1) Pojman, J. A.; Tran-Cong-Miyata. *Nonlinear Dynamics in Polymeric Systems*; American Chemical society, 2003.

(2) Burgess, I. B.; Shimmell, W. E.; Saravanamuttu, K. *J. Am. Chem. Soc.* **2007**, *129* (15), 4738–4746.

(3) *Spatial solitons*; Trillo, S., Torruellas. W., Eds.; Springer, 2001.

(4) Zhang, J.; Kasala, K.; Rewari, A.; Saravanamuttu, K. *J. Am. Chem. Soc.* **2006**, *128*, 406–407.

(5) Li, H.; Qi, Y.; Malallah, R.; Sheridan, J. T. *J. Opt. Soc. Am. B* **2015**, *32* (5), 912.

(6) Li, H.; Dong, Y.; Xu, P.; Qi, Y.; Guo, C.; Sheridan, J. T. *Ootics Lett.* **2015**, *40* (13), 2981–2984.

(7) J. S. Yuan, K. H. Tiller, H. Al-Ahmad, N. R. Stewart, C. N. S. J. *Trends in Plant Science*. 2008, p 421.

(8) Burgess, I. B.; Ponte, M. R.; Saravanamuttu, K. *J. Mater. Chem.* **2008**, *18* (35), 4133.

(9) Ponte, M. R.; Welch, R.; Saravanamuttu, K. *Opt. Express* **2013**, *21* (4), 4205–4214.

(10) Kasala, K.; Saravanamuttu, K. *J. Mater. Chem.* **2012**, *22*, 12281.

(11) Kasala, K.; Saravanamuttu, K. *Langmuir* **2013**, *29*, 1221–1227.

(12) Li, Y.; Krinsky, S.; Lewellen, J. W.; Kim, K.-J.; Sajaev, V.; Milton, S. V. *Phys. Rev. Lett.* **2003**, *91* (24), 243602.

(13) Mitchell, M.; Segev, M. *Nature* **1997**, *387* (6636), 880–883.

(14) Schwartz, T.; Carmon, T.; Buljan, H.; Segev, M. *Phys. Rev. Lett.* **2004**, *93* (22), 1–4.

(15) Zhang, J.; Saravanamuttu, K.; Ls, O. *J. Am. Chem. Soc.* **2006**, *280* (23), 14913–14923.

(16) Kasala, K.; Saravanamuttu, K. *Appl. Phys. Lett.* **2008**, *93* (5), 111–114.

(17) Stegeman, George I and Segev, M. *Science (80-.).* **1999**, *286*, 1518–1522.

(18) Ana B. Villafranca, and K. S. *J. Phys. Chem. C* **2015**, *112* (44), 17388–17396.

(19) Villafranca, A. B.; Saravanamuttu, K. *J. Opt. Soc. Am. B* **2012**, *29* (9), 2357–2372.

(20) Villafranca, A.; Saravanamuttu, K. *Opt. Express* **2011**, *19* (16), 15560–15573.

(21) Villafranca, A. B.; Saravanamuttu, K. *J. Opt. A Pure Appl. Opt.* **2009**, *11* (12), 125202.

(22) Crivello, J. V. *J. Polym. Sci. Part A Polym. Chem.* **2009**, *47*, 866–875.

(23) Crivello, J. V.; Acosta Ortiz, R. *J. Polym. Sci. Part A Polym. Chem.* **2002**, *40* (14), 2298–2309.

(24) Chen, Z.; Klinger, J.; Christodoulides, D. N. *Phys. Rev. E - Stat. Nonlinear, Soft Matter Phys.* **2002**, *66* (6), 1–5.

(25) LaBianca, N.; Delorme, J. High Aspect Ratio Resist for Thick Film Applications. *Proc.SPIE* **1995**, *2438*, 846−852.

(26) Socrates, G. *Infrared and Raman Characteristic Group Frequencies*; John Wiley & Sons: Hoboken, 2004.

(27) Refractive index change (Δn) measurements were carried out by Hao Lin and Ian Hosein

(28) Born, M.; Wolf, E. *Principles of Optics, Electromagnetic Theory of Propagation,Interference and Diffraction of Light*, 7th ed.; Cambridge University Press: UK, 2002; Ch. 7.

(29) Andersen, P.; Munk, M. E.; Pollock, J. M.; Doherty, T. M. 2000, pp 1099–1104.

(30) Allan, F. M. Barton *Handbook of Solubility Parameters and Other Cohesion Parameters*; second printing, CRC Press: Florida, US, 1985.

(31) Iijima, T.; Fujimoto, K. I.; Tomoi, M. *J. Appl. Polym. Sci.* **2002**, *84* (2), 388–399.

Supplementary information

1. Differential Scanning calorimetry curves.

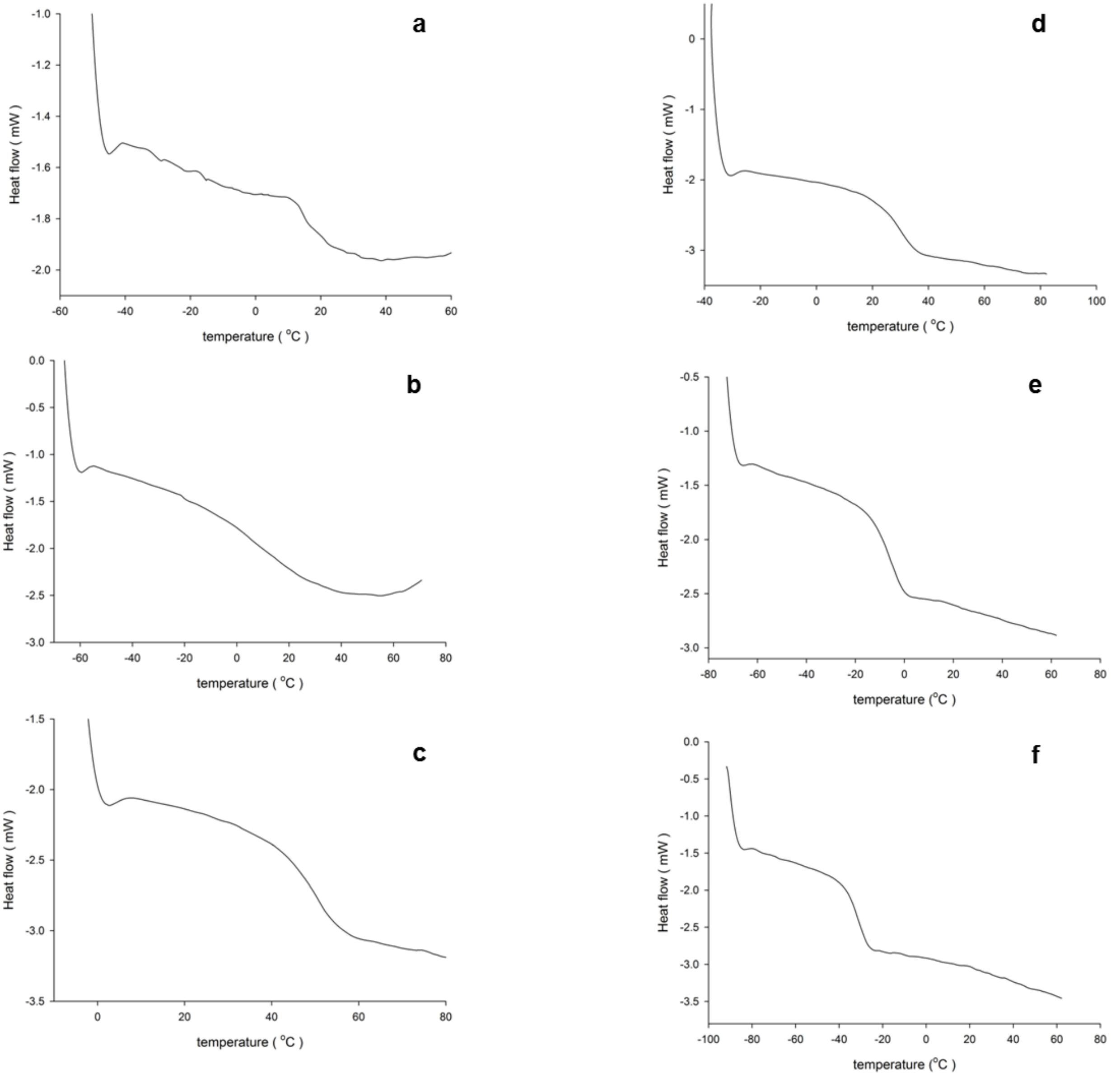

Figure S2.1 DSC curves for the samples a) EB10 b) EB15 c) EB25 d) EB30 e) EB40 f) EB50

2. FTIR spectrum

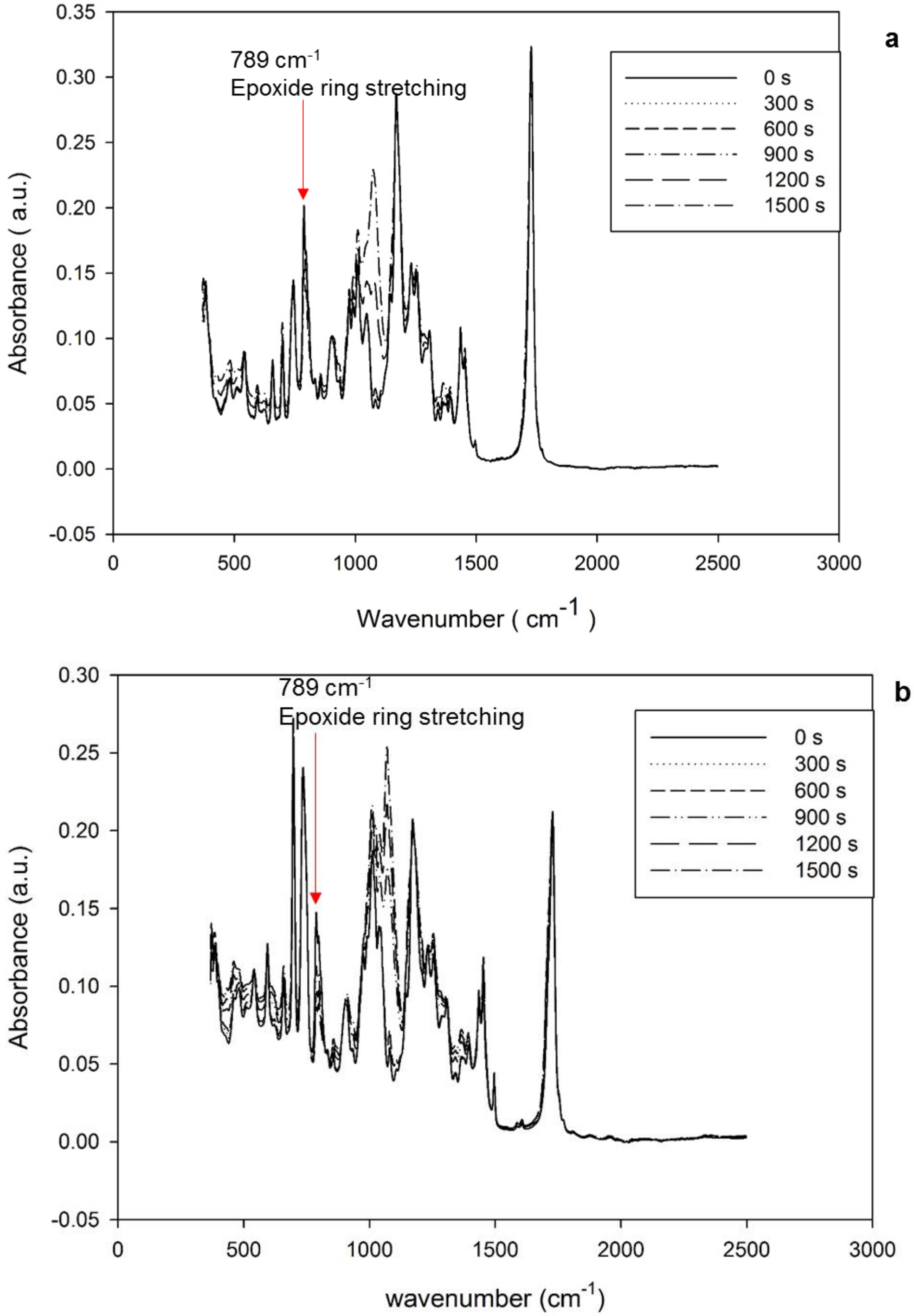

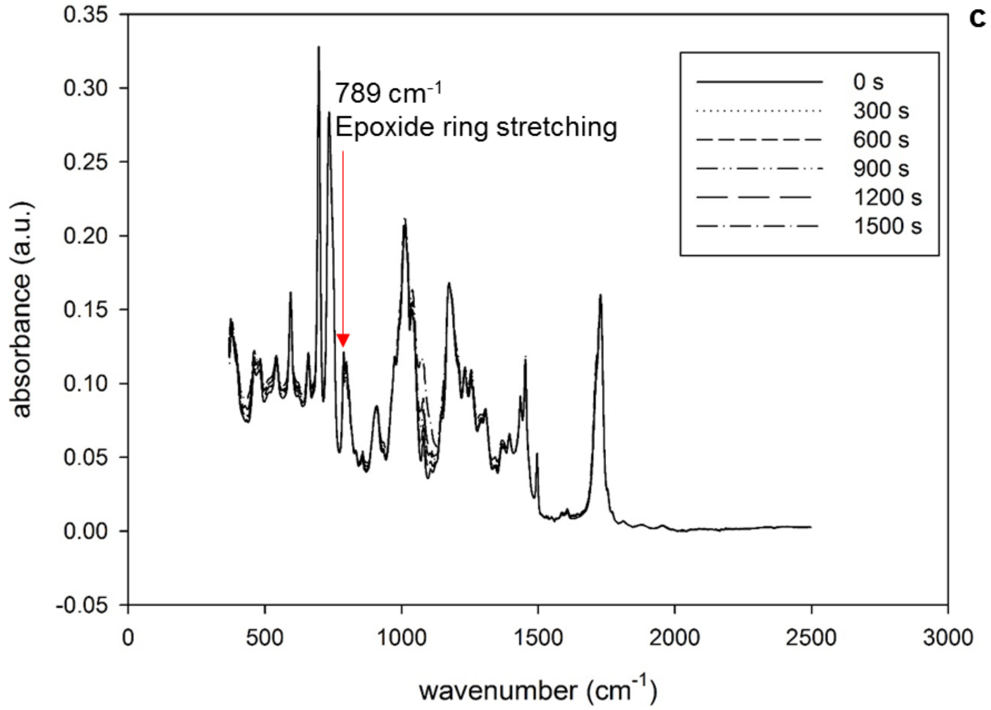

Figure S2.2 Temporal change of FTIR spectra of epoxy a) EB10 b) EB35 c) EB 50

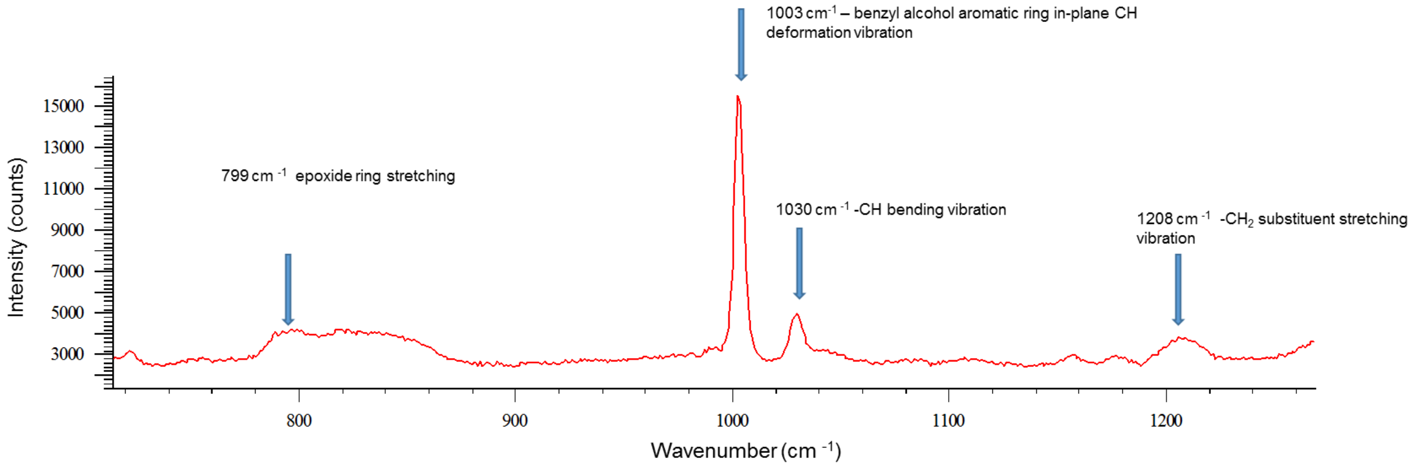

Figure S2.3 Raman spectrum of EB25 with waveguides

Chapter 3

Highly thermomechanically stable waveguides induced by modulation instability of white light in epoxide systems

Abstract

Thermomechanically stable epoxide/siloxane blend systems capable of exhibiting modulation instability induced waveguide microstructures were developed by mixing epoxypropoxypropyl terminated polydimethylsiloxane (EDMS) with 3,4-epoxycyclohexylmethyl-3',4'-epoxycyclohexane carboxylate (ERL). Visible light photopolymerizable blend systems containing 0 to 46 wt % of EDMS were prepared in presence of polybutanediol (pTFH) to study the effect of EDMS on mechanical, thermal and optical properties of the blends. Our results show that the addition of 10 wt% of EDMS increases the elongation at break by three times (from 2.65 % to 7.5 %) with modulus (0.9 GPa) comparable to neat ERL system (1.1 GPa), showing enhancement in toughness without deterioration in mechanical strength of blend. Thermal stability parameters namely initial decomposition temperature (IDT) and integral procedural decomposition temperature (IPDT) for the blend with 10 wt% of EDMS were similar to the neat ERL composition but the glass tranisition temperature (T_g) reduced by 30 ^{0}C (from 156± 1.15 ^{0}C to 117± 14.8 ^{0}C). Further increase in EDMS content (from 26 wt % upto 41 wt %) deteriorates the mechanical properties of the blends. Our findings show that EDMS can be used to toughen ERL without degrading its mechanical, thermal and optical properties.

3.1. Introduction

Epoxide resins are widely used in micro and nanofabrication technologies such as e-beam lithography,[1] soft lithography,[2] RIE masking layers,[3] proton beam writing,[4] electrodeposition molds[5] because of their excellent processibility, superior mechanical properties and good thermal and chemical resistance. However, their highly cross-linked structure after polymerization results in brittleness, making them susceptible to failure by brittle fracture.[6–8]Off the various approaches used to enhance the toughness of these materials, blending with reactive toughening agents is one of the prominent ways to improve the toughness of epoxides. Polydimethylsiloxane (PDMS), a soft, flexible, optically transparent, low glass transition temperature, thermally stable polymer used for soft lithography,[9] micro-[10] and nano-fluidic[11] and flexible electronics[12] has been suggested as toughening agents for epoxide.[13–17] Soft siloxane units dispersed in epoxide matrix enhances toughness by different mechanisms such as crack trapping and bridging,[13] localized shear band yielding[17] and cavitation of the dispersed phase followed plastic deformation of the matrix.[17] However, pure PDMS has very little use as a toughening agent due to the incompatibility between soft siloxane units and hard polar epoxide units. The incompatibility results from lack of hydrogen bonding between siloxane and epoxide groups. It was shown elsewhere, that the compatibility of siloxane with epoxide can be improved by using epoxide,[13] hydroxide,[18] carboxyl[19] and amino functionalized siloxane.[20]

In this work, we used epoxide functionalized siloxane (epoxypropoxypropyl terminated polydimethylsiloxane, EDMS), as toughening agent and made mechanically tough, thermally stable epoxide/siloxane blend systems that can elicit modulation instability (MI), a nonlinear optical phenomenon. In our previous work, we showed a uniform broad incoherent polychromatic beam launched into photocationcally polymerizable epoxide systems experiences MI and spontaneously splits into dense array of identical filaments of light.[21] MI process in nonlinear systems has been detailed elsewhere.[22] Briefly, MI originates from the amplification of inherent noise embedded in the system. Under nonlinear conditions, the noise gets amplified and makes the initially uniform beam inhomogeneous. Because of the inhomogeneity in the optical field, the rate of photopolymerization experiences corresponding variation. Regions with slightly higher intensity polymerize faster resulting in higher refractive index change (Δn) than regions with slightly lower intensity. Light gets preferentially trapped in these higher Δn regions and leads to reciprocal amplification of polymerization rate and intensity. This amplification causes the spontaneous division of uniform broad beam into individual filaments. The beam gets self-trapped in these individual filaments and propagate without divergence by inscribing an optical waveguide along its propagation direction. As the polymerization enabling the Δn is an irreversible process, optical waveguides generated during this process transform into permanent 3D polymer waveguide microstructures. Because the waveguide structures originate from noise, they are randomly positioned in space. In our earlier works, we have fabricated ordered waveguide microstructured lattices like woodpile,[23] hexagonal,[24] square,[22] simple cubic,[25] near cubic[26] and body centered cubic geometries by controlling the spatial distribution of noise using amplitude masks and developed this nonlinear phenomenon into a high throughput, single-step room temperature technique for fabricating tens of thousands of cylindrical polymer waveguide microstructures. In our recent work, we showed that MI in photocationic polymerizable systems occur only when the photoresponsive time is fast enough to record the noise in the system and the magnitude of Δn is high enough to initiate MI. The former is dictated by the polymerization rate of the system and the later by the degree of cross-linking.[21]Having these as guidelines, in this work we have developed epoxide/siloxane photopolymerizable blend systems that meet the polymerization kinetics requirements for the occurrence of MI as well as show mechanical toughness and thermal stability. Mechanical and thermal properties of the blends were investigated by tensile testing, thermogravimetric analysis (TGA) and dynamic mechanical analysis. Morphology of the blends were examined by scanning electron microscopy. Occurrence of MI in the blend systems was captured using CCD camera and the waveguide structures were characterized by optical microscope.

3.2. Experimental

3.2.1. Materials

3,4-epoxycyclohexylmethyl-3',4'-epoxycyclohexane carboxylate (ERL) (1), camphorquinone (97% purity) (2) , poly(tetrahdrofuran) (pTHF) (3), were purchased from Sigma Aldrich (oakville, ON) and used without further purification. Epoxypropoxypropyl terminated polydimethylsiloxane (EDMS) (4) was purchased from Gelest Inc., and used without further purification. Camphorquinone (λ_{max} = 468 nm) and bis(4-t-butyl)iodonium hexafluroantimonate (5) (Hampford research Inc., Starford, CT, United states) were used as photosensitizer (PS) and initiator (I) as shown by Crivello *et al*[27]

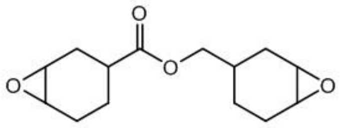
1

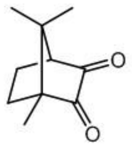
2


3

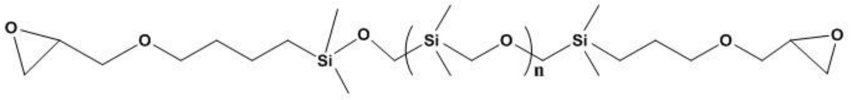
4

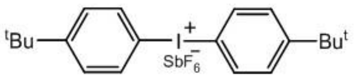
5

3.2.2. Sol preparation ERL/EDMS/pTHF blend

Sols for MI induced waveguide fabrication were made by mixing PS, I and pTHF with biscycloaliphatic epoxide and EDMS monomers and stirred under dark for 48 hours. Compositions listed in table 3.1 were labelled based on the weight percent of pTHF and EDMS. 2.5 wt % of I and 1.5 wt % of PS were used in all compositions. Homogenized sols were filtered through a polytetrafluoroethylene (PTFE) membrane (0.2 µm pore size, Pall Corporation USA) and filled in a homemade, cylindrical PTFE cell with optically transparent, glass windows and with a physical pathlength of 4.0 mm and 15 mm diameter. The different compositions are shown in the table 3.1.

Table 3.1 Various ERL/EDMS/pTHF blend compositions.

Material Code	ERL (Wt %)	EDMS (Wt %)	pTHF (Wt %)
ET10	86	0	10
ET10D10	76	10	10
ET20D06	70	6	20
ET10D26	60	26	10
ET20D26	50	26	20
ET20D41	35	41	20
ET10D46	40	46	10

3.2.3. Optical assembly

Optical assembly shown in figure 3.1 used for this work is an adaptation from the previous work.[21] Optical components used were mounted in a rail with carrier which was movable with a resolution of 0.25 mm. The entire setup on the whole is fitted over an optical table (flatness of ±0.13 mm) having a tuned damping to prevent the setup from vibration. The optical and mechanical components used in the experiment were purchased from Newport Corporation, CA, USA. Quartztungstenhalogen (QTH) lamp (Cole-Parmer 9741-50, Illinois, USA) was used as white light source, incoherent beam was collimated by a planoconvex lens (F.L = 250 mm, d=25.4 mm) and launched onto the entrance face of the sample cell (path length = 4 mm, transparency = 320 nm- 800 nm) containing the sol. Beam intensity profile at the exit face of the sample cell was monitored by focusing the output beam through a pair of plano-convex lenses (F.L. =250 mm, d=25.4mm) onto a high-resolution, progressive scan, charged-coupled device (CCD) chip (D, 1360 (H) x 1024 (V) of 4.65 µm square pixels, sensitivity range = 350 nm to 1150 nm; WinCamD^{TM} digital camera, Data Ray Inc., USA).

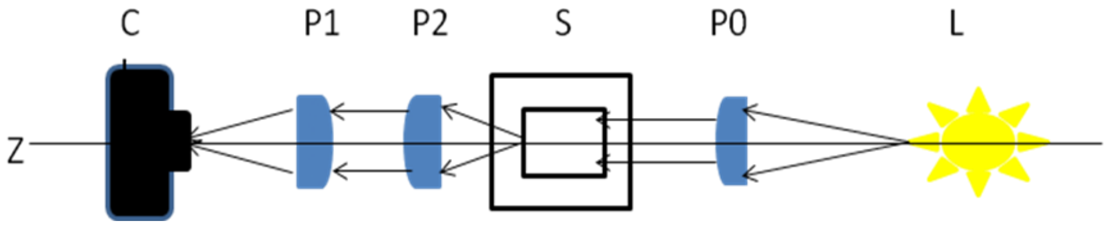

Figure 3.1. Optical assembly for the MI induced waveguide formation experiment, light from the QTH lamp (L) is collimated by a plano convex lens (P0) and focused onto the entrance face of the sample cell (S), which is mounted on a micrometer controlled linear stage and rail carrier. The output beam intensity profile is monitered through a pair of plano convex lens (P1 and P2) onto the CCD chip camera (C).

3.2.4. Photopolymerization

Epoxide/siloxne sols were photopolymerized with a constant intensity of 8 mW using the above mentioned optical setup. Optical intensity corresponding to 468 nm wavelength at the entrance face of the sample cell was measured by a power meter. Change in the beam intensity profile at the exit face of the 4mm sample cell during the course of polymerization was monitored and recorded simultaneously through CCD camera.

3.2.5. Optical Microscopy

Microstructured waveguide in polymerized samples were studied using an Olympus BX51 optical microscope fitted with a Q-Imaging Retiga EXi digital camera and Image pro software. The images were taken in transmission mode with 5x objective.

3.2.6. Thermogravimetric analysis (TGA)

TGA analysis for samples were conducted using TA instruments with standard ceramic crucible at a heating rate of 3 ^{0}C/ min with air circulation. Temperature range covered was 30 ^{0}C- 900 ^{0}C.

3.2.7. Dynamic mechanical analysis (DMA)

Storage modulus and Tg of the different blends were measured using DMA in tension mode. Sample dimension was 8 mm x 3 mm x 2mm. The temperature ramp was 3 ^{0}C/ min for all the experiment and measurements were performed at a frequency of 1 Hz with a displacement of 0.05mm.

3.2.8. Tensile testing

Sample dimensions for the tensile properties measurement were 10.5 mm x 50 mm x 1.6 mm. Testing was done at a displacement rate of 10 mm/min using a 5 KN load cell. Young's modulus was obtained from the slope of the stress-strain curve.

3.2.9. Scanning electron microscopy

SEM micrographs were acquired with a Vega Tescan instrument at an accelerating voltage of 10 KV in secondary electron modes.

3.3. Results and discussion

3.3.1 Photopolymerizable epoxide system

The epoxide/siloxane systems used for fabricating MI induced waveguide microstructures are based on the dye-sensitized visible light photoinitiator system developed by Crivello for cationic polymerization of wide range of epoxides.[27] The initiation and propagation mechanisms explained by Crivello is shown in scheme 3.1[27,28] Dye photosensitizer, camphorquinone (λ= 468 nm) upon irritation by incandescent white light in presence of suitable nonbasic hydrogen donor, polybutanediol,[29,30] generates α-hydroxypolybutanediol and hydroxycamphorquinone radicals (scheme 3.1, eq. 1). The former species is capable of reducing the diarlyiodonium salt, bis(4-butylphenyl) iodonium hexafluoroantimonate. Diarlyiodonium salt is reduced by α-hydroxypolybutanediol radical to form α-hydroxypolybutanediol cation and diarlyiodine radical (scheme 3.1, eq. 2). The cation undergoes deprotonation to form hydroxyterminal polybutanal and Bronsted acid, $HSbF_6$ (scheme 3.1, eq. 3). Cationic ring opening polymerization is initiated by the attack of this Bronsted acid on the epoxide monomer (scheme 3.1, eq. 5). The unstable diarlyiodine radical decomposes to aryliodide and aryl radical ((scheme 3.1, eq. 4)). This aryl radical can abstract hydrogen from polybutanediol to generate α-hydroxypolybutanediol radical, which in turn would consume diarlyiodonium salt by a nonphotochemical process resulting in generation of reactive species capable of initiating cationic polymerization. Apart from participating in the initiation, polybutanediol accelerates the rate of polymerization by inducing a rapid propagation mechanism called active monomer mechanism. In addition to the usual ring opening polymerization mechanism (scheme 3.1, eq. 6), epoxide monomers polymerize *via* active monomer mechanism in presence of alcohols.[31] This mechanism is shown in scheme 3.1 eq. 7 & eq. 8, where the growing oxiranium chain end gets a nucleophilic attack from alcohol to generate a protonated ether. Deprotonation of this species by epoxide monomer leads to chain termination and the protonated epoxide monomer can thereafter start a new chain. It is shown elsewhere, that the polymerization of epoxide monomer is accelerated by the presence of this active monomer mechanism. Epoxide terminated polydimethyl siloxane is used in the blend to improve the toughness of biscycloaliphatic epoxide.

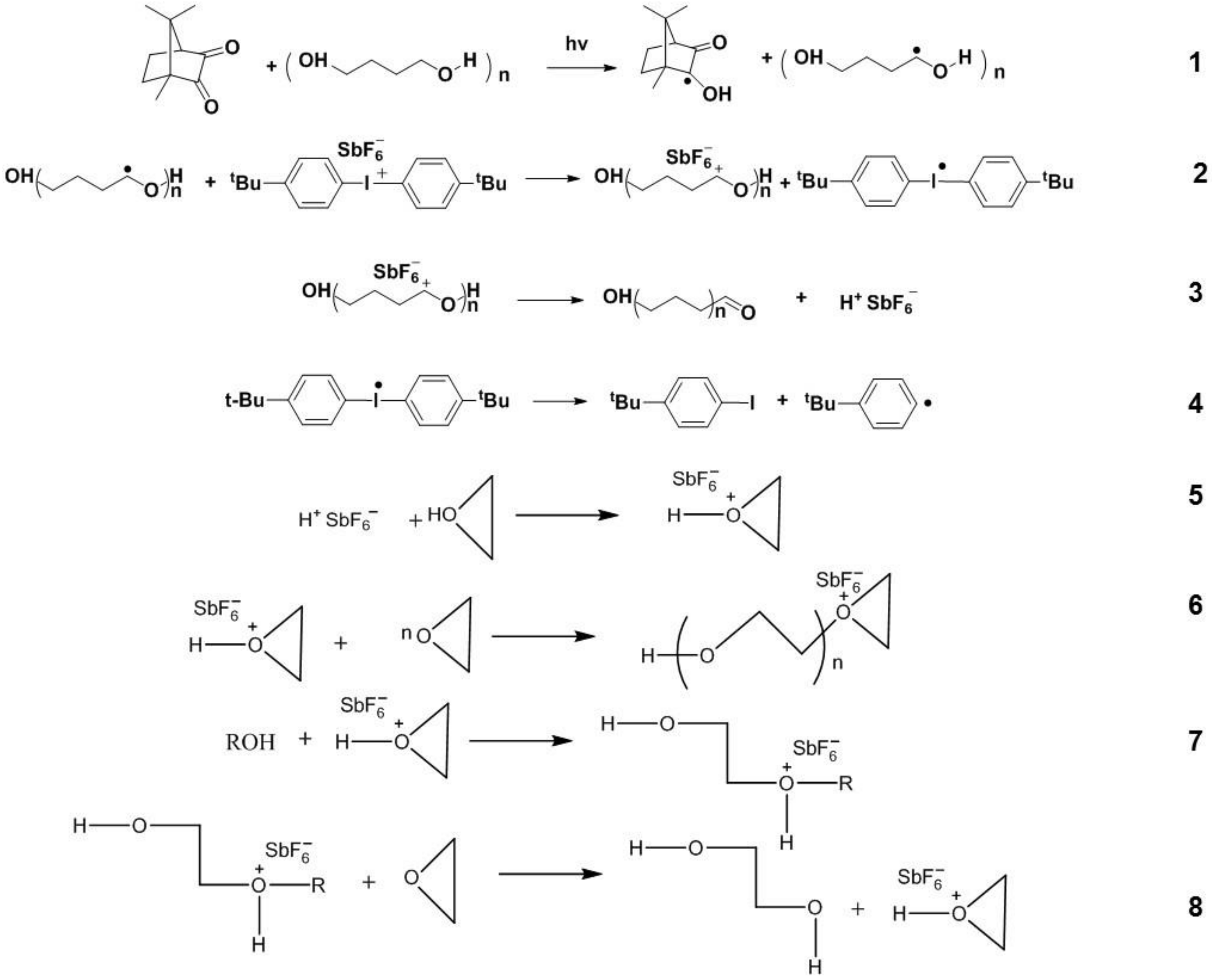

Scheme 3.1[27,28,31] Visible light cationic ring opening polymerization of epoxide

Presence of polar epoxide groups in EDMS, enables its compatibility in epoxide matrix. Because of the enhanced compatibility, the blends were clear and optically transparent solutions. Blends with different ratios of ERL/EDMS/pTHF were prepared as mentioned in table 3.1 to fabricate MI induced waveguide fabrication and to study the effect of EDMS on the mechanical and thermal properties of the blends.

3.3.2. Modulation instability induced waveguide microstructure fabrication

Waveguide microstructures were fabricated by exploiting the spontaneous pattern formation of incoherent light in nonlinear media. Pattern formation was studied using a broad beam of white light (λ 400 nm - λ 800 nm) emitted by the quartz tungsten-halogen (QTH) lamp. The randomly polarized, polychromatic, spatially and temporally incoherent light was collimated into a broad beam with uniform intensity profile using a planoconvex lens. The beam was shone uniformly onto the entrance face of the cell containing 50/26/20 weight percent of ERL/EDMS/pTHF mixture. Changes to the spatial intensity profile of the beam after it had propagated 4 mm inside the sample was monitored over time with a high resolution, charge coupled camera. Intensity profile of the beam collected during photopolymerization (figure 3.2) shows that the beam is uniform at time 0s in the absence of polymerization. Under these linear conditions, the weak amplitude and phase perturbations, (noise), become insignificant with increasing propagation distance. This is because the noise weakens and disappears due to natural diffraction of light. Once the beam initiates the cationic polymerization of the epoxide monomers, it develops weak intensity modulations and transforms into bright (high intensity) and dark (low intensity) stripes (figure 3.2b & 3.2c). The contrast (modulation depth) of the 1-D stripe pattern gets amplified over time due to the increase and decrease of intensity in the bright and dark regions respectively. As the polymerization proceeds further, the bright stripes develop minor variations in intensity which gets amplified with time and ultimately leads to the spontaneous transformation of each stripes into spots (figure 3.2e & 3.2f). Even though the absolute intensity of the spots changed over time, there was no change in their spatial position or size as long as they were monitored.

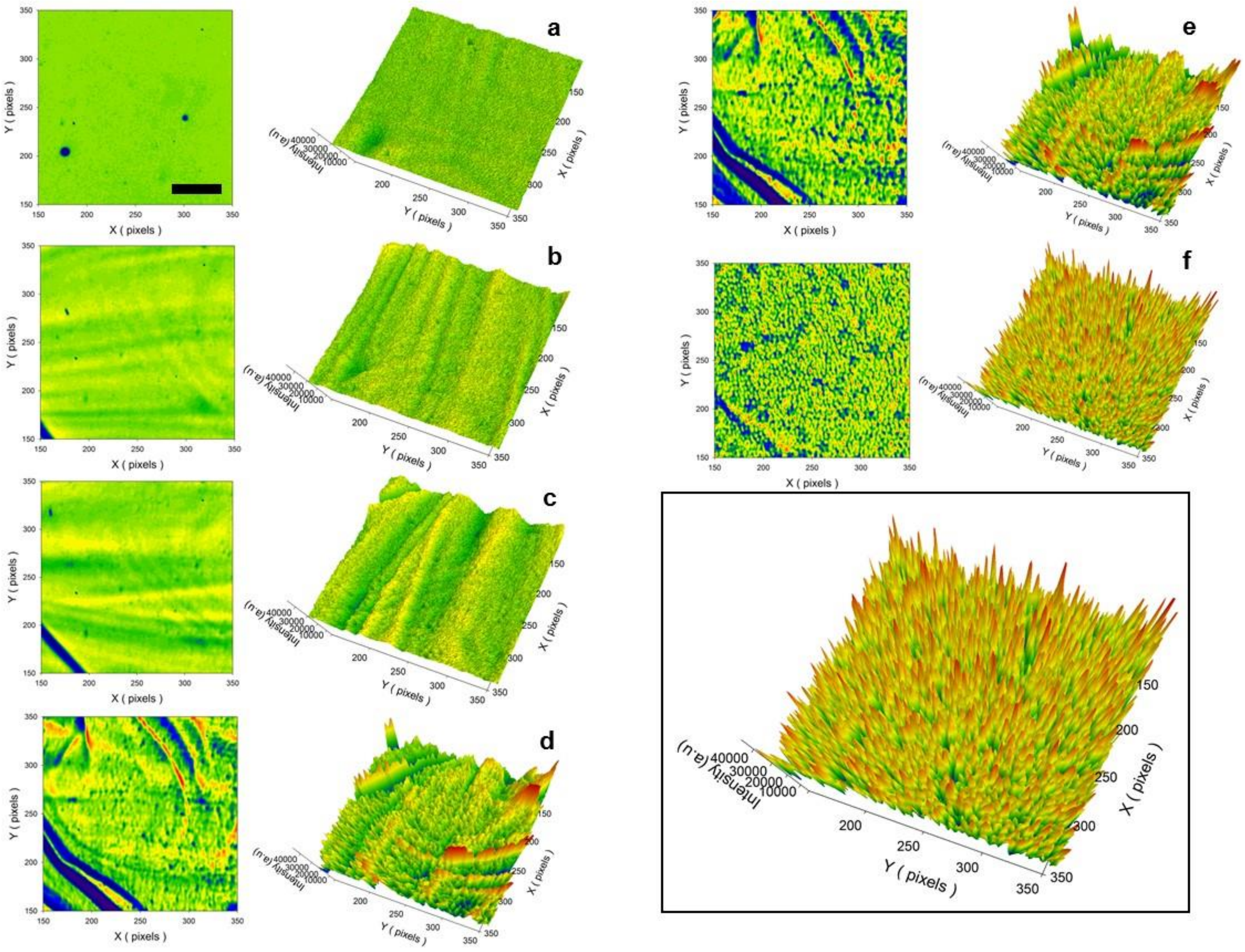

Figure 3.2. Temporal evolution of the spatial intensity profile of a white light beam at the exit face (z = 4 mm) of a photopolymerizable epoxide sample at t = (a) 0 s, (b) 240 s (c) 245 s (d) 255 s (e) 280 s (f) 1255 s . 2-D and 3-D profiles are shown. Scale bar in (a) = 500 μm and applies to all images. The inset is a magnified version of (f)

3.3.3. Mechanism of waveguide microstructure formation

It is evident from figure 3.2, that the refractive index change Δn induced by the cross-linking polymerization of epoxide group in the blend causes MI of optical field. The process can be explained as follows: MI of the white light is seeded by the inhomogeneities (noise) in the optical field and local concentration fluctuations in epoxide/siloxane sol. Because of the noise, there are minor spatial variations in intensity leading to corresponding difference in the rate of polymerization. These regions (with slightly higher intensity compare to surrounding regions) with slightly higher rate of polymerization result in higher Δn compare to the surrounding regions. Light gets concentrated in these higher Δn regions and thereby increases the rate of polymerization further. Under these nonlinear conditions, insignificant noise gets amplified through the reciprocal interaction between rate of polymerization and the intensity of optical field. Due to this increased perturbation, the optical field collapses into large population of self-trapped individual filaments to attain stability. These self-trapped filaments travel longer distances (>> Rayleigh range) without divergence by inscribing optical waveguides along its propagation direction. Because the photopolymerization is an irreversible process, optical waveguides generated through this process inscribe corresponding permanent microstrutures in the epoxide/siloxane blend. Figure 3.3 shows the permanent optical waveguide microstructures generated in the epoxide/siloxane blend. Three dimensional cylindrical geometry of these microstructures is evident from the longitudinal cross-section (figure 3.3 a). Concentrating and waveguiding of light by these microstructures is clearly visible in the transverse cross-section (figure 3.3 b).

EDMS used as toughening agent, as a significant effect in the MI process. In our previous work, we showed MI in photocationic polymerizable epoxide systems occurs only when the polymerization rate (which is directly related to the photoresponsive time of the system) is fast enough to capture the noise in the system.[21] Epoxide group in terminal position of EDMS is less reactive[15] compare to the ring strained epoxide group in ERL and so the ratio of EDMS in the blend as a direct bearing on the polymerization rate of the system. Blend systems with increasing amount of EDMS from 0 wt % to 46 wt % were prepared to study the effect of EDMS on MI. Figure 3.4 shows the CCD image of the optical field (at the exit face of the sample cell) in the blend systems after 20 min of irradiation. Figure 3.4a to 3.4g correspond to blend systems with EDMS content of 0 wt % to 46 wt %. Adding EDMS up to 41 wt % did not show significant effect on MI, which is evident from the CCD images. But increasing from 41 wt % (figure 3.4f) to 46 wt % (figure 3.4g) arrests MI. This is because at 46 wt %, rate of polymerization of the blend is predominately dictated by terminal epoxide group of EDMS and this lower reactive moiety reduces the polymerization rate (photoresponsive time) of the blend below a critical speed and

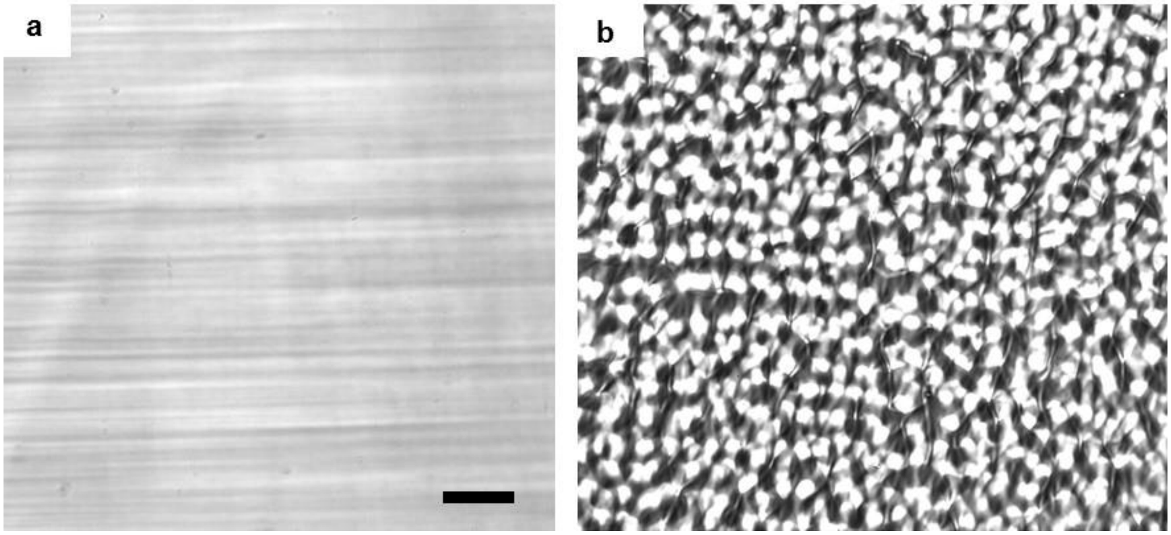

Figure 3.3. Optical micrographs showing a) longitudinal cross-section and b) transverse cross-section of ET20D26, scale bar = 100 μm

thus prevents the blend from recording the noise in the system, which in turn prohibits the occurrence of MI. This suggests that EDMS can only be added up to 41 wt % in the blend. Optical micrographs of the photopolymerized blends clearly support the above mentioned argument, where the MI induced microstructures are elicited in blends having EDMS up to 41 wt % (figure 3.5a to 3.5f) and absent in blend with 46 wt % (figure 3.5g).

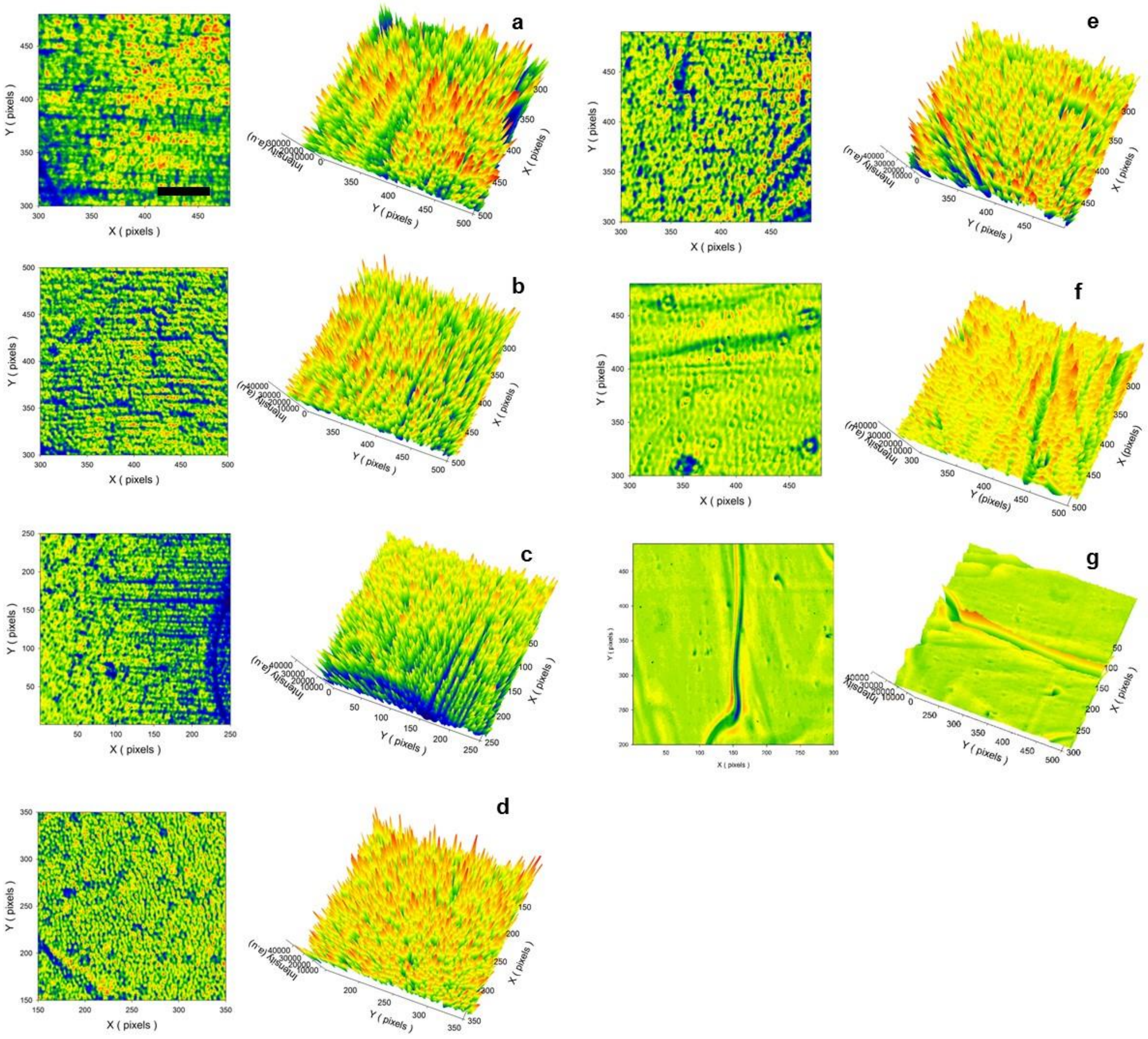

Figure 3.4. 2-D and 3-D spatial intensity profiles of white light after propagation through epoxide samples over a pathlength (*z*) of 4 mm.Profiles acquired in samples after irradiation for 20 min a) ET10 b) ET20D06 c) ET10D10 d) ET20D26 e) ET10D26 f) ET20D41 g)ET10D46. Scale bar in (a) = 500 μm and applies to all images.

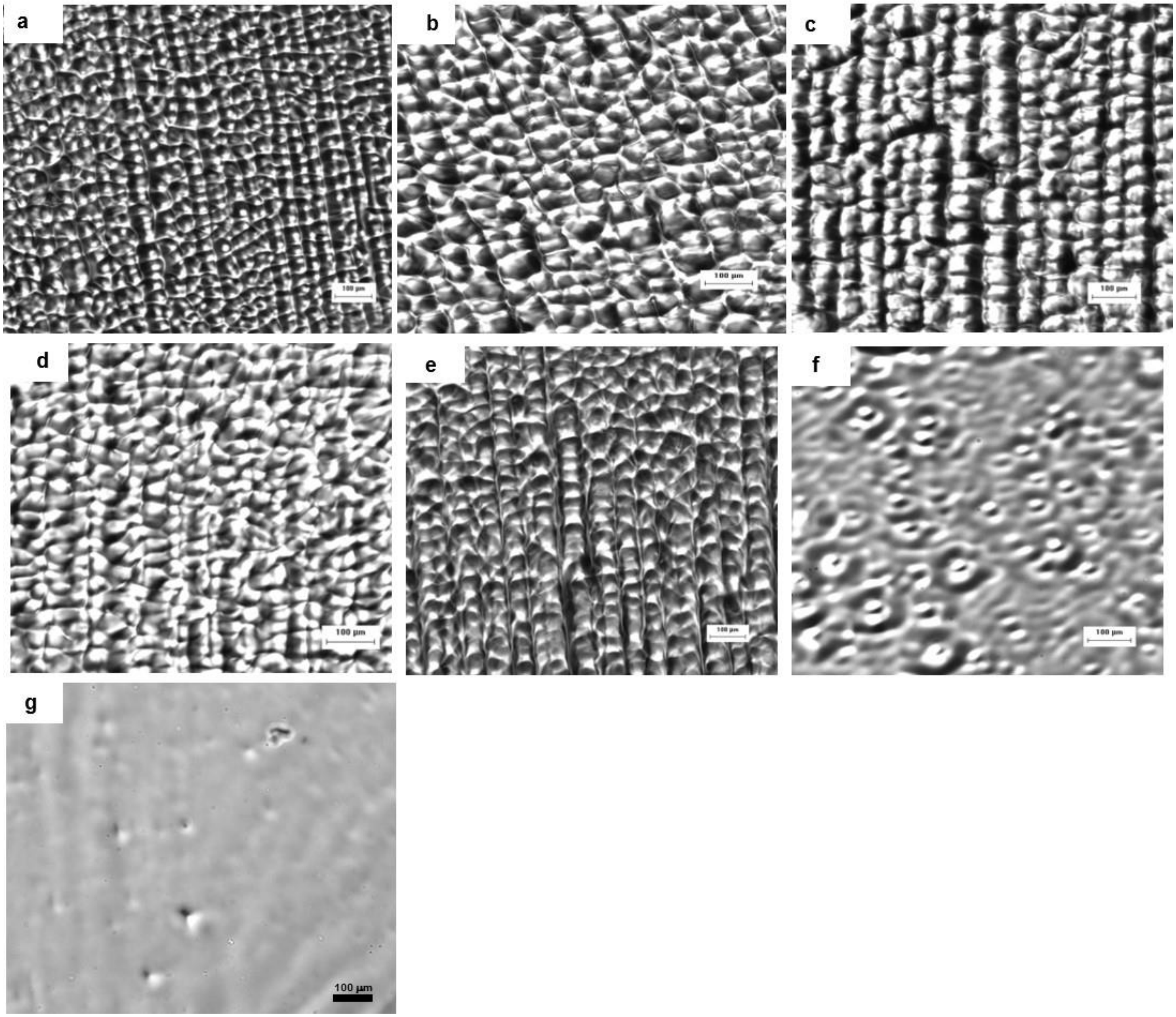

Figure 3.5. Optical micrographs showing the transverse cross-section of the waveguide microstructures in a) ET10 b) ET20D06 c) ET10D10 d) ET20D26 e) ET10D26 f) ET20D41 g) ET10D46.

3.3.4. Mechanical properties

Brittle behaviour of epoxides originate from the lack of molecular segmental motion.[6–8] Free energy requirement for the segmental motion of cross-linked epoxide is high and so at room temperature epoxide polymeric chains are static, behaving more like brittle glass. One of the ways to reduce brittleness or to impart toughness is to increase the molecular segmental motion of epoxide.[7] Siloxanes, with their highly flexible Si-O-Si backbone, which enables free segmental motion at room temperature have been used as toughening agents for epoxides.[13–15,18] However, pure PDMS has little use as toughening agent due to the incompatibility between the flexible, soft siloxane units and rigid polar epoxide units. Therefore, we used epoxide terminated polydimethylsiloxane (EDMS) to improve the toughness of biscycloaliphatic epoxide (ERL). Terminal epoxide groups in EDMS improves the compatibility between ERL and EDMS.[13] Various blends of ERL/EDMS were prepared and toughness enhancement was studied in terms of tensile properties. We show the dependence of stress-strain behaviour, elongation at break and Young's modulus of the blends on the weight ratio of EDMS. Figure 3.6 shows the comparison of stress–strain curves of the different blends. Increase in toughness with increasing EDMS content is evident from the area under the stress-strain curve, which provides the toughness of the material.[9] For the neat epoxide an obvious brittle fracture, without yielding, is observed (inset in figure 3.6). This is because rigid epoxide networks break easily under tensile loading, which prevent load transfer through these networks and thus they fails without yielding. With the addition of 10 wt % of EDMS, keeping the pTHF at 10 wt%, area under the stress-strain curve increased significantly due to the efficient energy absorption ability of flexible siloxane units, indicating the increase in toughness of the blend.[9] At 26 wt % of EDMS (pTHF 20 wt %) the blend shows ductility and yield behaviour which is apparent from the corresponding stress-strain curve.[32] Rubber like behaviour sets in with rapid decrease in modulus for the blend with 41 wt % of DMS (pTHF at 20 wt %).[33] It can be seen by comparing the area under the stress-strain curves, the blends show a transition from hard brittle to soft rubbery behaviour with increasing EDMS content.

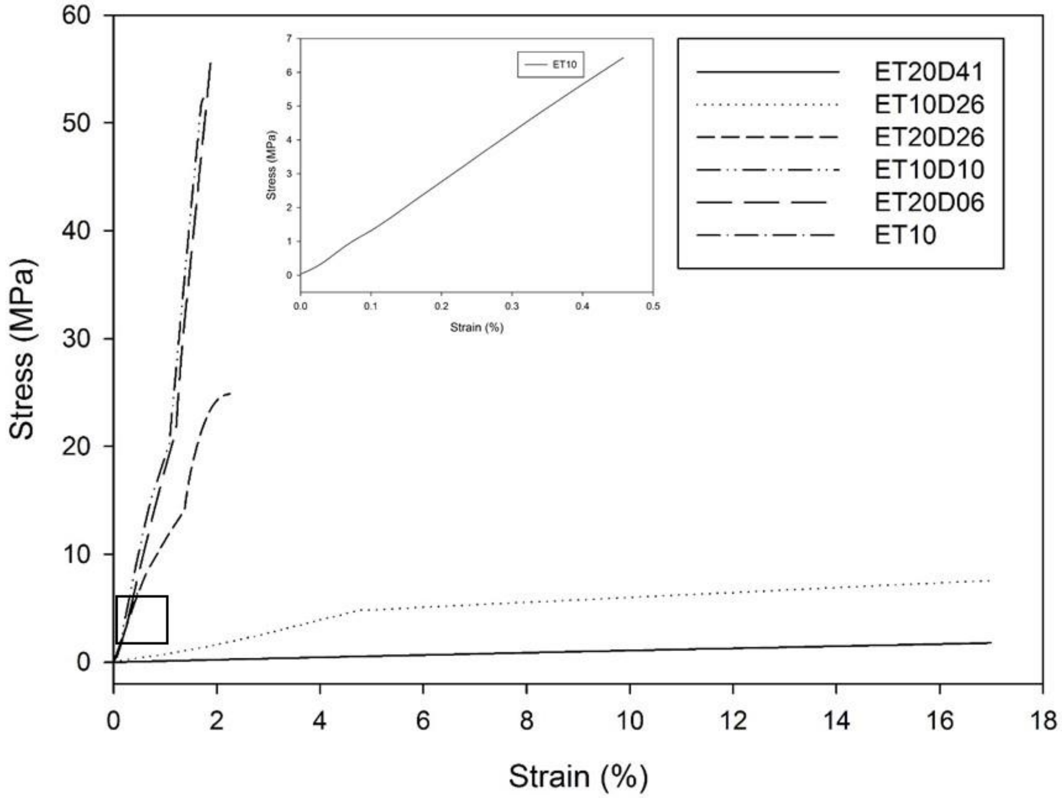

Figure 3.6. Stress-strain behaviour of ERL/DMS blends, inset showing stress-strain curve of ET10

Figure 3.7 shows elongation at break as a function of EDMS content, providing further evidence for toughness enhancement with addition of EDMS. Neat ERL is highly brittle, showing only 2.5 % elongation at break, whereas blend with 10 wt% of EDMS shows an elongation at break of 7.5 %, indicating the transformation of brittle to ductile material. At 41 wt% of EDMS, the blend exhibits rubber like behaviour with elongation at break exceeding 20 %. Thus incorporation of EDMS to ERL converts the brittle material to soft flexible material, which can be attributed to the flexible siloxane[33] units acting as oligomeric plasticizers.[16] The increase in ductility is accompanied by the loss in Young's modulus (table 3.2). It can be observed that the Young's modulus drops from 1.2 GPa to 0.012 GPa with increasing EDMS content (figure 3.8) but at optimal EDMS concentration (26 wt%) Young’s modulus is comparable with the commercial available epoxide photoresist SU8 (table 3.2). Decrease in modulus with increasing EDMS can be attributed to the low modulus (modulus≈ 3 MPa)[33] of flexible siloxane groups and the incompatibility of siloxane with epoxide at high EDMS content.

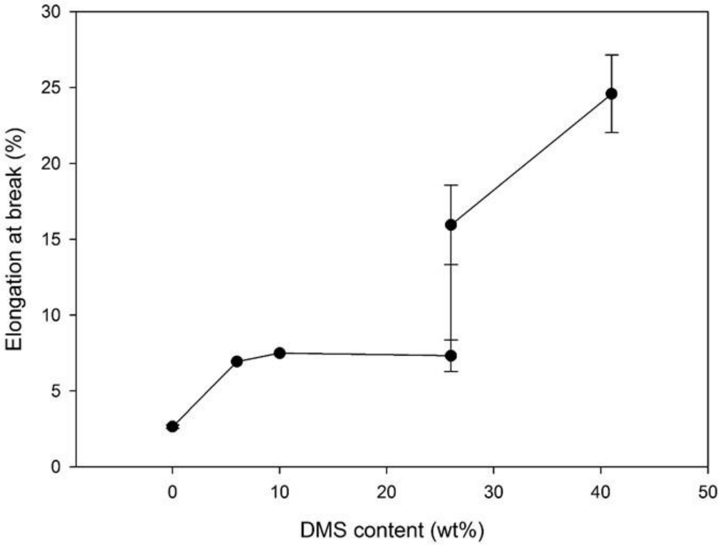

Figure 3.7. Elongation at break as a function of EDMS content (error bars obtained from standard deviation)

Table 3.2 Young's modulus and elongation at break of different ERL/EDMS blends compared with SU-8

Material code	Young's Modulus (GPa)	Elongation at break (%)
ET10	1.20± 0.07	2.65 ± 0.11
ET20D06	0.937	6.94
ET10D10	0.877	7.5
ET10D26	0.677±0.04	7.33 ± 1.04
ET20D26	0.669 ±0.05	15.95 ± 2.61
ET20D41	0.013 ±0.002	24.59 ± 2.55
SU-8[34]	0.700	24

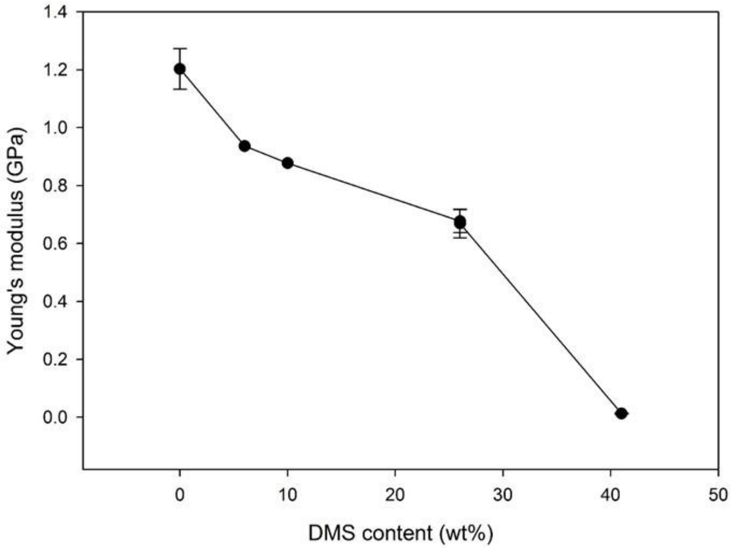

Figure 3.8. Young's modulus as a function of EDMS content (error bars obtained from standard deviation)

3.3.4.a. Morphology of the fractured samples

SEM micrographs of the fractured surfaces of neat epoxide, blend with 10, 26 and 41 wt% of EDMS are shown in figure 3.9a, 3.9b, 3.9c, 3.9d respectively. Neat epoxide shows clear and glassy surface representing the occurrence of brittle failure.[13] Under tensile load, brittle epoxide with an inability to absorb energy fails by rapid fracture. With the addition of 10 wt% of EDMS, the surface got rough with visible micro cracks. It is shown elsewhere, these cracks result from shear banding of the flexible siloxane units.[35] These flexible units absorb energy by undergoing shear deformation and provide path for the crack propagation. Because of the shear deformation of flexible siloxane units, the amount of energy required for fracture (toughness) of the blend increases. This argument is consistent with the increased toughness observed from the tensile properties

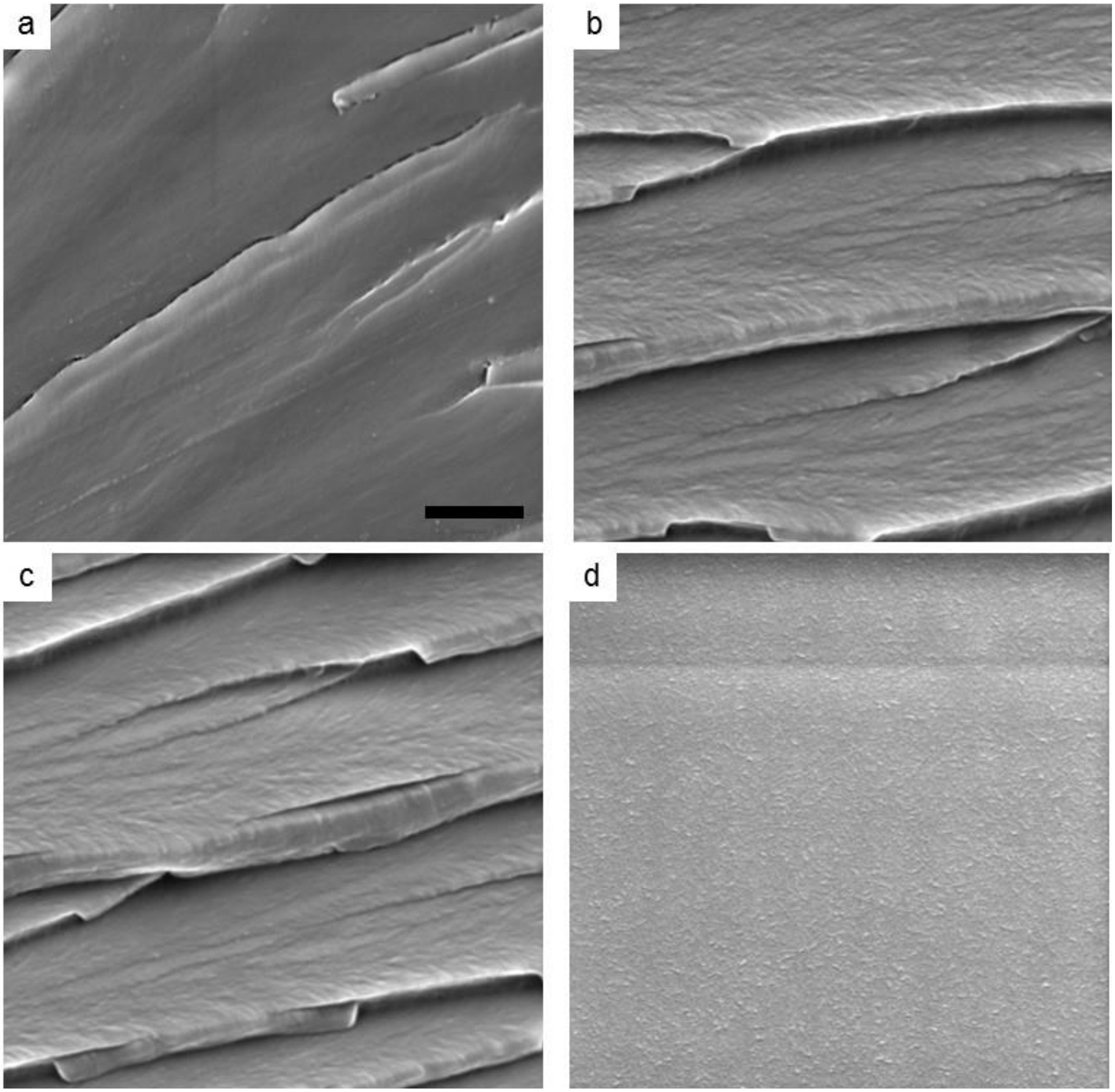

Figure 3.9. SEM of fractured surface of a) ET10 b) ET10D10 c) ET20D26 d) ET20D4. Scale bar of (a) = 5 µm, applies to all images

measurement. The fractured surface looks homogenous with no visible particles until 26 wt% of EDMS. When the EDMS content increased to 41 wt%, the surface shows the presence of micro particles dispersed in epoxide matrix, indicating the poor compatibility of EDMS with epoxide at high loading. This explains the rapid decrease in modulus of ET20D41.

3.3.5. Thermal properties

Thermal stability of the blends was measured using thermogravimetic analysis (TGA). To get the best properties from a blend it is necessary to make a homogenous blend prior to polymerization. Thermograms of different blends were superimposed in figure 3.10. The decomposition curves of all the blends show single decomposition temperature indicating that the components (ERL, EDMS and pTFH) got blended homogeneously without any macroscopic phase separation.[36] Thermal stability parameters such as initial decomposition temperature (temperature at 5% weight loss, IDT) and integral procedural decomposition temperature (IPDT) were studied. IDT of all compositions are shown in table 3.3. From the results, it can be observed that pTHF has a considerable effect on IDT, when its concentration increased from 10% to 20 %, IDT decreased from 304 ^{0}C to 279 ^{0}C. This is due to the fact, that the unreacted low molecular weight pTHF easily undergoes thermal decomposition/weight loss at relatively low temperature and so IDT decreases with increasing pTFH content.[37] Apart from pTHF, composition with 41% of EDMS shows a drastic decrease in IDT. This is because, terminal epoxide group in EDMS is less reactive compared[15] to the ring strained epoxide group in cycloaliphatic epoxide, resulting in reduced crosslink density of the blend and making it prone to thermal degradation at relatively lower temperature and so IDT decreases with increasing EDMS content.

Besides IDT, another reliable thermal stability parameter, IPDT, was also analysed using the method developed by Doyle.[38] IPDT provides quantitative measure of ultimate thermal stability of the material at high temperature. It encompasses all the procedural details such as size and shape of the sample, sample testing container, type of atmospheric gas and its flow rate and most importantly the rate of heating which are not included in IDT.[38] IPDT is determined by integration of thermal decomposition curve (thermogram) using the expression given by Doyle's work.

$$IPDT = T_i + (T_f - T_i) * A * K$$

$$A = (S_1 + S_2) / (S_1 + S_2 + S_3)$$

$$K = (S_1 + S_2) / (S_1)$$

where A is the area ratio of total experimental curve defined by the thermogram of the material. T_i and T_f are the initial and final temperature respectively. Thus the integration of thermogram sums up all the procedural details. IPDT and other individual parameters are given in table 3.4. From IPDT results, it is evident that increasing siloxane content, increases overall thermal stability of the polymer at high temperature. This can be attributed to the thermally stable siloxane bond and also the decomposition product of siloxane (silicone dioxide, SiO_2), which cannot be decomposed further, leading to high char yield,[39] resulting in increased IPDT. But this effect is felt till 26% of EDMS, any further increase has no significant effect on IPDT. Thus, addition of EDMS enhances the overall thermal stability of the blends.

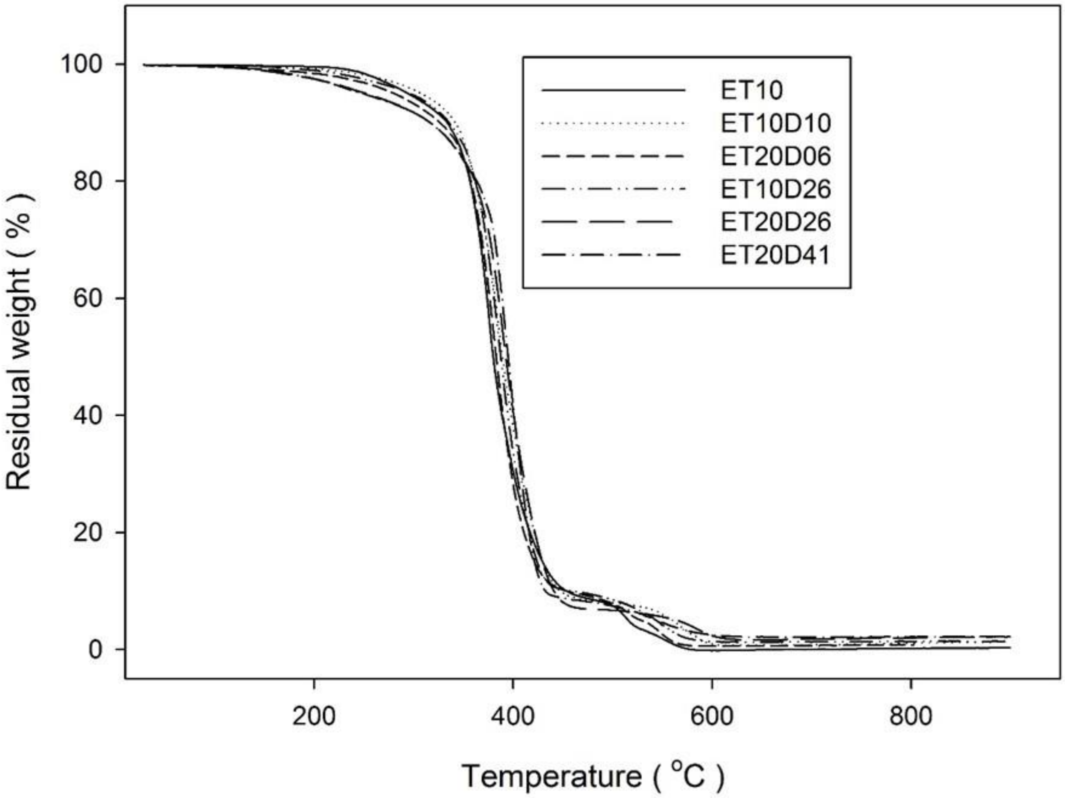

Figure 3.10. TGA thermogram of ERL/EDMS/pTHF blends

Table 3.3 IDT for different ERL/EDMS/pTHF blends

Material Code	ERL(Wt %)	EDMS (Wt %)	pTHF (Wt %)	IDT (°C)
ET10D10	76	10	10	304
ET10D26	60	26	10	296
ET10	86	0	10	295
ET20D06	70	6	20	279
ET20D26	50	26	20	248
ET20D41	35	41	20	243

Table 3.4 IPDT and other thermal stability parameters for different ERL/EDMS/pTHF blends

Material Code	ERL(Wt %)	EDMS (Wt %)	pTHF (Wt %)	A*	K*	$A^* K^*$	IPDT (°C)
ET20D41	35	41	20	0.4402	1.0536	0.4638	432.3
ET20D26	50	26	20	0.43909	1.05265	0.4622	431.6
ET10D26	60	26	10	0.4359	1.0327	0.4502	420.6
ET10D10	76	10	10	0.4339	1.0322	0.4479	418.5
ET20D06	70	6	20	0.4237	1.03193	0.4372	408.9
ET101809	86	0	10	0.4156	1.0072	0.4186	393

3.3.5.a. Effect of siloxane on glass transition temperature (T_g)

T_g was measured from the peak of the tan delta curves (which is the ratio of loss modulus to storage modulus). Results are presented in table 3.5. It can be seen that T_g decreases with increasing EDMS content (figure 3.11). This trend can be explained based on the dependence of glass transition temperature on chain flexibility and crosslink density.[40] Incorporation of flexible siloxane units increases the segmental motion of the chains leading to corresponding decrease in T_g. With the addition of 10 wt% of EDMS, T_g reduces by 30 ^{0}C compare to neat epoxide, still this value is on par with other epoxide systems.[34] Upon increasing the siloxane content to 26 wt% Tg reduces further, due to the increased volume fraction of flexible siloxane units in the blend. At 41 wt% of EDMS, Tg reduces below room temperature, which can be attributed to both the chain flexibility of siloxane and the low reactivity of terminal epoxide groups present in EDMS. Because of low reactivity, the crosslink density of the blend reduces at higher loading of EDMS. This argument is consistent with the observed mechanical properties of the blend.

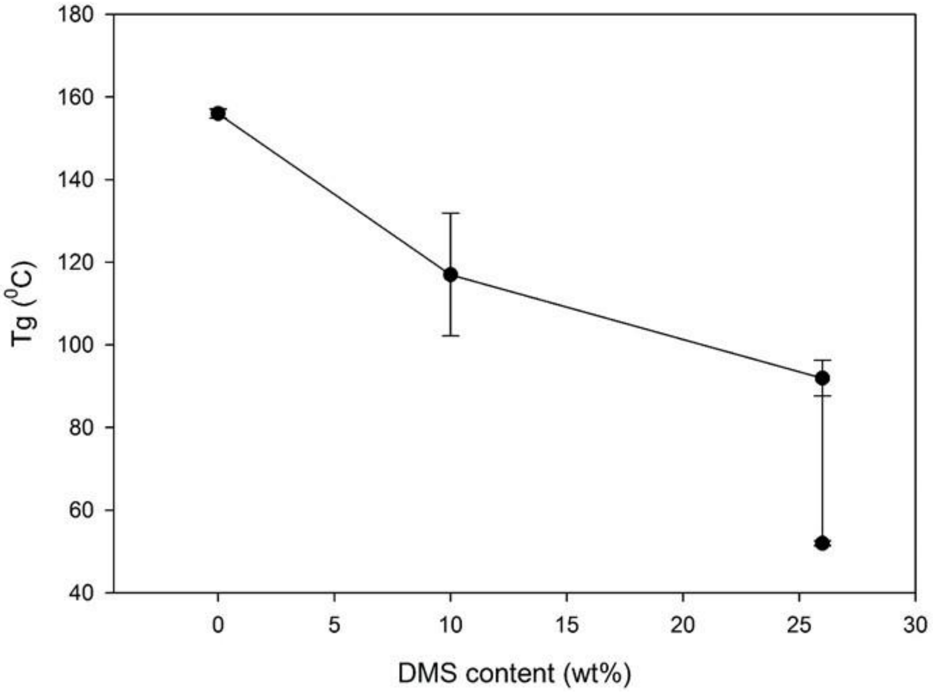

Figure 3.11. Glass transition as a function of EDMS content (error bars obtained from standard deviation)

Table 3.5 Glass transition temperature of different ERL/EDMS blends

Material code	T_g (^{0}C)
ET10	156 ± 1.15
ET10D10	117 ± 14.8
ET10D26	92 ± 4.30
ET20D26	52 ± 0.550

3.4. Summary and outlook

Our results show that the addition of EDMS increases toughness of biscycloalipatic epoxide without deteriorating the mechanical, thermal and optical properties of blends. Addition of 10 wt % of EDMS results in an elastic modulus of 0.9 GPa with an elongation at break of 7.5 % indicating the improvement in toughness with good mechanical strength. Also at 10 wt % of EDMS, thermal properties such as glass transition temperature (117 ^{0}C), IDT (304 ^{0}C) and IPDT (418.5 ^{0}C) are comparable with other epoxide systems.[34] At higher loading (41 wt %) of EDMS, the blend becomes highly flexible (0.012 GPa elastic modulus with 24.5 % elongation at break), due to the increased volume fraction of flexible siloxane units and reduced crosslink density. Of the difference ratios of ERL/EDMS/pTFH blends tested, the blend with 76, 10 and 10 wt % of ERL, EDMS, pTHF respectively shows the best mechanical and thermal properties. And these blends elicit MI of optical field, which was used as an efficient single step, room temperature, spontaneous process for fabricating thermomechanically stable polymer waveguides.

References

(1) Campo, A. del; Greiner, C. *J. Micromechanics Microengineering* **2007**, *17* (6), R81–R95.

(2) Paul, K. E.; Prentiss, M.; Whitesides, G. M. *Adv. Funct. Mater.* **2003**, *13* (4), 259–263.

(3) Ray, T.; Zhu, H.; Meldrum, D. R. *J. Micromechanics Microengineering* **2010**, *20* (9), 097002.

(4) Ynsa, M. D.; Shao, P.; Kulkarni, S. R.; Liu, N. N.; Van Kan, J. A. *Nucl. Instruments Methods Phys. Res. Sect. B Beam Interact. with Mater. Atoms* **2011**, *269* (20), 2409–2412.

(5) Lee, C. H.; Jiang, K. *J. Micromechanics Microengineering* **2008**, *18* (5), 055032.

(6) Mohan, P. *Polym. Plast. Technol. Eng.* **2013**, *52* (October), 107–125.

(7) Garima Tripathi, D. S. *Jounral App* **2009**, *114*, 2769–2776.

(8) Iijima, T.; Fujimoto, K. I.; Tomoi, M. *J. Appl. Polym. Sci.* **2002**, *84* (2), 388–399.

(9) Choi, K. M.; Rogers, J. A. *J. Am. Chem. Soc.* **2003**, *125* (14), 4060–4061.

(10) Kim, K. S.; Zhao, Y.; Jang, H.; Lee, S. Y.; Kim, J. M.; Ahn, J.-H.; Kim, P.; Choi, J.-Y.; Hong, B. H. *Nature* **2009**, *457* (7230), 706–710.

(11) Oh, Y. J.; Park, S. G.; Kang, M. H.; Choi, J. H.; Nam, Y.; Jeong, K. H. *Small* **2011**, *7* (2), 184–188.

(12) Sun, Y.; Rogers, J. A. *Adv. Mater.* **2007**, *19* (15), 1897–1916.

(13) Ma, S.; Liu, W.; Gao, N.; Yan, Z.; Zhao, Y. *Macromol. Res.* **2011**, *19* (9), 972–979.

(14) Hou, S. S.; Chung, Y. P.; Chan, C. K.; Kuo, P. L. *Polymer (Guildf).* **2000**, *41* (9), 3263–3272.

(15) Ma, S.; Liu, W.; Li, H.; Tang, C.; Wei, Z. *J. Macromol. Sci. Part B* **2011**, *50* (5), 975–987.

(16) Shih, W. C.; Ma, C. C. M.; Yang, J. C.; Chen, H. De. *J. Appl. Polym. Sci.*

1999, *73* (13), 2739–2747.

(17) Chen, J.; Kinloch, A. J.; Sprenger, S.; Taylor, A. C. *Polym. (United Kingdom)* **2013**, *54* (16), 4276–4289.

(18) Lin, S.; Huang, S. K. *J. Polym. Sci. Part A Polym. Chem.* **1996**, *34*, 1907–1922.

(19) Ochi, M.; Takemiya, K.; Kiyohara, O.; Nakanishi, T. *Polymer (Guildf).* **2000**, *41* (1), 195–201.

(20) Gonzalez, M.; Kadlec, P.; Štěpánek, P.; Strachota, A.; Matějka, L. *Polymer (Guildf).* **2004**, *45* (16), 5533–5541.

(21) Basker, D. K.; Brook, M. A.; Saravanamuttu, K. *J. Phys. Chem. C* **2015**, *119* (35), 20606–20617.

(22) Burgess, I. B.; Shimmell, W. E.; Saravanamuttu, K. *J. Am. Chem. Soc.* **2007**, *129* (15), 4738–4746.

(23) Kasala, K.; Saravanamuttu, K. *J. Mater. Chem.* **2012**, *22*, 12281.

(24) Kasala, K.; Saravanamuttu, K. *Langmuir* **2013**, *29* (4), 1221–1227.

(25) Ponte, M. R.; Welch, R.; Saravanamuttu, K. *Opt. Express* **2013**, *21* (4), 4205–4214.

(26) Burgess, I. B.; Ponte, M. R.; Saravanamuttu, K. *J. Mater. Chem.* **2008**, *18* (35), 4133.

(27) Crivello, J. V. *J. Polym. Sci. Part A Polym. Chem.* **2009**, *47*, 866–875.

(28) Crivello, J. V.; Acosta Ortiz, R. *J. Polym. Sci. Part A Polym. Chem.* **2002**, *40* (14), 2298–2309.

(29) J. Kijeski , J. Ruszczyski, I. K. and M. G. *React. Kinet. Catal. Lett.*, **1993**, *49* (2), 287–291.

(30) Tasdelen, M. A.; Moszner, N.; Yagci, Y. *Polym. Bull.* **2009**, *63* (2), 173–183.

(31) James V. Crivello, S. L. *J. Polym. Sci. Part A Polym. Chem.* **2000**, *38* (12), 389–401.

(32) Guo, Q.; Zheng, H.; Zheng, S. *J. Mater. Sci.* **1999**, *34*, 123–128.

(33) Seghir, R.; Arscott, S. *J. Polym. Sci. Part B Polym. Phys.* **2015**, *53* (18), 1281–1291.

(34) Feng, R.; Farris, R. J. *J. Micromechanics Microengineering* **2002**, *13* (1), 80–88.

(35) Pearson, R. A.; Yee, A. F. *Polymer (Guildf).* **1993**, *34* (17), 3658–3670.

(36) Kwak, G. H.; Park, S. J.; Lee, J. R. *J. Appl. Polym. Sci.* **2000**, *78* (2), 290–297.

(37) Soo-Jin Park, Hyun-Chel Kim, H. and D.-H. S. *Macromolecules* **2001**, *34* (22), 1–3.

(38) Doyle, C. D. *Anal. Chem.* **1961**, *33* (1), 77–79.

(39) Chiang, C. L.; Chang, R. C.; Chiu, Y. C. *Thermochim. Acta* **2007**, *453* (2), 97–104.

(40) Elrehim, M. A.; Voit, B.; Bruchmann, B.; Eichhorn, K. J.; Grundke, K.; Bellmann, C. *J. Polym. Sci. Part A Polym. Chem.* **2005**, *43* (15), 3376–3393.

Supplementary information

Glass transition temperatures (Tg) of epoxide/siloxane blends were measured using dynamic mechanical analyzer (DMA). Oscillating shear force applied by DMA provides the viscous component (loss modulus) as well as the elastic component (storage modulus). Ratio of loss modulus to elastic modulus gives the damping factor or tan delta. At and above glass transition temperature, viscous behaviour (loss modulus) dominates the elastic behaviour (elastic modulus). Thus, the peak in the plot of damping factor or tan delta as a function of temperature provides the glass transition temperature of a polymer. Tg of the blends were extracted from the data shown in Figure S1.

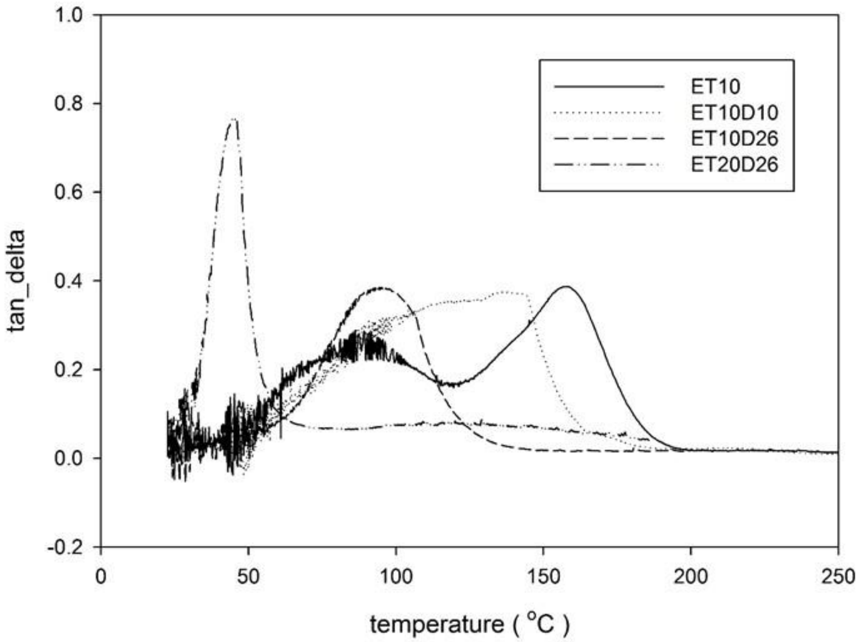

Figure S3.1 Tan delta as a function of temperature for various epoxide/siloxane blends.

Chapter 4

Modulation instability of incoherent beam in epoxide systems with *in-situ* metal nanoparticles synthesis: a new route to metallodielectric waveguides structures

Abstract

Our approach combines the modulation instability (MI) and spontaneous pattern formation of broad incoherent beam in photopolymerizable media with *in-situ* metal nanoparticles generation for fabricating metallodielectric waveguide structures. Metal nanoparticles (Ag & Au) embedded waveguide structures are generated in a photopolymerizable medium comprising cycloaliphatic and poly dimethylsiloxane- terminated epoxide monomers and poly(tetrahydrofuran); the system is sensitized to visible light with camphorquinone, which upon irradiation with LED (460 nm) light initiates epoxide polymerization in presence of diaryliodonium salt and simultaneously reduces silver hexafluroantimonate and gold(III) tetrachloride to silver and gold nanoparticles respectively. The uniform beam of incoherent LED (460 nm) suffers modulation instability and spontaneously divides into multiple self-trapped filaments as it propagates through a photopolymerisable cycloaliphatic epoxide system. Refractive index changes due to polymerisation render the optical field unstable, triggering its division into a large population of stable, self-trapped filaments of light, which propagated through the medium without diverging. Because polymerization is irreversible, the self-trapped optical fields permanently inscribe optical waveguide structures with metal nanoparticles in the medium. Through this approach, we show that it is possible to generate metal nanoparticles-rich epoxide waveguides, which exhibit plasmon resonance and to the best of our knowledge would be impossible to generate with conventional lithographic techniques.

4.1. Introduction

Surface plasmon resonance (SPR) of metal nanoparticles has enabled a wide variety of applications.[1,2] The resonance, due to the collective oscillation of conduction band electrons on the surface of metal nanoparticles and nanostructures provides huge enhancement of the exciting electromagnetic field.[3] This exorbitant increase of electromagnetic field fuels the enormous amount of research carried out with metal nanoparticles in a range of emerging applications such as nanophotonic,[4–6] biological and chemical sensing,[7–9] biomedicine, [10–13] and surface enhanced Raman spectroscopy.[14–16] To realize the extraordinary properties of metal nanoparticles in optical devices and technologies, it is essential to generate stable homogenous dispersion of metal nanoparticles in soft dielectric materials. Efforts have been made to incorporate metal nanoparticles in polymers[17–22] which can be processed into functional devices used in optical sensors,[23] spectroscopy[24] and optoelectronics.[25] Particularly, metal nanoparticles embedding in optical waveguide configuration is gaining attention in surface plasmon resonance (SPR) sensors.[26–31] The core of SPR sensors is the extreme sensitivity of surface plasmons (propagating in the metal-dielectric interface) to the change in refractive index. These sensors are illuminated in Kretschmann–Raether prism geometry,[32] which provides the phase matching condition between the plasmonic wave at the metal-analyte interface and the incident electromagnetic wave at a particular angle of incidence and wavelength. Replacing the prism configuration by an optical waveguide configuration offers a high degree of integration, miniaturization and remote sensing capabilities.[33,34] Motivated by these possibilities, there have been considerable efforts to incorporate plamonic particles in optical waveguide structures.[35–37] In spite of the considerable progress, it is still challenging to make polymer optical waveguide structures with metal nanoparticles.

Previously we have shown the formation of optical waveguides in a silver nanoparticles doped organosiloxane polymer medium using self-trapping of laser light[38] and modulation instability[39] of incoherent white light. The organosiloxane based polymer does not exhibit the required stability and also the particles are formed before the photopolymerization, which limits the control of spatial distribution of nanoparticles in the waveguide structure. Recently, we demonstrated MI in cationic polymerizable epoxide systems.[40] In this work, we are showing the fabrication of three dimensional polymer optical waveguide microstructures embedded with metal nanoparticles in robust cycloaliphatic epoxide by combining *in-situ* generation of metal nanoparticles with nonlinear propagation of electromagnetic field. Our work shows a potential route for spontaneously generating large populations of robust cylindrical metal nanoparticles embedded waveguide structures in epoxide system.

4.2. Experimental

4.2.1. Materials

3,4-epoxycyclohexylmethyl-3',4'-epoxycyclohexane carboxylate (ERL) (**1**), poly (1,4-butanediol (M_n 250)) (pTHF) (**2**), silver hexafluroantimonate, gold (III) tetrachloride, camphorquinone (**3**) (97% purity) were purchased from Sigma Aldrich (Oakville, ON). Epoxypropoxypropyl terminated polydimethylsiloxane (DMS) (**4**) was purchased from Gelest Inc. Bis(4-t-butyl)iodonium hexafluroantimonate (5) was obtained from Hampford research Inc.. Camphorquinone is used as photosensitizer (PS) which has an absorption band at 468 nm and Bis(4-t-butyl)iodonium hexafluroantimonate used as photoinitiator (PI). All reagents were used without further purification.

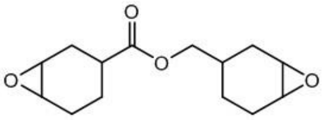

1

2

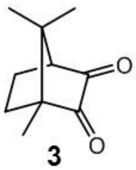

3

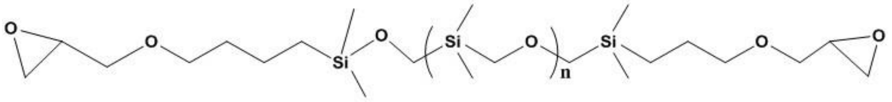

4

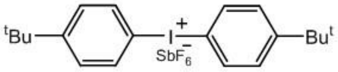

5

4.2.2. Sols containing metal salts for *in-situ* photolytic generation of metal nanoparticles

The sol for Ag nanoparticle *in-situ* synthesis was made by mixing pTHF, PS and $AgSbF_6$ and a homogenous dispersion of these 3 components was obtained by constant stirring for 30 min, after which 60 wt% of ERL and 10 wt%

of DMS were added, the entire sol was left under constant stirring for 4 hours. Different compositions are listed in table 4.1.

Table 4.1 Compositions of silver nanoparticles-epoxide systems, named according to the amount of $AgSbF_6$, all the compositions contained 60 wt% of ERL, 10 wt% of DMS and 0.5 wt % of camphorquinone.

Sol	pTFH (wt %)	$AgSbF_6$ (wt %)
EAg-0.05	29.45	0.05
EAg-0.1	29.40	0.1
EAg-0.2	29.30	0.2

The sol with gold salt was prepared in two parts, first $HAuCl_4$ was mixed with pTHF (pTHF facilitates the solubility of the gold salt) and the gold salt with pTHF was then mixed with solution containing 75 wt% of ERL, 10 wt% of DMS and 2 wt% of camphorquinone and 2 wt% of iodonium salt (all weight percent are with respect to the total weight of the sol). Different compositions prepared by varying $HAuCl_4$ and pTFH are listed in table 4.2. Sol preparation was done under minimal exposure to ambient light as it is sensitive to visible light (400-700 nm).

Table 4.2 Compositions of gold nanoparticles-epoxide systems, named according to the amount of $HAuCl_4$, all the compositions contained 75 wt% of ERL, 10 wt% of DMS and 2 wt% of camphorquinone and 2 wt% of iodonium salt

Sol	pTFH (wt %)	$HAuCl_4$ (wt %)
EAu-0.1	10.9	0.1
EAu-1	10	1.0
EAu-2	9	2.0

4.2.3. Optical assembly

The optical assembly employed for modulation instability experiments shown in figure 4.1 is adopted from previous work.[40] The optical components used were mounted in a rail with carrier, which was movable with a resolution of 1 mm. The optical and mechanical components used in the experiment were purchased from Newport Corporation, CA, USA. The incoherent, blue LED (supplied by Kerber Applied Research Inc) was collimated by a planoconvex lens (F.L = 100 mm, d=25.4 mm) and launched onto the entrance face of the sample cell (path length = 10 mm, transparency = 320 nm- 800 nm) containing the sol. The beam intensity profile in the exit face of the sample cell was monitored by focusing the output beam through a pair of plano-convex lenses (F.L. =250 mm, d=25.4mm) onto a high-resolution, progressive scan, charged-coupled device (CCD) chip (D, 1360 (H) x 1024 (V) of 4.65 μm square pixels, sensitivity range = 350 nm to 1150 nm; WinCamD^{TM} digital camera, Data Ray Inc., USA).

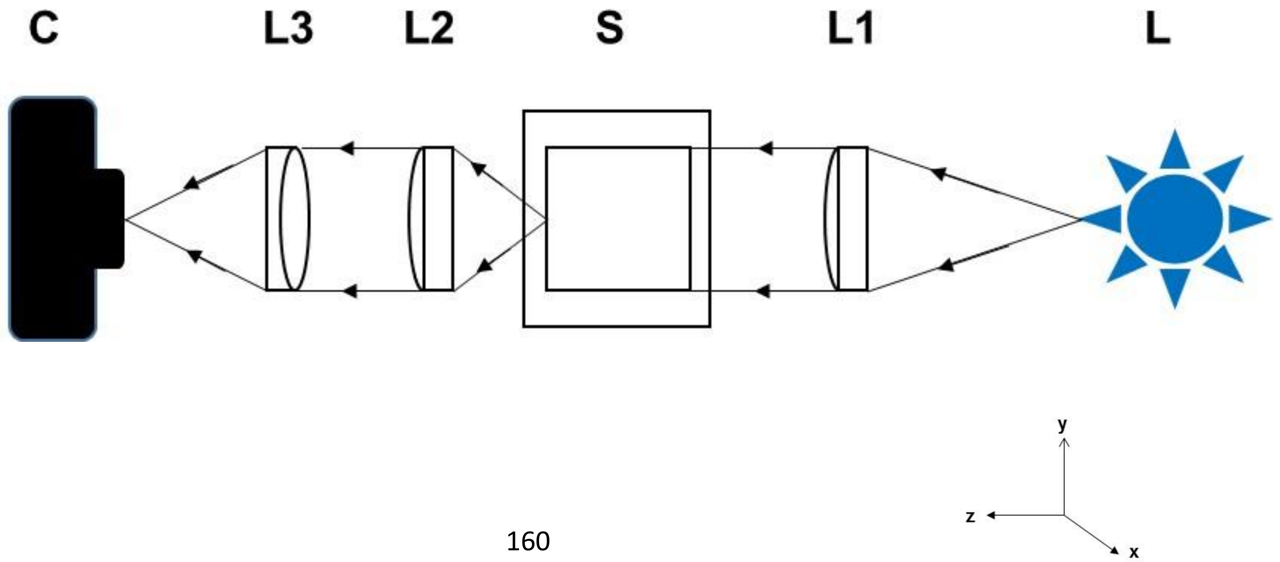

Figure 4.1. Optical assembly for the MI induced waveguide formation experiment, light from the blue LED lamp (L) is collimated by a plano convex lens (L1) and focused onto the entrance face of the sample cell (S), which is mounted on a micrometer controlled linear stage and rail carrier. The output beam intensity profile is monitered through a pair of plano convex lens (L1 and L2) onto the CCD chip camera (C).

4.2.4. *In situ* generation of metal nanoparticles during MI

MI induced waveguides with silver and gold nanoparticles were fabricated with an optical power corresponding to 468 nm wavelength of 20 and 40 mW respectively. Preliminary MI experiments with both the systems were conducted using white light. Power was measured at the entrance face of the sample cell using a power meter. The change in the beam intensity profile at the exit face of the 10 mm sample cell during the course of polymerization was monitored and recorded simultaneously through the CCD chip camera.

4.2.5. Characterization of metal nanoparticles embedded waveguide structures

Waveguides with metal nanoparticles were studied using an Olympus BX51 optical microscope fitted with a Q-Imaging Retiga EXi digital camera and Image pro^{TM} software. The images were taken in transmission mode with 5x objective. Metal nanoparticles were characterized using the JEOL 2010F field emission transmission electron microscopy equipped with EDS X-ray spectrometer. Samples for the TEM was prepared using ultramicrotome, where the samples were sliced to about 70 nm. UV-Vis absorbance spectrometry was carried out with Cary 5000 UV-Vis-NIR Spectrophotometer.

4.3. Results and discussion

4.3.1. Photoinduced *in-situ* synthesis of silver-epoxide nanocomposite

The epoxide photopolymerization system with *in-situ* metal nanoparticle synthesis was developed by Yagci *et al*[41–43] based on the principle that photoexcited ketones can be oxidized by onium slats, silver salts with non-nucleophilic counteranions and gold precursor ($HAuCl_4$). Our system with *in-situ* synthesis of silver nanoparticles was adopted from one of their works where it was shown that camphorquinone in conjugation with silver hexafluorantimoate ($AgSbF_6$) can be used for visible light induced electron transfer to generate silver nanoparticles and to initiate cationic polymerization simultaneously. We combined the *in-situ* synthesis approach developed by Yagci with MI for fabricating silver nanoparticles embedded waveguide structures. Visible light polymerizable systems capable of *in-situ* silver nanoparticles synthesis were prepared by dispersing silver salt into the monomer mixture in the range between 0.2 to 0.05 wt% (as shown in table 4.1), keeping the proportion of camphorquinone and monomers constant. The systems with 0.2 and 0.1 wt% of silver salt polymerized without light exposure. This might be due to the reduction of silver salt by the polyether groups present in EDMS[44,45] (one of the monomers in the system). The reduction reaction results in the formation of Bronsted acid initiator species and elemental silver nanoparticles, as the silver salt acts as both initiator as well as silver nanoparticles precursor.[43] These initiator species initiate the ring opening polymerization of the epoxide groups, resulting in gelation of the sol in non-photolytic way. This was confirmed by observing the system made without EDMS (other components were kept constant). Because of this non-photolytic reduction of silver salt by EDMS, significantly lesser amount (0.05 wt %) of the silver salt used in the system to make a stable sol. Photolytic *in-situ* synthesis of silver nanoparticle and simultaneous ring opening polymerization of epoxide groups was studied by irradiating the sol uniformly with white light (24 W fluorescent light). Initially yellow coloured sol turned brown after 10 min of irradiation. Camphorquinone upon irradiation with white light, in presence of non-basic hydrogen donor (polybutanediol) undergoes Norrish type II reaction to generate reactive radicals. $AgSbF_6$ oxidizes these radicals to form Bronsted acid and silver nanoparticles simultaneously. The acid initiates the cationic polymerization of biscycloaliphatic epoxide. The overall process is shown in Scheme 4.1. Formation of silver nanoparticles was confirmed by UV-Vis spectrum, which showed the typical surface plasmon resonance band of silver nanoparticles (figure 4.2a). In addition to the biscycloaliphatic epoxide, 10 wt % of siloxane terminated epoxide was added to the formulation to improve the toughness of the waveguide structures.[46]

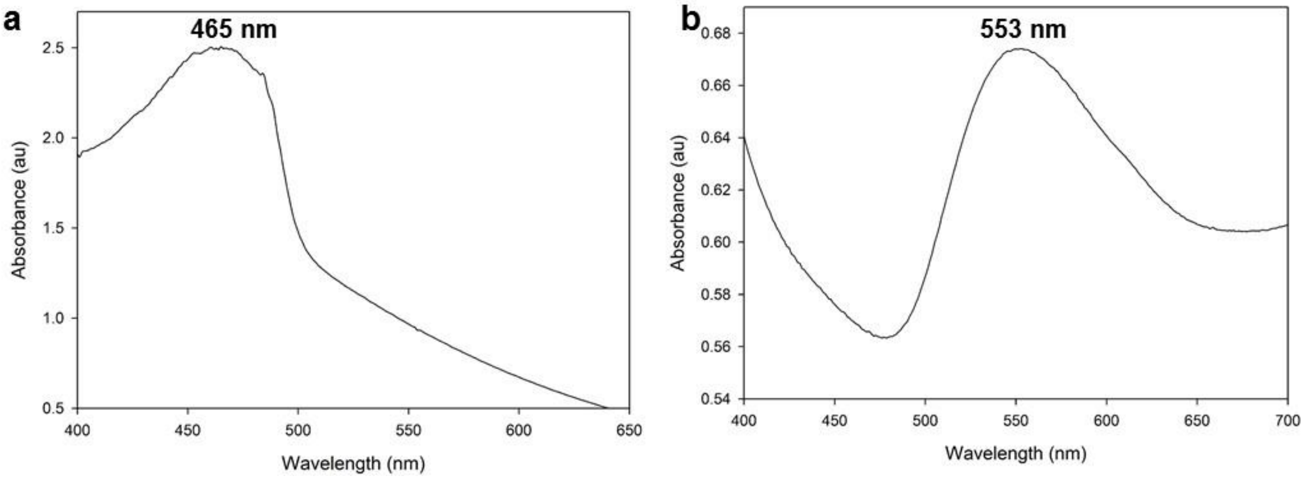

Figure 4.2 UV-Vis spectrum of (a) Ag nanoparticles in epoxide system (b) Au nanoparticles in epoxide system

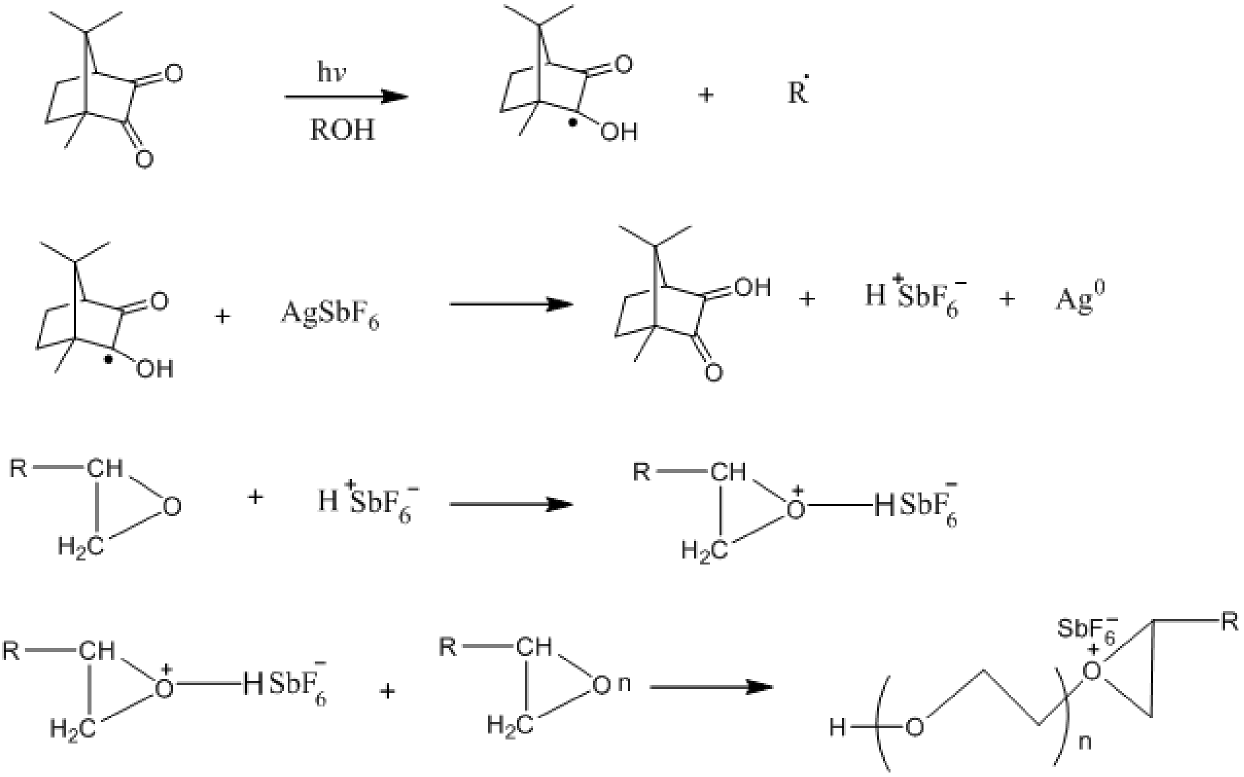

Scheme 4.1 In-situ synthesis of silver nanoparticles and simultaneous polymerization of epoxide groups[41]

4.3.2. Photoinduced *in-situ* synthesis of gold-epoxide nanocomposite

Similar approach was employed for developing visible light polymerizable systems with *in-situ* gold nanoparticles synthesis. However, the *in-situ* synthesis of gold nanoparticles and polymerization initiating species were generated by oxidizing the photogenerated free radicals by two different oxidizing agents instead of one, used in the silver nanoparticles system. This is because, unlike $AgSbF_6$, $HAuCl_4$ (gold nanoparticles precursor) does not carry non-nucleophilic counteranion to enable cationic chain propagation. So, in addition to $HAuCl_4$ and visible light sensitizer (camphorquinone), a photoacid generator (bis(4-t-butyl)iodonium hexafluroantimonate) was used in the formulation. Thus the gold nanoparticles *in-situ* synthesis and photopolymerization were achieved through two different photochemical routes, which is significantly different from the silver nanoparticles system. As the polymerization and gold nanoparticles generation were simultaneously achieved through two different photochemical routes, the concentration of $HAuCl_4$ added in these systems was an order of magnitude higher than the silver system. Systems capable of *in-situ* gold nanoparticles synthesis and polymerization by visible light irradiation were developed by dispersing $HAuCl_4$ salt into the monomer mixture in the range between 2 to 0.1 wt % (as shown in table 4.2), keeping the camphorquinone and PI concentration constant. Because of the separation of gold nanoparticles synthesis and polymerization routes, even at 2 wt % of gold salt, stable sol without gelation was obtained. This is significantly different from silver nanoparticles systems, where the maximum silver salt concentration for a stable sol was 0.05 wt %. Also in these systems, the reduction of $HAuCl_4$ by EDMS was not significant, which was visually observed (the sols remind yellow until photoirradiation). This may be due to the lower reduction potential of $HAuCl_4$ compare to $AgSbF_6$.[43] Photogeneration of gold nanoparticles and simultaneous ring-opening polymerization of epoxide groups were studied by uniformly irradiating the system using white light (24 W fluorescent lamp). Photogenerated camphorquinone radicals were oxidized by $HAuCl_4$ to form gold nanoparticles. At the same time, a portion of camphorquinone derived radicals are oxidized by bis(4-t-butyl)iodonium hexafluroantimonate to the corresponding carbocations, which initiate the cationic polymerization of epoxide. The gold nanoparticles and the initiating cations are formed by different oxidants but both the processes occur simultaneously. *In-situ* synthesis and the polymerization process is shown in Scheme 4.2. All three systems polymerized within 2 minutes following the irradiation and the *in-situ* synthesis of gold nanoparticles was evident from the gradual change of color from yellow to purple. And the UV-Vis absorption spectrum confirmed the presence of gold nanoparticles by showing the maximum absorbance at 553 nm, which is the typical surface plasmon absorption band for gold nanoparticles. The system with 2 wt % of $HAuCl_4$ turned dark purple after irradiation. This may hinder the MI process and so for the MI experiment system with 1 wt % of $HAuCl_4$ was used.

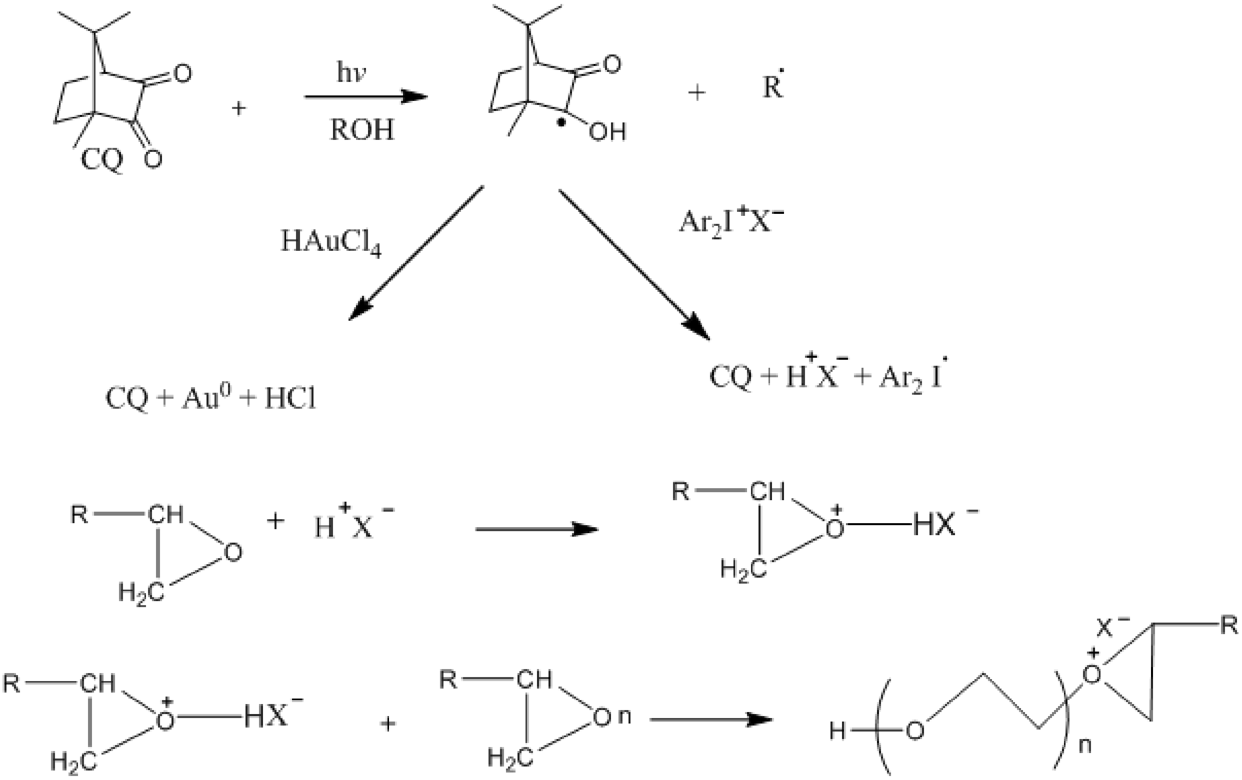

Scheme 4.2 In-situ synthesis of gold nanoparticles and simultaneous polymerization of epoxide groups[42]

4.3.3. MI induced cylindrical waveguides doped with metal nanoparticles

The origin of MI and subsequent filamentation in photopolymeriable media is due to the nonlinear intensity dependent refractive index change along the polymerization front, causing the small amplitude and phase perturbations or noise, arising on top of the uniform wavefront to grow rapidly.[47] Consequently, the uniform broad beam disintegrates into individual filaments, which in turn splits into narrow self-trapped beamlets. During this process, the self-trapped beamlets inscribe a permanent cylindrical structure along its path and as the polymer system undergoes *in-situ* generation of metal nanoparticles, cylindrical waveguides doped with metal nanoparticles are formed. This process is schematically depicted in figure 4.3.

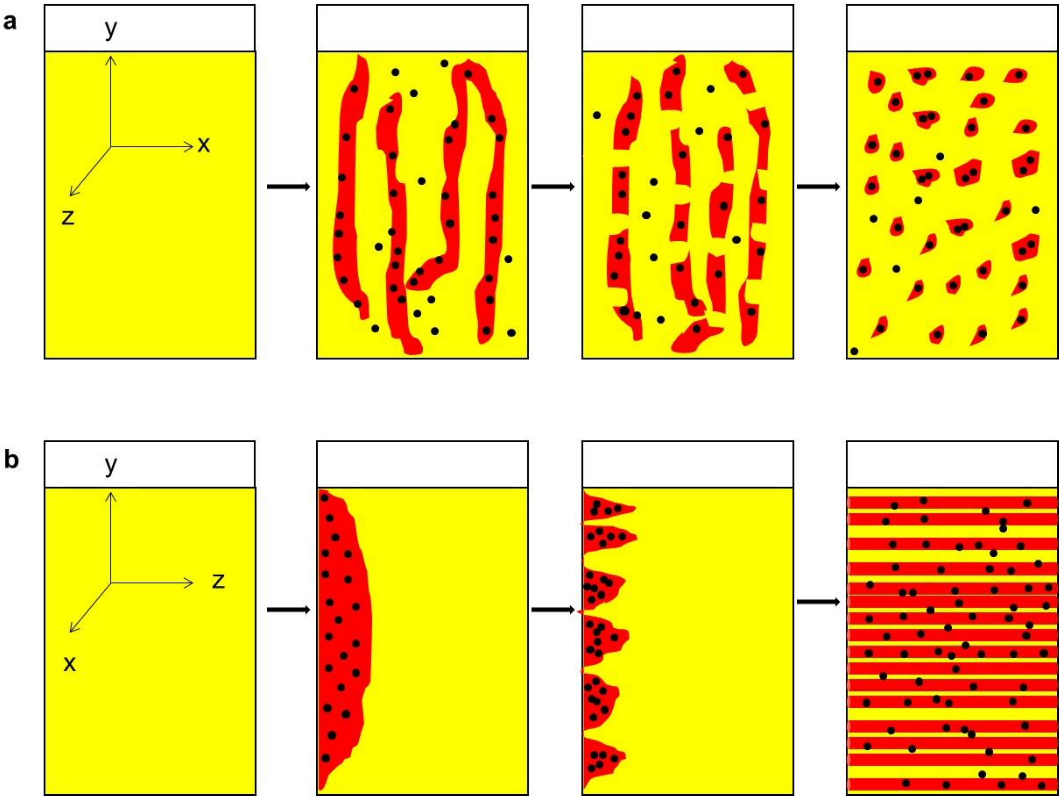

Figure 4.3. Scheme showing temporal evolution of modulation instability induced waveguide formation with simultaneous *in-situ* metal nanoparticles synthesis. (a) transverse and (b) longitudinal view with respect to the beam propagation axis z. Yellow = monomer fluid; Red polymerized region ; Black dots = metal nanoparticles.

The formation of waveguide structure in the photoresponsive medium can be explained from the principles of MI. MI occurs under the similar conditions for self-trapping of light beam in nonlinear medium. Non-linear Schrodinger equation describes the self-trapping of a Gaussian beam,

$$2ikn_o(\partial \Psi / \partial z) + \nabla^2_{\perp} \Psi + k^2 (n^2 - n_o^2) \Psi = 0 \qquad (1)$$

where the electric field $E = \Psi e^{ikn_o z}$ and $k = 2\pi / \lambda$, self-trapping arises from the competition between the natural divergence of the beam ($\nabla^2_{\perp} = (\partial^2/\partial x^2 + \partial^2/\partial y^2)$) and the polymerization induced refractive index change ($n - n_o$) along the beam propagation path (z).[48] Under the nonlinear conditions, negligible amplitude and phase perturbations get amplified due to the reciprocal interplay between refractive index change and natural diffraction as described in eqn(1).[49–55] This leads to the instability of the beam, resulting in splitting of uniform beam to individual self-trapped filaments allowing each beamlet to travel as a localised wave packet within the filaments. These self-trapped filaments are permanently imprinted in the medium, as they originate from an irreversible polymerization induced refractive index change.

4.3.4. MI induced waveguide in silver nanoparticles-epoxide system

We elicited MI in silver nanoparticles-epoxide system with a monochromatic, spatially and temporally incoherent blue LED (λ_{max} = 460nm). In a typical experiment, collimated broad beam from the LED was launched onto the entrance face of the 10 mm plastic cuvette containing the photopolymerizable epoxide. Temporal changes to the spatial intensity profile of the beam at the exit face of the cuvette was monitored using a CCD camera. Figure 4.4 shows the MI of LED beam in epoxide medium with silver nanoparticles. At t= 0 s (figure 4.4a) in the absence of polymerization, the beam looks uniform at the exit face. At this time, under linear conditions, the random phase and amplitude fluctuations or noise embedded in the beam is negligible, due to the natural divergence of the beam. However, with the commencement of polymerization, the system is pushed into a nonlinear regime due to the polymerization induced refractive index change (Δn), where the noise gets amplified. Because of the amplified noise, the initially homogeneous beam disintegrates into bright and dark stripes (figure 4.4b) corresponding to higher and lower intensity regions respectively. As photopolymerization is an intensity dependent process, higher intensity regions result in higher crosslink density and corresponding increased Δn compare to lower intensity regions. Light gets preferentially trapped in these higher Δn regions, enabling the bright stripes to propagate further into the medium without divergence (figure 4.4c & 4.4d). With time, increase in polymerization and corresponding gain in Δn triggers the amplification of the noise embedded in the bright stripes and their consequent division into bright and dark spots (figure 4.4e & 4.4f). Each bright spot corresponded to a self-trapped filament of incoherent light. Because of the reciprocal interaction between the polymerization and refractive index change, these self-trapped filaments preferentially grow along the propagation direction of light and they reach the exit face of the sample cell. As the silver nanoparticles are generated *in-situ* during the polymerization process and the self-trapped filaments originate from an irreversible polymerization reaction, each self-trapped filament transform into a permanent cylindrical waveguide doped with silver nanoparticles. Based on the knowledge from our previous works,[39,40] initial MI experiments with silver nanoparticles-epoxide system were carried out using white light (results in Supporting information). It was observed that white light required significantly higher power (50 mW) to elicit MI in the silver nanoparticles-epoxide system compare to LED. This is due to the fact that the energy from the white light is spread across the entire visible spectral range (400-700 nm), whereas only a portion of energy corresponding to the absorption maximum of the photosensitizer (~460 nm) is required for photopolymerization induced MI and *in-situ* synthesis of silver nanoparticles, the rest of the energy from white light is neither utilized for MI nor for silver nanoparticles synthesis. Hence, MI and *in-situ* silver nanoparticles synthesis occur at higher power with polychromatic irradiation source compare to monochromatic LED source used in our final experiment.

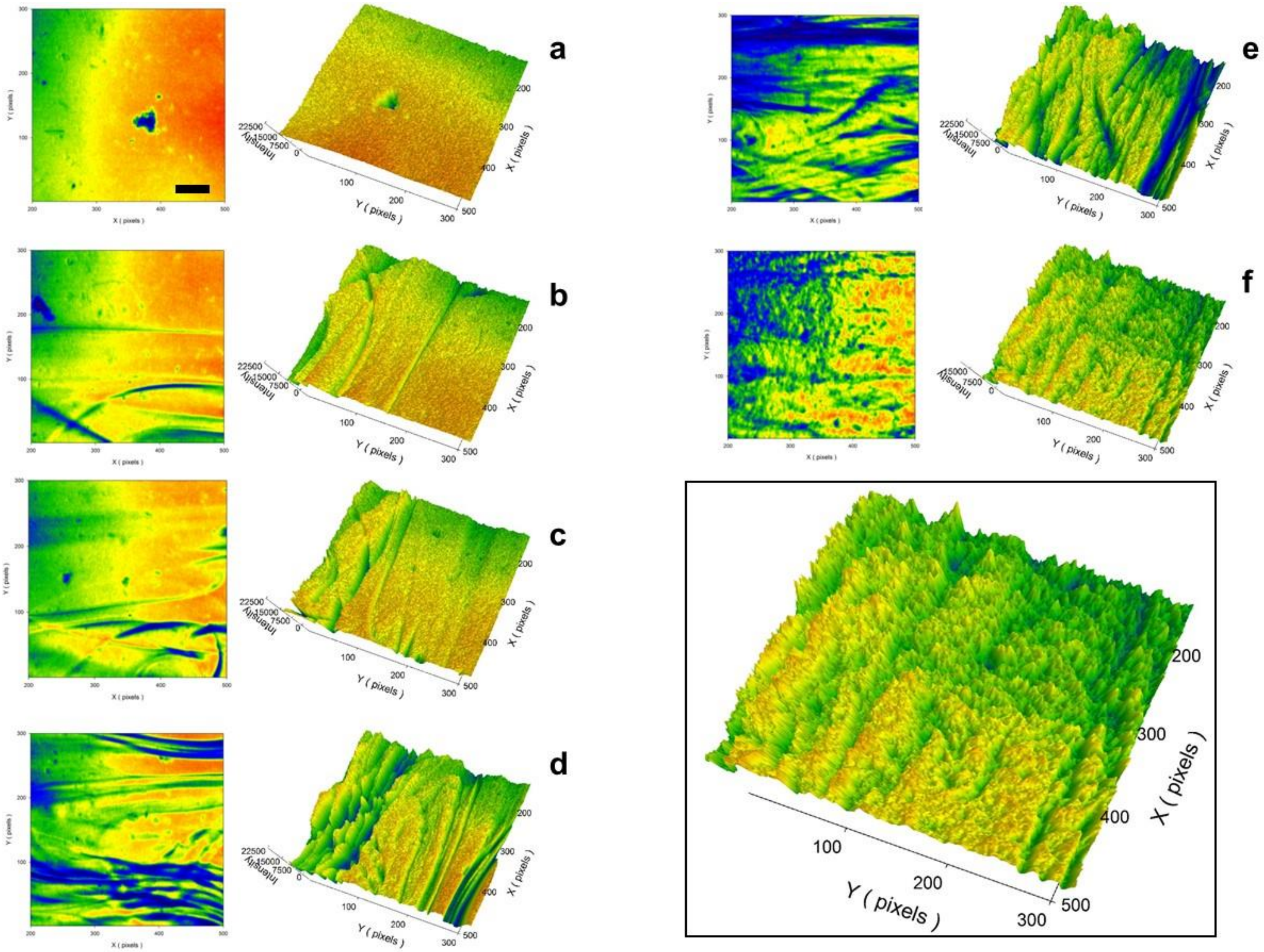

Figure 4.4. Temporal evolution of the spatial intensity profile of an incoherent blue LED beam (20 mW) propagating through the epoxide by depositing silver nanoparticles *via in-situ* synthesis. Profiles were acquired at the sample exit face (pathlength 10 mm) at time t = a) 0 s b) 176 s c) 186 s d) 540 s e) 618 s f) 810 s. The scale bar in a = 500 µm, applies to all images. The inset is the magnified version of (f)

4.3.5. MI induced waveguide in gold nanoparticles-epoxide system

MI in gold nanoparticles-epoxide system was demonstrated using the optical assembly similar to the silver nanoparticles-epoxide system. Spatiotemporal changes to the intensity profile of the LED beam is shown in figure 4.5. Before the beginning of polymerization at t = 0 s, under linear conditions, the beam essentially looks uniform at the exit face, as the random phase and amplitude fluctuations or the noise embedded in the system gets washed out under these linear conditions (figure 4.5a). Within 250 s, a spatial variation is developed in the beam intensity profile, disintegrating the system into bright and dark (higher and lower intensity) regions due to the nonlinearity provided by polymerization. The intensity dependent photopolymerization process leads to higher degree of crosslinking in these bright regions compare to dark regions and results in corresponding difference in refractive index change, with higher and lower refractive index changes in bright and dark regions respectively. Over time (500 s) the contrast between the bright and dark regions increases (figure 4.5c), as light preferentially attracts toward and becomes entrapped in these higher refractive index bright regions. Shortly (750 s), the bright regions develop minor intensity variations (figure 4.5d), which in turn get amplified and eventually lead these bright region to spontaneously divide into multiple self-trapped spots (figure 4.5e & 4.5f). These spots are nothing but individual self-trapped filaments. Because of the nonlinearity offered by the polymerization, these self-trapped filaments travel without divergence along the

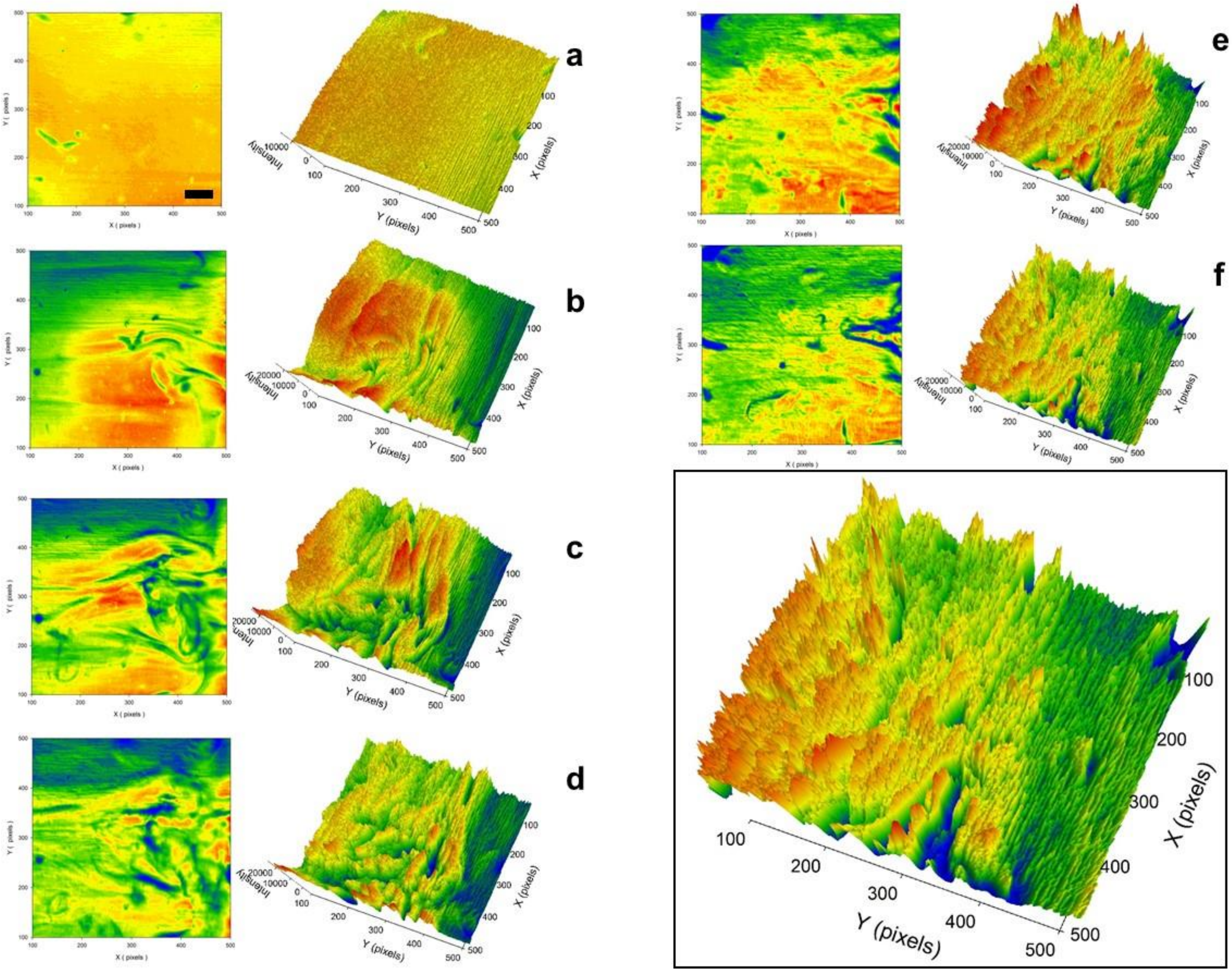

Figure 4.5. Temporal evolution of the spatial intensity profile of an incoherent blue LED beam (40 mW) propagating through the epoxide by depositing gold nanoparticles *via in-situ* synthesis. Profiles were acquired at the sample exit face (pathlength 10 mm) at time t = a) 0 s b) 250 s c) 500 s d) 750 s e) 1000 s f) 1500 s. The scale bar in a = 500 µm, applies to all images. The inset is the magnified version of (f)

propagation direction of the beam and ultimately reach the exit face of the sample cell. As the irreversible polymerization reaction supporting the propagation of self-trapped filaments and *in-situ* synthesis of gold nanoparticles happen simultaneously, these filaments result in cylindrical waveguides embedded with gold nanoparticles. Similar to the silver nanoparticles-epoxide system, the MI experiments in gold nanoparticles-epoxide system was also studied with white light. Like the silver nanoparticles-epoxide system MI occurred at higher power with the gold nanoparticle-epoxide system as well. But the difference is, white light power (90 mW) required to elicit MI in gold nanoparticle-epoxide system is considerable higher than in silver nanoparticles-epoxide system (results in supporting information). This may be due to the difference in concentration of nanoparticles in these two systems. Concentration of metal precursor (1 wt %) used in gold nanoparticles system is an order of magnitude higher than in silver nanoparticles system (0.05 wt %) and this results in higher concentration of nanoparticles generation in the former system compare to the later. As the nanoparticles absorb considerable amount of light due to the surface plasmon resonance, the gold nanoparticles-epoxide system with higher nanoparticles concentration required higher power to elicit MI than the silver nanoparticles system. Similar trend is visible when comparing the LED power required to invoke MI in these two systems (20 mW for silver nanoparticles system, whereas 40 mW for gold nanoparticles system).

4.3.6. Permanent waveguide structures embedded with metal nanoparticles

Because of polymerization induced MI and simultaneous *in-situ* metal nanoparticles synthesis, the initially fluid medium transforms into a dense population of solid 3D waveguide structures doped with metal nanoparticles. Micrographs in figure 4.6a, 4.7a & 4.6b, 4.7b show the transverse and longitudinal cross section of the waveguide structures with silver and gold nanoparticles respectively. The transverse cross-section of the structures (figure 4.6a & 4.7a) look brightly lit, as each filament with refractive index greater than the surrounding, traps and guides a portion of incident light from the microscope. The longitudinal cross-sections (figure 4.6b & figure 4.7b) show that each bright spot in transverse cross-section corresponds to a cylindrical waveguide microstructure propagating through the medium. Transmission electron micrographs obtained from the ultramicrotome sample of waveguide structures confirm the presence of metal nanoparticles. TEM micrographs and corresponding EDX spectrum (figure 4.6c, 4.6d, 4.6e) from the waveguide structures fabricated with silver salt show the presence of spherical silver nanoparticles with an average diameter of 1.7 ± 0.5 nm (figure 4.6f) (error obtained from standard deviation). UV-vis spectrum (figure 4.6g) of corresponding sample showed an absorption maximum at 457 nm associated with the dipolar surface plasmon resonance of silver nanoparticles embedded in polymer matrices. The extinction maximum is mainly due to absorption as

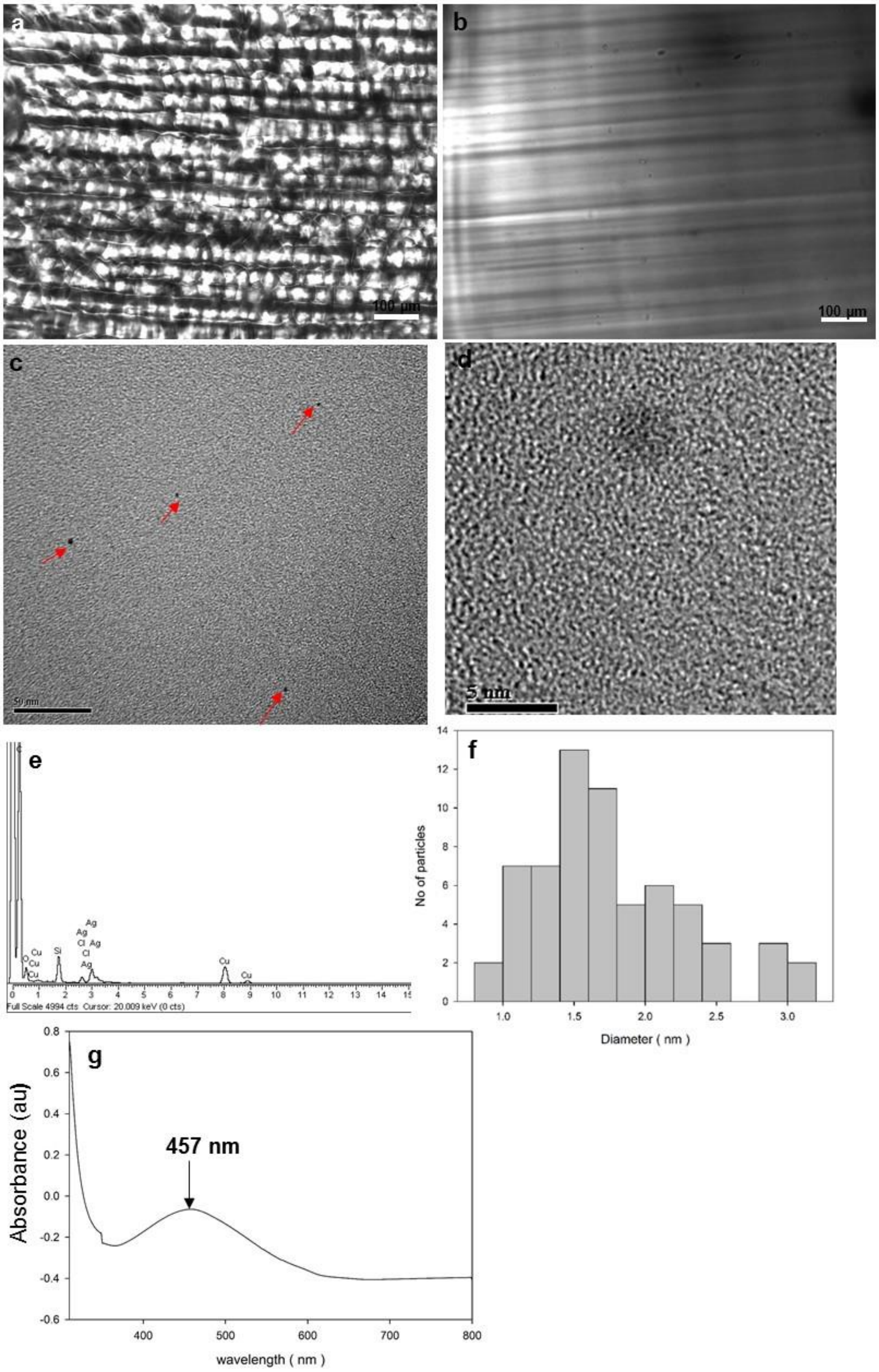
a
100 µm
b
100 µm
c
50 nm
d
5 nm
e
C
O
Cu
Cu
Cu
Si
Ag
Ag
Cl
Ag
Cl
Ag
Cu
Cu
0 1 2 3 4 5 6 7 8 9 10 11 12 13 14 15
Full Scale 4994 cts Cursor: 20.009 keV (0 cts)
f
No of particles
0 2 4 6 8 10 12 14
1.0 1.5 2.0 2.5 3.0
Diameter (nm)
g
Absorbance (au)
-0.6 -0.4 -0.2 0.0 0.2 0.4 0.6 0.8
457 nm
400 500 600 700 800
wavelength (nm)

Figure 4.6. Optical micrographs of cylindrical waveguide structures induced by MI in epoxide medium with silver nanoparticles a) transverse cross-section of waveguide structures with silver nanoparticles b) corresponding longitudinal cross-section. TEM micrographs of waveguides with silver nanoparticles c) the arrows point at the Ag nanoparticles d) high resolution image showing the presence of single particle e) EDX spectrum confirming the presence of elemental silver f) particles size distribution (population ≈ 60 particles) g) UV-vis absorption spectrum of silver nanoparticles in waveguide structure

scattering is insignificant at this particle dimension. Comparing the UV-Vis spectrum (figure 4.6g) of silver nanoparticles embedded in waveguide structures with uniformly irradiated sample (figure 4.2a) reveals that the presence of waveguides did not significantly affect the properties of silver nanoparticles. This may be due to the very low concentration of silver nanoparticles in the system. In our previous work,[39] we observed the alignment of nanoparticles along the direction of waveguides but here the concentration of nanoparticles is considerably less to get such alignment and so the nanoparticles are not affected by the micron scale waveguide structures.

Analysis of TEM micrographs and EDX spectrum (figure 4.7c, 4.7d, 4.7e) obtained from the waveguide structures made using gold salt show the presence of 10 ± 3 nm diameter (figure 4.7f) spherical gold nanoparticles. The UV-vis spectrum of the gold nanoparticles in waveguide structures is shown in figure 4.7g. It exhibits a maximum at 562 nm corresponding to the dipolar plasmon resonance of gold nanoparticles embedded in polymers. Similar to the silver nanoparticles system, the UV-Vis spectrum of gold nanoparticles embedded in

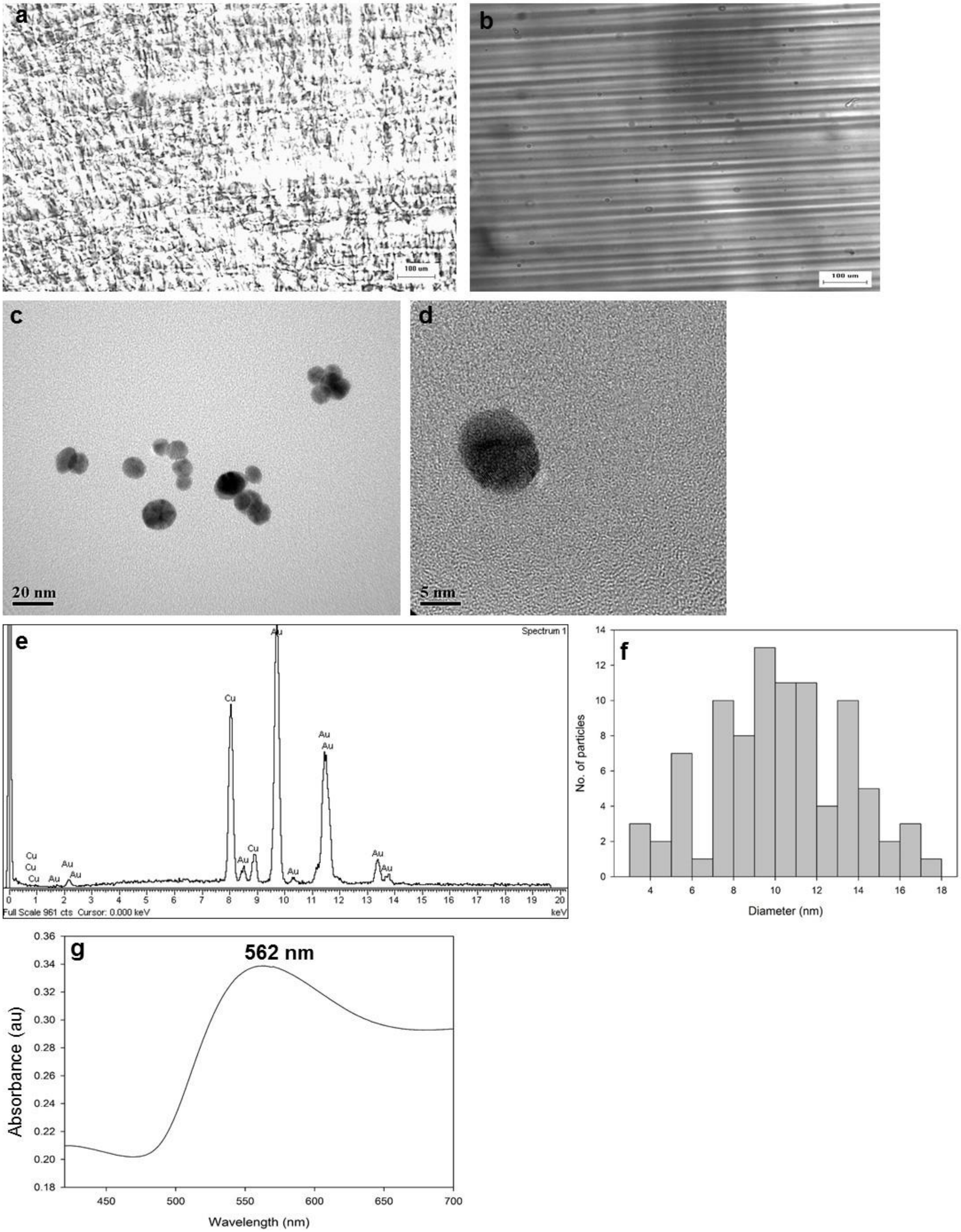
a
100 um
b
100 um
c
20 nm
d
5 nm
e
Spectrum 1
Au
Cu
Au
Au
Cu
Au
Au
Cu
Cu
Cu
Au
Au
Au
Au
Au
0 1 2 3 4 5 6 7 8 9 10 11 12 13 14 15 16 17 18 19 20
keV
Full Scale 961 cts Cursor: 0.000 keV
f
No. of particles
0 2 4 6 8 10 12 14
Diameter (nm)
4 6 8 10 12 14 16 18
g
562 nm
Absorbance (au)
0.18 0.20 0.22 0.24 0.26 0.28 0.30 0.32 0.34 0.36
Wavelength (nm)
450 500 550 600 650 700

Figure 4.7. Optical micrographs of cylindrical waveguide structures induced by MI in epoxide medium with Au nanoparticles a) transverse cross-section of waveguide structures with Au nanoparticles b) corresponding longitudinal cross-section. TEM micrographs of waveguides with Au nanoparticles c) distribution of Au nanoparticles in epoxide d) high resolution image showing the presence of single particle e) EDX spectrum confirming the presence of elemental gold f) particles size distribution (population ≈ 60 particles) g) UV-Vis absorption spectrum of gold nanoparticles in waveguide structures.

waveguide structure (figure 4.7g) and uniformly irradiate samples were compared (figure 4.2b). Here also the spectra remind identical, showing that the properties of gold nanoparticles are not affected by the presence of waveguide structures.

Our group has fabricated silver nanoparticles embedded waveguide structures using MI before in free radical polymerizable organosiloxane system.[39] Not only the organosiloxane system used in those works lacked physical stability but also it had limitations in terms of propagation distance of the waveguide structures. In presence of silver nanoparticles, waveguides fabricated using MI in organosiloxane medium did not propagate over 4 mm. This was due to the attenuation of the beam caused by the scattering from silver nanoparticles. But in the present systems (both silver and gold nanoparticles systems), the waveguide structures propagate upto 10 mm (results in supporting information) and limited only by the size of the sample cell. This is because the *in-situ* metal nanoparticles synthesis and MI occur simultaneously (figure 4.3). Metal nanoparticles are not formed until the beam undergoes MI / (in the absence of polymerization) and so the beam is not attenuated by the metal nanoparticles. Because of this the waveguide structures can propagate over long distance in the present system. This is significantly different from the organosiloxane system, where the silver nanoparticles are formed before MI.

Comparing the silver and gold nanoparticles systems, the silver nanoparticles-epoxide system has an upper limit for the concentration (0.05 wt %) of metal precursor that can be added to the system. Above this limit, the sol polymerizes by non-photolytic chemical route, preventing its usage for MI process and subsequent waveguide fabrication as the silver metal precursor is also acting as initiator. Because of this, the concentration of silver metal salt used in the present system is two orders of magnitude lesser than the organosiloxane system used in our previous work. This limitation is resolved in gold nanoparticles systems by separating the *in-situ* gold nanoparticles synthesis photochemical reaction from the photopolymerization reaction. Here the gold nanoparticles are generated from the metal precursor without effecting the polymerization reaction, which is initiated by a separate photoinitiator. Thus the *in-situ* gold nanoparticles synthesis and photopolymerization occur simultaneously without effecting one another. Because of this the gold nanoparticles system offers scope for adding significantly higher concentration (1 wt %) of metal precursor than the silver nanoparticles system.

4.4. Summary and Outlook

In summary, combining MI with *in-situ* synthesis is found to be a facile single-step route for fabricating metal nanoparticles (Ag & Au) embedded polymer optical waveguide structures. Camphorquinone generates metal nanoparticles and bronsted acid initiator *via* photoinduced electron transfer to metal salts and photoinitiator respectively. Crosslinking polymerization of epoxide stabilized the metal nanoparticles and also provided the required Δn for the MI. Our approach provides a convenient route for fabricating functional waveguide structures with metal nanoparticles, which has significant role in SPR sensor.

References

1 R. Karlsson, *J. Mol. Recognit.*, 2004, **17**, 151–161.

2 C. J. Murphy, T. K. Sau, A. M. Gole, C. J. Orendorff, J. Gao, L. Gou, S. E. Hunyadi and T. Li, *J. Phys. Chem. B*, 2005, **109**, 13857–13870.

3 U. Kreibig and M. Vollmer, *J. Am. Chem. Soc.*, 1995, 118.

4 M. a Noginov, G. Zhu, a M. Belgrave, R. Bakker, V. M. Shalaev, E. E. Narimanov, S. Stout, E. Herz, T. Suteewong and U. Wiesner, *Nature*, 2009, **460**, 1110–1112.

5 M. W. Knight, H. Sobhani, P. Nordlander and N. J. Halas, *Science*, 2011, **332**, 702–704.

6 S. Khatua, W. S. Chang, P. Swanglap, J. Olson and S. Link, *Nano Lett.*, 2011, **11**, 3797–3802.

7 B. Sepúlveda, P. C. Angelomé, L. M. Lechuga and L. M. Liz-Marzán, *Nano Today*, 2009, **4**, 244–251.

8 K. M. Mayer, J. H. Hafner and A. À. Antigen, *Chem. Rev.*, 2011, **111**, 3828–3857.

9 N. Liu, M. L. Tang, M. Hentschel, H. Giessen and a P. Alivisatos, *Nat. Mater.*, 2011, **10**, 631–636.

10 X. H. Huang, I. H. El-Sayed, W. Qian and M. a El-Sayed, *J. Am. Chem. Soc.*, 2006, **128**, 2115–2120.

11 C. J. Murphy, A. M. Gole, J. W. Stone, P. N. Sisco, A. M. Alkilany, E. C. Goldsmith and S. C. Baxter, *Acc. Chem. Res.*, 2008, **41**.

12 S. Lal, S. E. Clare and N. J. Halas, *Acc. Chem. Res.*, 2008, **41**, 1842–1851.

13 C. M. Cobley, J. Chen, E. C. Cho, L. V Wang and Y. Xia, *Chem. Soc. Rev.*, 2011, **40**, 44–56.

14 C. E. Talley, J. B. Jackson, C. Oubre, N. K. Grady, C. W. Hollars, S. M. Lane, T. R. Huser, P. Nordlander and N. J. Halas, *Nano Lett.*, 2005, **5**, 1569–1574.

15 J. M. McLellan, Z. Y. Li, A. R. Siekkinen and Y. Xia, *Nano Lett.*, 2007, **7**, 1013–1017.

16 J. F. Li, Y. F. Huang, Y. Ding, Z. L. Yang, S. B. Li, X. S. Zhou, F. R. Fan, W. Zhang, Z. Y. Zhou, D. Y. Wu, B. Ren, Z. L. Wang and Z. Q. Tian, *Nature*, 2010, **464**, 392–395.

17 a S. Korchev, M. J. Bozack, B. L. Slaten and G. Mills, *J. Am. Chem. Soc.*, 2004, **126**, 10–11.

18 W. K. Lee, Z. Dai, W. P. King and P. E. Sheehan, *Nano Lett.*, 2010, **10**, 129–133.

19 J. Greener, T. H. Van Der Loop, C. Paquet, G. Scholes and E. Kumacheva, *Langmuir*, 2009, **25**, 3173–3177.

20 H. Kong and J. Jang, *Chem. Commun. (Camb).*, 2006, 3010–3012.

21 K. Liu, A. Lukach, K. Sugikawa, S. Chung, J. Vickery, H. Therien-Aubin, B. Yang, M. Rubinstein and E. Kumacheva, *Angew. Chemie - Int. Ed.*, 2014, **53**, 2648–2653.

22 G. Yun, Z. Hassan, J. Lee, J. Kim, N. S. Lee, N. H. Kim, K. Baek, I. Hwang, C. G. Park and K. Kim, *Angew. Chemie - Int. Ed.*, 2014, **53**, 6414–6418.

23 B. Park, S. H. Yun, C. Y. Cho, Y. C. Kim, J. C. Shin, H. G. Jeon, Y. H. Huh, I. Hwang, K. Y. Baik, Y. I. Lee, H. S. Uhm, G. S. Cho and E. H. Choi, *Light Sci. Appl.*, 2014, **3**, e222.

24 D. He, B. Hu, Q. Yao, K. Wang and S. Yu, *ACS Nano*, 2009, **3**, 3993–4002.

25 T. Kim, H. Kang, S. Jeong, D. J. Kang, C. Lee, C. Lee, M. Seo, J. Lee and B. J. Kim, *Appl. Mater. Interfaces*, 2014, **6**, 16956–16965

26 Y. Gu, S. Xu, H. Li, S.Wang, M. Cong, J.R. Lombardi and W. Xu., *J.Phys.Chem.Lett.*, **2013**, *4*, 3153−315.

27 E. Hariprasad and T. P. Radhakrishnan, *Langmuir*, 2013, **29**, 13050–13057.

28 D. Monzón-Hernández, J. Villatoro, D. Talavera and D. Luna-Moreno, *Appl. Opt.*, 2004, **43**, 1216–1220.

29 M. A. Skorobogatiy and A. Kabashin, *Opt. Express*, 2006, **14**, 8419–8424.

30 J. H. Ahn, T. Y. Seong, W. M. Kim, T. S. Lee, I. Kim and K.-S. Lee, *Opt. Express*, 2012, **20**, 21729.

31 M. Chamanzar, Z. Xia, S. Yegnanarayanan and A. Adibi, *Opt. Express*, 2013, **21**, 32086–98.

32 E. Kretschmann and H. Raether, *Z. Naturforsch.*, 1968, **23**, 2135–2136.

33 a. K. Sharma, R. Jha and B. D. Gupta, *IEEE Sens. J.*, 2007, **7**, 1118–1129.

34 A. Hassani and M. Skorobogatiy, 2007, **24**, 1423–1429.

35 A. Prabhakar and S. Mukherji, *Lab Chip*, 2010, **10**, 3422–3425.

36 P. Wang, L. Zhang, Y. Xia, L. Tong, X. Xu and Y. Ying, *Nano Lett.*, 2012, **12**, 3145–3150.

37 Y. Taguchi, E. Takano and T. Takeuchi, *Langmuir*, 2012, **28**, 7083–7088.

38 L. Qiu and K. Saravanamuttu, *J. Opt. Soc. Am. B*, 2012, **29**, 1085.

39 L. Qiu and K. Saravanamuttu, *J. Opt.*, 2012, **14**, 125202.

40 D. K. Basker, M. a. Brook and K. Saravanamuttu, *J. Phys. Chem. C*, 2015, **119**, 20606–20617.

41 Y. Yagci, M. Sangermano and G. Rizza, *Polymer (Guildf).*, 2008, **49**, 5195–5198.

42 Y. Yagci, M. Sangermano and G. Rizza, *Macromolecules*, 2008, **41**, 7268–7270.

43 M. Sangermano, Y. Yagci and G. Rizza, *Macromolecules*, 2007, **40**, 8827–8829.

44 P. P. Ethers, *J. Am. Chem. Soc.*, 1979, **101**, 4249–4258.

45 L. Longenberger, *J. Phys. Chem.*, 1995, **99**, 0–3.

46 S. Lin and S. K. Huang, *J. Polym. Sci. Part A Polym. Chem.*, 1996, **34**, 1907–1922.

47 I. B. Burgess, W. E. Shimmell and K. Saravanamuttu, *J. Am. Chem. Soc.*, 2007, **129**, 4738–4746.

48 A. W. Snyder, *Science (80-.).*, 1997, **276**, 1538–1541.

49 T. Schwartz, T. Carmon, H. Buljan and M. Segev, *Phys. Rev. Lett.*, 2004, **93**, 1–4.

50 H. Buljan, A. Šiber, M. Soljačić and M. Segev, *Phys. Rev. E - Stat. Nonlinear, Soft Matter Phys.*, 2002, **66**, 1–4.

51 D. N. C. Detlef Kip, Marin Soljacic, Mordechai Segev, Eugenai Eugenieva, *Science (80-.).*, 2000, **290**, 495–498.

52 J. Klinger, H. Martin and Z. Chen, *Opt. Lett.*, 2001, **26**, 271–273.

53 Z. Chen, J. Klinger and D. N. Christodoulides, *Phys. Rev. E - Stat. Nonlinear, Soft Matter Phys.*, 2002, **66**, 1–5.

54 Z. Chen and K. McCarthy, *Opt. Lett.*, 2002, **27**, 2019–2021.

55 M. Soljacic, M. Segev, T. Coskun, D. Christodoulides and A. Vishwanath, *Phys. Rev. Lett.*, 2000, **84**, 467–470.

Supplementary information

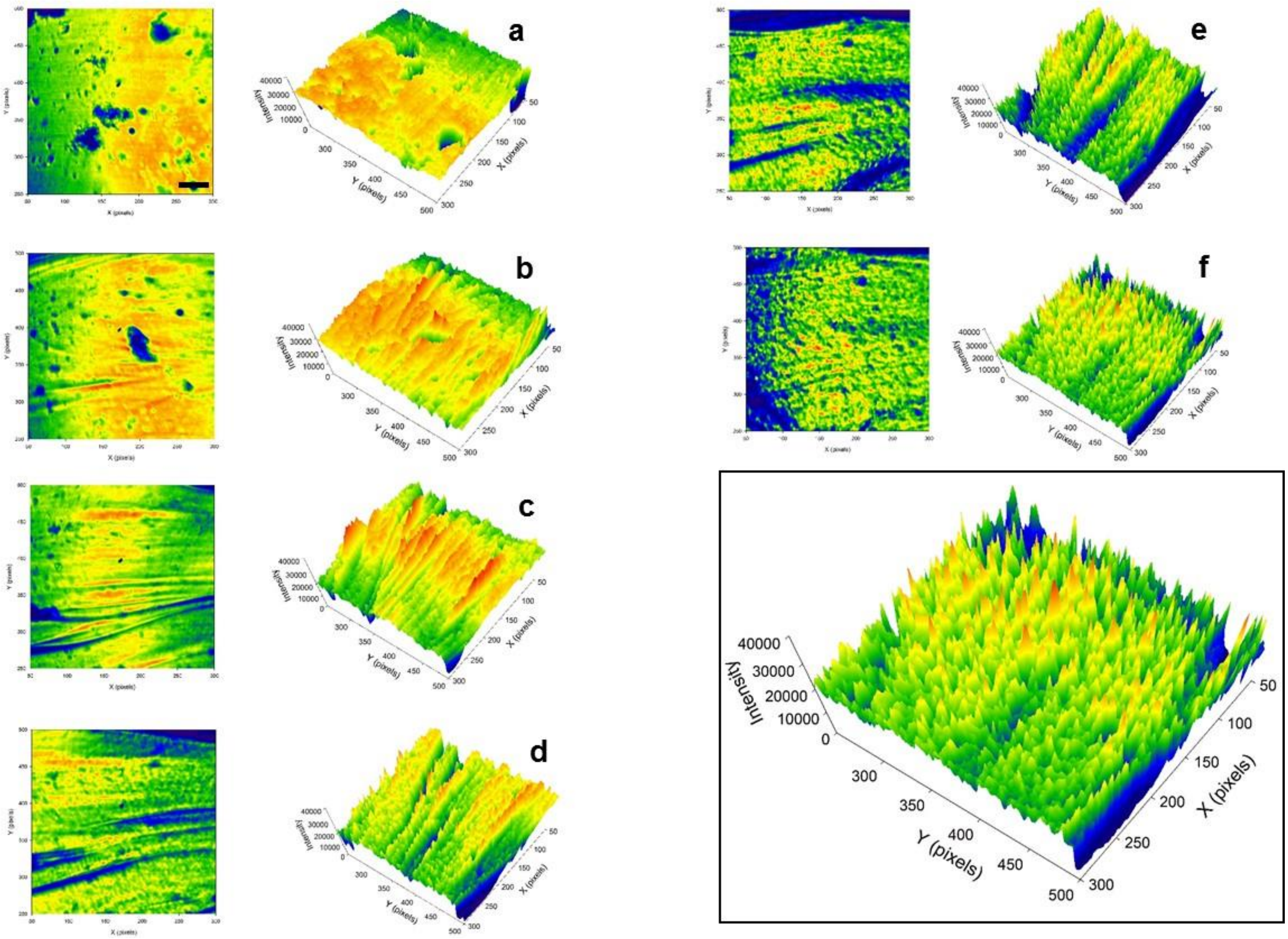

Figure S4.1 Temporal evolution of the spatial intensity profile of an incoherent white light beam (50 mW) propagating through the epoxide by depositing silver nanoparticles *via in-situ* synthesis. Profiles were acquired at the sample exit face (pathlength 10 mm) at time t = a) 0 s b) 225 s c) 310 s d) 560 s e) 720 s f) 870 s. The scale bar in a = 500 µm, applies to all images. The inset is the magnified version of (f)

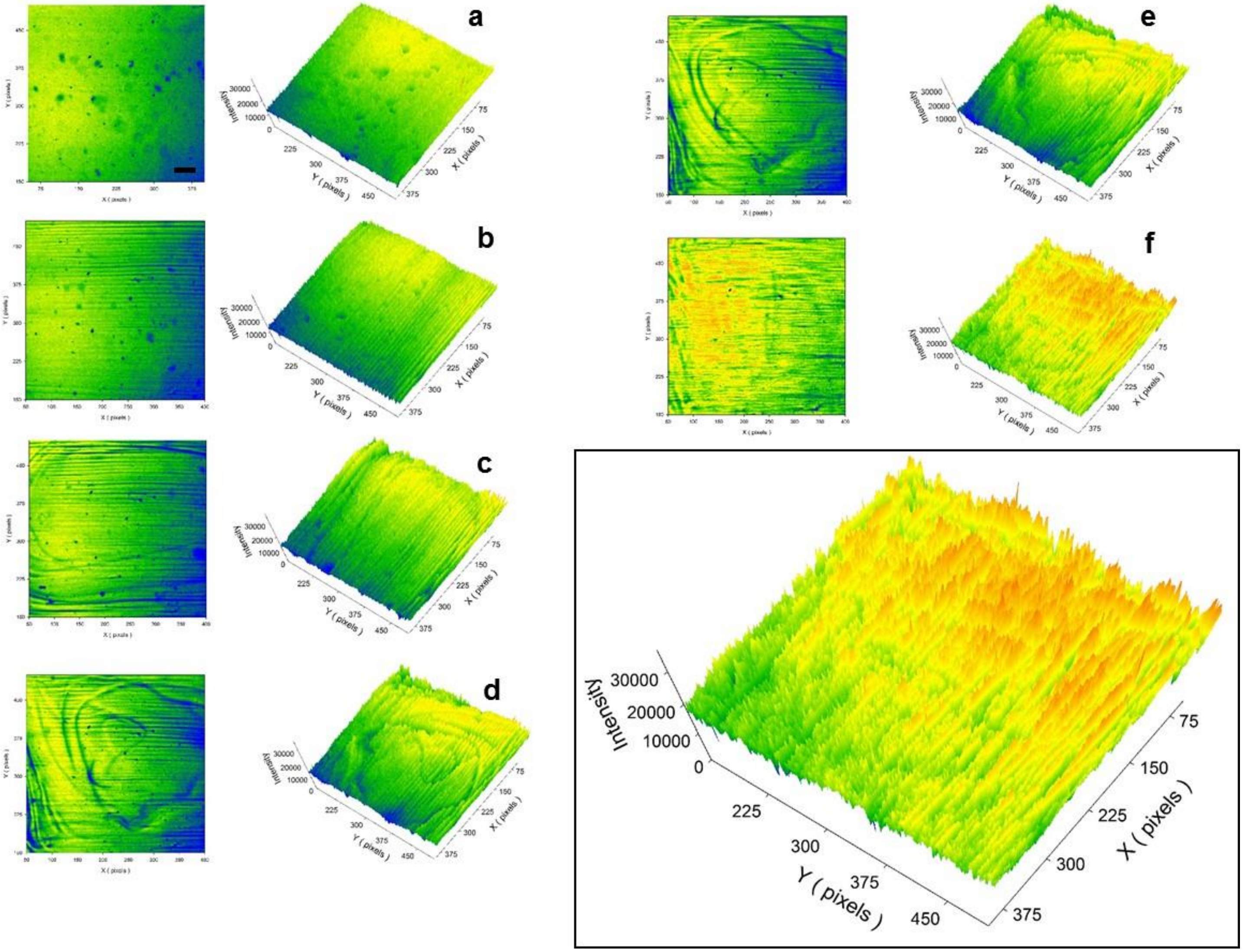

Figure S4.2 Temporal evolution of the spatial intensity profile of an incoherent white light beam (90 mW) propagating through the epoxide by depositing gold nanoparticles *via in-situ* synthesis. Profiles were acquired at the sample exit face (pathlength 10 mm) at time t = a) 0 s b) 295 s c) 560 s d) 810 s e) 1100 s f) 1460 s. The scale bar in a = 500 µm, applies to all images. The inset is the magnified version of (f)

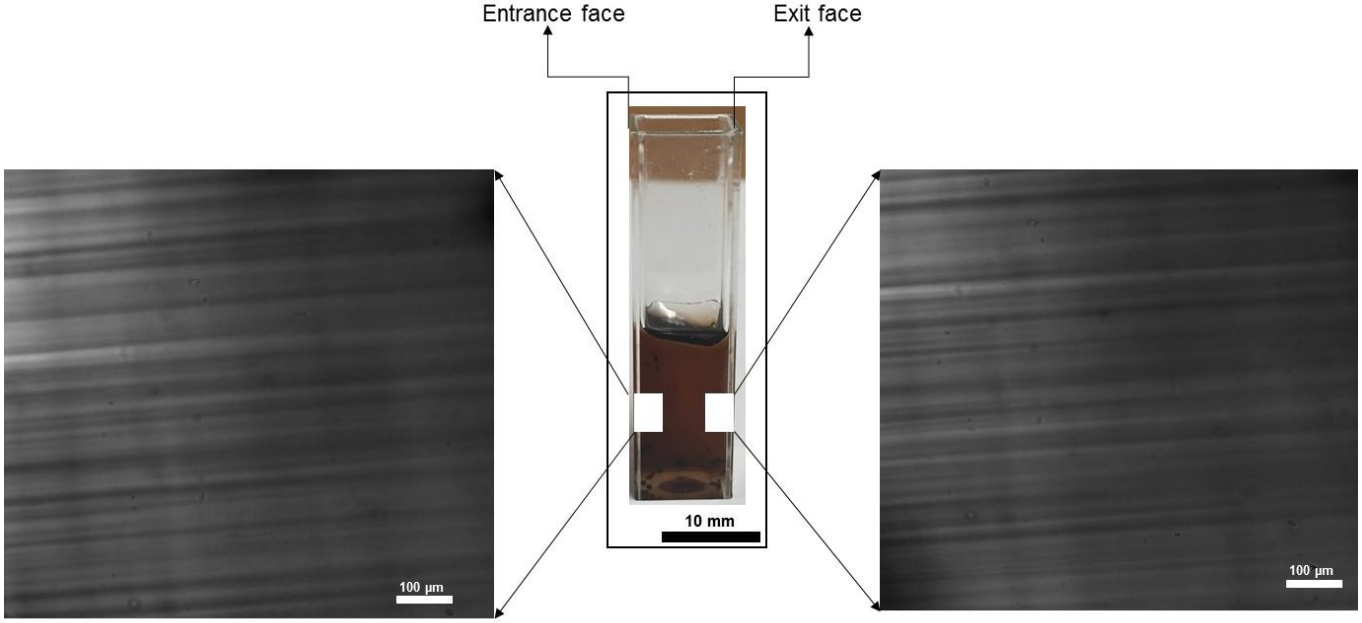

Figure S4.3 Micrographs taken at the entrance face and exit face of the 10 mm cuvet containing silver nanoparticles embedded waveguide structure, demonstrating the formation of 10 mm waveguide structure.

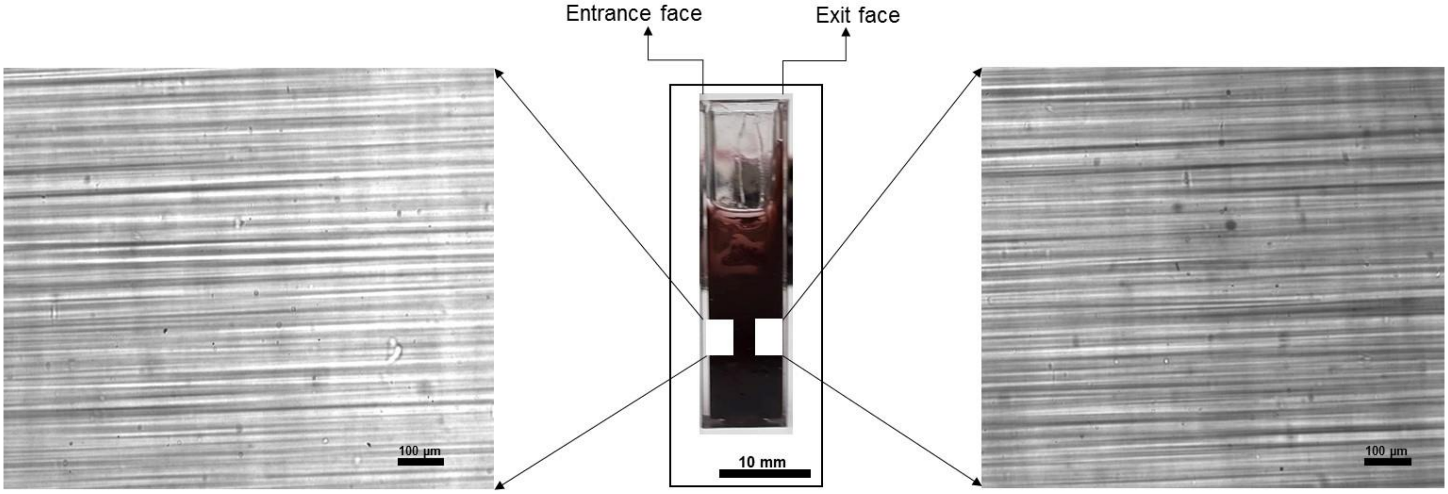

Figure S4.4 Micrographs taken at the entrance face and exit face of the 10 mm cuvet containing gold nanoparticles embedded waveguide structure, demonstrating the formation of 10 mm waveguide structure.

Chapter 5

Spontaneous formation of Au nanoparticle fractals in epoxy films and their application as free-standing substrates for NIR Surface Enhanced Raman Spectroscopy

Abstract

We present a facile, room-temperature route to robust, free standing, flexible epoxide-siloxane based substrate embedded with fractal Au nanoparticles aggregates for near-infrared (NIR) SERS by combining photocationic polymerization with drop casting technique. Au nanoparticles aggregates were generated *in-situ* through the reduction of gold (III) chloride trihydrate $HAuCl_4 \cdot 3H_2O$ in epoxypropoxypropyl terminated polydimethyl siloxane (EDMS). The monomer serves the dual purpose of reducing the Au salt and stabilizing the resulting Au nanoparticles aggregates. Aggregates were transformed to fractal structures using drop casting technique. UV-initiated cationic polymerization of the epoxide groups in EDMS resulted in free-standing substrate with fractal aggregates of Au nanoparticles. Electron and optical microscopy confirmed the formation of fractal aggregates in the free-standing polymer substrate. UV-Vis-NIR spectrometry of substrates showed the NIR (700 nm – 900 nm) plasmon resonance exhibited by the fractal aggregates of Au nanoparticles. Fractality of the aggregates was analyzed using box counting method. Substrates doped with fractal Au nanoparticles aggregates showed excellent SERS signals for the analyte Eosin Y at NIR excitation wavelengths with an enhancement factor of 3.1×10^3.

5.1. Introduction

Raman scatter from inelastic collisions between photons and molecules reveal highly specific, vibrational signatures of molecules[1, 2] but characteristically weak scattering cross-sections (typically ranging from 10^{-35} to 10^{-25} cm^2 per molecule) pose challenges for practical application of this spectroscopic technique.[3] Surface enhanced Raman scattering (SERS) overcomes this limitation by increasing scattering cross sections by several orders of magnitudes (e.g. 10^{-16} cm^2 per molecule).[4,5] Such enhancement is possible when scattering occurs in the vicinity of roughened metallic surfaces or nanoparticles.[6–8] In these systems, the optical field excites surface plasmons (SPs) – considered to be collective oscillations of conduction band electrons[9] – which in turn greatly enhance the electromagnetic field experienced by adsorbed analyte molecules.[3,10,11] The resulting powerful combination of molecular specificity with high levels of sensitivity has been exploited in SERS-based applications ranging from biomedical systems to industrial processes.[10,12–18]

Theoretical and experimental studies have shown that the enhancement of the electromagnetic field is particularly significant at the junctions between nanoparticles and therefore in nanoparticle clusters and aggregates compared to individual nanoparticles.[4,19–25] Placing nanoparticles in close proximity (~ 1 nm) leads to the coupling of their dipoles; coherent interference of coupled dipoles in turn can enhance the electromagnetic field up to 10^{10}-fold.[22] For example, Brus *et* *al* showed single molecule detection through SERS at the junction between two silver nanoparticles[21] while Xu *et al* estimated an effective electromagnetic field enhancement factor of 10^{10} in the interstitial space between silver nanospheres.[22] Nanoparticle aggregates with fractal structure show exceptional SERS enhancement; [23, 26–29, 30–37] plasmonic waves become localized within fractals, which due to their characteristic dilation symmetry cannot support ordinary wave propagation.[37, 38] Because long-range interactions are suppressed in this way, individual dipolar modes of metallic particles become spatially localized and enhance the field within these nanoscopic regions. When compared to non-fractal aggregates, where the surface plasmon modes are delocalized over larger regions through long range dipole-dipole interactions, electromagnetic field enhancement can be an order of magnitude higher in fractal aggregates.[38] Furthermore, fractal nanoparticle aggregates can be composed of variety of different local configurations leading to a broad range of dipolar modes spread across a wide spectral range (400 nm to 1750 nm). This is different from monodisperse spherical or cuboid particles:[37,38] discrete, monodisperse noble metal nanoparticles with diameters ranging from 10 nm to 100 nm dispersed in colloidal form typically exhibit plasmon resonance in the visible region of the electromagnetic spectrum. Even though the aggregation of these particles can lead to the characteristic bathochromic shift of plasmon resonance to lower frequencies, often in the NIR region through interparticle coupling, it is hard to control the position of the plasmon resonance. In fractal aggregates, similar interparticle dipole coupling can lead to plasmon resonance in NIR region[37,38] but the position of plasmon resonance can be preciously controlled by controlling the local configuration of the fractal aggregates. Thus, in addition to local field enhancement, fractal structures exhibit SPR in the near-IR (NIR) spectral region.[37,39,40]

Significant effort has been devoted to fabricating[30,36,41–45] and understanding field enhancement[23,37–39,46] in fractal metal structures for potential applications. For example, fractal substrates would be important in NIR SERS-based detection techniques of biomolecules as tissues show minimal absorbance in the NIR region.[47–49] However, it remains experimentally challenging to inexpensively generate NIR SERS substrates in the form of fractal metal nanoparticles embedded in transparent, flexible films. Such functionalized films are necessary for facile integration with sensing device architectures, be disposable and rapidly replaceable. Films containing fractal arrays of metal nanoparticles have previously been generated through lithographic techniques,[50] sophisticated synthetic colloidal methods,[35,51] electrochemical reduction.[44] Drop casting techniques based on evaporation-induced self-assembly have also been successfully employed to fabricate thin film SERS substrates.[52–54] Here we report an especially facile, two-step, room temperature and spontaneous route to mechanically robust, flexible, optically transparent and free-standing polymer films embedded with fractal aggregates of Au nanoparticles. This technique involves the *in situ* reduction of Au salts to elemental Au nanoparticles in a fluid epoxy-siloxane medium; fractal aggregates of Au nanoparticles form spontaneously upon drop-casting of the solution and become permanently immobilized in the matrix upon photoinitiated cationic polymerization of epoxide moieties, which transforms the fluid into a thin film. We examine the microstructure of these metallodielectric films and study their effectiveness as NIR SERS substrates.

5.2. Experimental

5.2.1 Fabrication of polymer films doped with Au nanoparticle aggregates

0.03 g (7.4×10^{-5} mol) of gold (III) chloride trihydrate ($HAuCl_4 \cdot 3H_2O$) (Sigma-Aldrich, Oakville, ON, Canada) dissolved in 0.5 g (1.7×10^{-4} mol) of polytetrahydrofuran (Sigma-Aldrich, Oakville, ON, Canada) was mixed with 4.375 g (1.2×10^{-2} mol) of epoxypropoxypropyl terminated polydimethyl siloxane (EDMS) (Gelest, Inc. USA) and 0.1 g (1.6×10^{-4} mol) of bis (4-tert-butylphenyl) iodoniumhexafluroantimonate (Hampford Research Inc., Stratford, CT, United states). The solution was stirred for 8 hrs. under minimal light exposure. Reduction of $HAuCl_4 \cdot 3H_2O$ by EDMS resulted in the formation of aggregates of Au nanoparticles. Free standing polymer films doped with Au nanoparticles were prepared as follows: 2 g of EDMS containing gold nanoparticle aggregates was mixed with 7.5 mL of acetone and drop cast on a glass substrate, air-dried for 1 hr and irradiated with UV light (λ= 254 nm; power = 26 mW intensity) for 3 hr and the free standing thin film was peeled off from glass substrate.

5.2.2. Characterization techniques

UV-Vis-NIR absorbance spectra of polymer films doped with Au nanoparticle aggregates supported on glass substrates were acquired with a Cary 5000 UV-Vis-NIR spectrophotometer. Optical micrographs were acquired in transmission mode with an Olympus BX51 microscope fitted with a Q-Imaging Retiga EXi digital camera and ImagePro software. Scanning electron micrographs (SEM) were recorded with a VEGA3 SB instrument with an accelerating voltage of 10 KV in back scattering mode. Transmission electron microscopy (TEM) and energy dispersive x-ray spectrometry (EDX) were carried out with a Philips CM12 instrument at an accelerating voltage of 200 KV. Samples for SEM and TEM from thin films were ultramicrotomed under cryogenic conditions. TEM samples of Au nanoparticles (after 30 mins. of stirring) and aggregates (after 8 hrs. of stirring) were prepared by diluting the colloids in acetone and drop-casting onto Cu grids.

5.2.3. Fractal dimension measurement

We used the box counting method[55] to obtain the Hausdroff dimension (D) or the fractal dimension. In this method, D is measured by placing a grid perpendicular lines separated by distance ϵ onto the image of the aggregate structure and by counting the number of grid boxes (n) containing the aggregated structure (thus leaving behind the grid boxes containing empty space). The slope of the square linear fit of log n verses log (ϵ) yields D.

$$D = \log n / \log \epsilon \quad lim\ \epsilon \rightarrow 0$$

We used the ImageJ plugin FracLac[55] to execute the box counting method. FracLac was first verified using the Sierpinski triangle, a known fractal structure, which yielded D = 1.535; the corresponding error is 3% (D for Sierpinski triangle = 1.585). Settings used were (a) Grid positions = 12 and (b) Scaling grid calibre = default sampling size. Optical micrographs taken over an area of 0.15 mm^2 on thin films embedded with Au nanoparticle aggregates were converted into binary images through ImageJ before executing box counting method in FracLac. A sample calculation is provided as supplementary Information.

5.2.4. SERS experiments

Eosin Y (2’,4’,5’,7’-tetrabromo-3’,6’-dihrdroxyspiro[2-benzofuran-3,9’-xanthene]-1-one) (99%; Sigma Aldrich, Oakville, ON, Canada) was used without further purification. 50 µL of a 1 mM solution of Eosin Y in methanol was spread homogeneously on a polymer film containing Au nanoparticle aggregates and air-dried for 30 min. Raman spectra were acquired at excitation wavelength = 785 nm with a Reinshaw Invia Laser Raman Spectrometer (~1.5 mW, exposure time = 10 s). Control spectra were acquired with 1 M of dye solution coated on polymers films that did not contain Au nanoparticle aggregates; identical preparation and spectral acquisition conditions were employed.

5.3. Results and discussion

5.3.1. Generation of Au nanoparticles in the epoxy medium

Au nanoparticles were generated through *in-situ* chemical reduction of gold (III) chloride trihydrate by EDMS.[56–58] When 7.4 x 10^{-5} mol of Au salt dissolved in 0.5 g (1.7 x 10^{-4} mol) of pTHF was mixed with EDMS, and stirred under minimal exposure to light for 30 mins. the originally yellow coloured Au salt solution turned deep purple. Au nanoparticles formation is evident from the change in UV-Vis absorbance of Au salt in pTFH solution after the addition of EDMS. Au salt solution has an absorbance at ~ 420 nm[57] (Fig. 5.1a), when EDMS was added to this solution, a new band maximizing at ~ 590 nm (Fig. 5.1b). This new band at ~ 590 nm corresponds to dipolar plasmon resonance of spherical Au nanoparticles.[59] Appearance of this new absorbance band confirms the reduction of Au salt to elemental Au nanoparticles. The plasmon resonance peak is broader due to the polydispersity of the particles size and bathochromic shift of this peak from the characteristic resonance wavelength of Au nanoparticles at ~520 nm originates from the greater dielectric constant of the EDMS medium (~1.5) compared to the typically employed H_2O medium (~1.3).[60, 61] Transmission electron micrographs of the sol cast onto a Cu grid revealed a polydisperse distribution of Au nanoparticles with an average diameter of 25 ± 12 nm (Fig. 5.1c & d). EDX carried out on the particles confirmed them as elemental Au (Fig. 5.1e).

Au nanoparticles in this system are formed by the chemical reduction of Au(III) salt by ether moieties of the EDMS.[56–58] Particle formation is initiated through the binding of $[AuCl_4]^-$ ions to pseudocrown ether cavities formed by EDMS oligomers.[56–58] Bound Au (III) ion metal centers are then reduced to Au (I) by the ether groups in EMDS as shown in 1.

$$[AuCl_4]^- + \text{EDMS} \rightarrow \text{Au (I)} + 4Cl^- + 2H^+ + \text{oxidation product} \qquad [1]$$

Because of the above mentioned redox reaction, the pseudocrown ether cavities get disrupted and sets free Au (I) species, which undergo following equilibrium 2.

$$3\ \text{Au (I)} \rightleftharpoons 2\text{Au} + \text{Au (III)} \qquad [2]$$

Individual Au atoms resulting from equilibrium 2, coalesce into atomic ensembles of Au, which in turn combine to form Au nanoparticles through Ostwald ripening.[62] Size of the individual nanoparticles formed is strongly influenced by the weight ratio of ether moieties to Au (III) ions, as it controls the kinetics of particle forming reactions 1 and 2.[58]

Upon continued stirring (over 8 hrs.), individual Au nanoparticles in the colloid form fractal aggregates. The formation of fractal aggregate structures from individual nanoparticles can be explained by well-established diffusion limited aggregation (DLA) mechanism.[63–67]According to the DLA mechanism, particles undergoing random Brownian motion attach one by one to a seed particle irreversibly to form the aggregate structure. In our system, particles formed at the initial stage (first 30 minutes) act as seeds, with time additional particles are formed, which by random Brownian motion attach to the seeds to form fractal aggregate structures. Fractal dimension obtained from the fractal analysis of the optical micrographs of aggregates are consistent with the DLA aggregation mechanism.[65] Also comparison of TEM micrographs taken at 30 min (fig. 5.1c) and 8 hours (fig. 5.2a) support DLA fractal aggregate forming mechanism, where the former shows the presence of seeds (individual nanoparticles) and the later shows the typical fractal aggregate structure formed through DLA mechanism.[66,67]

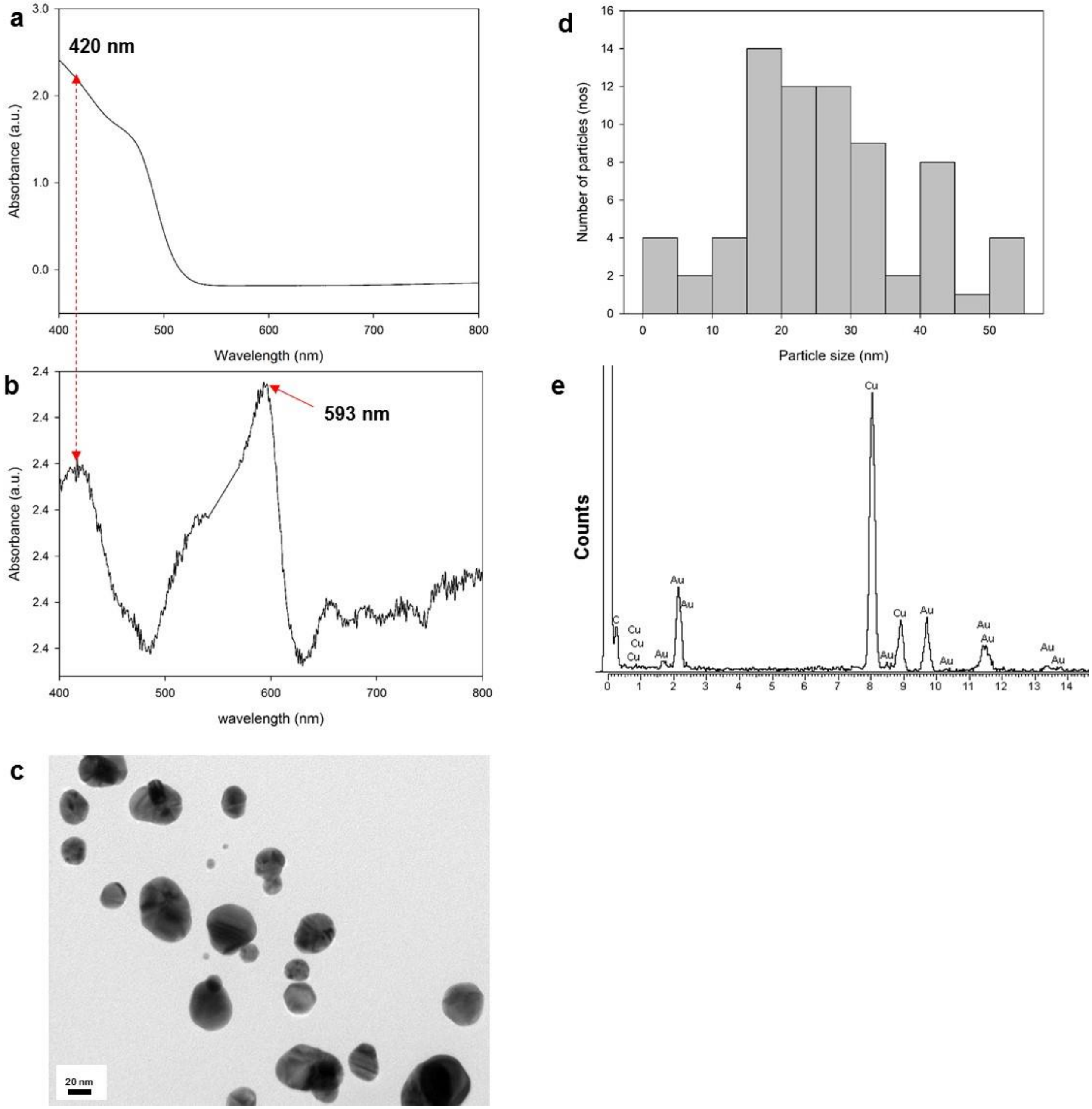

Figure 5.1. Au nanoparticles formed through reduction of Au(III) salt by EDMS after 30 min. of stirring were characterized through (a) UV-Vis spectrum of 7.4 x 10^{-5} mol Au salt in pTFH is included for comparison. (b) UV-Vis absorbance spectrum of Au nanoparticles after chemical reduction (c) and (d) transmission electron microscopy analyis of size distribution (population ~ 70 particles) (e) Energy dispersive X-ray spectrum

Absorption spectrum of the resulting fractal structures is significantly different from the absorption of single particle shown in fig. 5.1b. While the individual particles in colloid show a single maximum, the fractal aggregates show two maxima (Fig. 5.2b). The first maximum at the visible region, located close to the resonance of single particle, is attributed to the quadrapole plasmon resonance of the aggregated particles, while the second maximum at the NIR region is attributed to the dipole plasmon resonance.[68–71] NIR absorption of Au nanoparticles aggregate is due to the interparticle coupling effect. Change in interparticle distance leads to near-field coupling, which in turn red shifts the dipole resonance. As the interparticle distance decreases, the first maximum at the visible region becomes weaker, while the second maximum shifts to longer wavelength and grows in intensity. In the aggregated nanoparticles systems, the oscillating electrons from one particle couple to oscillating electrons of a neighbouring particle through near field coupling, leading to a collective plasmon oscillation of the aggregated system. Because of this coupling, the plasmon resonance shifts to longer wavelength as a function of interparticle spacing.[69] Maximum shift is observed, when the particle spacing approaches zero. In our system Au nanoparticles are overlapping to form fractal aggregates through the DLA mechanism. (supported by the TEMs), which explains the NIR absorption. This dipolar resonance at NIR is broader compare to the dipolar resonance of individual nanoparticles due to the fractal nature of the aggregates, which are well known to show inhomogenous broadening.[37]

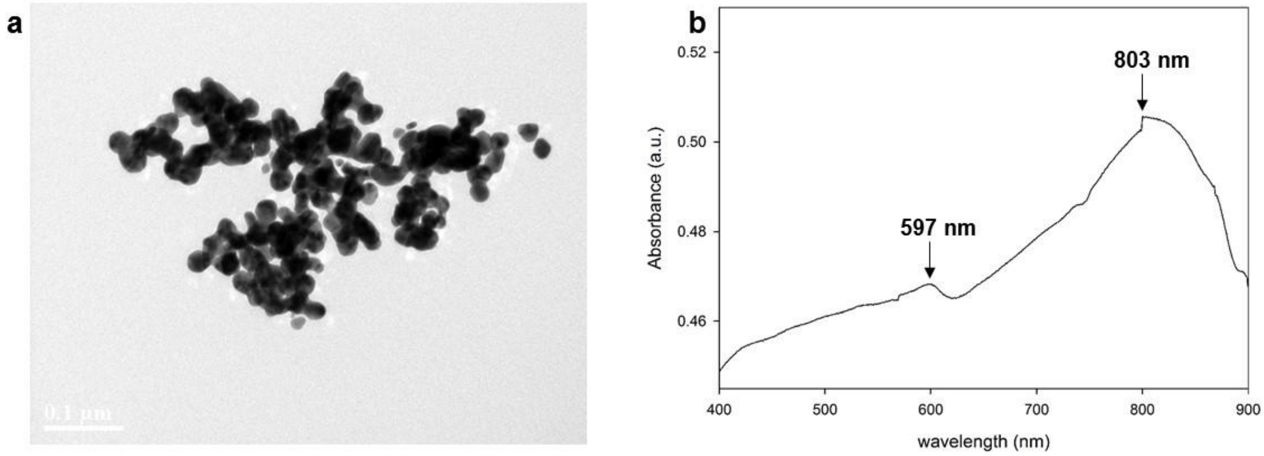

Figure 5.2. (a) TEM of Au nanoparticles aggregate after 8 hrs of stirring in EDMS sol (b) corresponding UV-Vis-NIR spectrum showing the dipole (803 nm) and quadrupole (597 nm) resonance absorbance

And the maximum located close to the plasmon resonance of single Au nanoparticle (597 nm) originates from the quadrapole plasmon excitation in coupled nanoparticles. Quadrapole plasmon resonance is visible because of the red shift of the dipole plasmon resonance and also the electric field required for excitation of quadrapole moment is lesser in aggregated systems compare to single particle.[69–71] This kind of extinction spectra are also observed in asymmetric Au nanoparticles such as gold nanorod and gold nanoshells.[6,48,49] But in these cases, multiple maxima in extinction spectra originate from the difference in longitudinal and transverse polarizabilities.[6,48,49] Thus the multiple maxima observed in our system originating from fractal aggregate structure through interparticle coupling is fundamentally different from asymmetric nanoparticle systems.

5.3.2. Flexible, free-standing thin film embedded with fractal aggregates

Thin films embedded with aggregates of Au nanoparticles were prepared through drop- casting. EDMS sol containing the Au fractal aggregates was first diluted in acetone (2 g of EDMS containing gold nanoparticle aggregates was dissolved in 7.5 mL of acetone) and then cast onto a glass substrate. The sample was air-dried and then irradiated with UV light, which initiated polymerization of epoxide moieites in the medium through the mechanism outlined in Scheme 5.1.[72] UV irradiation of diaryl iodonium salt in presence of the nonbasic hydrogen donor EDMS generates a Bronsted acid, which in turn initiates the ring opening polymerization of terminal epoxide present in EDMS. Polymerization transforms the sol into a free standing, flexible thin film (Fig 5.3d). TEMs of the thin film showed that the Au nanoparticles aggregates formed in the EDMS solution was preserved in the thin film (fig. 5.3a,b) and the optical property (NIR absorbance) of the aggregates was not significantly affected by the polymerization process, which was evident by comparing the position of absorbance maxima of the aggregates in EDMS sol (803 nm, fig. 5.2b) and the thin film (810 nm, figure 3c). Thus the UV irradiation polymerized

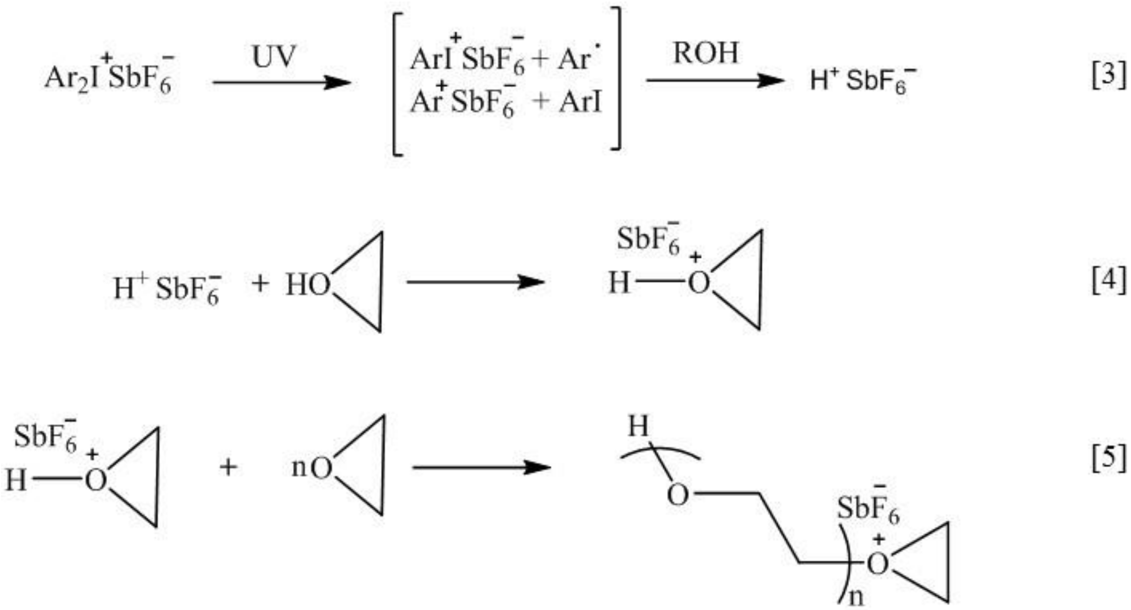

Scheme 5.1. UV polymerization of epoxide groups in EDMS[72]

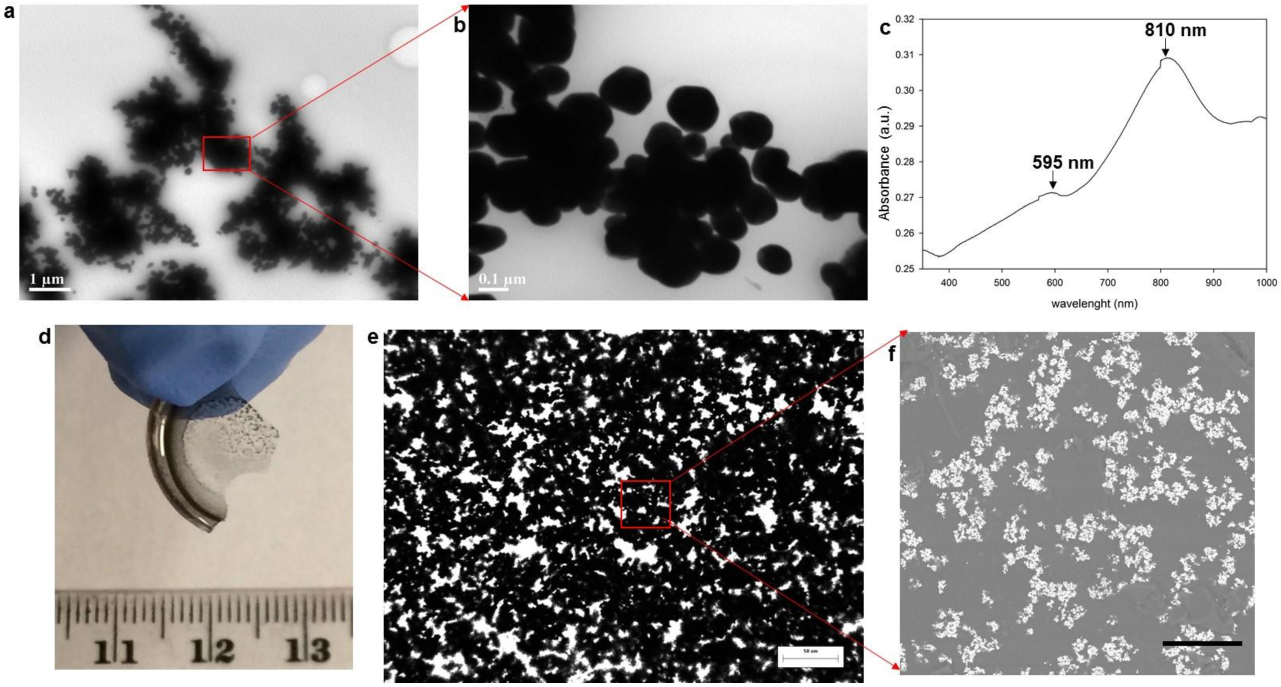

Figure 5.3. (a) TEM of Au nanoparticles aggregates in thin film (b) magnified view; (c) UV-Vis-NIR spectrum of thin film embedded with Au nanoparticle aggregate (d) photography of free standing thin film Au nanoparticle aggregate (e)

optical micrograph showing the presence of closely packed Au nanoparticle aggregate in the film (scale bar = 50 μm) (f) SEM backscattered micrograph confirming the presence of Au nanoparticle aggregate (scale bar = 20 μm)

the sol without affecting the aggregate structure. Optical micrographs and the SEM image of the thin film revealed that the Au nanoparticles aggregates were closely packed and spread uniformly throughout the entire film (area ~ 5 cm^2) (Fig. 5.3e, f). They also reveal the typical fractal aggregate structure formed through DLA mechanism.[66,67]

5.3.3. Fractal dimension of aggregates of Au nanoparticles

The fractality of the Au nanoparticle aggregates was assessed through the Hausdroff dimension or fractal dimension D; this parameter also provided insight into the complexity of the fractal structure. For example, a structure with D = 1.9 is considered more complex than one with D = 1.2;[27] furthermore, the former provides greater enhancement of the incident electromagnetic field enhancement, an essential feature for SERS substrate.[27] Fractal dimension of D = 1.801, was obtained for our aggregate structures, indicating the fractal nature of these structures.[64] As obtained fractal dimension also confirms the DLA aggregation mechanism.[65] Values were obtained by averaging the values from 10 optical micrograph images. Each optical micrograph, having several aggregated structure, covered an area of 0.15 mm^2 of the thin film.

Hausdroff dimension obtained from FracLac for the aggregate proves the fractal nature of the aggregates in our system and SERS enhancement in such a fractal geometry can be explained as follows:[28,29,37,38] Surface plasmons responsible for enhancement of Raman scattering can be typically classified into two types:[37,38] 1) localized surface plasmon modes and 2) propagating surface plasmon modes. Contribution to the electromagnetic enhancement among these two modes is strongly dependent on the morphology of the substrate. Enhancement observed in fractal geometry, which is lacking translational invariance (therefore cannot support propagating surface plasmon modes) is attributed to the localized surface plasmon modes.[37,38] This is fundamentally different from the enhancement observed in periodically arranged nanostructures such as nanoparticle (spherical, rod and cubic) arrays, nanometallic grating and nanohole array, where the enhancement is predominately due to the propagating surface plasmons. In fractal structures, surface plasmon modes originate from the dipole-dipole coupling interaction of the individual metal particles present in the fractal cluster.[37,38] These modes observed in fractal geometries are shown to be giant fluctuations of electric field spatially confined in nanometer regions generating “hotspots”. Local field enhancement in these “hotspots” can exceed upto 10^3 compare to average surface enhancement.[27–29,37,38] This clearly shows the significance of forming SERS substrate with fractal geometry.

5.3.4. Surface enhanced Raman scattering characterization

SERS effect of the fractal structured substrate was demonstrated using Eosin Y, one of the dyes used as biological stain.[73]Raman spectrum obtained for 10 mM solution of Eosin Y on the thin film substrate and 1 M solution on glass substrate is shown in Figure 5.4. The spectral peaks used as marker for Eosin Y (as shown in Table 5.1)[74] are enhanced on the thin film substrate, showing the SERS efficiency of the substrate. Enhancement factor was calculated by comparing the xanthane and benzene ring stretching mode (1310 cm^{-1}) in SERS substrate and the corresponding peak measured for 1 M solution on EDMS thin film without Au nanoparticles aggregates. SERS enhancement factor is given by

$$EF = (I_{SERS} / N_{SERS}) \ x \ (I_{NOR}/N_{NOR})$$

where I_{SERS} and I_{NOR} are the SERS and normal Raman intensities respectively.[75] N_{SERS} and N_{NOR} are corresponding number of molecules probed in SERS substrate and EDMS thin film without Au nanoparticle aggregates, respectively. For calculating the number of molecules on the SERS substrate and EDMS thin film, the probed volume was approximated as a cylinder[75] with diameter of 65 µm (laser spot size) and depth of 1 µm (laser focus depth). The number of molecules probed on the EDMS thin film $N_{NOR} = 6.15 \times 10^{10}$ and the number of molecules probed on SERS substrate $N_{SERS} = 6.1 \times 10^{7}$. With these values EF was calculated to be 3.1×10^{3}. This quantitatively shows the SERS efficiency of the substrate.

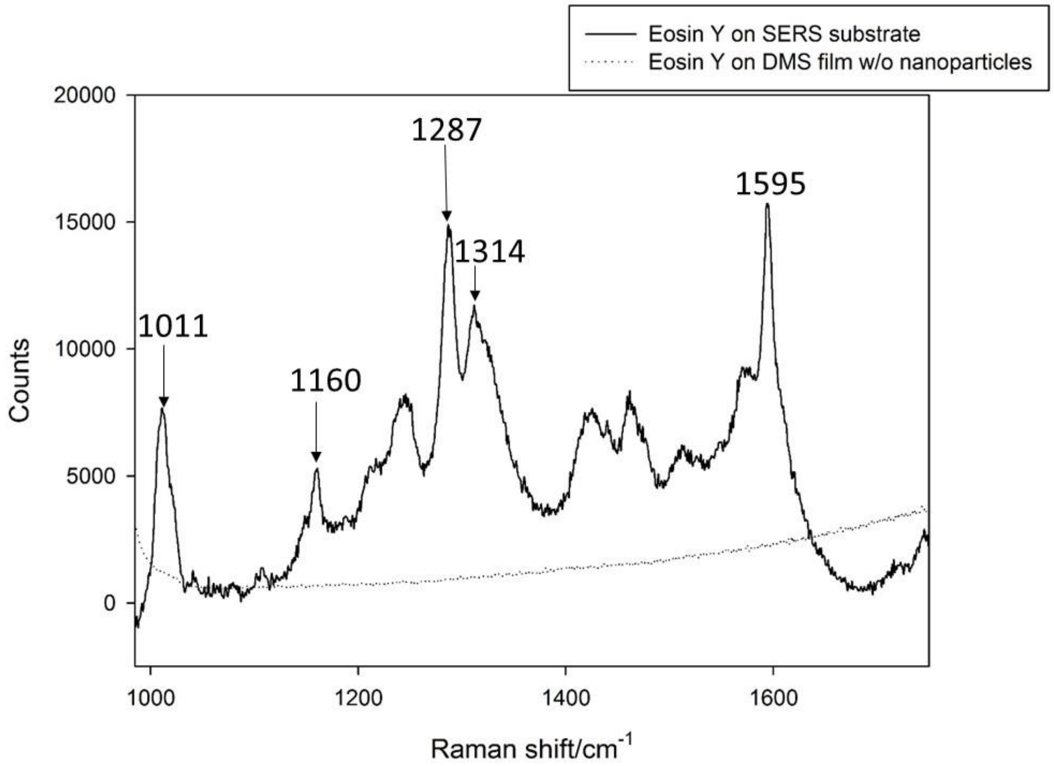

Figure 5.4. SERS spectrum of 1 mM solution of Eosin Y collected on Au nanoparticles fractal aggregates embedded thin film and Raman spectrum of 1 M solution of Eosin Y on DMS thin film without nanoparticles, both taken at the same excitation power and collection time

.

Use of NIR laser (785 nm) for Raman scattering measurement of Eosin Y prohibited resonance effect: Eosin Y has vibronic exciton band between 450 -550 nm,[76] thus the enhancement observed in our system originates predominantly from surface plasmon enhancement.

Table 5.1[74] Calculated and experiment Raman scattering modes of Eosin Y at 785 nm excitation

Shifted calculated mode cm^{-1}	Description	Experimental shift cm^{-1}
1003	xanthene ring breathing + C−Br stretches	1011
1158	xanthene and benzene ring stretches and symmetric CO_2 stretch	1160
1260	xanthene and benzene ring C−C stretches	1287
1310	xanthene and benzene ring stretches and symmetric CO_2 stretch	1314
1579	xanthene and benzene ring stretches and symmetric CO_2 stretch	1579

EF is three to four orders of magnitude less than the available rigid SERS substrate with fractal Au nanostructures.[27,35] SERS substrates with higher EF are made using expensive and complex techniques like electron beam lithography,[50] sophisticated synthetic colloidal techniques[35,51] and electrochemical reduction.[44] Although SERS substrates made using these techniques provide higher EF, the high cost, substrate rigidity and the complexity of these processes prevent them from converting to high throughput processes and practical applications. Ours is one of the first works combining the drop casting technique with photopolymerization to fabricate flexible, free standing SERS substrate with Au fractal nanostructures showing NIR SERS activity on epoxide siloxane matrix. Drop casting is an effective nonlithographic route for fabricating patterns of metal nanoparticles in polymer thin films.[52–54] The thickness of the film can be easily controlled by the volume of the solution casted and the concentration of metal nanoparticles in the thin film can be controlled by controlling the concentration of metal nanoparticles in the solution. Few works utilized this elegant technique to fabricate SERS substrate[52–54] but to our knowledge, this is the first work combining the drop casting technique with photopolymerization for making flexible free standing SERS substrate. Usually thin films made of drop casting is limited to thermoplastic polymers or linear polymers as it involves dissolution of polymer in a suitable solvent.[52,53] Our approach is unique as we extended this technique to thermosetting polymer like epoxide. This was made possible as we dissolved the monomer (which is soluble in polar solvent) along with Au metal nanoparticles and not the polymer (which is impossible in case of thermosets) and the fractal aggregates of Au metal nanoparticles formed through DLA were preserved by photocrosslinking the epoxide monomer through cationic polymerization. Because of our new approach, drop casting can be extended to variety of photocationically polymerizable monomers. Also fabricating SERS substrates from robust epoxide matrix as its own advantages. Epoxide matrix is thermomechanically stable and has very good solvent resistance.[77] The matrix swells in solvents and does not dissolves, thus the analytes dissolved in solvents can permeate the matrix and access the hot spots generated by the fractal aggregates of metal nanoparticles, which is ideal for SERS substrate. Also the excellent transparency of epoxide thin film towards NIR (probing laser) allows the laser to pass through the film to excite the SPR of Au nanoparticles fractal aggregates. One of the drawbacks of epoxide matrix is its rigidity, we mitigated that by using a siloxane epoxide monomer, which provides the flexibility without hampering the transparency or the thermomechanical stability.

5.4 Conclusions

In summary, we have presented for the first time a facile route for fabricating free-standing, flexible epoxide/siloxane based SERS substrate incorporated with fractal aggregates of Au nanoparticles by combining *in-situ* synthesis, drop casting and UV polymerization. Formation of fractal aggregate structures was thoroughly characterized by electron and optical microscopy and also by UV-Vis-NIR spectroscopy. Fractality of the structures was analyzed by box counting method. NIR plasmon resonance absorbance shown by the fractal aggregates was used to demonstrate the SERS activity of the substrate and electromagnetic field enhancement was explained in terms of the fractal geometry of the gold nanoparticles aggregates. These inexpensive, easily fabricated substrates have considerable promise as practical SERS substrates; the embedded fractal arrays of Au nanoparticles exhibit NIR plasmon resonance and possibility of excellent interactions with analytes including biomolecules[48,49] while the epoxide matrix imparts excellent mechanical stability, adhesion to analytes and transparency in the visible and NIR spectral regions.[76] Also our approach provides a way to extend this inexpensive techniques to a variety of photocationcally polymerizable matrices.

References

(1) C.V. Raman; Krishnan, K. S. *Nature* **1928**, *121*, 501.

(2) McCreery, R. L. *Raman Spectroscopy for Chemical Analysis*; John Wiley & Sons, Inc.: New York, 2000.

(3) Kneipp, J.; Kneipp, H.; Kneipp, K. *Chem. Soc. Rev.* **2008**, *37* (5), 1052–1060.

(4) Kneipp, K.; Wang, Y.; Kneipp, H.; Perelman, L. T.; Itzkan, I.; Dasari, R. R.; Feld, M. S. *Phys. Rev. Lett.* **1997**, *78* (9), 1667–1670.

(5) Nie, S.; Emory, S. R. *Science* **1997**, *275* 1102–1106.

(6) Grant, C. D.; Schwartzberg, A. M.; Norman, T. J.; Zhang, J. Z. *J. Am. Chem. Soc.* **2003**, *125* (2), 549–553.

(7) Lim, D.-K.; Jeon, K.-S.; Hwang, J.-H.; Kim, H.; Kwon, S.; Suh, Y. D.; Nam, J.-M. *Nat. Nanotechnol.* **2011**, *6* (7), 452–460.

(8) Wang, X.; Wang, C.; Cheng, L.; Lee, S.; Liu, Z. *J. Am. Chem. Soc.* **2012**, *134*, 7414–7422.

(9) Lal, S.; Link, S.; Halas, N. J. *Nat. Photonics* **2007**, *1* (11), 641–648.

(10) Ko, H.; Singamaneni, S.; Tsukruk, V. V. *Small* **2008**, *4* (10), 1576–1599.

(11) Wang, A. X.; Kong, X. *Materials (Basel).* **2015**, *8*, 3024–3052.

(12) Sha, M. Y.; Xu, H.; Natan, M. J.; Cromer, R. *J. Am. Chem. Soc.* **2008**, *130*, 17214–17215.

(13) Piorek, B. D.; Lee, S. J.; Santiago, J. G.; Moskovits, M.; Banerjee, S.; Meinhart, C. D. *Proc. Natl. Acad. Sci. U. S. A.* **2007**, *104* (48), 18898–18901.

(14) Monolayers, S.; Paxton, W. F.; Kleinman, S. L.; Basuray, A. N.; Stoddart, J. F.; Duyne, R. P. Van. *J. Phys. Chem. Lett.* **2011**, *2*, 1145–1149.

(15) Kleinman, S. L.; Ringe, E.; Valley, N.; Wustholz, K. L.; Phillips, E.; Scheidt, K. A.; Schatz, G. C.; Duyne, R. P. Van. *J. Am. Chem. Soc.* **2011**, *133*, 4115–4122.

(16) Leona, M. *Proc. Natl. Acad. Sci. U. S. A.* **2009**, *106* (35), 14757–14762.

(17) Stoddart, P. R.; White, D. J. *Anal Bioanal Chem* **2009**, *394*, 1761–1774.

(18) Sharma, B.; Frontiera, R. R.; Henry, A.; Ringe, E.; Duyne, R. P. Van. *Mater. Today* **2012**, *15* (1-2), 16–25.

(19) Knoll, B Keilmann, F. *Nature* **1999**, *399* (May), 134–136.

(20) Pozzi, E. A.; Zrimsek, A. B.; Lethiec, C. M.; Schatz, G. C.; Hersam, M. C.; Duyne, R. P. Van. *J. Phys. Chem. C* **2015**, *119*, 21116–21124.

(21) Michaels, A. M.; Brus, L. *J. Phys. Chem. B* **2000**, *104* (50), 11965–11971.

(22) Xu, H.; Bjerneld, E.; Käll, M.; Börjesson, L. *Phys. Rev. Lett.* **1999**, *83* (21), 4357–4360.

(23) Mark I. Stockman, Shalaev, V. M.; Moskovits, M.; Botet, R. and T. F. G. *Physcial Rev. B* **1992**, *46* (5), 2821–2831.

(24) Nikoobakht, B.; El-Sayed, M. a. *J. Phys. Chem. A* **2003**, *107* (18), 3372–3378.

(25) Karen Faulds; Rachael E. Littleford; Duncan Graham; Geoffrey Dent; Smith, W. E. *Anal. Chem.* **2004**, *76* (3), 592–598.

(26) S. V and S. M. *Z.Phys.D-Atoms,Molecules Clust.* **1988**, 1–9.

(27) Garcia-Ramos, J. A. S.-G. and J. V. *J.Chem.Phys* **1998**, *108* (January), 317–325.

(28) Wang, Z.; Pan, S.; Krauss, T. D.; Du, H.; Rothberg, L. J. *Proc. Natl. Acad. Sci. U. S. A.* **2003**, *100* (15), 8638–8643.

(29) Li, K.; Stockman, M. I.; Bergman, D. J. *Phys. Rev. Lett.* **2003**, *91* (22), 1–4.

(30) Qiu, T.; Wu, X. L.; Shen, J. C.; Xia, Y.; Shen, P. N.; Chu, P. K. *Appl. Surf. Sci.* **2008**, *254*, 5399–5402.

(31) Zhang, P.; Wang, S. *ChemPhysChem Minireviews* **2014**, 1–13.

(32) Wen, X.; Xie, Y.; Wing, M.; Mak, C.; Cheung, K. Y.; Li, X.; Renneberg, R.; Yang, S. *Langmuir* **2006**, *22* (17), 4836–4842.

(33) Dong, J.; Qu, S.; Zheng, H.; Zhang, Z.; Li, J.; Huo, Y.; Li, G. *Sensors Actuators B. Chem.* **2014**, *191*, 595–599.

(34) Kim, W.; Safonov, V. P.; Shalaev, V. M.; Armstrong, R. L. *Physcial Rev. Lett.* **1999**, *82* (24), 4811–4814.

(35) Lili He, Nam_Jung Kim, Hao Li, Z. H. and M. L. *J.Agric.Food Chem* **2008**, *56*, 9843–9847.

(36) Amarandei, G.; Arshak, A.; Corcoran, D. *Appl. Mater. Interfaces* **2013**, *5*, 8655–8662.

(37) V. A. M. and V. M. Shalaev, *Phys. Rev. B* **1996**, *53* (5), 2425–2436.

(38) M.Shalaev, V. *Phys. Rep.* **1996**, *272*, 61–137.

(39) Brouers, F.; Blacher, S.; Sarychev, A. K. **1998**, *58* (23), 897–903.

(40) Chen, T. L.; Dikken, D. J.; Prangsma, J. C.; Segerink, F.; Herek, J. L. *New J. Phys.* **2014**, *16* (9), 093024.

(41) Liu, J.; Fu, Y.; Guo, A.; Wang, C.; Huang, R.; Zhang, X. *J.Phys.Chem.C* **2008**, *112*, 4242–4247.

(42) Cavaliere, E.; Ferrini, G.; Pingue, P.; Gavioli, L. *J. Phys. Chem. C* **2013**, *117*, 23305–23312.

(43) Agrawal, V. V.; Kulkarni, G. U.; Rao, C. N. R. *J. Colloid Interface Sci.* **2008**, *318*, 501–506.

(44) Dong, J.; Gong, J.; Liu, J.; Chen, M.; Yan, X. *Electrochim. Acta* **2012**, *60*, 264–268.

(45) Gottheim, S.; Zhang, H.; Govorov, A. O.; Halas, N. J. *ACS Nano* **2015**, *9* (3), 3284–3292.

(46) F.Brouers and S. Blacher, A.N.Lagarkov and Andrey K.Sarychev, P. G. and V. M. S. *Physcial Rev. B* **1997**, *55* (19), 234–245.

(47) Liu, R.; Xiong, Y.; Tang, W.; Guo, Y.; Yan, X.; Si, M. *J. Raman Spectrosc.* **2013**, *44* (3), 362–369.

(48) Samanta, A.; Maiti, K. K.; Soh, K. S.; Liao, X.; Vendrell, M.; Dinish, U. S.; Yun, S. W.; Bhuvaneswari, R.; Kim, H.; Rautela, S.; Chung, J.; Olivo, M.; Chang, Y. T. *Angew. Chemie - Int. Ed.* **2011**, *50* (27), 6089–6092.

(49) Von Maltzahn, G.; Centrone, A.; Park, J. H.; Ramanathan, R.; Sailor, M. J.; Alan Hatton, T.; Bhatia, S. N. *Adv. Mater.* **2009**, *21* (31), 3175–3180.

(50) Cakmakyapan, S.; Cinel, N. A.; Cakmak, A. O.; Ozbay, E. *Opt. Express* **2014**, *22* (16), 531–537.

(51) Adams, S. M.; Campione, S.; Caldwell, J. D.; Bezares, F. J.; Culbertson, J. C.; Capolino, F.; Ragan, R. *Small* **2012**, *8* (14), 2239–2249.

(52) Roth, S. V; Herzog, G. *J.Phys.;Condens.Matters* **2011**, *23*, 254208–254217.

(53) Kuhlmann, M.; Feldkamp, J. M.; Patommel, J.; Roth, S. V; Schroer, C. G.; Timmann, A.; Gehrke, R.; Peter, M. *Langmuir* **2009**, *25* (13), 7241–7243.

(54) Gebhardt, R.; Burghammer, M.; Riekel, C.; Roth, V.; Mu, P. *Macromol. Biosci.* **2008**, *8*, 347–354.

(55) Hecht, A.; Commiskey, P.; Lazaridis, F.; Argyrakis, P.; Kopelman, R. *ChemPhysChem* **2014**, *15* (16), 3444–3446.

(56) Ethers, P. P. *J. Am. Chem. Soc.* **1979**, *101* (15), 4249–4258.

(57) Longenberger, L and Mills, G. *J. Phys. Chem.* **1995**, *99* (2), 475–478.

(58) Ishii, T.; Otsuka, H.; Kataoka, K.; Nagasaki, Y. *Langmuir* **2004**, *20* (8), 561–564.

(59) Ghosh, S. K.; Pal, T. *Chem. Rev.* **2007**, *107*, 4797–4862.

(60) Jain, P. K.; Lee, K. S.; El-Sayed, I. H.; El-Sayed, M. A. *J. Phys. Chem. B* **2006**, *110* (14), 7238–7248.

(61) Kelly, K. L.; Coronado, E.; Zhao, L. L.; Schatz, G. C. *J. Phys. Chem. B* **2003**, *107*, 668–677.

(62) Pong, B. K.; Elim, H. I.; Chong, J. X.; Ji, W.; Trout, B. L.; Lee, J. Y. *J. Phys. Chem. C* **2007**, *111* (17), 6281–6287.

(63) Jr Witten, T. . and; Sander, L. *Physcial Rev. Lett.* **1981**, *47* (19), 1400–1403.

(64) Wang, S.; Xin, H. *Journa Phys. Chem. B* **2000**, *104*, 5681–5685.

(65) Halsey, T. C. *Phys. Today* **2000**, *53* (11), 36.

(66) Enculescu, M.; Enculescu, I.; Topa, V. *J. Optoelectron. Adv. Mater.* **2006**, *8* (3), 1230–1233.

(67) Cheng, W.; Dong, S.; Wang, E. *J. Phys. Chem. B* **2005**, *109* (41), 19213–19218.

(68) Su, K. .; Wei, Q. .; Zhang, X. *Nano Lett.* **2003**, *3* (8), 1087–1090.

(69) Jensen, T.; Kelly, L.; Lazarides, A.; Schatz, G. C. *J. Clust. Sci.* **1999**, *10* (2), 295–317.

(70) Zhong, Z.; Patskovskyy, S.; Bouvrette, P.; Luong, J. H. T.; Gedanken, A. *J. Phys. Chem. B* **2004**, *108*, 4046–4052.

(71) Chegel, V.; Rachkov, O.; Lopatynskyi, A.; Ishihara, S.; Yanchuk, I.; Nemoto, Y.; Hill, J. P.; Ariga, K. *J. Phys. Chem. C* **2012**, *116* (4), 2683–2690.

(72) Crivello, J. V. *Adv. Polym. Sci.* **1984**, *62*, 1–48.

(73) Walker, J. M. *The Protein Protocols Handbook*, Second.; Humana Press Inc.: Totowa, New Jersey, 2002; Vol. 3.

(74) Greeneltch, N. G.; Davis, A. S.; Valley, N. a.; Casadio, F.; Schatz, G. C.; Van Duyne, R. P.; Shah, N. C. *J. Phys. Chem. A* **2012**, *116* (48), 11863–11869.

(75) Payne, E. K.; Rosi, N. L.; Xue, C.; Mirkin, C. a. *Angew. Chemie - Int. Ed.* **2005**, *44* (32), 5064–5067.

(76) Fornasiero D and Kurucsev T, *J. Chem. SOC., Faraday Trans. 2*, **1986**, *82*, 15-19

(77) Takahiro, G.; Itagaki, S.; Kajiwara, T.; Abe, Y.; Hatakeyama, T.; Aoki, R. *Polym. J.* **2009**, *41* (7), 541–546.

Supplementary information

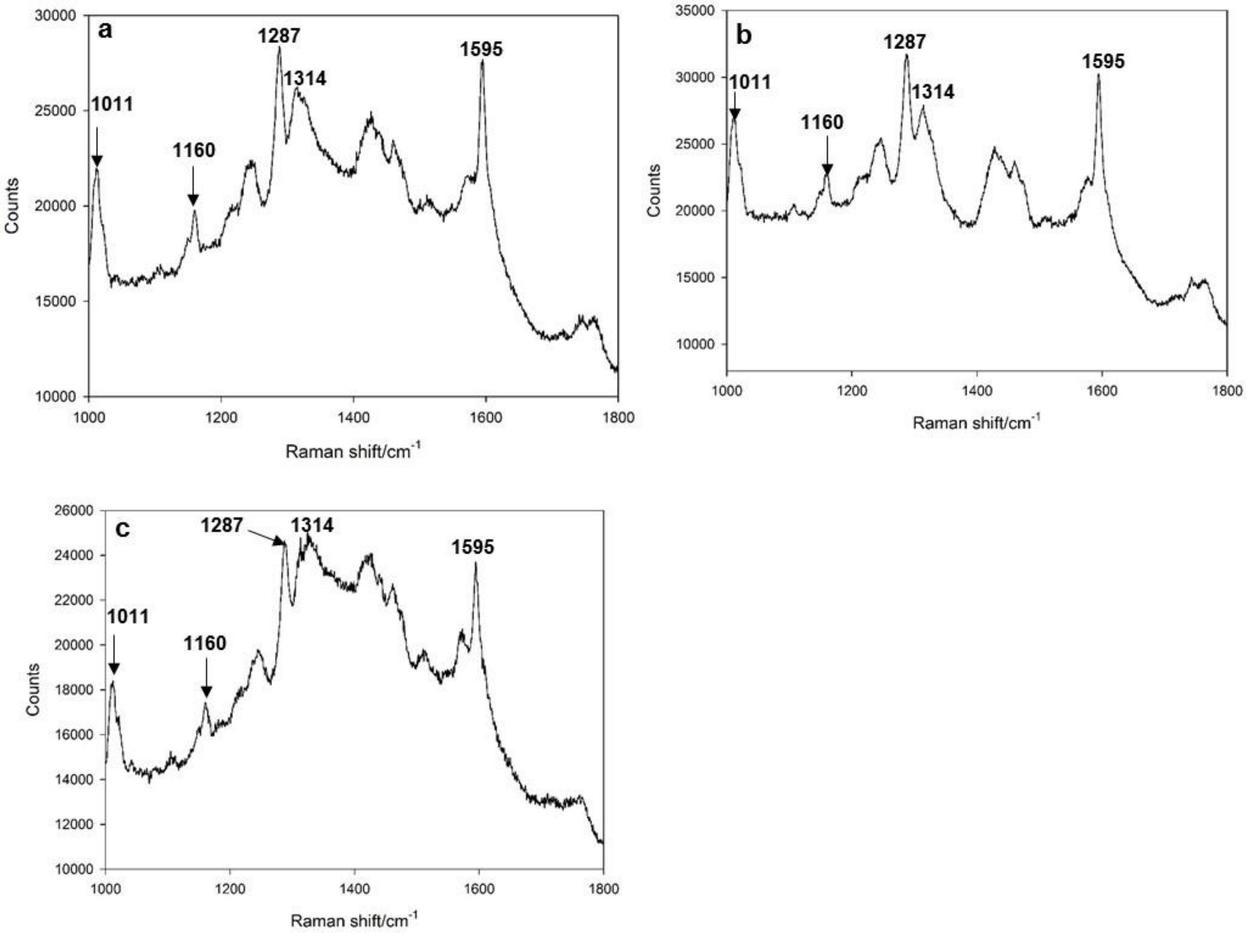

Figure S5.1. SERS spectrum of 1 mM solution of Eosin Y reproduced on 3 different Au nanoparticles fractal aggregates embedded thin films a) thin film 1 b) thin film 2 c) thin film 3. All the spectra are taken under same experimental conditions.

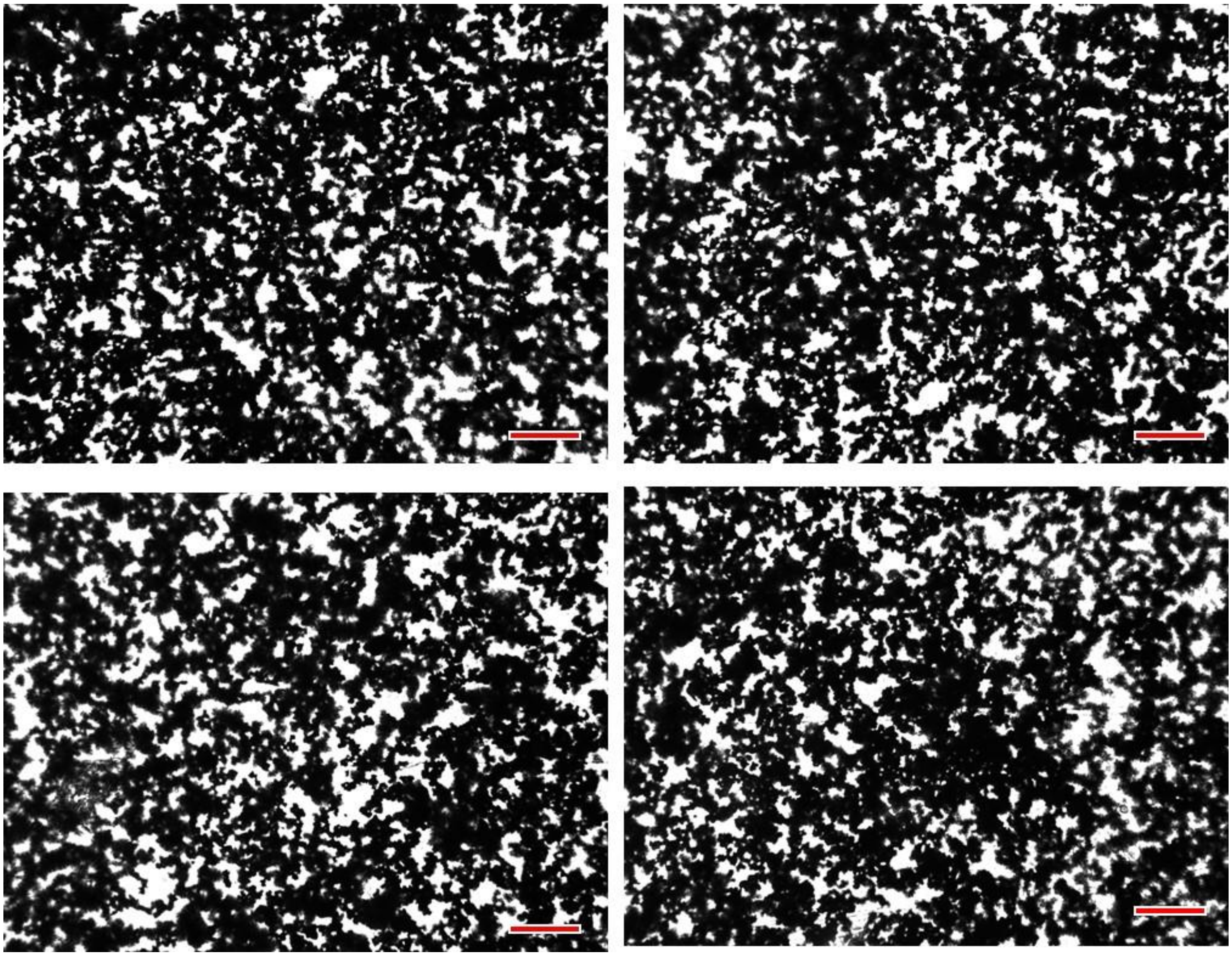

Figure S5.2. Samples of optical micrograph used for fractal dimension calculations, showing the presence of closely packed Au nanoparticle aggregate in the film (scale bar = 50 μm)

Fractal dimension measurement

Fractal dimension D was measured using box counting method. In this method, D is measured by placing several grids of decreasing box size and by counting the number of boxes containing the parts of fractal structure. The slope of the log-log plot of number of boxes containing the parts of fractal structure (n, count) *versus* size of the box (ε), gives the fractal dimension D.

$$D = \log n / \log \epsilon \quad \lim \epsilon \rightarrow 0$$

Measurement was done on binary image (optical micrographs were converted to binary image) as the program reads only binary image. A sample procedure is shown in figure S3, optical micrograph (figure S3a) is converted to binary image (figure S3b) and by applying the box counting method (using ImageJ plugin fraclac), a log-log plot of n versus ε is generated (figure S3c) and the slope of the line gives the fractal dimension.

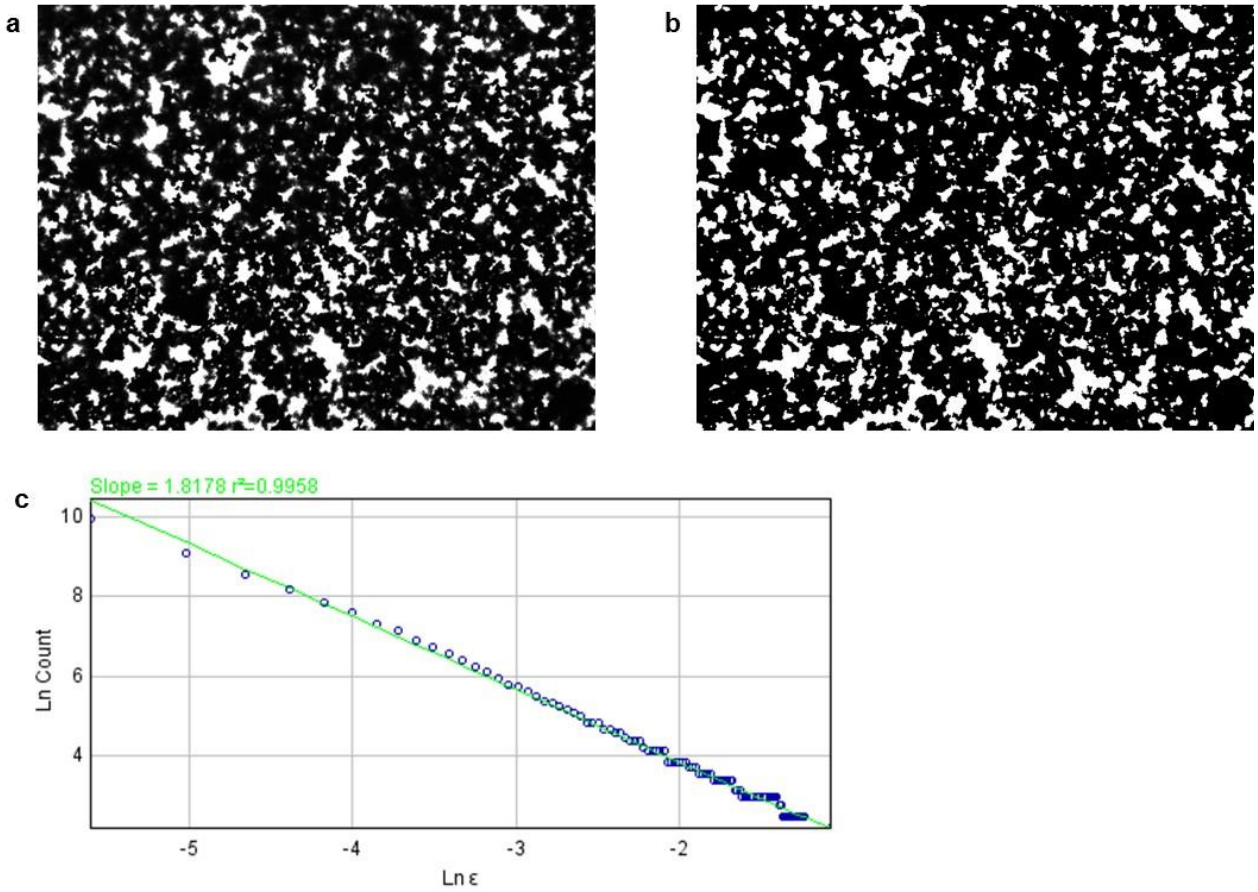

Figure S5.3. Determination of fractal dimension using box counting method (a) optical micrograph of thin film embedded with Au nanoparticles fractal aggregates (b) corresponding binary image (c) log-log plot of n *Versus* ε, with the slope giving the fractal dimension

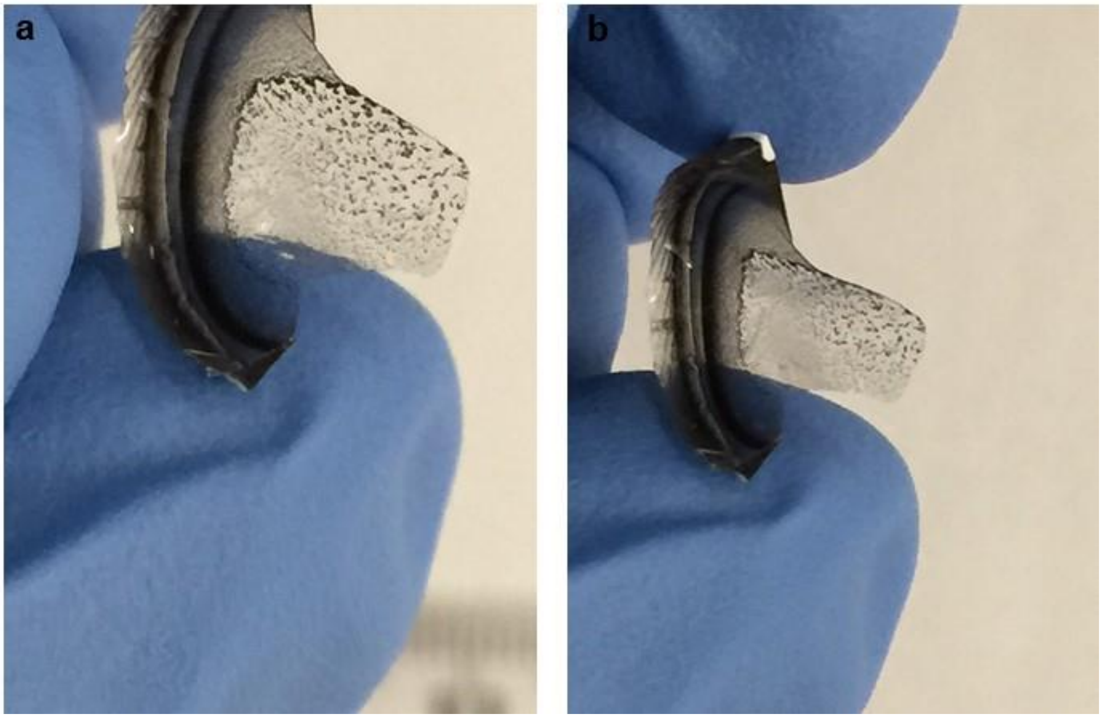

Figure S5.4. Picture showing the flexibility of the thin film a) Normal b) flexed

Chapter 6

3-D Nonlinear inSCRIption of complex micro-comPonenTs (3D-NSCRIPT): printing functional polymer structures with nonlinear waves of LED light

Dinesh Kumar Basker,

Note: Self-trapping time, used in this work was conducted by Oscar Alejandro Herrera Cortes

Abstract

We have developed an inexpensive, room-temperature technique for fabricating complex epoxide based 3D dieletric and metallodielectric microstructures and components with dimensions that range from 500 μm to centimeters (limited only by the experimental set-up). Our method is based on the nonlinear propagation of visible incoherent light through photopolymerizable media and simultaneous deposition of Au nanoparticles along the beam propagation path, which gives several key advantages over existing photolithographic based 3D printing methods: (i) generation of structures with "depths" that exceed several millimeters; (ii) ability to simultaneously employ multiple light beams, each introducing an additional degree of freedom in the design of the photofabricated structure and (iii) rapid illumination (eliminating the need for lengthy, layer-by-layer construction of 3-D structures). A typical protocol to microprint structures consists of launching a collimated beam of LED light into a cell containing a photoresponsive resin. Amplitude masks imprinted with patterns are placed on the different entrance faces of the sample cell; the patterns are designed to generate the required 3-D structure within the medium. The collimated beam the respective pattern into the medium by inducing permanent changes in refractive index as they propagate through the medium. The refractive index change creates nonlinear conditions in the medium, which leads to the self-trapping of beam allowing it to propagate over unusually long distances (several centimeters). In this way, self-trapped beam inscribes patterns with

unusually long depths. We also exploit the interactions between multiple, non-parallel self-trapped beams to create 3-D microstructures with a high degree of complexity that would be impossible to generate with conventional techniques.

6.1. Introduction

3-D printing of polymer structures has been extensively integrated into a variety of applications ranging from the manufacture of engineering components to biotechnology.[1–9] 3-D printers typically employ a stepwise approach to constructing the desired object. A stereolithographic printer, for example, photoinscribes cross-sections of the object at the surface of a fluid polymerizable resin; each printed slice is submerged in turn to expose fresh resin and the process repeated until fabrication of the entire 3-D structure is complete. [10, 11] In bottom-up stereolithographic printing, the resin is irradiated through the optically transparent base of its vat; printing speed can be significantly enhanced by always maintaining a thin layer of fresh resin immediately below the printed layer.[12] In another commonly employed technique - material jetting or polyjet - crosssectional layers are generated in turn by first patterning a surface with the liquid resin through a multi-nozzled print head and then fixing this 2-D pattern with UV light. This technique is particularly versatile as it allows tailoring of the material composition of each layer.[13, 14] In fused deposition modelling, thermoplastic materials are extruded and deposited layer-by-layer through the print-head onto a scaffold, which is ultimately removed, leaving behind the 3-D object.[15,16] Binder jetting or inkjet powder printing consists of binding successive layers of powders, typically thermoplastics, with glue applied through the print head.[17–19] Metals including stainless steel and copper can be printed using this process although high temperatures and additional infusion of metal powder are necessary.[20] In selective laser sintering, local heat from the laser scribe itself is employed to directly bind powders of metals, thermoplastics, glass and ceramics without the need for secondary heat treatment.[21–23] Selective heat sintering replaces the laser with a thermal print head to fuse successive layers of thermoplastic powders.[24]

The predominant approach of 3-D printing technologies is, as summarized above, to sequentially assemble thin layers into the custom-designed object. In the most commonly employed stereolithographic printing technique, the thickness or depth of each layer is typically limited to < 100 μm; this is because broadening caused by the natural diffraction – or divergence - of light and attenuation due to absorbance inherent to the photosensitized medium causes increasing blurring of the projected image with sample depth. While this layer-by-layer approach can build in considerable structural complexity both along the transverse and longitudinal dimensions of the object, the interfaces between layers inevitably introduce weakness such as fracture planes. Furthermore, this approach cannot generate thick *seamless* samples, which maintain their structural integrity and thereby, strength along their longitudinal axes.

Here we report a fundamentally new photolithographic route, which counters the limitations of optical divergence and generates seamless epoxide-based dielectric and metallodielectric structures. Termed 3-D Nonlinear inSCRIption of complex micro-comPonenTs (3D-NSCRIPT), our method harnesses nonlinear light waves that can be elicited in photopolymerizable resins with low-intensity, visible light from LEDs. When launched into a photopolymerizable epoxide resin, the LED beam initiates cationic polymerization along its propagation path; corresponding positive changes in the refractive index (Δn) of the medium counteract the natural divergence of the beam, enabling it to propagate without broadening or decreasing in intensity over very long distances (>> Rayleigh range).[25–29] This nonlinear waveform inscribes and becomes entrapped within a polymerized epoxy channel – or waveguide – and travels as a self-trapped beam, which characteristically retains its spatial intensity profile throughout propagation. In the case of beams with a radially-symmetric, near-Gaussian or parabolic profile, the self-induced polymer channel is cylindrical. In 3D-NSCRIPT, spatial intensity patterns designed to generate specific geometries are embedded in nonlinear waves, which carry them over long distances without blurring and in this way, inscribe seamless, solid objects. To demonstrate the versatility of this technique, we show that by coupling cationic polymerization of epoxides with the simultaneous reduction of gold salts[30] it is possible to fabricate thick metallodielectric structures. We also show that by exploiting interactions such as the fusion of counter-propagating nonlinear waves,[31] it is possible to introduce additional structural complexity to the object.

6.2. Experimental

6.2.1 Materials

3,4-epoxycyclohexylmethyl-3',4'-epoxycyclohexane carboxylate (**1**), gold(III) tetrachloride, the photosensitizer (PS), camphorquinone (**2**) (97 % purity), and poly (1,4-butanediol (M_n 250)) (pTHF) (**3**) were purchased from Sigma Aldrich (Oakville, Ontario). Epoxypropoxypropyl terminated polydimethylsiloxane (DMS) (**4**) was purchased from Gelest Inc. (Morrisville, USA). The photoinitiator (PI), [4-(octyloxy) phenyl] phenyliodonium hexafluroantimonate (**5**), was obtained from Hampford Research Inc. (Stratford, USA)

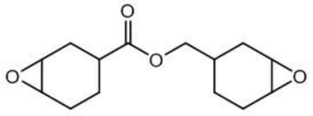

1

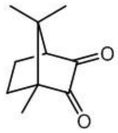

2

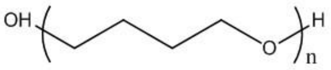

3

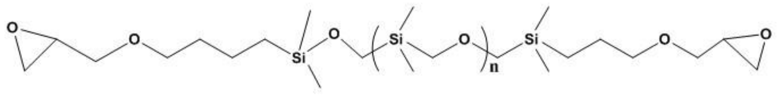

4

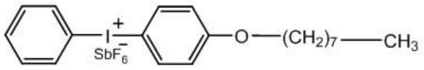

5

6.2.2. Preparation of photopolymerizable epoxides

Sols for the fabrication of 3-D microstructures were prepared by combining the biscycloaliphatic epoxide (76 wt. %), DMS (10 wt. %) and pTHF

(10 wt. %) with PS (2 wt. %) and PI (2 wt. %); the mixture was stirred for 48 hrs. prior to use. Sols containing Au were prepared by combining gold(III) tetrachloride (1 wt. %), pTHF (10 wt. %), epoxide (75 wt.%), DMS (10 wt.%), PS (2 wt. %) and PI (2 wt.%); the Au salt was first dissolved in pTHF prior to mixing with the remaining components.

6.2.3. Optical assembly

Schemes of optical set-ups employed for experiments are shown in Figure 1. Blue light (λ_{max} = 460 nm from a LED source (Kerber Applied Research Inc. Hamilton, Ontario) was collimated by a planoconvex lens (F.L = 250 mm, d = 25.4 mm) and launched onto the entrance face of a cylindrical (o.d. = 12 mm, i.d. = 10 mm; pathlength = 3 mm, 5 mm, 10 mm, 15 mm, 20 mm or 40 mm) or rectangular cuboid (L x W x H = 110 mm x 70 mm x 80 mm) cell containing photopolymerizable sol. The entrance and exit faces of sample cells were optically flat and transparent between 320 nm to 800 nm. An amplitude mask patterned with the desired feature to be imposed on the beam was placed at the entrance face of the sample cell. The spatial intensity profile of the optical field at the exit face of the sample cell was imaged through a pair of plano-convex lenses (F.L. = 250 mm, d = 25.4mm) onto a high-resolution, progressive scan, charged-coupled device (CCD) chip (D, 1360 (H) x 1024 (V) of 4.65 μm square pixels, sensitivity range = 350 nm to 1150 nm; WinCamD^{TM} digital camera, Data Ray Inc., USA). A Camcorder Handycam (Canon VIXIA HF R700, with 1920 x1080p resolution) positioned above the sample cell provided top-down photographs and videos of experiments. All optical components were purchased from Newport Corporation (CA, USA) and mounted on a rail with carriers that could be translated with a resolution of ± 0.25 mm.

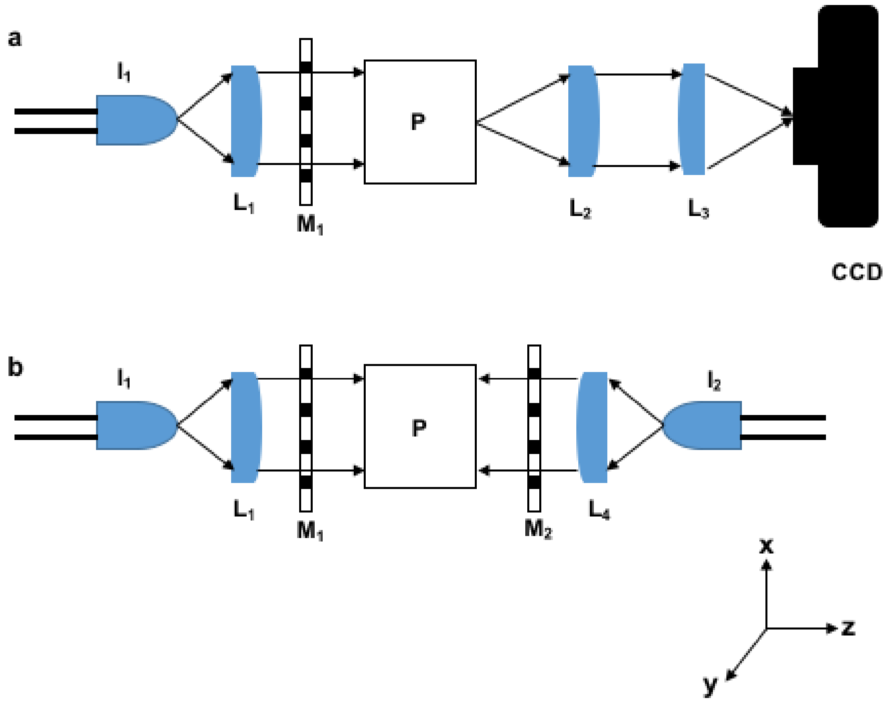

Figure 6.1. Schemes of optical assemblies for 3D NSCRIPT comprising (a) single LED beam (l_1), which is collimated by a plano-convex lens (L_1) and launched through an amplitude mask (M_1) onto the entrance face of a sample cell containing photopolymerizable epoxide (P). Spatial intensity profiles at the sample exit face are imaged through a planoconvex lens pair (L_2, L_3) onto a CCD camera and (b) counter-propagating LED beams (l_1, l_2), which are each collimated (L_1, L_4) and simultaneously launched into P through amplitude masks (M_1, M_2).

6.2.4. Extraction, processing and characterization of 3-D polymer microstructures

Once solid microstructures were generated through photopolymerization with nonlinear waves, they remained immersed in the fluid sol, which had been unexposed to light. The microstructures were extracted by first decanting the unpolymerized sol, detaching them from the entrance face of the sample cell, washing with acetone and then air-drying for eight hours. Finally, structures were polished with 80 grit grinding wheel and smoothened with 400 & 600 grit sandpaper. TEM of microstructures containing Au nanoparticles were acquired with a JEOL 2010F field emission microscope equipped with EDS X-ray spectrometer. ~70 nm-thick samples for TEM was prepared through ultramicrotomy. Scanning electron micrographs (SEM) were recorded with a VEGA3 SB instrument with an accelerating voltage of 10 KV in secondary electron mode.

6.3 Results and discussion

Figure 6.1 contains schemes of optical assemblies employed for 3D NSCRIPT; collimated light from a blue-emitting (460 nm) LED is first passed through an amplitude mask bearing a specific pattern and launched into the entrance face of a transparent cell containing fluid epoxide resin. Spatial intensity profiles of the optical field acquired at the sample exit face provide detailed insight into the temporal evolution of the optical field and growth of the 3D structure.

Figure 6.2 provides proof of concept and the typical experimental process of 3D NSCRIPT. We generated epoxide cylinders using circular LED beams with diameters ranging across at least two orders of magnitude (limited only by the experimental set-up); the beams in Figure 6.2(a-d) are 500 μm, 2000 μm, 10000 μm and 10000 μm - wide, respectively. Figure 6.2(a) traces the evolution of the narrowest beam at the exit face of the sample cell (pathlength = 3 mm). At t = 0 s - in the absence of polymerization and under linear conditions - the beam appears broad (501 μm) and weak (relative intensity = 10.1 %) at the exit face (Figure 6.2a) because it suffers divergence as it propagates from the entrance to the exit face of the sample cell; divergence is particularly significant for LED light due to its spatial and temporal incoherence.[32] However, as polymerization is initiated along its path through the epoxide resin, concomitant changes in refractive index counter the natural tendency of the beam to diverge; the resulting high-refractive index region is a self-induced waveguide, which entraps the beam and guides it through the medium without significant broadening or attenuation. At the exit face, the emergence of the self-trapped beam results in a significant increase in relative intensity from 10.1 % to 85.1 % with a corresponding decrease in width from 501 μm to 319 μm.

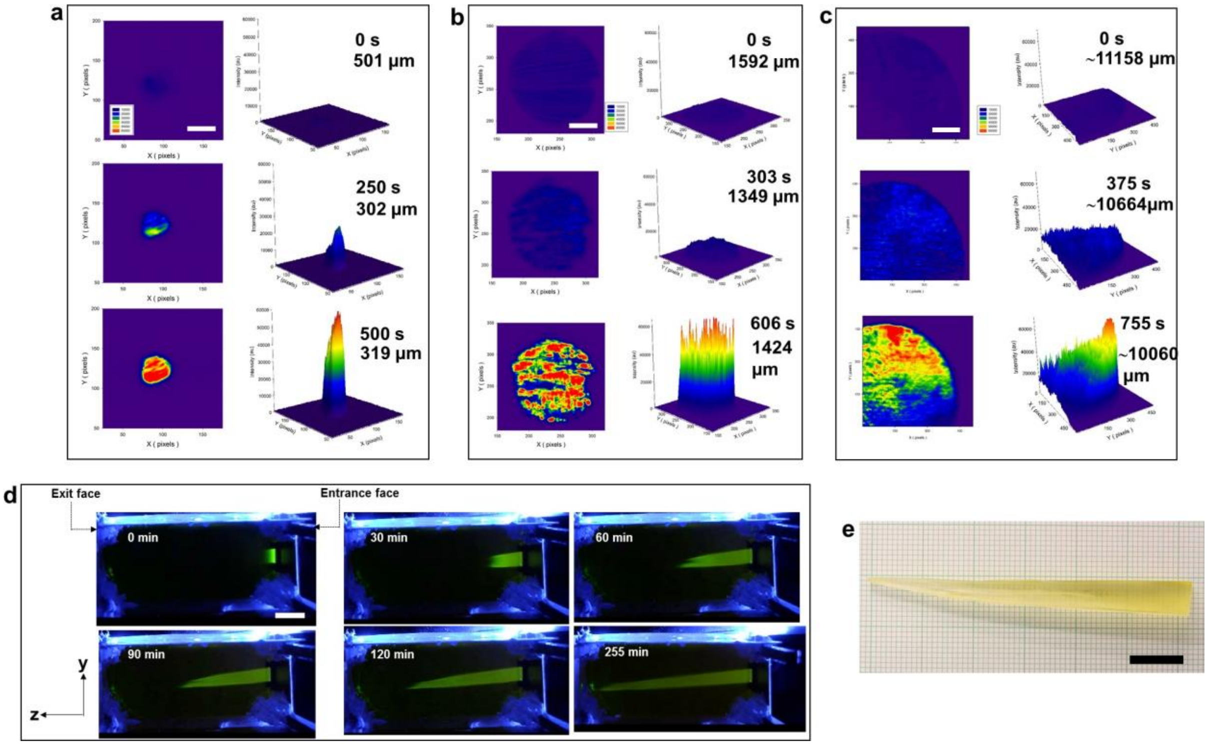

Figure 6.2. Representative examples of self-trapped beams in epoxide resins generated with LED beams with diameter (FWHM) at exit face, incident intensity and cell pathlengths respectively, of (a) 501 µm, 102 mWmm^{-2}, 3 mm (b) 1592 µm, 10 mWmm^{-2}, 5 mm and (c) ~11158 µm, 0.13 mWmm^{-2}, 5 mm. In (c), the ~5 mm^{2} CCD chip captures only a quarter of the beam. Self-trapped beam diameters at different times are indicated in individual images; scale bar in (a-c) = 500 µm; colour intensity scales are provided. (d) Side-view photographs tracing the evolution of a self-trapped beam generated with a 10 mm-wide LED beam at 0.13 mWmm^{-2} in a 7 cm-long cell and (e) corresponding self-induced microstructure after post-irradiation polishing. Scale bar in (d), (e) = 1 cm.

Comparable behaviour is observed for the mid-sized and large beams; both undergo a significant increase in relative intensity from 9.8 % to 99 % and 8.3 % to 100 %, respectively (Figure 6.2(b-c)). However, in these cases, the overall beam diameters remain approximately the same even as their intensities increase; intensity profiles at the exit face show that, instead of self-trapping as a whole, these beams spontaneously divide into filaments - multiple, localized regions of high intensity. We have previously shown that filamentation due to the modulation instability (MI) of optical fields in photopolymerizable systems occurs under the same conditions as self-trapping for beams.[25,33,34] MI occurs when the propagating beams are broad and possess a nearly flat-topped intensity profile instead of the narrow profiles with strong intensity gradients, which lead to self-trapping. Adventitious noise embedded in a broad beam becomes greatly amplified under the nonlinear conditions generated by polymerization and triggers its division into multiple filaments.[25,33,34] Like self-trapped beams, filaments become entrapped within microscopic, self-induced waveguides and propagate without diverging through the medium. Collectively, this ensemble of self-trapped filaments suppresses the *overall* divergence of the beam (leading to the intensity increase at the exit face) and inscribes the corresponding cylindrical object in the medium (*vide infra*).

While mask-based stereolithographic patterns in photopolymer resins typically propagate to < 100 μm, self-trapped beams in the epoxide medium can propagate over several cm (limited only by the experimental set-up). The sequence of photographs in Figure 6.2(d) acquired along the propagation-axis of an evolving self-trapped LED beam shows that it is at least 7 cm-long. Strikingly, light is confined to the propagation axis and does not escape the evolving self-induced waveguide. By contrast, under linear conditions, the same beam would diverge and diffuse throughout the medium. Indeed, the self-trapped beam in Figure 6.2d shows a distinct narrowing of its propagation front; this is consistent with theoretical simulations, which show that self-trapping results from the dynamic competition between the natural divergence and self-focusing of the beam.[29,35,36] Self-trapping of the beam in Figure 6.2d was deliberately arrested mid-way to preserve its tapered, focusing profile and the corresponding tapered epoxide structure (Figure 6.2e). Once the LED beam is switched off, the self-induced cylindrical structure, which is attached to the cell entrance face, remains suspended in the residual unpolymerized and entirely fluid epoxide sol. When detached, the structure is free-standing, mechanically and thermally robust.

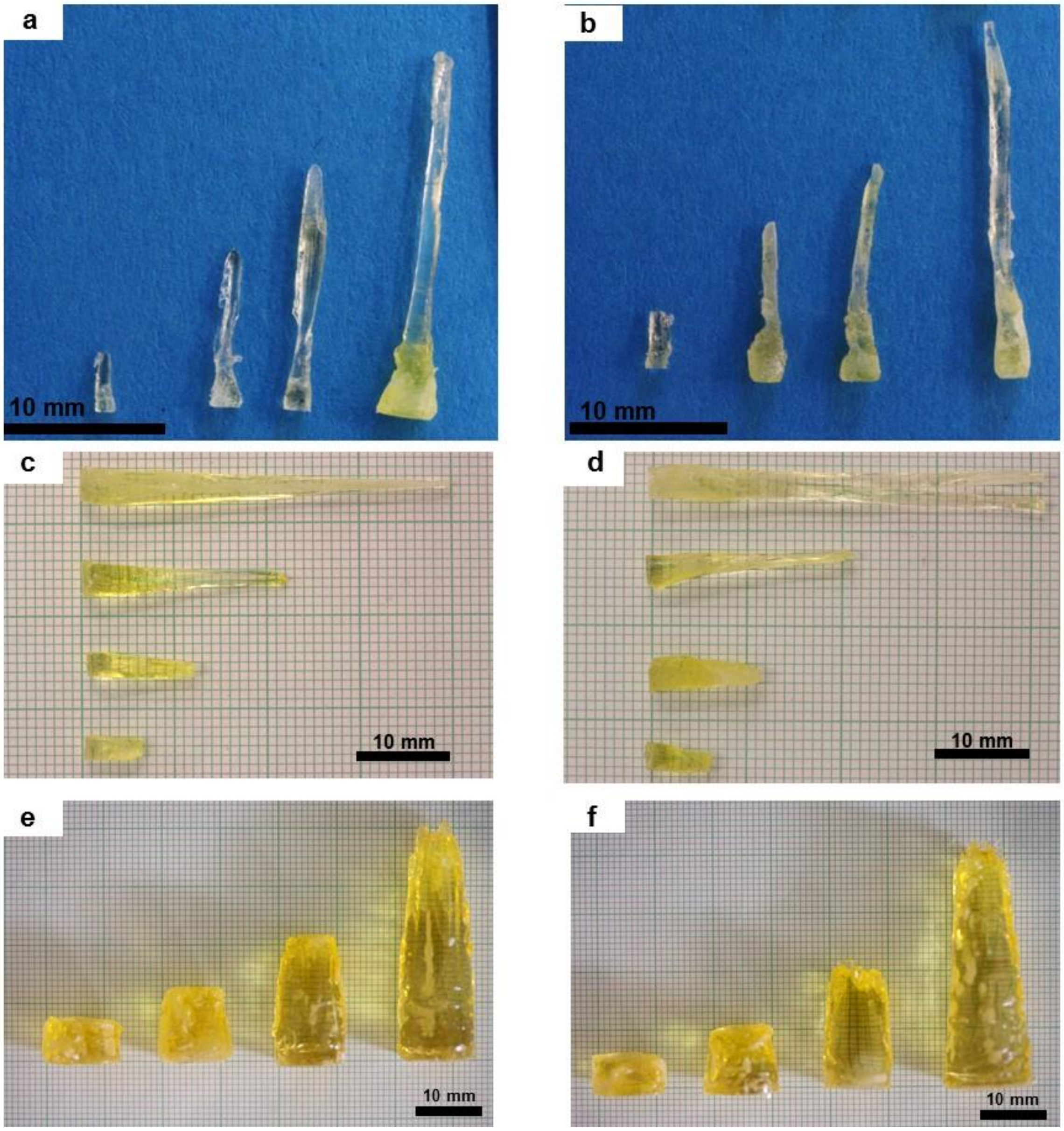

Figure 6.3. Photographs of unprocessed, free-standing epoxide structures self-induced by LED beams with (a) diameter = 0.5 mm in cell pathlengths = 3 mm, 10 mm, 15 mm, 20 mm and incident intensity 51 mWmm^{-2} and (b) 102 mWmm^{-2} (c) diameter = 2 mm in cell pathlengths = 5 mm, 10 mm, 20 mm, 40 mm with incident intensity = 10 mWmm^{-2} and (d) 22 mWmm^{-2} (e) diameter = 10 mm at sample pathlengths = 5 mm, 10 mm, 20 mm and 40 mm and incident intensity = 0.13 mWmm^{-2} and (f) 0.25 mWmm^{-2}

Table 6.1. Dependence of self-trapping time on beam diameter, incident intensity and cell pathlength

Beam diameter [mm]	**Intensity** [mWmm^{-2}]	**Self-trapping time** [s] at different **pathlengths [PL]** [mm]					
		PL = 3	**PL = 5**	**PL = 10**	**PL= 15**	**PL = 20**	**PL =40**
0.5	51	1578		2493	11764	11463	
	102	659		1655	5639	4914	
2.0	10		606	964		2712	5606
	22		297	375		802	2641
10.0	0.13		755	1399		4355	12806
	0.25		689	1013		2786	4706

A particularly significant feature of 3D NSCRIPT is that it employs relatively low intensity, continuous wave, visible wavelength from a LED light source. In addition to being miniaturized, commercially available, inexpensive and considerably safer than high intensity laser or high energy UV sources, LED light is also spatially and temporally incoherent. While coherent laser light was considered necessary to excite nonlinear waves, studies over the past fifteen years have shown that light sources such as incandescent bulbs can also generate a nonlinear waves.[32,34] We have shown that photopolymerization processes are particularly effective in eliciting nonlinear waves of incoherent light; the relative slow kinetics of polymerization (ms to s) respond to the time-averaged intensity profiles of incoherent beams and are entirely insensitive to the femtosecond-scale phase and amplitude fluctuations that could disrupt self-trapping in more sensitive systems.[26,27,33] Furthermore, photopolymers have a finite number of unsaturated moieties and therefore changes in refractive index, which saturate over time; this is critical as it prevents catastrophic self-focusing of the beam, which could generate extremely high intensities and damage the medium.

A wide range of structures can be obtained through 3D NSCRIPT through variation of parameters such as beam size, incident intensity and cell pathlength. Figure 6.3 collects representative photographs of (unprocessed) cylindrical samples generated by self-trapped LED beams with near-parabolic intensity profiles; corresponding Table 6.1 lists changes in self-trapping time (defined as the time at which the maximum intensity and minimum diameter of the beam is achieved) with beam size, intensity and pathlength. Corresponding plots are provided in Supplementary Figures S1-S2. In general, greater incident intensities increase the speed of sample generation although in the case of smaller beam features, rapid self-trapping and polymerization can lead to structural defects such as the branching observed in Figure 6.3d. LED beams that are wider require smaller intensities to form self-trapped beams and there is a general increase in self-trapping time with increasing pathlength. The structures in Figure 6.3 are raw and did not have post-irradiation processing; their uneven surfaces are due to partially polymerized epoxide gel, which can be easily removed through polishing to reveal the fully polymerized epoxide cylinder (*vide infra*).

Figures 6.2 and 6.3 show that by varying beam size, intensity and pathlength, it is possible to generate a wide range of cylindrical epoxide structures. Figure 6.4 shows that the 3D NSCRIPT technique can be extended to generate both metallodielectric and dielectric objects with varying geometries and structural complexity. To demonstrate, we fabricated a working model of the da Vinci catapult (inspired by the Pathfinders wooden catapult kit).[37] Figure 6.4(a-d, f) contains photographs of individual 3-D components of the catapult with different shapes and dimensions including the gear, launch arm, support slabs and drum, all of which were self-induced by self-trapped LED beams. We used the dependence of self-trapping on optical intensity, beam diameter and pathlength listed in Table 6.1 as a guide to identify and optimize the conditions necessary to fabricate these components. In addition to their unique geometries, the components have thicknesses – or depths - ranging from 5mm (gear), 10mm (support slabs), 6cm (drum) to 7cm (launch arm). While the gear and support slabs have uniform thickness, the drum and launch arm have tapered profiles. (Parts of the catapult such as the tension springs were sufficiently thin to construct through top-down irradiation).

The components in Figure 6.4(a-d) were generated with a single LED beam. The launch cup of the catapult consists of the cup and a narrow handle, which connects to the launch arm; to generate this structure as a seamless object, we launched two counter-propagating LED beams bearing the narrow and wide rectangular patterns corresponding to the cross-sectional profiles of the cup and handle, respectively. Once self-trapped, the counter-propagating beam pair propagated through the sample cell with pathlength = 3 cm. The intensity of each beam was adjusted so that the self-trapped beam bearing the handle pattern propagated to ~1.5 cm while that with the cup pattern propagated to ~1.5XX cm (can you please clarify this); side-view photographs in Figure 6.4e show that when the self-trapped beams were in each other's vicinity, they spontaneously fused, permanently connecting the two features together. The interactions of self-trapped beams rely on mutually induced refractive index changes;[38] we have previously shown that when separated by distances commensurate with the beam widths, two parallel beams of incoherent light propagating in a photopolymerizable medium fuse into a single self-trapped beam.[39] We reason that a similar mechanism underlies the fusion of the counter-propagating self-trapped LED beams. When sufficiently close to each other, the beams become entrapped in mutually induced regions of high refractive index and reinforce evolving structure.

The majority of components were all-dielectric and generated with the epoxide photopolymerizable resin (Supplementary Information, Scheme S1).[40]

Figure 6.4a is the gear of the waveguide, which was generated by launching a broad LED beam bearing the gear-pattern through the medium. In this case, the deep maroon colour of the resulting structure originates from the plasmon resonance of Au nanoparticles distributed in the epoxide medium. This was generated by *in situ* photo-generation of Au particles, which occurred simultaneously with polymerization. *In situ* synthesis of Au nanoparticles during photopolymerization was achieved by using two different salts namely $HAuCl_4$ (Au nanoparticles precursor) and iodonium salt (photoinitiator), which are capable of oxidizing photo generated free radical. Upon photoirradiation, visible light sensitizer, camphorquinone in presence of hydrogen donor (polybutanediol) generates free radicals, which reduce $HAuCl_4$ to Au nanoparticles and also part of the free radicals reduce the iodonium salt to form Bronsted acid, which initiates the ring opening polymerization of epoxide (Scheme S2). TEM and EDX analysis show the presence of 10±3 nm diameter spherical Au nanoparticles (Supplementary Information, Figure S3).[30] Figure 6.4h traces the spatial intensity profile of the beam generating a gear, confirming that nonlinear wave formation and self-induction also occurs in the case of the Au salt-doped system. SEM micrograph of the gear shows resolution upto 500 μm can be achieved (figure 6.4g). All of the components generated underwent post-irradiation polishing and smoothing to remove partially polymerized epoxide at the surface (photographs of unprocessed components are provided in Supplementary Information, Figure S4);

features such as the central hole of the gear and hollowed region in the launch cup were also mechanically drilled post-irradiation.

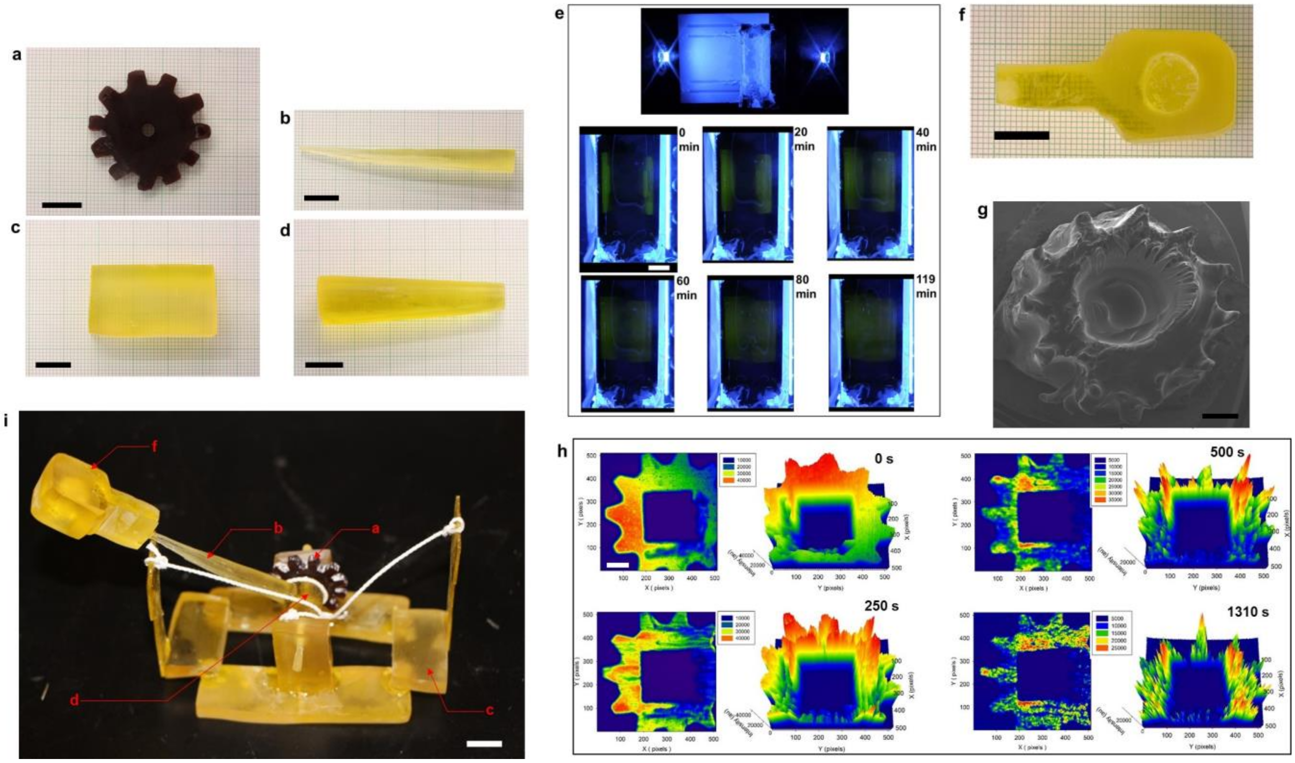

Figure 6.4. Components of catapult made of single beam and two beam self-trapping, (after polishing) a) gear b) launch arm launch cup c) support slab b), d) drum and e) simultaneous self-trapping of two beams over time, (top view pictures) f) lunch cup, formed by two beam self-trapping, scale bar in a-f = 10 mm, g) SEM micrograph of gear, scale bar = 1mm, h) temporal evolution of self-trapped beam with gear pattern at the exit face 5mm,2D and 3D intensity profiles scale bar = 1mm, intensity in each image is normalized to the maximum intensity i) assembled catapult, scale bar = 10 mm. Video of two beam self-trapping and working catapult attached in the supplementary.

6.4. Conclusion

In conclusion, we have developed a new photolithographic route for generating seamless epoxide dielectric and metallodielectric 3D structures by utilizing self-trapping of optical field in cationically polymerizable epoxide systems. By understanding the correlation between optical parameters (intensity, beam size and pathlength) and epoxide polymerization kinetics, single beam and two beam self-trapping were achieved. Complex functional dielectric and metallodielectric 3D components were fabricated by using the optical self-trapping and the capability of the technique was demonstrated by constructing a working da Vinci catapult.

References

(1) Brian, D. *Science*, **2012**, *338*, 921–926.

(2) Pearce, J. M. *Science,* **2012**, *337*, 1303–1304..

(3) Murphy, S. V; Atala, A. *Nat. Biotechnol.* **2014**, *32* (8), 773–785.

(4) Bi, G.; Sun, C. .; Chen, H. .; Ng, F. .; Ma, C. . *Mater. desing* **2014**, *60*, 401–408.

(5) Tekinalp, H. L.; Al, E. *Compos. Sci. Technol.* **2014**, *105*, 144–150.

(6) Guijun, B.; Ng, L. K. .; Teh, K. .; Jarfors, E. . *Mater. desing* **2010**, *31*, S112–S116.

(7) Paul, C. P.; Ganesh, P.; Mishra, S. K.; Bhargava, P.; Negi, J.; Nath, A. K. *Opt. Laser Technol.* **2007**, *39* (4), 800–805.

(8) Cesaretti, G.; Dini, E.; De Kestelier, X.; Colla, V.; Pambaguian, L. *Acta Astronaut.* **2014**, *93*, 430–450.

(9) Chua, C. .; Leong, K. .; Lim, C. . *Rapid prototyping-Principles and Applications*; John Wiley & Sons, 2003.

(10) Hull, C. W. Apparatus for production of three-dimensional objects by stereolithography. US 4,575,330, **1986**.

(11) Modrek, B.; Calif, A. Methods and Apparatus for production of three-dimensional objects by stereolithography. US 4,996,010, **1991**.

(12) Tumbleston, J. R.; Shirvanyants, D.; Ermoshkin, N.; Johnson, A. R.; Kelly, D.; Chen, K.; Pinschmidt, R.; Rolland, J. P.; Ermoshkin, A.; Samulski, E. T.; DeSimone. J.M. *Science*, **2015**, 347, 1349-1352.

(13) Gothait, H. Apparatus and method for three dimensional model printing. US 6,259,962 B1, **2001**..

(14) Singh, R. *J. Mech. Sci. Technol.* **2011**, *25* (4), 1011–1015.

(15) Crump, S. S. Apparatus and method for creating three-dimensional objects. US 5,121,329, **1992.**.

(16) Skowyra, J.; Pietrzak, K.; Alhnan, M. A. *Eur. J. Pharm. Sci.* **2015**, *68*, 11–17.

(17) Bredt, J. .; Anderson, T. Method of three dimensional printing. US 5,902,441, **1999**..

(18) Russell, I. D. B.; Bredt, J. F.; Vogel, M. J.; Seymour, M.; Boston, S.; Bornhorst, W. J.; Marina, I. Method and apparatus for prototyping a three-dimensional object. US 6,007,318, **1999**..

(19) Vorndran, E.; Klarner, M.; Klammert, U.; Grover, L. M.; Patel, S.; Barralet, J. E.; Gbureck, U. *Adv. Eng. Mater.* **2008**, *10* (12), B67–B71.

(20) Kruth, J. P.; Van der Schueren, B.; Bonse, J. E.; Morren, B. *CIRP Ann. - Manuf. Technol.* **1996**, *45* (1), 183–186.

(21) Deckard, C. .; Beaman, J. . Method for selective laser sintering with layerwise cross-scanning. US 5,155,324, **1992**..

(22) Schueren, B. Van Der; Kruth, J. P. *Rapid Prototyp. J.* **1995**, *1* (3), 23–31.

(23) Wiria, F. E.; Leong, K. F.; Chua, C. K.; Liu, Y. *Acta Biomater.* **2007**, *3* (1), 1–12.

(24) Hartmann, A. .; Tjellesen, F. . Three-dimensional printer. US 2012/0201960 A1, **2012**..

(25) Basker, D. K.; Brook, M. a.; Saravanamuttu, K. *J. Phys. Chem. C* **2015**, *119* (35), 20606–20617.

(26) Zhang, J.; Kasala, K.; Rewari, A.; Saravanamuttu, K. *J. Am. Chem. Soc.* **2006**, *128*, 406–407.

(27) Zhang, J.; Saravanamuttu, K.; Ls, O. *J. Am. Chem. Soc.* **2006**, *280* (23), 14913–14923.

(28) Villafranca, A. B.; Saravanamuttu, K. *Journa Phys. Chem. c* **2008**, *112*, 17388–17396.

(29) Monro, T. M.; Sterke, C. M. D. E.; Poladian, L. *Jounral Mod. Opt.* **2001**, *48* (2), 191–238.

(30) Yagci, Y.; Sangermano, M.; Rizza, G. *Macromolecules* **2008**, *41* (20), 7268–7270.

(31) Cohen, O.; Uzdin, R.; Carmon, T.; Fleischer, J. W.; Segev, M.; Odoulov, S. *Phys. Rev. Lett.* **2002**, *89* (22), 229901.

(32) Mitchell, M.; Chen, Z.; Shih, M.; Segev, M. *Phys. Rev. Lett.* **1996**, *77*, 490–493.

(33) Burgess, I. B.; Shimmell, W. E.; Saravanamuttu, K. *J. Am. Chem. Soc.* **2007**, *129* (15), 4738–4746.

(34) Buljan, H.; Šiber, A.; Soljačić, M.; Segev, M. *Phys. Rev. E - Stat. Nonlinear, Soft Matter Phys.* **2002**, *66* (3), 1–4.

(35) Monro, T. M.; Poladian, L.; Sterke, C. M. de. *Phys. Rev. E* **1998**, *57* (1), 1104–1113.

(36) Trillo, S., Torruellas, W., Eds. *Spatial Solitons*; Springer: New York, **2001**; pp 19-33

(37) http://www.mastermindtoys.com/Pathfinders-Leonardo-da-Vinci-Wooden-Catapult-Kit.aspx

(38) Stegeman, George I and Segev, M. *Science (80-.).* **1999**, *286* (November), 1518–1522.

(39) Kasala, K.; Saravanamuttu, K. *Appl. Phys. Lett.* **2008**, *93* (5), 111–114.

(40) Crivello, J. V. *J. Polym. Sci. Part A Polym. Chem.* **2009**, *47*, 866–875.

Supplementary Information

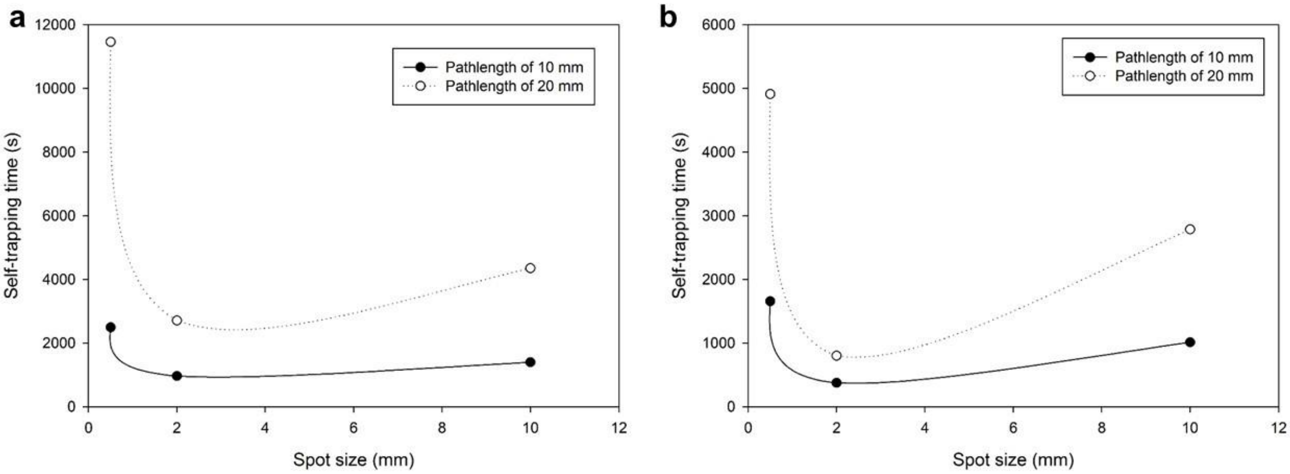

Figure S6.1 Dependence of self-trapping time on beam diameter at (a) lower intensity threshold for each diameter (51 mWmm^{-2} for 0.5 mm; 10 mWmm^{-2} for 2.0 mm; 0.13 mWmm^{-2} for 10.0 mm) and (b) upper intensity threshold (102 mWmm^{-2} for 0.5 mm; 22 mWmm^{-2} for 2.0 mm; 0.25 mWmm^{-2} for 10.0 mm). Results are provided for pathlengths of 10 mm and 20 mm. Lines are a guide to the eye only.

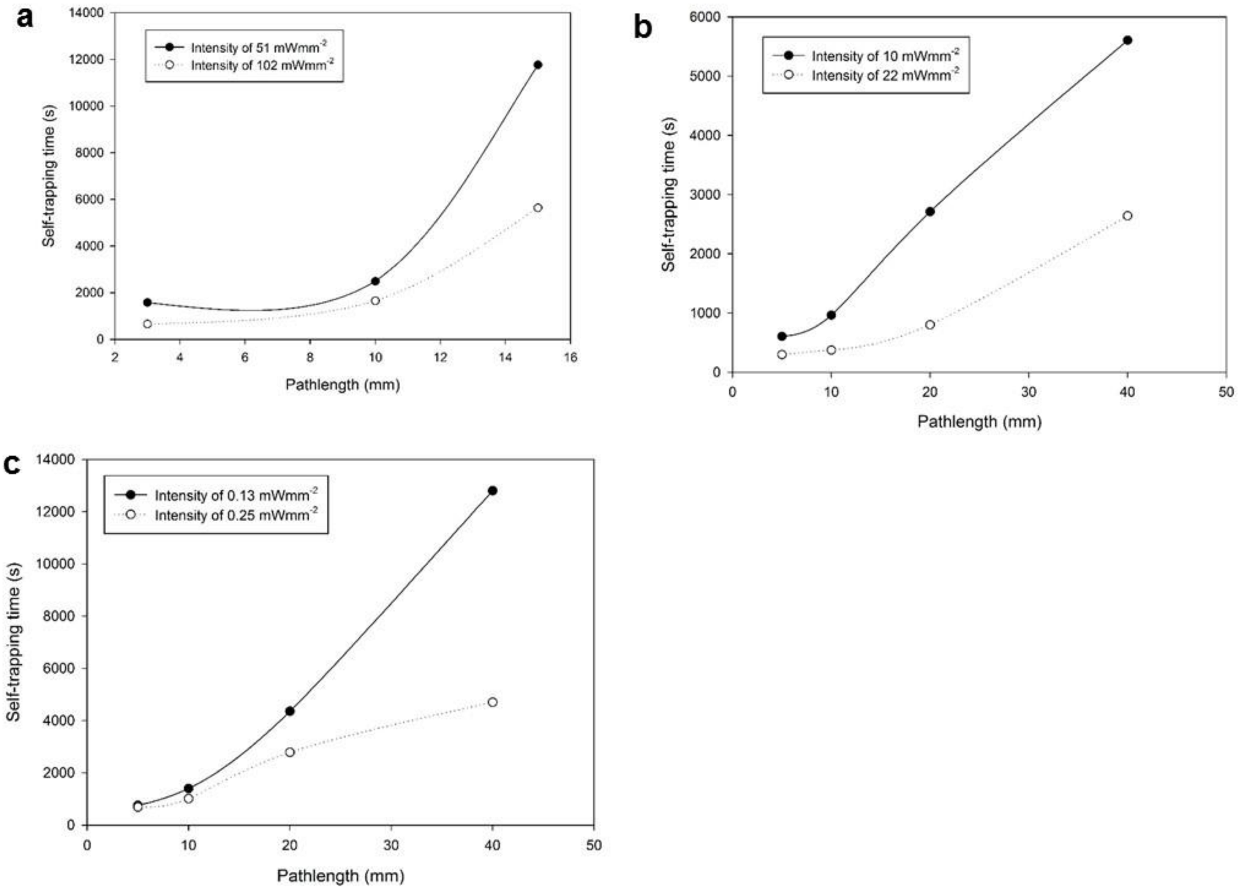

Figure S6.2 Self-trapping time as a function of pathlength at lower and upper threshold intensities for beams with diameter (a) 0.5 mm, (b) 2.0 mm and (c) 10.0 mm. Lines connecting points are guides to the eye only and were not fitted to data.

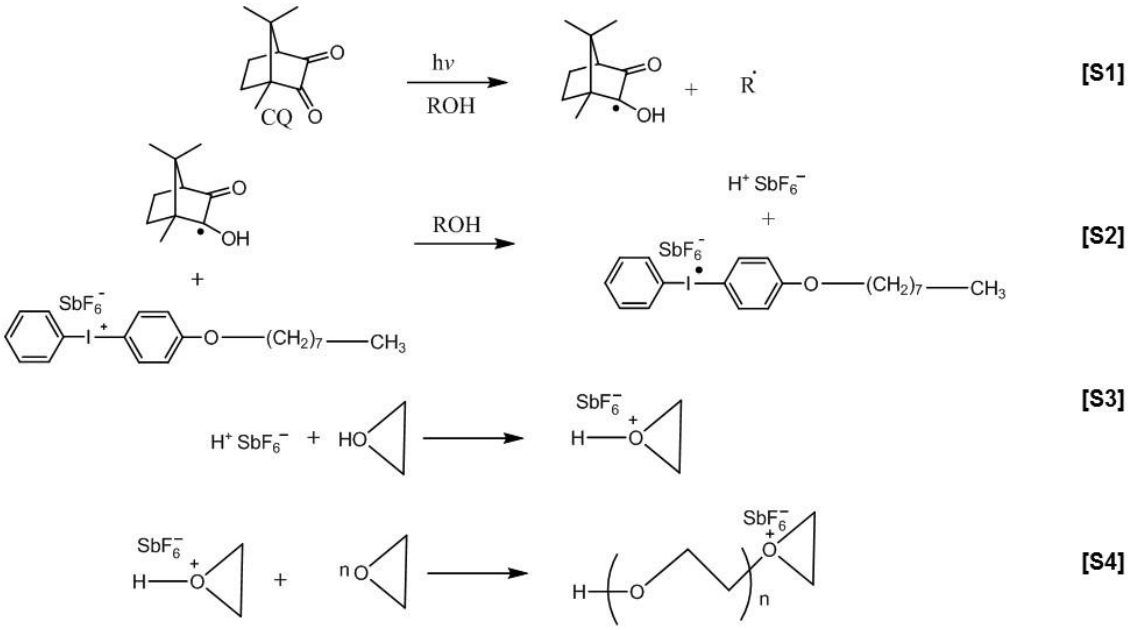

Scheme S6.1 Visible light photopolymerization of epoxide[40]

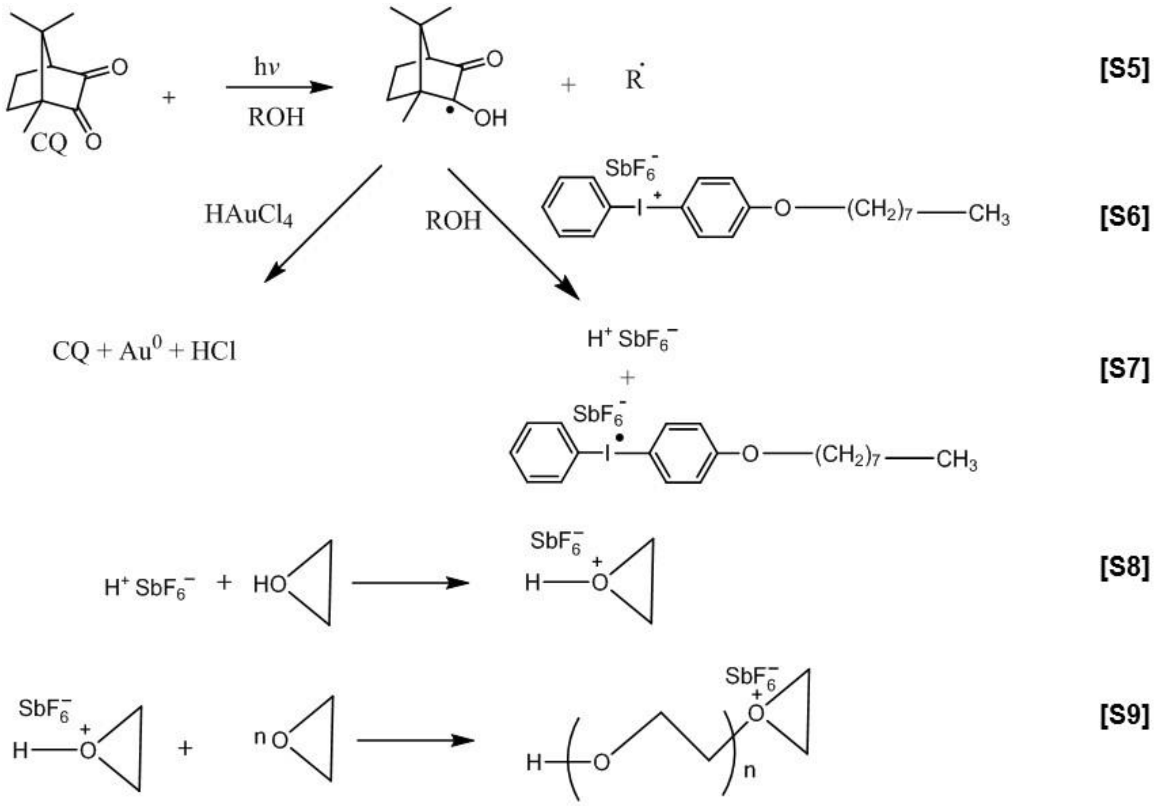

Scheme S6.2 *In-situ* synthesis of gold nanoparticles *via* photo-induced electron transfer[30]

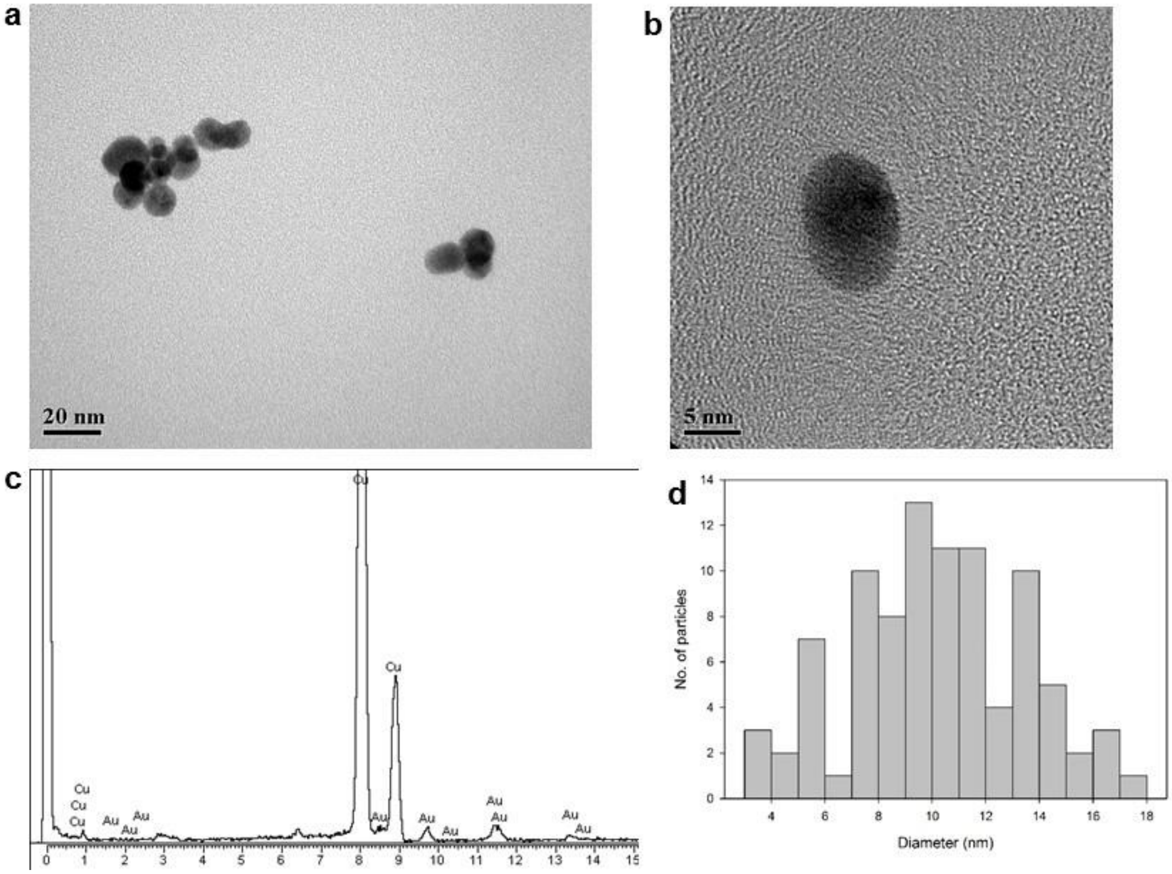

Figure S6.3 a) TEM micrograph showing the spheroid nanoparticles b) high resolution TEM micrograph showing the formation of single particles c) EDX spectrum confirming the nanoparticles as Au d) Histogram of the particle size distribution (70 individual particles studied).

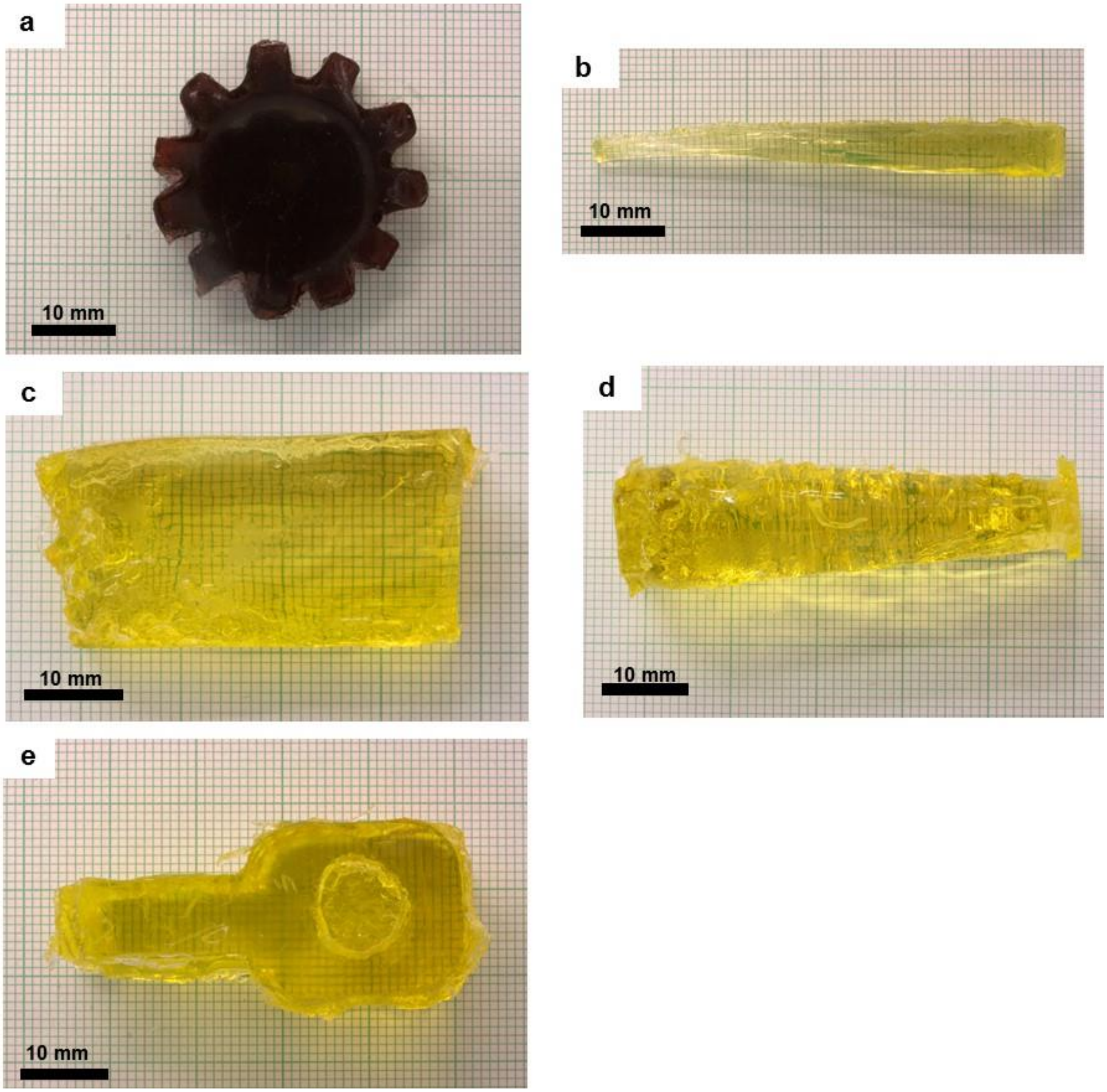

Figure S6.4 Photographs of unprocessed components of the catapult a) gear b) launch arm c) support slab d) drum and e) launch cup.

7. Conclusions and future directions

7.1 Conclusions

MI induced spontaneous pattern formation of a broad, uniform, incandescent beam was studied in photocationically polymerizable epoxide systems for the first time and we found that the dynamics of the MI process can be controlled by polymerization kinetics. This is a significant result, because over the past five decades MI process in nonlinear systems was controlled only through optical parameters such as intensity, wavelength and coherence of the light source. In this research, based on the works of Crivello, a visible light cationic polymerizable epoxide system with camphorquinone as visible light sensitizer, bis(4-tert-butyl)iodonium hexafluoroantimonate as photoinitiator and benzyl alcohol as non-basic proton donor was developed. Refractive index change (Δn) originating from the cross-linking polymerization of epoxide groups provided the nonlinear condition required for the MI of incandescent beam. Polymerization rate and extent of cross-linking were used to control the dynamics of MI process. The former determined the photoresponsive time on the system and the later determined the magnitude of Δn. We used benzyl alcohol (which participates in the initiation, propagation and termination steps of the cross-linking polymerization of epoxide) to systematically vary these two parameters and observed that MI occurs only within a narrow range of benzyl alcohol concentration, where the photoresponsive time of the system is fast enough to capture the noise in the system and the magnitude of Δn is large enough to initiate the MI process. When the concentration of benzyl alcohol was outside this range, MI was not observed. Epoxide systems used for the MI process were thoroughly characterized using IR and Raman spectroscopy, differential scanning calorimetry and gel content measurement. Occurrence of MI in these systems was captured using CCD camera. MI induced optical waveguides originating from the irreversible polymerization reaction (which provides the required Δn for the MI process) inscribed permanent 3D polymer optical waveguide structures in the medium. Thus, the MI induced spontaneous pattern formation of incoherent light was shown in cationcally polymerizable epoxide systems and the dynamics of the MI process was described using polymerization kinetics. Also we demonstrated a powerful, single-step, room-temperature technique to generate functional 3D waveguide structures in epoxide system using low energy visible light, which would be highly difficulty to fabricate using conventional techniques [chapter 2]. Cycloaliphatic epoxide systems used in this work has its own limitations in terms of physical properties, cross-linked polymer matrix is too brittle because of the highly cross-linked three dimensional molecular structure and also the presence of volatile benzyl alcohol in the polymer matrix makes the systems temperature sensitive.

For practical applications, the waveguide structures should be thermomechanically stable. Therefore, we made a blend of cycloaliphatic epoxide and siloxane terminated epoxide (epoxypropoxypropyl terminated siloxane, EDMS) and replaced the benzyl alcohol with polybutanediol (pTHF) to enhance the thermomechanical properties. EDMS was used as toughening agent, as it enhances the toughness of blend without deteriorating the optical transparency and inherent thermal stability of cycloaliphatic epoxide. Various ratios of cycloaliphatic epoxide, EDMS and pTFH were tried and off these different compositions, six compositions showed MI induced waveguide formation and these compositions were subjected to mechanical and thermal properties testing. Mechanical properties were studied using tensile strength measurements and thermal properties were evaluated using thermogravimetric analysis and dynamic mechanical analyzer. Compositions were made by varying the amount of EDMS (6 to 40 wt %) and pTHF (10-20 wt %). Addition of 10 wt% of EDMS improved the toughness of the blend (evident from the increase in elongation at break from 2.65 % (for neat cycloaliphatic epoxide) to 7.5 % (for the blend)) and maintained the thermal properties of the blend close to neat cycloaliphatic epoxide except for the reduction in glass transition temperature (reduced from 156± 1.15 ^{0}C to 117± 14.8 ^{0}C). Further increase in EDMS content upto 26 wt % did not show significant impact in toughness behaviour (elongation at break remind the same (~ 7 %)) but increasing EDMS from 26 wt % to 41 wt % had drastically deteriorated both mechanical and thermal properties of the blend because of the microscopic phase separation of the flexible siloxane units from the rigid epoxide matrix and also due to the decrease in cross-link density of the blend. Through this work, we developed thermomechanically stable epoxide/siloxane blend systems that can exhibit MI induced waveguide formation [chapter 3].

One of the objectives of this work is to develop simple yet elegant route for fabricating metal nanoparticles incorporated waveguide structures by using the nonlinear optical wave propagation in cationic polymerizable systems. Waveguide structure can enhance the optical properties of metal nanoparticles, as the characteristic surface plasmon resonance (SPR) of metal nanoparticles responsible for enhancement of variety of optical phenomena, originates from the collective oscillation of conduction band electrons on the surface of metal nanoparticles induced by electromagnetic field and waveguide structure is capable of efficiently concentrating and guiding electromagnetic field. However, dispersing metal nanoparticles in waveguide structures is highly challenging. We resolved this problem by utilizing our understanding of nonlinear optical wave propagation in photocationcally polymerizable systems and developed epoxide systems that can simultaneously undergo MI induced waveguide formation and *in-situ* metal nanoparticles generation. Silver (Ag) nanoparticles embedded waveguide structures were generated by photopolymerizing the cycloaliphatic/EDMS blend system containing silver salt and camphorquinone, through photoinduced electron transfer reaction. Similarly gold (Au) nanoparticles embedded waveguide structures were formed by dispersing gold salt, camphorquinone and photoinitiator in the blend and photopolymerizing the system. Metal nanoparticles in the waveguide structures were thoroughly characterized using UV-Vis spectroscopy and TEM imaging. Also we used LED (monochromatic, blue) lamp to induce MI in these systems and showed it is energy efficient to use LED compare to incandescent white light for eliciting MI. Cross-linking polymerization provides the Δn required for MI induced waveguide formation and *in-situ* synthesis enables simultaneous deposition of metal nanoparticles in these waveguide structures. Thus we generated cylindrical metallodielectric waveguide through a single-step, room temperature and spontaneous route [chapter 4].

In addition to fabricating MI induced metallodielectric waveguides from Au nanoparticles/epoxide-siloxane blend system, we also fabricated near infrared surface enhanced Raman scattering (NIR-SERS) substrate from the system by utilizing the SPR property of Au nanoparticles. Fractal aggregates of Au nanoparticles were generated through chemical reduction. EDMS acted both reducing as well as stabilizing agent. Fractal aggregates were generated by reducing gold salt using EDMS solution and they were stabilized by UV polymerization of the epoxide groups in EDMS. From our knowledge, this is the first work demonstrating the fabrication of epoxide-siloxane thin films embedded with Au fractal nanoparticles aggregates by combining drop casting technique with UV polymerization. SPR of the Au nanoparticles aggregates embedded in the thin film were thoroughly characterized by UV-Vis-NIR spectroscopy and the structure of the aggregates were analyzed by optical and electron microscopy.

Fractal analysis using box-counting method proved the fractal nature of the aggregates and the SERS efficiency of the substrate was demonstrated by detecting trace amounts of Eosin Y dye in solvent [chapter 5].

In the previous works, we have demonstrated MI, a nonlinear optical phenomenon, in photocationically polymerizable epoxide systems and fabricated 3D polymer and metallodielectric microstructures using MI induced spontaneous pattern formation. Using our understanding about the nonlinearity offered by the photocationically polymerizable systems (that enabled MI), we have developed a new 3D printing technique based on optical self-trapping, another nonlinear phenomenon closely related to MI. Both these phenomena occur under similar nonlinear conditions. Our 3D printing technique works based on the principle that an incoherent beam can self-trap in the epoxide medium by initiating cationic polymerization and the refractive index change induced in the medium transforms into a permanent 3D structure as it originates from an irreversible polymerization reaction. Self-trapping process was studied by analyzing self-trapping time (time taken by the beam to reach specific pathlength) as a function of other relevant parameters such as intensity, beam spot size and pathlength. Using the correlation between self-trapping time and other parameters, 3D polymer and metallodielectric structures in epoxide systems were made. The uniqueness of our 3D printing technique is the ability to make continuous 3D structures by optical self-trapping whereas other techniques available in the market rely on a layer-by-layer process. To demonstrate the capability of our technique, we made a working catapult model. Components of the catapult (polymeric and metallodielectric) were printed individually and assembled into a working model [chapter 6].

To summarize, nonlinear propagation of optical field in cationically polymerizable systems was demonstrated for the first time and it was used to make 3D polymeric and metallodielectric structures.

7.2 Future directions

Demonstration of nonlinear optical wave propagation in photocationic polymerizable systems can lead to variety of new works. We propose the following new research ideas based on this thesis work;

Apart from MI and self-trapping, previous works from our group have shown interesting self-action nonlinear phenomena such as diffraction ring formation,[1] filamentation of soliton,[1] attraction and repulsion of solitons,[2] and dark beam self-trapping.[3] Similar to the results from this research work (manipulation of MI dynamics through epoxide polymerization kinetics), dynamics of all these nonlinear phenomena can also be manipulated using polymerization kinetics. Studying these nonlinear phenomena in epoxide systems, which is offering control over polymerization kinetics, can lead to new understanding of these phenomena. And also as mentioned before, these nonlinear phenomena greatly depend on the type of nonlinear media used. Photocationic polymerization covers a wide range of monomers, it can be used to polymerize carbocationic addition polymerization of unsaturated monomers such as vinyl ethers, n-vinylcarbozole and styrene and also the ring opening polymerization of cyclic ethers, cyclic acetals and lactones.[4] Thus the above mentioned nonlinear phenomena can be studied in a wide range of cationic polymerizable systems.

Metal (Au &Ag) nanoparticles embedded epoxide waveguide structures fabricated in this research work by combining MI with *in-situ* metal nanoparticles synthesis provide interesting opportunities. As mentioned earlier, having metal nanoparticle in waveguide structures leads to enhancement of variety of optical phenomena exhibited by metal nanoparticles. One of these phenomena is second harmonic generation (SHG), through which two photons at fundamental frequency are combined to form one photon at harmonic frequency.[5] SHG is forbidden in materials with inversion symmetry as their first hyperpolarizability value is zero.[5] Interestingly symmetric metal (spherical Au & Ag) nanoparticles with centrosymmetric crystal lattices (with inversion symmetry) exhibit SHG.[5] Origin of SHG in symmetric Au & Ag nanoparticles is explained by breakdown of centrosymmetry at the surface of these nanoparticles.[5] Such symmetry breaking can occur due to irregularities at the surface of the particles[5] or due to surrounding dielectric media.[6] Epoxide medium making the waveguide structures in our system can lead to such symmetry breaking and therefore enable SHG from the embedded Au & Ag nanoparticles. Once the symmetry is broken, the first hyperpolarizability and thereby SHG in Au & Ag nanoparticles results from the excitation of electric dipole and quadrupole by electromagnetic field.[5,7] Waveguides can efficiently concentrate and transmit electromagnetic field. Thus our Au & Ag nanoparticles embedded waveguide structures can lead to symmetry breaking and also can enhance the excitation field, which would result in enhanced SHG. Because of these two effects our metallodielectric structures would serve as an ideal material for generating second harmonic frequency from fundamental frequency. In addition to this, the epoxide matrix shows negligible near IR (used as a fundamental source in SHG) absorption and high thermomechanical stability (IR irradiation results in heat generation and so thermal stability is essential). These factors would be an additional advantage in using our structures.

Following SHG, the metallodielectric structures can be used for supercontinuum generation, i.e., spectral broadening of the fundamental excitation wavelength by nonlinear media, another interesting nonlinear optical phenomenon.[8] The phenomenon offers rich fundamental physics to study and also has great potential in applications ranging from telecommunication to medicine.[9] It originates from complex nonlinear processes such as temporal modulation instability, self-phase modulation, stimulated Raman scattering, four-wave mixing (FWM). [9] Initially supercontinuum was studied in photonic crystal fibers[9] but later on it was observed in glasses,[9] semiconductors,[10] liquids[11] and metal nanoparticles.[8] One of the supercontinuum generation mechanisms, self-phase modulation, occurs by strong interaction of light with nonlinear media, which can be attained by high localization of light in both space and time.[12] Our waveguide structures are highly efficient in spatio-temporal confinement of light. In particular, waveguides embedded with intrinsically high nonlinear coefficient metal nanoparticles (Ag &Au), can be efficient in supercontinuum generation through self-phase modulation.[8,12] Thus, our metallodielectric structures would be an ideal platform to study supercontinuum generation.

Another interesting direction is the fabrication of surface plasmon polariton (SPP) waveguides using the epoxide/metal nanoparticles systems. SPP waveguides can provide lateral mode confinement at nanoscale dimension (which is not possible by conventional dielectric waveguides) and allow transmission of electromagnetic energy well below the diffraction limit, which is essential for photonics device applications.[13] Initially SPP waveguiding was demonstrated only in periodically arranged nanoparticle systems[13] (periodicity less than the wavelength of transmitted electromagnetic field) but later on it was shown in randomly arranged nanometallic structures as well.[14] Based on the latest works, our metallodielectric waveguide structures can be converted to SPP waveguides. Though the concentration of metal nanoparticles in our present structures is not sufficient to exhibit SPP, there is scope to increase the nanoparticles concentration, particularly for the Au nanoparticles system, where the polymerization and *in-situ* synthesis are achieved through two different chemical routes. Currently, SPP waveguides are fabricated using complex technique such as electron beam lithography,[13] laser evaporation[14] and self-assembly techniques.[15] Apart from the complexity of the fabrication process, it is highly challenging to couple electromagnetic field to metal nanostructures. Using our elegant metallodielectric waveguide structure fabrication process for SPP waveguide fabrication would eliminate both these problems. Our technique is a spontaneous, single step, room temperature technique done using low energy visible light which would eliminate the fabrication complexity and coupling of electromagnetic field to nanoparticles would be easier as the particles are embedded in a dielectric waveguide structures. Thus fabrication of SPP waveguides would be an interesting extension of present work.

On the whole, demonstration of nonlinear optical wave propagation in cationic polymerization systems takes the field of nonlinear optics to a significant step forward in terms of fundamental understanding about incoherent light propagation in nonlinear media and also leads to various potential applications in the field of photonics.

References

(1) Villafranca, A. B.; Saravanamuttu, K. *J. Opt. Soc. Am. B* **2012**, *29* (9), 2357–2372.

(2) Kasala, K.; Saravanamuttu, K. *Appl. Phys. Lett.* **2008**, *93* (5), 111–114.

(3) Kasala, K.; Saravanamuttu, K. *J. Am. Chem. Soc.* **2012**, *134*, 14195–14200.

(4) Sangermano, M.; Razza, N.; Crivello, J. V. *Macromol. Mater. Eng.* **2014**, *299* (7), 775–793.

(5) Nappa, J.; Revillod, G.; Russier-Antoine, I.; Benichou, E.; Jonin, C.; Brevet, P. F. *Phys. Rev. B - Condens. Matter Mater. Phys.* **2005**, *71* (16), 1–4.

(6) Butet, J.; Duboisset, J.; Bachelier, G.; Russier-Antoine, I.; Benichou, E.; Jonin, C.; Brevet, P. F. *Nano Lett.* **2010**, *10* (5), 1717–1721.

(7) Russier-Antoine, I.; Benichou, E.; Bachelier, G.; Jonin, C.; Brevet, P. F. *J. Phys. Chem. C* **2007**, *111*, 9044.

(8) Driben, R.; Husakou, A.; Herrmann, J. *Opt. Express* **2009**, *17* (20), 17989–17995.

(9) Dudley, J. M.; Genty, G.; Coen, S. *Rev. Mod. Phys.* **2006**, *78* (4), 1135–1184.

(10) Gu, F. X.; Yu, H. K.; Fang, W.; Tong, L. M. *Opt. Express* **2012**, *20* (8),

8667–8674.

(11) Wang, C.; Fu, Y.; Zhou, Z.; Cheng, Y.; Xu, Z. *Appl. Phys. Lett.* **2007**, *90* (18).

(12) Kandidov, V. P.; Kosareva, O. G.; Golubtsov, I. S.; Liu, W.; Becker, A.; Akozbek, N.; Bowden, C. M.; Chin, S. L. *Appl. Phys. B Lasers Opt.* **2003**, *77* (2-3), 149–165.

(13) Maier, S. a; Kik, P. G.; Atwater, H. a; Meltzer, S.; Harel, E.; Koel, B. E.; Requicha, A. a G. *Nat. Mater.* **2003**, *2* (4), 229–232.

(14) Bozhevolnyi, S. I.; Volkov, V. S.; Leosson, K. *Phys. Rev. Lett.* **2002**, *89* (18), 186801.

(15) McMillan, R. A.; Paavola, C. D.; Howard, J.; Chan, S. L.; Zaluzec, N. J.; Trent, J. D. *Nat. Mater.* **2002**, *1* (4), 247–252.